NASA/CR-2002-211672

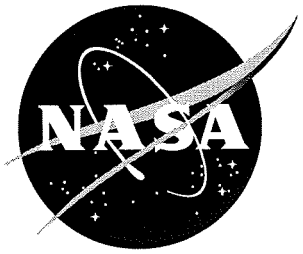

Advanced Nacelle Acoustic Lining Concepts Development

G. Bielak, J. Gallman, R. Kunze, P. Murray, J. Premo, and M. Kosanchick
Boeing Commercial Airplane Company, Seattle, Washington

A. Hersh, J. Celano, and B. Walker
Hersh Acoustical Engineering, Westlake Village, California

J. Yu, H. W. Kwan, and S. Chiou
BF Goodrich, Chula Vista, California

J. Kelly, J. Betts, J. Follet, and R. Thomas
Virginia Consortium of Engineering & Sciences Universities, Hampton, Virginia

National Aeronautics and
Space Administration

Langley Research Center
Hampton, Virginia 23681-2199

Prepared for Langley Research Center
under Contract NAS1-97040, Task 4

August 2002

Available from:

NASA Center for AeroSpace Information (CASI)
7121 Standard Drive
Hanover, MD 21076-1320
(301) 621-0390

National Technical Information Service (NTIS)
5285 Port Royal Road
Springfield, VA 22161-2171
(703) 605-6000

ABSTRACT

The work reported in this document was conducted under NASA contract NAS1-97040 Aircraft and Engine Noise - Task 4 (Advance Nacelle Acoustic Lining Concepts). The task was managed by the Fluid Mechanics and Acoustics Division of NASA Langley Research Center. Mr. Tony Parrott, and Mr. Mike Jones were the Technical Monitors for this task. This work was a continuation of the AST lining development work started at Boeing in 1994. Studies reported in this document include:

Analysis of Model Scale ADP Fan Duct Lining Data	Boeing
Bias Flow Liner Investigation	Boeing, VCES
Grazing Flow Impedance Testing	Boeing, GE, NASA, BFG
Development of Micro-Perforate Acoustic Liner Technology	BFG, HAE, NG
Extended Reaction Liners	Boeing, NG
Development of a Hybrid Active/Passive Lining Concept	HAE

Page intentionally left blank

TABLE OF CONTENTS

Appendicies

LIST OF FIGURES

LIST OF TABLES

1.0 INTRODUCTION

The Advanced Subsonic Technology Noise Reduction Program (AST) goal is to develop technology to reduce aircraft noise by 10 EPNdB, relative to 1992 technology, by the year 2000. The technology development strategy is a coordinated effort among government, industry and academia addressing engine source understanding and reduction, nacelle aero-acoustics, engine/airframe integration and flight procedures. Interim goals were established which includes a goal to validate concepts to improve nacelle treatment effectiveness by 25% relative to 1992 technology by the second quarter of FY'97. A model fan rig test using the NASA/PW 22 in. diameter ADP model fan was conducted in 1996 to provide data to demonstrate achievement of the 25% goal. A final goal was established at 50% improvement in nacelle attenuation by the year 2000. It is believed that this goal can be achieved with improved nacelle design which goes beyond passive liner efficiency improvements. For example a directional inlet with more efficient application of acoustic lining and active noise control are being developed to help meet this goal. Under AST Noise Reduction Task 5, Boeing has supplied design and analysis tools which substantiate the superior acoustic performance of directional inlets (Ref. 1). Using internal funds, Boeing is aggressively pursuing implementation of directional inlets and has designed and manufactured a full scale test article for a 1998-99 AST Pratt & Whitney (PW) static engine test. The test objective is to evaluate noise reduction concepts for demonstration of the 2000 AST goals.

Boeing has been working to improve nacelle acoustic lining technology under the AST program since 1994. The basis for the early Boeing AST lining technology work, (NAS1-200090 Task 1)1994-1996 (Ref. 2), was a Boeing study conducted in 1993-94 under a preliminary NASA/FAA contract investigating broadband acoustic liner concepts (summarized in Ref. 2). As a result of this work, it was recommended that linear double layer, triple layer, parallel element and bulk absorber liners be further investigated to improve nacelle treatment effectiveness. NASA Langley also suggested that "adaptive" liner concepts, which would allow "in-situ" acoustic impedance control, be considered. As a result, bias flow and high temperature liner concepts were added for investigation.

Using mostly existing tools and past Boeing experience with parallel element and double layer liners, a number of linings were designed, manufactured and tested in Boeing's grazing flow impedance measurement facility during the period 1994-1996. This facility propagates the fundamental mode over the acoustic liner with a flow Mach number up to M=0.5 and determines the effective liner impedance from measurement of the complex acoustic pressure pattern over the length of the liner. The purpose of the testing was to verify the designed impedance spectrum of the liners. In addition, an analytical, lining trade study was conducted to evaluate the potential benefits of these advanced design liners to a mid-sized twin airplane. Lastly, advanced double layer liners were designed for a model scale fan test using the NASA/PW 22 in. diameter ADP model fan to provide data to demonstrate achievement of the 25% goal.

This report presents the results of the Boeing AST nacelle aero-acoustics work conducted in 1997-2000 under NAS1-97040 Task 4. The statement of work is first presented, followed by a summary of the accomplishments relative to the statement of work. More in depth reports are contained as appendicies or referenced.

2.0 STATEMENT OF WORK

The objective for NASA Contract NAS1-97040 Aircraft and Engine Noise -Task 4, "Advanced Turbofan Duct Liner Concepts," was to develop technical knowledge and design

concepts for advanced turbofan duct acoustic linings to help attain the AST goal of 50% nacelle noise reduction capability relative to the year 1992 by the year 2000. The following requirements are set forth in the Statement of Work:

2.1 Analysis of ADP model fan lining test data.

Analyze the results of the model scale test of the advanced fan duct liner Boeing designed in 1995 for the P&W 22 in. ADP model fan tested at the NASA 9x15 acoustic wind tunnel in 1996.

2.2 Bias flow liner investigation

Measure the effect of grazing flow on impedance in the frequency range 1000 to 6000 Hz for bias flow and high temperature liners.

Develop a time-domain modeling process to analyze the effect of bias flow on liner impedance.

Give a sub-contract to the Virginia Consortium of Engineering & Science Universities to study the application of bias flow for controling perforate liner impedance.

2.3 Grazing flow impedance testing

Participate in the NASA/GE/Boeing grazing flow impedance measurement technique evaluation study.

Study the possibility of using steady-flow measurements to determine frequency dependent orifice impedance changes with grazing flow using time-domain analysis.

2.4 Development of micro-perforate acoustic liner technology.

Give sub-contracts to Hersh Acoustical Engineering and BF Goodrich to perform grazing flow and normal incidence impedance measurements of small orifice perforates and develop mathematical models for small orifice impedance based on their results.

Give a sub-contract to Northrop Grumman to investigate the application of ultra-violet lasers for drilling micro-perforate holes for nacelle acoustic lining application.

2.5 Extended reaction lining study

Conduct studies with the Boeing analytical duct propagation computer program to design porous core (extended reaction) liners to be built and tested in a rectangular duct with no flow.

2.6 Development of a hybrid active/passive lining concept

Give a sub-contract to Hersh Acoustical Engineering to conduct analysis and testing to improve their hybrid active/passive lining system in preparation for a full-scale engine demonstration.

3.0 SUMMARY OF ACCOMPLISHMENTS.

The objective of Task 4 of the NASA AST contract, "Advanced Nacelle Acoustic Lining Concepts," is to develop technical knowledge and design concepts for advanced turbofan duct acoustic linings. This work included subcontracts to BF Goodrich, Hersh Acoustical Engineering and Virginia Consortium of Enginering & Science Universities. There are six sub-tasks for Task 4.

- Analysis of Model Scale ADP Fan Duct Lining Data
- Bias Flow Liner Investigation
- Grazing Flow Impedance Testing
- Development of Micro-Perforate Acoustic Liner Technology
- Extended Reaction Liners
- Development of a Hybrid Active/Passive Lining Concept

The following are summaries of the accomplishments for each task. More in-depth reports are contained as appendicies and, for selected tasks, in references.

3.1 Analysis of Model Scale ADP Fan Duct Lining Data (Detailed report in Appendix 1)

The NASA Advanced Subsonic Technology (AST) Noise Reduction Program set an interim goal to validate concepts to improve nacelle treatment effectiveness by 25% relative to 1992 technology by the second quarter of FY'97. Analytical design studies were conducted within the AST program to develop liner concepts to help achieve this goal. The objective of the program described below was to use the results of the above design studies to design liners for a specific fan/nacelle and demonstrate the resulting benefits.

The demonstration test took place in 1996. The fan used for this demonstration was a NASA Lewis 22 in. diameter Pratt Whitney (PW) Advanced Ducted Propeller (ADP) model fan rig with 18 blades and 45 stators. The model was equipped with fan duct acoustic linings designed by Boeing using the most advanced design technology then available. Advanced inlet and fan case linings were designed by PW as well. A schematic of the fan rig is shown in Figure 1.

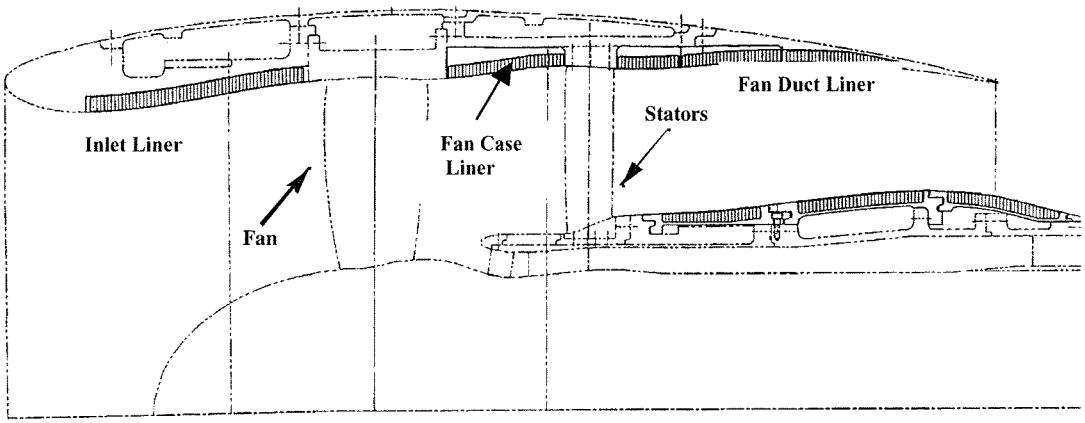

Figure 1: ADP Cutaway Schematic

The test matrix included a variety of lining configurations in the inlet, fan case and fan duct sections of the rig, including hardwall (see Table 1). Several different lining types were used in this test including single layer (single degree of freedom - SDOF), double layer (double degree of freedom - DDOF), and bulk liners. The Boeing designed single layer and double layer liners used woven wire for the resistive elements. Both of these liners were linear, meaning that the impedance is nearly independent of sound pressure level (SPL).

The baseline liner for 1992 level comparisons, was a liner produced by Dynamic Engineering, Inc. (DEI), which approximately scaled the liners tested by PW in the ADP engine demonstrator test conducted in 1992. Table 1 lists the lining type and location for each configuration to be discussed in this report.

Table 1: Test Configurations

Configuration	Treatment Type		
	Inlet	Fan Case	Fan Duct
1	HW	HW	HW
2	DEI	DEI	DEI
3	SDOF	DDOF	SDOF
4	DDOF	DDOF	DDOF
5	BULK	DDOF	DDOF
6	DDOF	HW	DDOF
7	HW	DDOF	HW

Far–field measurements were made for each configuration tested. In addition, an aft barrier was used to acquire inlet data for several key configurations, (Configurations #1, #3, #4, #5), to keep aft fan noise from contaminating the inlet radiated noise data. The aft barrier was placed parallel and offset from the exterior nacelle so as not to affect the flow in the tunnel around the engine model itself.

The aft fan liners consisted of six different liner sections, each with its own geometric constraints. The scope of this report is limited to analysis of the performance of the Boeing designed lining within the fan duct. Analysis of the PW designed inlet and fan case lining data are not included in this report. A detailed description of the Boeing designed fan duct linings and the design processes are contained in Ref. 2.

The model data was scaled to a hypothetical, full–sized engine chosen to fit on a Boeing 747 derivative. The conversion was from the 22″ Fan Rig model to a 130″ full–scale engine. PW used the scale factor to shift the frequencies to full–scale as well as distance corrections to radiate the levels to a 150′ polar arc.

The evaluation of the nacelle liners relative to the 1997, 25% peak aft angle PNLT attenuation improvement goal shows that the Boeing fan duct liner designs met the goal. At the approach condition, both the Boeing single and double layer liner fan ducts showed a very large percentage improvement (230%) relative to the DEI liner. At cutback the Boeing double layer liner showed a 51% improvement relative to the DEI liner and a 35% improvement relative to the Boeing single layer liner. At sideline the Boeing double layer liner showed a 109% improvement relative to the DEI liner and 56% improvement relative to the Boeing single layer liner.

There were some concerns associated with this evaluation of the Boeing liners however. The main concern is associated with the constraints of model scale acoustic liner testing. Model scale testing of nacelle liners is not an established procedure. It is not possible to scale the full scale designs because of the small curvature radii in model scale systems, the strength limitations for a scaled sheet thickness and the manufacturing limitations associated with the small orifice holes used with nacelle liners. In addition, it is not possible to verify that the liner built for the model test has the desired acoustic impedance spectrum. While care was taken to minimize these concerns by using woven wire resistance elements without perforated plate and careful manufacturing procedures, the lack of ability to confirm the design impedance is a major difficulty. Therefore it is difficult to draw conclusions relative to full scale lining capability from the model test results. In addition, a significant difficiency with the DEI liner was that its tuning frequency was about two 1/3 octaves lower than optimum. It is not known if this was a design choice or a manufacturing error. Again the lack of a method to measure lining impedance at high model scale frequencies makes it impossible to determine if a model scale liner is manufactured to meet the design impedance target.

Relative to the Boeing single layer liner fan duct, the double layer fan duct liner showed consistent improvement between bands 25 and 30. However, the improvement was not as large as predicted (except for the sideline condition). The high frequency (> band 30) attenuation improvement predicted for the double layer liner, was not observed. In fact, in the very high frequencies, bands 36-40, the single layer liner data show more attenuation than the double layer liner data. The problem was that the very high frequency attenuation of the double layer lining was much poorer than predicted when tested with the treated fan case for the approach and cutback conditions.The single layer liner high frequency attenuation was about the same as predicted at approach and cutback. (measured with a treated fan case). When the double layer liner fan duct was evaluated with a hardwall fan case, its high frequency attenuation was found to increase to the predicted levels. This can be interpreted in terms of modal attenuation. If the fan case has already attenuated the more easily attenuated modes, the fan duct lining efficiency drops because it must attenuate a larger percentage of more difficult to attenuate modes.

The double layer liner fan case attenuation measured with hardwall fan duct showed more attenuation at the higher frequency bands than with the treated fan duct. This is also probably

a modal effect. The fan case lining is not as important if another liner, the fan duct liner, is available to attenuate the same modes that the case attenuates.

3.2 Bias Flow Liner Investigation.

3.2.1 Grazing flow test (Detailed report in Appendix 2)

Boeing conducted grazing flow impedance testing in late 1996 to investigate effects of acoustic lining impedance control through heating the acoustic lining as well as bias air flow through the acoustic lining. The bias airflow lining panel consisted of a double layer Helmholtz resonator configuration, with a 200 cgs Rayl (4.8 ρc) porous mesh skin replacing the standard impervious backing sheet. The bias airflow was introduced via a plenum chamber attached on the back side of the lining. The lining geometric parameters are shown in Table 2:

Table 2: Bias Flow Liner Description for Grazing Flow Testing

Face sheet	14.7% open area.
Septum	6.0% open area
Face sheet to septum	3.14"
Septum to back sheet	0.76"

The heated lining panel was a standard double layer configuration with the impervious backing sheet replaced with a thick aluminum sheet. This aluminum backing sheet had slots machined in one side to accept electric heating rods. Thermocouples were installed during panel fabrication. These were located at four levels in the double layer, at six locations spread over the lining, nominally in the centers of honeycomb cells. The levels were 1) just beneath the face sheet; 2 & 3) just above and just below the buried septum; and 4) at the lining interior surface of the heated aluminum backing sheet. The lining geometry parameters are shown in Table 3:

Table 3: Heated Liner Description for Grazing Flow Testing

Face sheet	6.9% open area.
Septum	4.2% open area
Face sheet to septum	2.63"
Septum to back sheet	1.31"

The grazing flow test conditions included :

- Up to four grazing flow Mach numbers (0.00., 025, 0.35, and 0.50)

- Two sound levels - maximum achievable -approximately 160 dB OASPL- and nominally 10 dB down from maximum . The spectrum consisted of a 1KHz tone and harmonics superposed on the airflow broadband noise.

- Bias air flow – nominal 120 cm/sec average flow through the liner (M=.004), both pressure (air exiting the face sheet into the test duct) and vacuum (air entering the lining from the test duct)

- Temperature – maximum heating not to exceed the 350 °F limit of the liner bonding adhesive.

At the high SPL's tested, 160 dB and 150 dB, the bias flow test liner impedance did not show a strong dependence on changes in grazing flow up to M=0.5, or bias flow up to average M=0.004. The small grazing flow dependence is predicted by the Boeing impedance model at high SPL's. The Dean/Hersh impedance model predicts stronger dependence on grazing flow and bias flow than was measured. The bias flow test was of limited success primarily because no data could be measured at lower duct SPL's similar to those within the engine at the airplane landing condition (130 dB – 140 dB). This is where bias flow effects would be the strongest and where its application as a nacelle design concept was envisioned. With the liner design chosen for testing no effect of bias flow was observed for a mean bias flow Mach number of .004 over a range of grazing flow Mach numbers from 0.0 to 0.5 and SPLs of approximately 150 dB and 160 dB. It was recommended that more fundamental impedance modeling data be obtained and incorporated into an improved computer model before additional nacelle design studies using bias flow liners are considered. This was the objective of the time-domain analysis and VCES studies discussed below.

The elevated temperature liner test qualitatively verified the pre-test calculation predicting decreased liner resistance with increased liner temperature. The change in reactance however was quite different from the shift with frequency expected and is not understood.

3.2.2 Time-domain analysis (Detailed report in Ref. 3)

The time-domain impedance modeling of perforates uses a time marching scheme to solve the nonlinear momentum equation coupled to an acoustic cavity. This is accomplished by assuming the instantaneous unsteady resistance is the same as the steady-flow resistance at a given in flow velocity. (i.e. a pseudo-steady assumption where the flow is always in equilibrium across the orifice). This method may help one understand the physics associated with current semi-empirical acoustic impedance models and has been extended to predict the effect of bias flow. The objectives of the Boeing time-domain impedance modeling effort are to: (1) Develop models to predict the impedance of perforate linings in the time-domain using measured DC flow resistance data. (2) Use time-domain models to evaluate bias flow and frequency scattering for improved liner performance. (3) Determine if the grazing flow effect can easily be added to the time domain models.

A model has been implemented in Matlab code and testing has been conducted to measure flow resistance and impedance data for comparison to the model. Two liners were manufactured at the Boeing Wichita Nacelle Responsibility Center for testing. These liners were made using the same manufacturing processes used for airplane engine nacelles. Specifically, a honeycomb core was bonded to the facesheet using a core reticulation process which is used for nearly all the nacelle lining applications at Boeing. Both 8% and 12% open area (OA) samples were made. These open areas were chosen because they are representative of engine nacelle applications. The flow bench was used to measure the resistance versus particle velocity of a test sample. The resistance was measured in both directions through the

samples over the range of 25 to 250 cm/s. The acoustic impedance of the samples was also measured with and without bias flow with an impedance tube. A test assembly was designed and built to measure the normal impedance of the test assemblies with bias flow. The objective of the test assembly was to pass bias flow through the liner while maintaining a boundary condition on the back side of the liner that approaches that of a hard-wall. The device is basically made up of a plenum with a highly resistive layer (nominally 190 cgs Rayls at 105 cm/s) that will pass air, a plenum to hold the air, an air supply, and a mass flow measurement device. This allows a controlled mass flow and thus a bias flow velocity to be put through the lining. A vacuum system was not available during testing so all the bias flow testing was with flow exiting the lining. A typical plot of the impedance tube measured versus TD-predicted acoustic resistance at 1000 Hz is shown in Figure 2 for no bias flow. For this case the impedance measurements were made with a nonporous backwall.

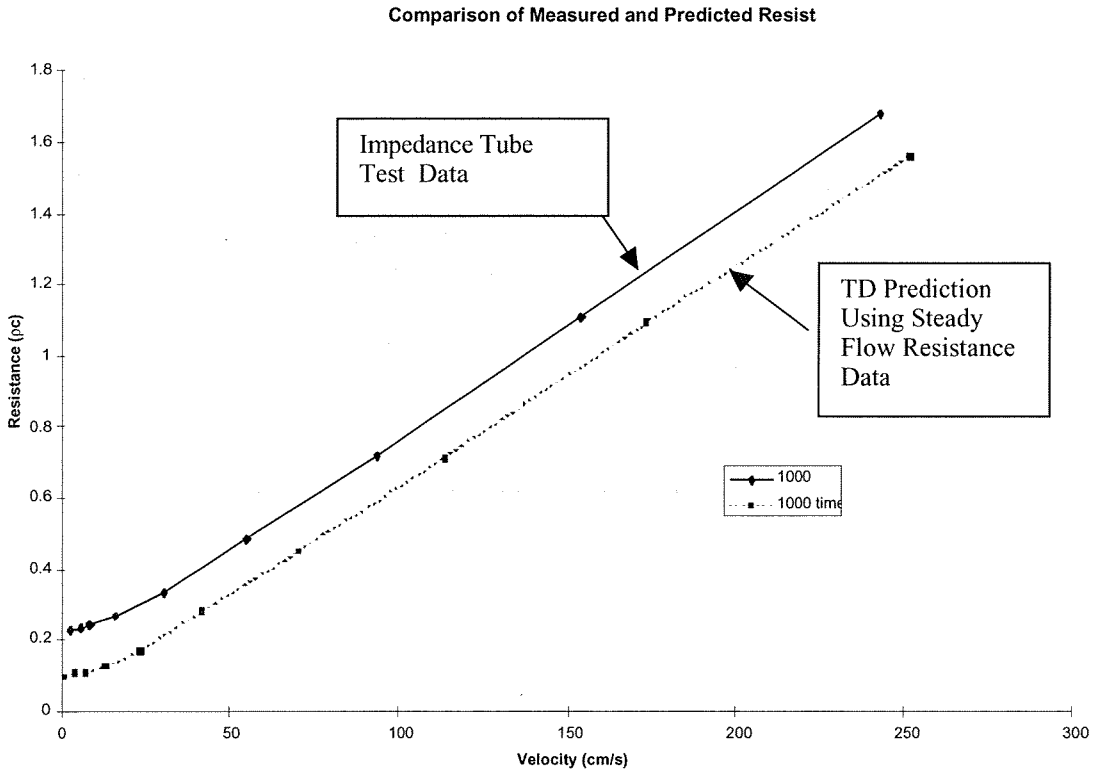

Figure 2: Resistance (ρc) versus Particle Velocity (cm/s) for the 8% OA Lining

This particular liner has 8% OA. This comparison is representative of other perforate samples at 1000 Hz in that the resistance is under-predicted slightly, but the slopes of the acoustic resistance versus particle velocity are well predicted. The good agreement in the slope shows that there is not a strong frequency dependence on the discharge coefficient of the orifice at 1000 Hz. The under-prediction of the resistance at 1000 Hz can be explained best by examining the form of the semi-empirical frequency domain (FD) impedance prediction models. The Boeing semi-empirical FD models are comprised of a DC viscous term, an AC viscous term, and an AC inertial term. The AC viscous term accounts for the frequency-dependent increase in resistance due to the reduction of the acoustic boundary layer thickness in the orifice as frequency is increased. The TD formulation is based on the zero-frequency, steady-flow resistance and thus has no measure of this effect. Assuming an

infinite duct with a boundary layer profile dependent on frequency, as described by Allard (Ref. 4), the AC viscous increase in the acoustic resistance at 1000 Hz is predicted to be 0.07 ρc. Adding this to the TD predicted data results in a prediction that better matches the absolute levels of the measured data. Figure 3 shows the measured resistance for the different bias flows for the 8% OA liner at 1000 Hz and Figure 4 shows the TD predictions of the same lining face sheet with the impedance of the porous backing sheet and back cavity accounted for. The TD predictions clearly do well at representing the data.

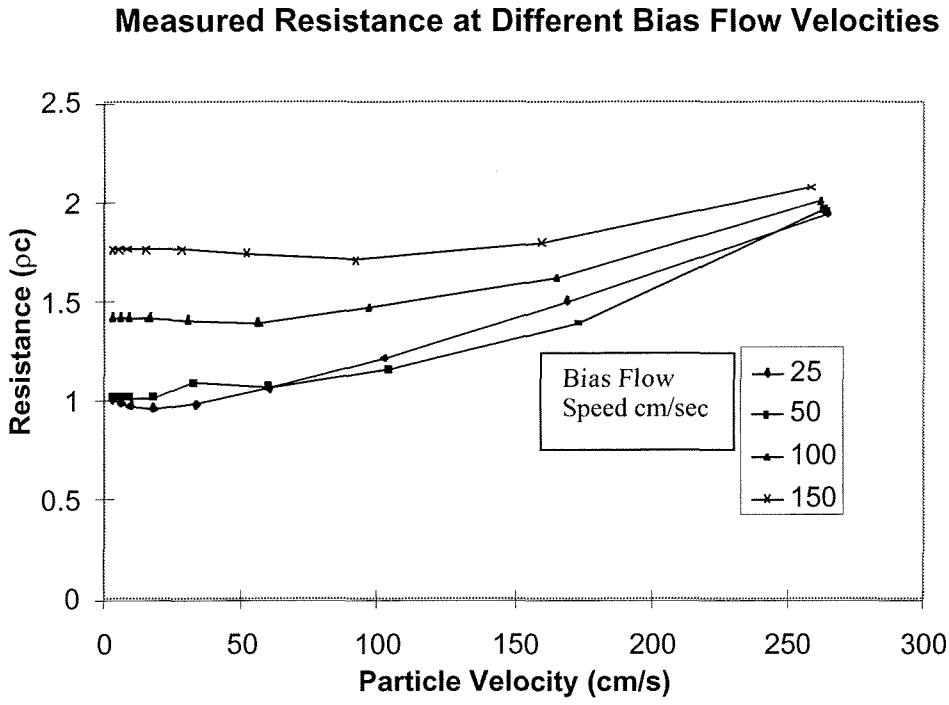

Figure 3: Measured Resistance at Different Bias Flow Velocities

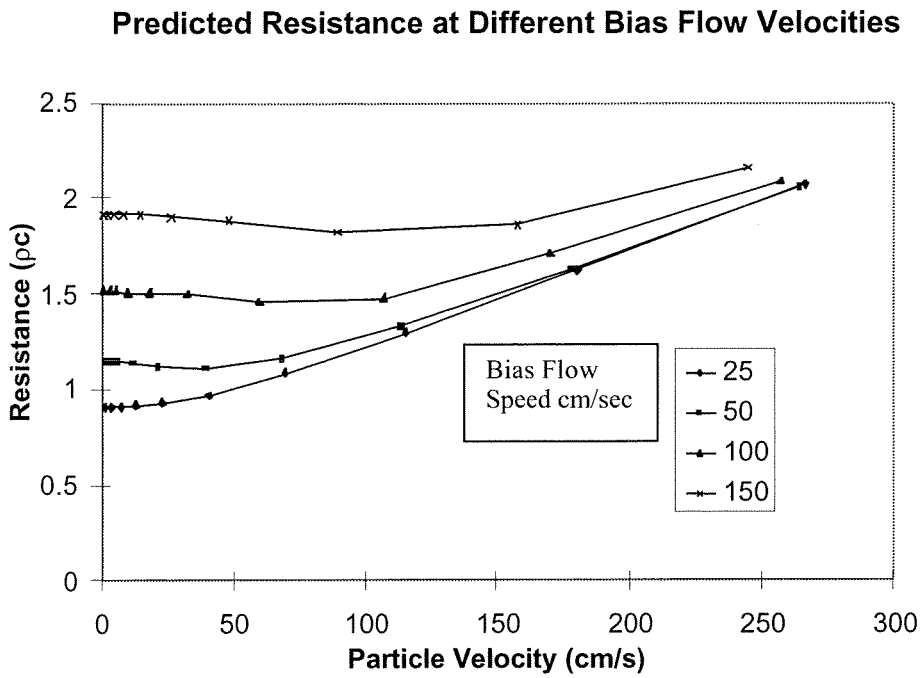

Figure 4: TD Predicted Resistance at Different Bias Flow Velocites

Notice that both the measured data and the predictions show that the bias flow effect diminishes with increasing RMS acoustic velocity. The data show that with bias flow the acoustic resistance initially starts out flat (maybe even dropping slightly) and then starts to increase as the RMS acoustic velocity increases. Clearly, the physics represented in the TD model predict the effect of bias flow on the acoustic resistance.

The TD model, based on the non-linear differential equation (DE) from the momentum equation, was used to make improvements to the semi-empirical orifice resistance FD models generally used for nacelle lining design studies. The steady flow resistance model consists of the sum of a linear (viscous) and non-linear (inertial) loss mechanisms. This gives a form $R(V) = R_{lin} + R_{nl}|V|$ that closely represents the measured steady-flow resistance data.

The semi-empirical FD impedance models predict R_{lin} and R_{nl} in terms of the hole diameter, open area, plate thickness, and frequency. The linear resistance for these models, R_{lin}, is composed of AC and DC components and the inertial term of the resistance, R_{nl}, is based on the DC non-linear component corrected for frequency. The results of a TD numerical study show that the linear or viscous part of the TD-predicted acoustic resistance is nearly identical to the current FD model.

The TD study also showed that the non-linear or inertial part of the resistance can be modeled as approximately (1.15) times the RMS acoustic velocity times the steady-flow slope, R_{nl}. Therefore, a new model is proposed to predict the acoustic resistance using the steady-flow parameters, R_{lin} and R_{nl}, and the RMS acoustic velocity, V_a:

$$R_a(V_a) = R_{lin} + (1.15)R_{nl}V_a$$

The semi-empirical model of the acoustic resistance can be extended to include bias flow by examining the behavior of the DE describing the perforate resistance. A scheme for predicting the effects of both acoustic RMS and bias flow velocity based on the steady-flow resistance is suggested:

$$R_a = R_{lin} + R_{nl}V_{RMS} \text{ where } V_{RMS} = \sqrt{(1.15V_a)^2 + (2V_b)^2}$$

Reference 4 plots the TD model and the resulting FD models with different bias flows. Note the FD predictions are very close to the TD solutions except near $V_b/V_a \approx 1$, where they are slightly high.

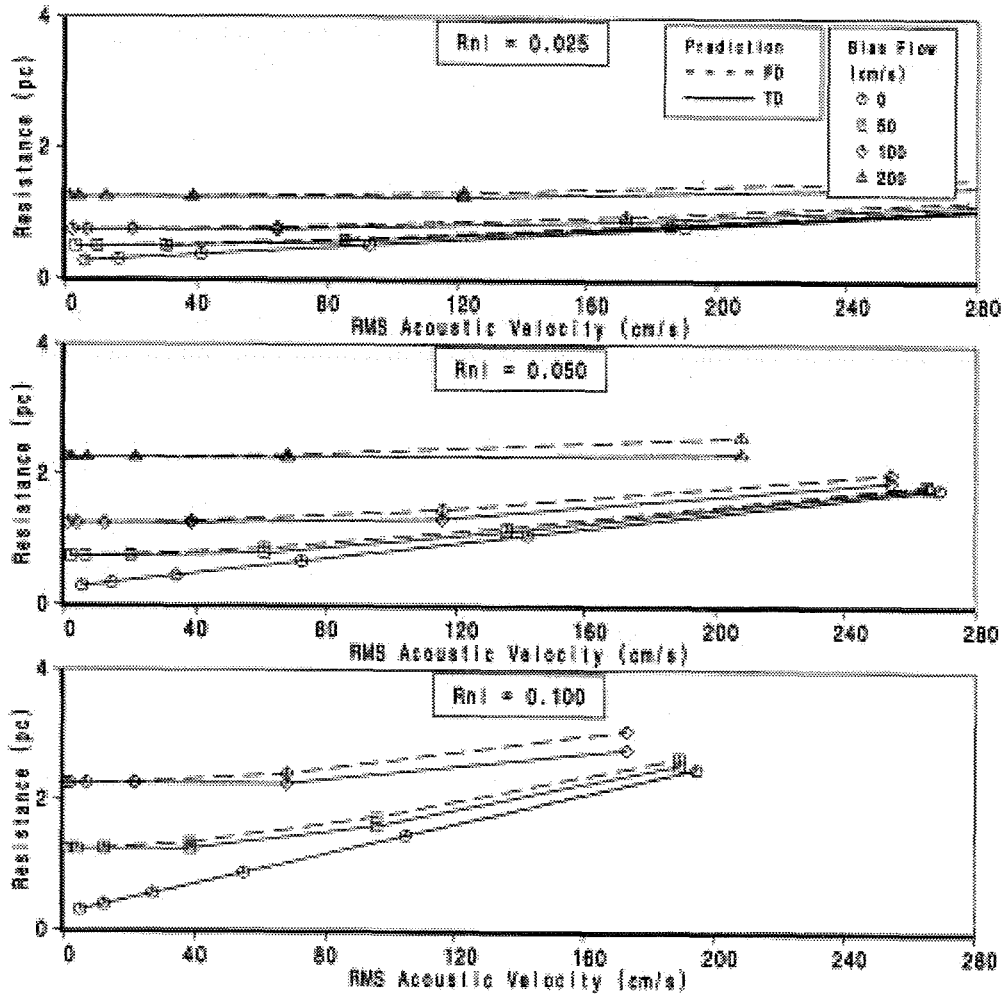

Figure 5: Comparison of TD and FD Predictions of Acoustic Resistance

A correction could be applied to the model near $V_b/V_a \approx 1$ to reduce the difference, but it was determined that the models were close enough (within a couple of tenths of a ρc).

3.2.3 Sub-contract with the Virginia Consortium of Engineering & Science Universities (Detailed report in Ref. 5)

(The following is the Introduction from Ref. 5.) The initial purpose of this study is the experimental determination of liner impedance and the validation of impedance models using data obtained from the NASA Langley Normal Incidence Tube (NIT). An experimental database was produced which included both fibermetal and perforate samples tested with and without bias flow in a single-degree-of-freedom (SDOF) liner configuration. The database was used to validate available impedance models and develop improvements in order to produce the best available frequency domain impedance model that includes the effect of bias flow. With this model, the ultimate goal is the design of double-degree-of freedom (DDOF) liners representing optimum passive and bias flow liner configurations in the presence of grazing flow. A multi-layer configuration will allow bias flow to affect the total resistance through the resistance of the septum.

The surface impedance predictions were obtained with the NASA Langley Zwikker-Kosten Transmission Line Code (ZKTL). This computer program is based on Zwikker and Kosten's theory for sound propagation in channels. In general, the model is composed of continuous arrays of multi-degree-of-freedom liner elements. The ZKTL program can compute absorption coefficients, reflection factors and insertion losses for free-field excitation. Matrix techniques are employed to compute the composite impedance due to the liner elements. For a nonlinear liner, an iteration scheme determines the impedance based on a given incident sound-pressure level (SPL). In this study, the NIT was treated as a distributed element (channel) and the liner sheets with the backing cavity as lumped elements. The different perforate impedance models were implemented in the lumped element part of the modular structure of ZKTL, minimizing coding modifications. Approximately twenty impedance models were used representing derivatives from five baseline models. For example, one of the baseline models was the existing standard model in ZKTL. In the original ZKTL code, a rigid terminating condition (infinite impedance) was imposed for each channel. For this investigation, a finite impedance boundary condition was developed to simulate a porous back plate that was used to introduce the bias flow.

The error criteria used was a least squares linear fit (with zero intercept) between the experimental and numerical results. The slope of the fit indicated the difference between experimental and numerical values, and the coefficient of determination (the correlation squared) indicated whether they were following the same trend. A slope and coefficient of determination of one indicated a perfect match between experiments and predictions.

The error criteria was the basis for a large search and optimization routine that was programmed to evaluate the twenty impedance models against the more than one hundred sets of experimental data. The routine was also used to evaluate improvements to the impedance models as an optimum bias flow model was developed.

Initial results of the comparison between prediction and experiment indicated that the resistance term needed more improvement than the reactance. The linear term of the resistance in the standard ZKTL model became one focus of attention for correction. This observation was due to the fact that the slope and coefficient of determination between

prediction and experiment improved with increasing incident SPL, which indicated that the cause of the problem was the linear component. For example, sample 52 with thickness to diameter ratio of 1.67 and percent open area of five produced results indicating a slope of 2.51 and 1.65 for sound pressure levels of 120 and 140 respectively at zero bias flow. The coefficient of determination also improved from 0.07 to 0.92. These are significant improvements for the slope and coefficient of determination for a 20 dB increase in SPL. Based on these observations the resistance term in the standard model could be improved by including a frequency dependent term similar to that found in the Crandall impedance model. The result is a significant improvement in the prediction when compared to the experiment. This illustrates the use of this data and error criteria in evaluating and improving the twenty impedance models. Full results are shown in the report with rankings of the models and the development of the impedance model that best predicts the behavior of the bias flow effect.

Experiments were performed to determine the impedance of lumped single degree of freedom liners with bias flow. These liners were composed of nonlinear perforate facesheets followed by a 1.7" cavity and a high resistance fibermetal backing. The high resistance fibermetal was necessary in order to introduce the bias flow into the cavity. Data will show the determination of the resistance of the fibermetal and the minimal effect on the impedance of liner material as opposed to having a hardwall non-porous backing. The bias flow was fed into a plenum chamber 3 inches in length with a cross sectional area 2x2 inches before flowing through the high resistance fibermetal. The perforate samples were structurally resonating in the middle to upper range of the frequencies tested. A post was inserted through the fibermetal to support the perforate sample in the center. Adding the post support shifted the resonance above 3 kHz which is out of the frequency range of interest. A thin nut was used to secure the fibermetal that also had resonant frequencies within the range tested. Other than eliminating the structural resonance, the data showed that the post and the nut supports had a minimal effect on the impedance measurements. This determination was achieved by comparing the continuity in resistance and reactance of the experimental impedance results (as a function of frequency).

Impedance was measured using three stationary microphones. The first microphone was used to set the reference sound pressure level (SPL) at the sample, the other two microphones measured the transfer function between two points on the standing wave produced by the superposition of incident acoustic waves, produced by the acoustic drivers, and reflected waves from the perforate sample. The transfer function was then used to create a least squares fit of the standing wave to calculate the overall impedance of the sample and cavity. Since only two points were used for the transfer function, the least squares fit reduced to a deterministic closed form solution.

The perforate samples tested varied in open area from 1 - 15% with thickness to diameter ratios from 0.71 to 1.8. Twenty three perforate samples were tested in all. The bias flow velocities tested ranged from -25 to 600 cm/s (negative indicating suction, positive, blowing) in the cavity used with all samples. The frequency range tested was between 1000 to 3000 Hz, one tone at a time (i.e. did not study frequency interaction effects), in increments of 100 Hz. The reference SPL was set at 120, 130, and 140 dB for low flow rates and at 130 dB at high flow rates where changing SPL had no effect on measured impedance based on a few measurements over the SPL range.

Acoustic resistance and reactance were acquired for all samples. Overall, resistance increased with bias flow for all samples. At zero and low bias flow, increasing the reference SPL increased the resistance. Above a certain critical bias flow velocity, changing the reference SPL had no effect on the resistance and the samples exhibited linear behavior with respect to SPL. The reactance was minimally affected at low bias flow rates, but at high bias flow rates the reactance was significantly reduced. The effect was most noticeable as the velocity in the

holes approached choked condition. The data is presented using the best non-dimensional groupings of the parameters tested. In addition to the acoustic impedance, flow resistance was measured for all samples. This was used to determine an effective discharge coefficient that, together with microscopic measurements of the geometric parameters, provides a complete specification of the samples.

Together this data set does provide the necessary careful parametric study that is used to improve the ability to model the impedance of liner elements with bias flow. In turn, that will create the ability to design optimum bias flow liners providing a means to in-situ control liner impedance with no grazing flow.

3.3 Grazing Flow Impedance Test Data Analysis (Detailed report in Ref. 6)

Boeing participated with NASA and GE in a grazing flow impedance measurement technique evaluation study. This study was motivated by the large differences between AST participants GE and Boeing in their models for the effects of grazing flow on acoustic impedance of perforate acoustic liners. It is generally recognized that the acoustic resistance of a perforate single layer liner is dominated by the grazing flow contribution. Double layer liners are less affected by grazing flow but the effect cannot be ignored. A comparison of the magnitude of the difference between the Boeing and GE estimates for the effect of grazing flow on perforate resistance is shown in Figure 6.

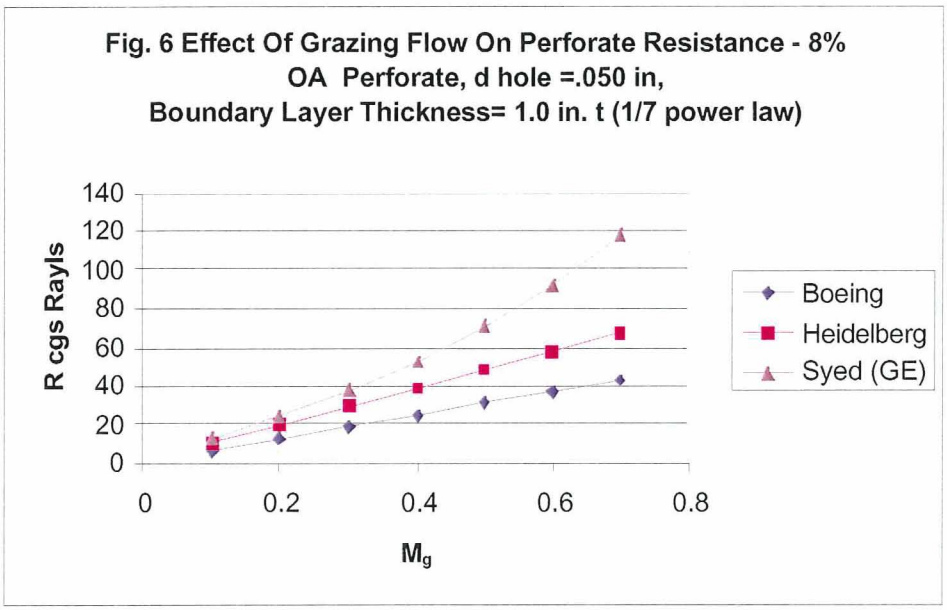

Figure 6: Effect of Grazing Flow on Perforate Resistance

At the time the study was planned GE was using the Heidelberg relationship shown in Figure 6. GE has since collected new data as part of the present study which results approximately in the curve labeled "Syed (GE)". It is seen that the new Syed (GE) relationship deviates from the Boeing relationship even more than the Heidleberg curve. A major parameter used by both the Boeing and Heidelberg relationships is the boundary layer thickness. The Boeing model, for low SPL, is of the form:

$$\frac{R}{\rho c} = .28\sqrt{\left(.05 + .11\frac{d}{\vartheta}\right)} M_g / c_d \sigma$$

Where d is the orifice hole diameter, ϑ is the boundary layer momentum thickness, M_g is the grazing flow Mach number, c_d is the orifice discharge coefficient and σ is the liner POA.

The Heidelberg model is:

$$\frac{R}{\rho c} = M_g / \left(\sigma\left(2 + 1.26\frac{\delta^*}{d}\right)\right)$$

Where δ^* is the boundary layer displacement thickness.

The Syed model is:

$$\frac{R}{\rho c} = (1/\sigma)(.29M_g^{\,3} - .08M_g^{\,2} + .25M_g)$$

The Syed (GE) model is independent of the boundary layer thickness and is only a function of M_g and σ. The dependence on boundary layer (for a 1/7 power law boundary layer shape) for these relationships is demonstrated in Figure 7 for M_g =0.4.

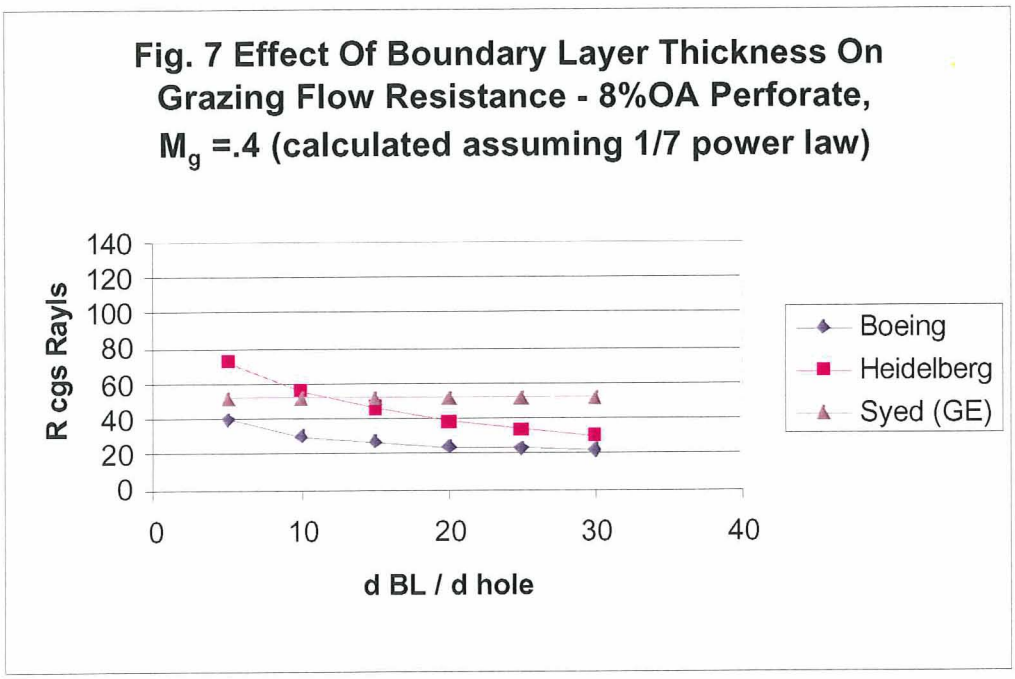

Figure 7: Effect of Boundary Layer Thickness on Grazing Flow Resistance

Note that the Boeing and Heidlelberg models approach each other at large "d BL/d hole". It is also noteworthy that (for M_g=0.4 and below) the Boeing and Syed models approach each other at small "d BL/d hole". This is shown more clearly in Figure 8. Syed's data was collected at relatively small values of momentum thickness (stated as ϑ=0.045 in.). The major discrepencies between the Boeing calculation and Syed's are the dependence on boundary layer and the high Mach number results.

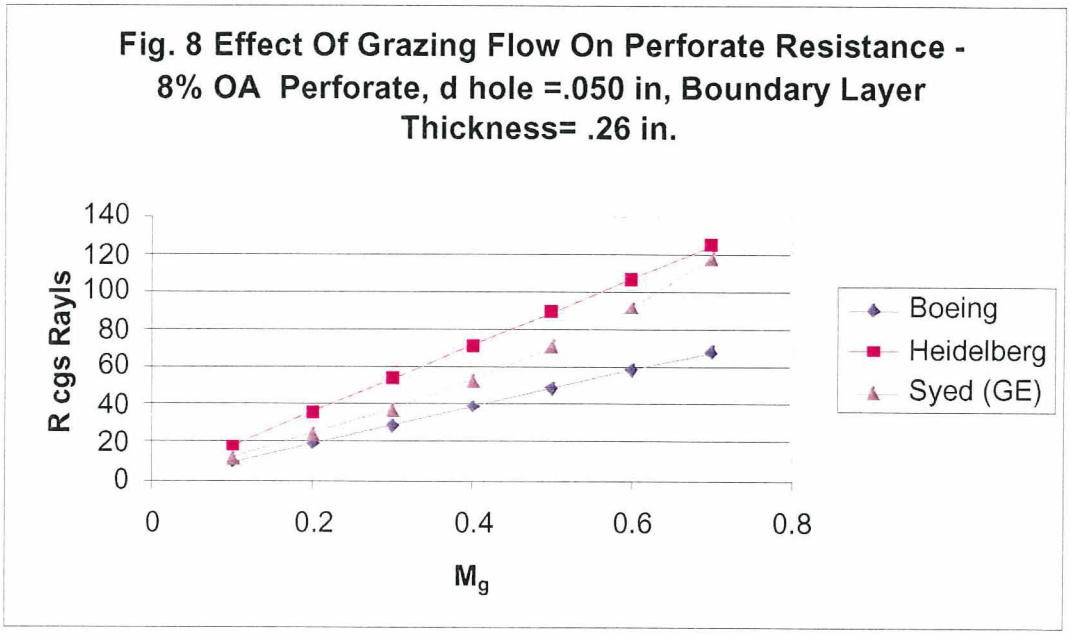

Figure 8: Effect of Grazing Flow on Perforate Resistance

The plan for the grazing flow study was for Boeing, GE and NASA to each measure the effect of grazing flow at their test facilities for comparison. Table 4 is a listing of the test samples chosen for testing.

Table 4: Impedance Measurement with Grazing Flow Test Matrix

Candidates	Initial Open Area Ratio (POA)	Hole Diameter (inch)	Plate thickness (inch)	Core Depth (inch) (GE/NASA)
Base liner	8.7	.039	.025	1.5
Min POA	6.4	.039	.025	1.5
Max POA	15	.039	.0252	1.5
Min Dia	13.3	.039	.025	1.5
Max Dia	13.0	.093	.032	1.5
Min Thk	7.3	0.05	.02	1.5
Max Thk*	7.3	0 05	.04	1.5
Min/Max Core	8.7	.039	.025	0.75/3
Special 1	10.5	.039	.028	1.5
Special 2	8.7	.050	.045	1.5
Composite	8.3	0.062	0.028	1.5
PU film	18/34	.0062/0.05	0.015/0.032	1.5

The effects of perforate sheet thickness, POA, hole diameter, core depth and face sheet material are investigated with the geometries shown in the table. It is believed that the boundary layer momentum thickness is relatively small at each of the facilities. A perforate hole diameter variation at constant POA is included in the test matrix and could be used to examine the effect of the ratio of the boundary layer thickness to hole diameter, but the parametric change is not very large. To examine the boundary layer thickness dependance it will be preferable that at least one of the facilities test with a thickened boundary layer as well. Something of the order ϑ=0.1 in. is necessary to simulate the engine nacelle situation. This was not part of the plan for the Boeing testing. Also, Boeing only tested a subset of the configurations shown in Table 4. Specifically, Boeing tested the first 5 configurations and the last configuration. All of these data were provided to NASA.

Boeing and NASA use very similar facilities for measuring grazing flow impedance; however Boeing's testing process is very different from NASA's. The NASA test process is to run a single tone (500 Hz to 3000 Hz in steps of 500 Hz) at 120 dB, 130 dB and 140 dB for grazing flow Mach numbers of 0, .1, .3 and .5. The Boeing process used for this test ran various multi-tone combinations at OASPL's of 140 to 160 dB for grazing flow Mach numbers approximately 0, .1, .2, .3, .4, .5. The details of the tone combinations are

contained in Reference 6 which contains the test report documenting the Boeing measurements.

Comparisons with NASA test data should be done versus acoustic particle velocity. This will require calculation of the acoustic particle velocities using the deduced acoustic impedances and the measured SPL's.

Boeing received data from GE for the baseline liner for steady flow resistance measured with grazing flow. This data is shown in Figure 9. Also shown on the plot are estimates of the acoustic resistance based on the steady flow resistance curves. One set is the GE (Syed) estimate. The other was calculated by Boeing using the time-domain code discussed earlier with the GE steady flow curves as inputs. Both estimates are seen to agree very well. Preliminary measurements of acoustic resistance from the Boeing Wichita facility are also shown. The orifice flow particle velocity was estimated for the Wichita data using the OASPL at the leading edge of the 12 in. long test panel and the measured resistance. This means that the estimated particle velocities for the Wichita data plots may be too high. Given this concern it appears that the Wichita data may be somewhat consistent with the GE acoustic curves for $M_g = 0.1$ and 0.35 but the $M_g = 0.50$ resistance values are clearly lower than the GE values.

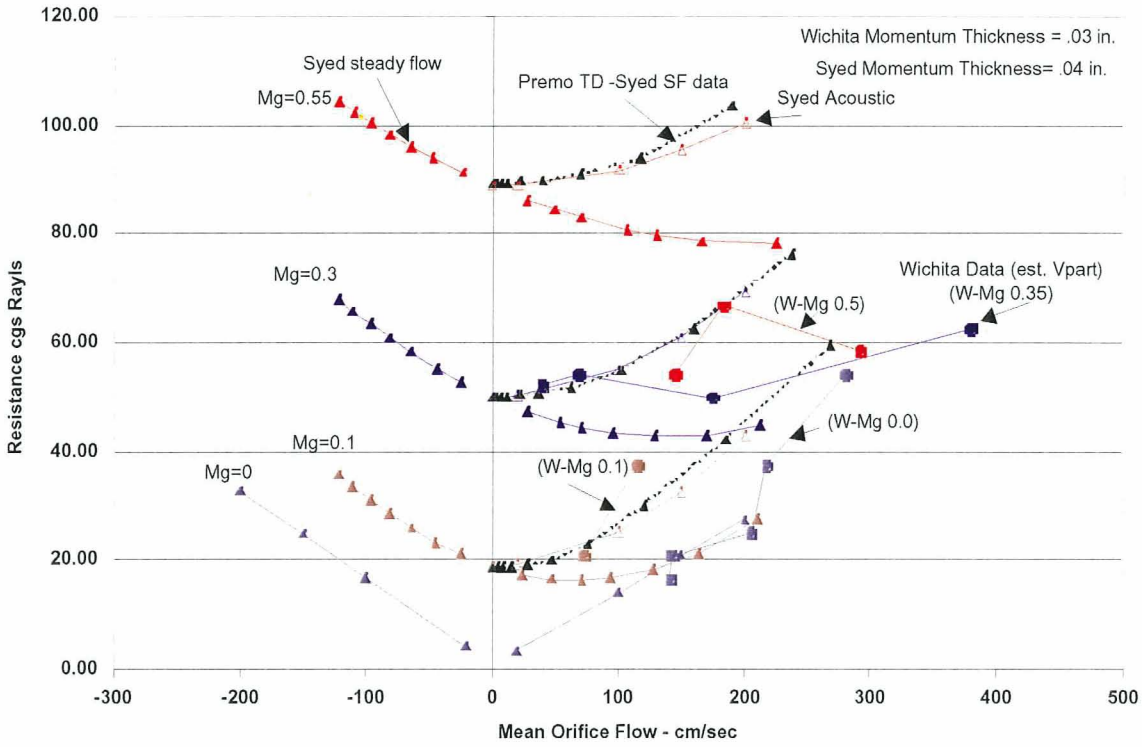

Figure 9: Resistance vs. Orifice Flow and Grazing Flow For 8.7% Open Area Perforate

3.4 Development of Micro-Perforate Acoustic Technology (Detailed reports in Refs. 7 and 8 and Appendix 3)

The subcontract work done by BF Goodrich, Hersh Acoustical Engineering (HAE) and Northrop Grumman was aimed at developing micro-perforate face sheet and septa capability. Micro-perforate resistance elements have acoustic characteristics which show small dependence on local sound level and grazing flow conditions and give better high frequency attenuation characteristics compared to conventional perforates. BF Goodrich is investigating methods to obtain micro-perforate holes (order of 4 mil) in Aluminum as well as developing a semi-empirical math model to predict the acoustic properties of micro-perforates. An initial model has been completed by BF Goodrich based on testing with Perfolin micro-perforate material. The BF Goodrich model is very similar to the Boeing perforate impedance model. For micro-perforates, the primary resistance element is the Poiseuille (P) flow term. For standard perforates Boeing increases this term by 75% relative to basic P flow. For micro-perforates (d<.005in., t/d.>5) however the basic P form is maintained. The main difficulty associated with calculating the acoustic impedance for micro-perforates is specifying the perforate geometry. The P calculation is very sensitive to orifice diameter (d^3) and an effective diameter is difficult to determine for irregular shaped holes common with laser drilling. BF Goodrich used a process to estimate the perforate diameter and percent open area using optical measurements and steady flow resistance data. The BF Goodrich detailed report is contained in Reference 7.

HAE is also developing a math model for micro-perforates using more idealized test samples with drilled holes in Plexiglas with thickness and hole diameters scaled up by a factor of approximately 10. Examing HAE's test results it appears that t/d scaling was not sufficient to reproduce the trends observed from the micro-perforate testing conducted in 1996 (Ref. 2). Two reasons suggested for this are the (t/d^{2}) dependency of resistance expected for Poiseuille flow and the lack of scaling of the boundary layer thickness to orifice hole diameter. A first cut model which includes the (t/d^{2}) dependence (Appendix 3) has been completed by HAE and reviewed by Boeing. Questions about the impedance model formulation have been raised and passed on to HAE.

Northrop Grumman was contracted to investigate the use of ultra-violet lasers for manufacturing micro-perforates. Their report is contained in Reference 8. Ultra-violet lasers have the potential for drilling much cleaner holes at much more rapid rates than is realized with carbon dioxide lasers today. Also a free electron laser with very high energy density is currently in development which offers even better potential. This project investigated the feasibility of laser-machining high-aspect-ratio micro-holes in structural composite and aluminum face-sheet skins. The holes were nominally 0.004 in. in diameter. The skins had 4% open area and were 0.040-in.-thick composite laminates, thermoset and thermoplastic, and 0.040-in.-thick aluminum sheet. The diameter and thickness were selected to achieve the desired 10:1 skin-to-hole size ratio for improved attenuation performance.

The thermoset material was graphite-epoxy, and the thermoplastic material was glass-reinforced polyetherimide. This thermoplastic material was selected because of its high impact strength, its ability to be post-formed after laser drilling in the flat, and its ability to achieve cauterized hole walls, thereby improving resistance to moisture and oxidation. The original plan called for manufacturing test specimens for flow resistance and structural testing. Only the initial manufacturing investigations were conducted however because of funding limitations.

3.5 Extended Reaction Liners (Detailed report in Appendix 4)

The extended reaction liner concept allows acoustic propagation within the liner. Current liners are "locally reacting" in that this propagation is not present because it is blocked by the non-porous honeycomb core. The purpose of this study is to investigate the potential for attaining additional improvements in attenuation, relative to the locally reacting case, by allowing acoustic propagation inside the liner. In a duct, a phase difference exists between neighboring acoustic lining cells. The phase difference is a function of incidence angle (effectively mode number for a given frequency, as each mode can be thought of as striking the liner at a different incidence) and the spatial separation between cells. This phase difference leads to a varying pressure distribution across the two neighboring cells, which, in turn, will drive the 'in-liner' propagation for acoustically connected cells. Two approaches have been adopted for this study. The first involves the validation and investigation of two codes designed to predict the impedance of an experimental configuration, with two cells linked by a resistive element, and the phase of the source to each being independently controlled. These codes can then be used to model a finite length, non-locally reacting liner, where, as previously stated, a phase difference exists between neighboring cells.

The second study is being performed using the Boeing liner optimization and duct attenuation program (MELO). The code is being used to investigate the modal duct attenuation of various configurations of extended reaction liners, with downstream propagation only, simulating a fan duct.

The calculation of duct lining attenuation can be conceptualized by imagining a wave reflecting from the lined walls of the duct as it propagates down the duct. At each reflection some energy is absorbed by the lining reducing the downstream-propagated noise. The energy fraction absorbed at each reflection (absorption coefficient) can be easily calculated if the acoustic impedance at the lining face is known as well as the incidence angle of the duct propagating wave. The acoustic impedance at the lining face depends on the manner in which sound is propagated within the lining itself. The superposition of the sound incident on the lining and the sound within the lining determines the lining acoustic impedance. For a non -porous honeycomb core lining the sound propagation within the lining is limited to being along the axis of the honeycomb down to the backsheet and reflected back to the face sheet. The propagation within the lining is therefore the same no matter the angle of incidence of the duct wave. This is called a "locally reacting" lining. The acoustic impedance only depends on the local properties of the lining and the duct sound field.

For a porous core lining there is the opportunity for sound to propagate laterally within the lining through the core as well as along the axis of the honeycomb. The lateral propagation within the lining must be analytically "connected" to the duct wave since the duct wave is continuing to influence the lateral wave as it propagates. The superposition of the duct wave and the lining lateral wave at the lining face is therefore dependent on the angle of incidence of the duct wave and the lateral wave propagation properties within the lining. This is called an "extended reaction" lining. The Boeing analytical calculation for a duct with porous core models the lateral propagation within the lining for each incident mode at a given frequency (incidence angle) separately, calculating a unique lining impedance for each incident mode and then calculating the attenuation of that mode as for a "locally reacting" lining. The analytical "connection" of the duct wave with the lining lateral wave is obtained by forcing the lateral wave numbers of the duct wave and lining wave to be the same (same lateral wave length and propagation speed). The lumped resistive and reactive effects of the core pores are used to determine properties of a homogeneous medium with equivalent dissipation and propagation speed which is used to model the lateral wave propagation.

The report in Appendix 4 detailes the analytical extended reaction study. The objective is to investigate the concept thoroughly through the validation of MELO with a 2D duct propagation test scheduled at Northrop Grumman. Then the validated code can be used for assessment of these liners for 'real' applications. The Northrop Grumman test was funded by NG with NASA funded consultation by Boeing. Boeing defined the details of the two dimensional propagation duct and anechoic section for measuring far-field propagation.

Figure 10 shows a schematic of the test set-up. The lined duct dimensions were chosen to represent a typical fan duct. The duct height at 22" was chosen to conveniently mount the four speaker horns necessary for the combined requirements of a broadband source and tones with a preferred modal content. The lined duct length of 3' gives an L/H of 1.64. A higher L/D would compromise the overall length of the device, given the size of the anechoic chamber. The duct width was chosen at 1.3" to be shallow enough to ensure the acoustic pressure didn't vary in that plane over the frequency range of interest (500Hz to 4000Hz).

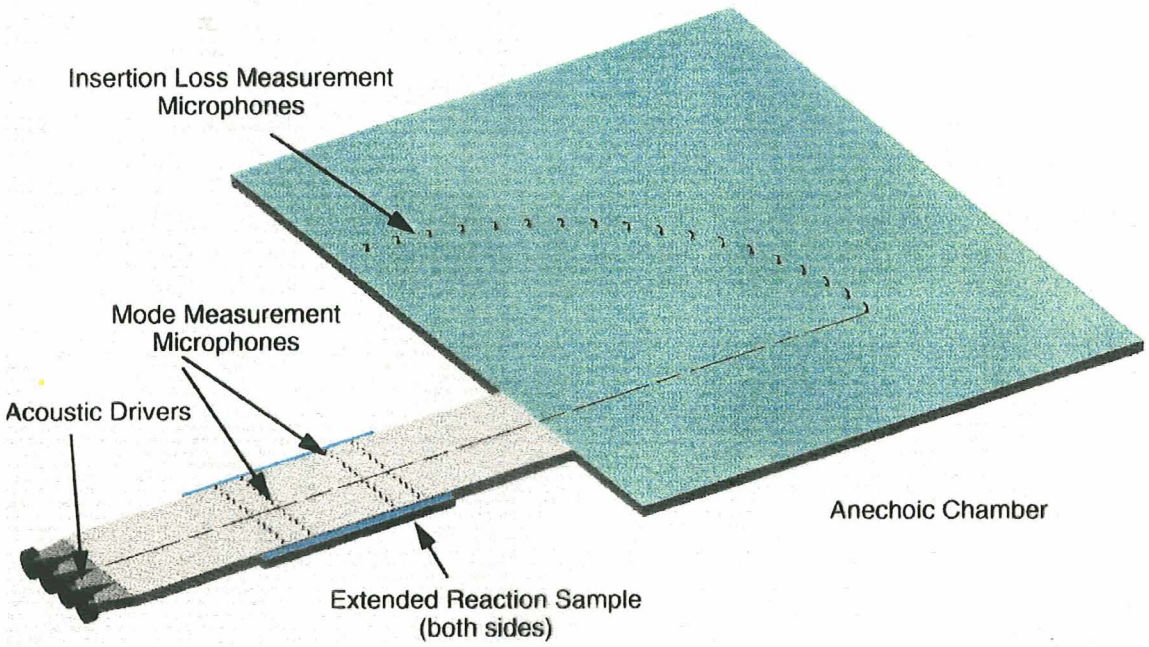

Figure 10: Schematic of 2D Duct and Anechoic Chamber

The exponential horns on the speakers are designed to give a cut-off frequency well below 500Hz. Fiberglass wool is placed in the horns to reduce the interference between them. A microphone is also inserted in each horn to ensure consistency in level between runs.

The test samples, both locally reacting and extended reaction, were constructed from wire mesh facing sheets and, if applicable, wire mesh walls. Table 5 shows the specifications for the test samples. Sample liner 2 is an optimized single layer liner for a representative fan duct application. Sample liner 3 is an optimized porous core liner. The liner designs were done with the Boeing duct propagation code MELO.

Table 5: Extended Reaction Test Samples

Sample #	Face Sheet DC Flow Resistance (cgs Rayls)	Core Depth (cm)	Common Wall Resistance (cgs Rayls)
1	50	3.2	20
2	90	3.2	Hard (i.e locally reacting)
3	50	3.2	40
4	50	3.2	0 (i.e. no cells)
5	50	3.2	Hard

Only insertion loss measurements were made, the mode measurement microphones shown in Fig. 9 were not installed. The insertion loss for a given liner was obtained from the difference of the logarithmic sum of the SPL's from the anechoic chamber microphones for the hardwall duct and the lined duct. The measured insertion loss spectra are shown in Figure 11. This data was taken with the drivers driven by uncorrelated broadband noise sources. The MELO predictions for the tested configurations are shown in Figure 12.

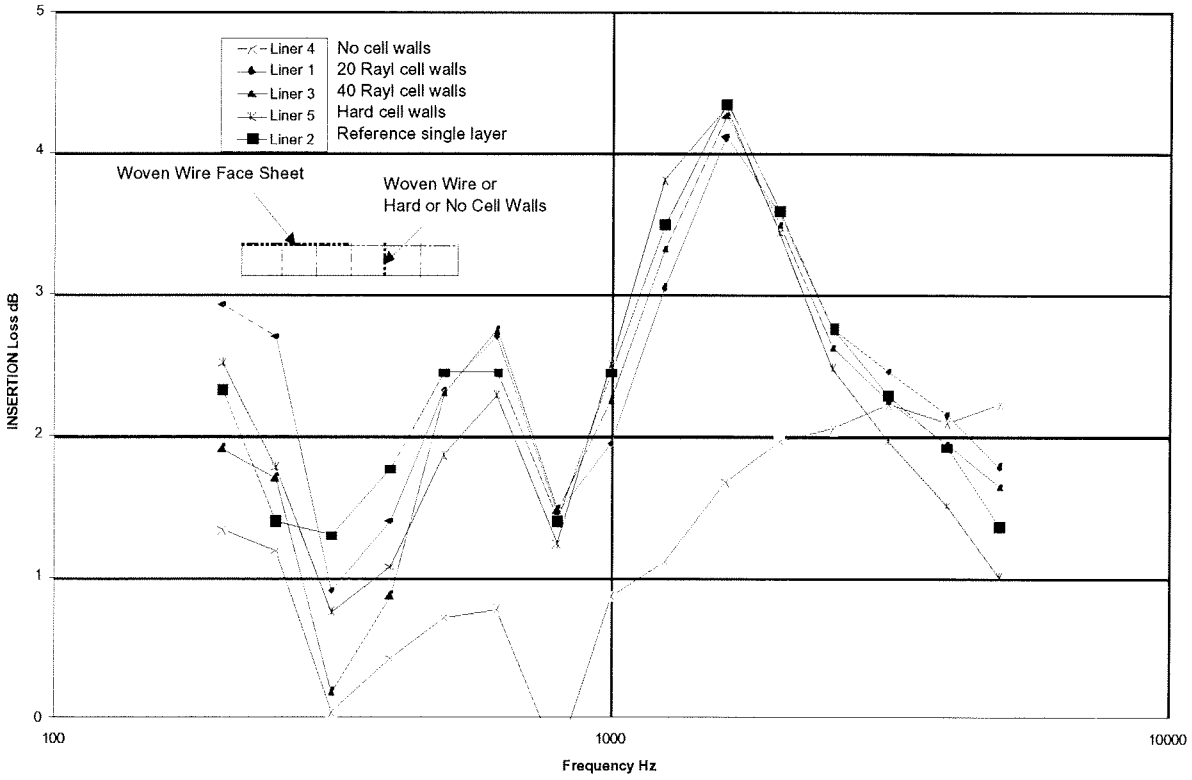

Figure 11: Measured 1/3 Octave Band Insertion Loss (with permission from NG)

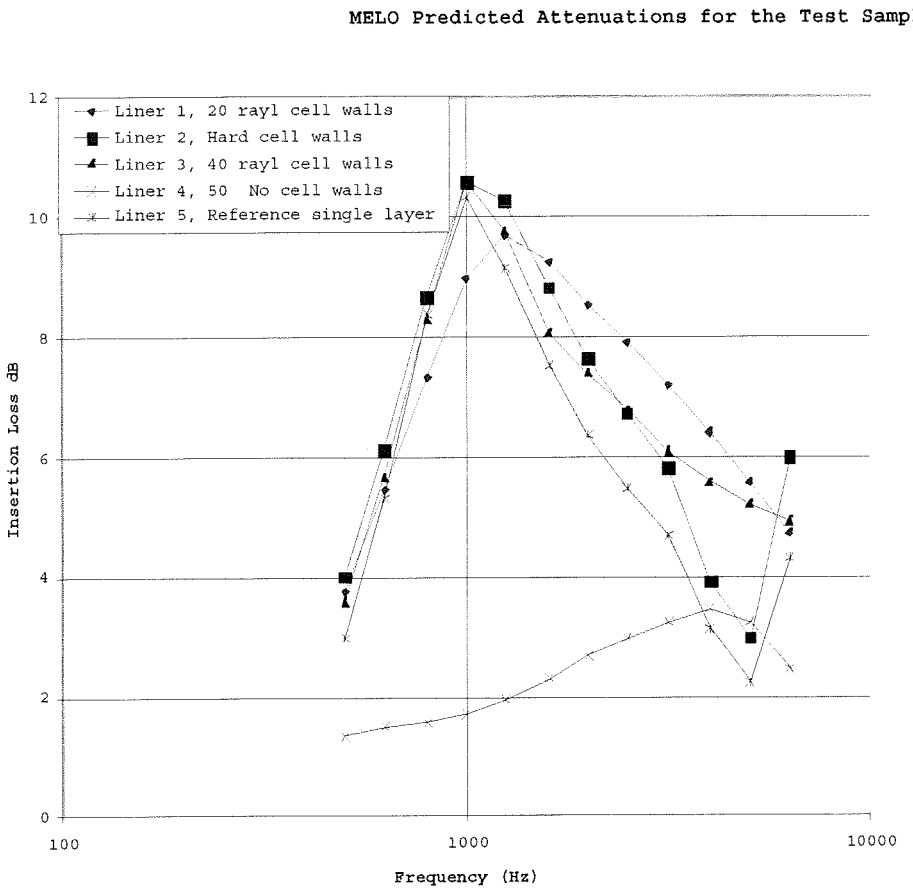

Figure 12: MELO Predicted 1/3 Octave Band Insertion Loss for the NG Test Samples

It is clear that there are some major differences between the measured and predicted results. The measured lining tuning frequencies were two 1/3 octaves higher than predicted and the measured insertion losses were generally about half of that predicted. However, it appears

that the effects of using porous cell walls and eliminating the cell walls altogether were well predicted. The reason for the prediction/measurement discrepencies are not known. An independent prediction for the locally reacting lining using the Boeing C-Duct code tended to verify the MELO code predictions. Therefore, there is probably something about the test that is not being modeled. One possibility is that the modal assumptions used by the codes are incorrect. Another is that the anechoic chamber microphones were not far enough from the duct exit for the radiated energy calculation to be correct. However, it does not seem likely that either of these could explain the tuning discrepency. In any case there does appear to be a bandwidth benefit for a single layer porous core liner compared to a single layer hardwall core liner with a small penality in peak attenuation for the aft fan duct application. However, the improvement in attenuation bandwidth is not as great as that obtainable with a conventional double layer liner.

No conclusion can yet be drawn for inlet application of extended reaction liners for inlets. It is felt that there is the possiblity of using extended reaction to develop a liner which can be optimized for a larger range of modes (incidence angles) but this was not investigated in the current study.

3.6 Development of a hybrid active/passive lining concept (Detailed report in Appendix 5)

Under sub-contract, Hersh Acoustical Engineering (HAE) conducted an analysis and testing study to improve their hybrid active/passive lining system in preparation for a full scale engine demonstration. HAE undertook a four-part initial investigation of simplifications that might be applied to active control of rotor/stator tones in turbofan engine inlets. The underlying concept upon which this investigation was based assumed that only a subset of the total number of cut-on modes would have a significant impact on sideline tone nose. If this subset could be controlled with a less extensive array of active control actuators than required by the full sound field, reduced active control system complexity and space/weight would be achieved.

The four major parts of the project were as follows:

1. Design and construction of a static test facility for generating and measuring multiple spinning order and multiple radial order propagation modes in a circular duct.

For this a rooftop static 48-inch test duct facility was designed, constructed and calibrated for radiation of modes (2,0) - (2,2) either in isolation or in combination.

2. Establish microphone arrays and signal processing systems for simultaneous measurement of in-duct and far-field radiated sound.

For this the radiation characteristics for the individual modes were computed in near and far field

3. Design and fabricate a linear microphone array to be mounted alongside the duct inlet and used as an error signal sensor for far-field radiation in specific directional sectors.
4. Install an active/passive hybrid liner in the test duct and incorporate it with the linear microphone array to assess feasibility of simplified ANC to suppress multi-radial order tones.

Far-field sideline radiation suppression was demonstrated using a hybrid active/passive liner employing two rows of active Helmholtz resonators to control a four-radial in-duct sound field.

4.0 CONCLUSIONS & RECOMMENDATIONS

To a large degree the work reported in this document was a continuation of the AST lining development work started at Boeing in 1994. This is particularly true regarding the bias flow and the micro-perforate development work. The ADP model scale, lining test was an application of the design tools and ideas developed up to 1995. The GE/Boeing/NASA grazing flow impedance measurement study was initiated when it was realized that GE and Boeing used very different modeling relations for calculating the effect of grazing flow on liner impedance. In addition Boeing had had difficulties with this measurement with liners designed as part of 1995-96 AST investigations. The extended reaction liner study was new to the Boeing AST program for this Task and was added after it became apparent that the European RANNTAC program had claimed some success with this concept. The hybrid active/passive lining concept study was a continuation of work HAE had done under AST contract for NASA Glenn.

The ADP model scale fan duct lining test demonstrated that linings could be manufactured to meet a 25% improvement relative to the designated baseline liner (DEI). However, it may be questionable whether the designated model scale baseline represents 1992 engine lining technology. The DEI single layer liner was tuned to a lower frequency than the Boeing optimized single layer liner. This was partly due to the difficulty in scaling an engine test liner. The engine test liner that the DEI liner attempted to scale was manufactured with a high POA perforate bonded to the underside of the face woven wire. The model scale liner used a felt metal face sheet with properties very similar to the full-scale face sheet and eliminated the perforate back sheet. This results in a higher mass reactance for the model scale liner at a scaled frequency. The resulting tuning frequency of the model scale liner was probably about 1 one-third octave lower than the full scale liner. Unfortunately this could not be verified because of the difficulty in measuring lining impedance at model scale frequencies.

While it is true that wire mesh, linear single layer liner technology was commonly used by many nacelle manufactures in 1992, this was not the case at Boeing. In 1992 Boeing utilized a double layer perforate liner with a laser-drilled septum and punched aluminum face sheet. This liner is believed to give approximately 20% better noise attenuation for a fan duct application than an optimized single layer wire mesh liner (Ref. 2).

The double layer wire mesh liner is believed to give approximately 5% improvement relative to the Boeing double layer perforate liner (Ref. 2). Unfortunately, it was not possible to manufacture a model scale double layer perforate liner for the ADP model fan test, so a measurement of the benefit of the double layer, linear liner relative to the conventional double layer, perforate liner was not conducted. The Boeing designed linear, double layer liner showed about the expected improvement relative to the Boeing designed linear, single layer liner at cutback, but showed slightly less than the expected improvement at approach. One could therefore conclude that the test results demonstrated approximately 5% improvement relative to 1992 technology if the Boeing double layer perforate liner is assumed as the base. Some other significant technical conclusions from the ADP fan duct test were:

- There is a need to be able to measure model scale liner impedance at frequencies to 20 kHz. The demonstrated capability today is about 12 kHz.
- The acoustic treatment in the fan case strongly affected the performance of the fan duct liner. It appears that the fan case treatment attenuated noise in higher order modes and the stators did not scatter the remaining energy back into higher order modes as it propagated into the fan duct. Therefore, analytical lining evaluation assuming uniform modal energy distribution results in optimistic expectations. This suggests that if an efficient method of modal scattering near the stators could be devised, an increase in fan

duct liner attenuation (closer to that predicted assuming equal energy distribution), relative to that currently observed, would result.

- Lining tone attenuation was significantly different than the broadband attenuation and generally better. This suggests there is a different modal energy distribution for tones compared to broadband noise.

Significant progress has been made on bias flow acoustic liners. Boeing and VCES have developed similar analytical expressions for the effect of bias flow on the resistance of perforates. Boeing conducted a limited test to verify its formulation. More extensive testing was conducted by VCES. The VCES testing also showed the need to incorporate a reactance dependence on bias flow impedance models. The effect of bias flow with grazing flow is still undefined. VCES is planning a series of tests at the NASA Langley acoustics laboratory to investigate this dependence.

Boeing used their bias flow formulation to examine the impact of bias flow through the water drainage system found in an actual inlet acoustic liner. It was determined that the bias flow has a minimal impact on the acoustic impedance for the double layer perforate liner considered in the study. VCES will investigate the potential to utilize bias flow to change nacelle liner acoustic impedance as the engine operating point or liner environment (grazing flow or SPL) changes.

As part of their bias flow studies VCES made a series of impedance and flow resistance measurements over a wide range of perforate geometries. This was done to establish a good baseline for determining the effect of bias flow over a range of perforate geometries. This data will be valuable for verifying existing non-bias flow impedance models.

No comparisons have yet been done for the grazing flow resistance and reactance measurements made at the Boeing, NASA Langley and GE test facilities. One problem, which will have to be addressed, is the fact that the boundary layer characteristics are probably different for the three facilities. Data collected by Boeing a number of years ago showed a significant dependence of the grazing flow resistance with boundary layer thickness. In particular, Boeing uses the boundary layer momentum thickness to define this dependence. Although not currently part of the defined study, this dependence will have to be further investigated.

Ref. 2 demonstrated the linearity and independence to grazing flow benefits of micro-perforates (d = 4 mil, th = 40 mil) compared to conventional perforates (d = 40 mil, th = 40 mil). A major problem observed, however, was hole shape inconsistency in the manufacturing process. This makes it difficult to characterize the micro-perforate geometry and construct an impedance model. BF Goodrich demonstrated that if the hole geometry is well controlled, as is the case for the Electro-Deposit Nickel Micro-perforate plates they tested, the acoustic resistance is well modeled by the Poiseuille flow equation. However they found significant variable hole distortion with the CO laser drilled, as well as the electron beam drilled, aluminum plate samples. Northrop Grumman has demonstrated potential for using ultra-violet lasers for drilling quality micro-perforate holes in aluminum sheet. They were able to develop a process for achieving maximum out of roundness of ± .001 in and maximum half-angle taper of 3° for holes with exit diameter of .004 ±- .0005 in. Eventually the availability of the high power free electron laser (FEL) is expected to make drilling these holes sufficiently inexpensive for production applications.

The analytical and experimental study of a porous core lining for fan duct application did not show a significant noise attenuation improvement potential relative to conventional non-porous core liners used today. Small improvement in attenuation bandwidth was both

predicted and measured. However, there were predicted vs. measured differences in the tuning frequency and attenuation amplitudes that could not be explained. Engine inlet application of porous core liners was not studied. There may be potential for optimization for a range of modes which could be useful in inlets where many more modes can be propagated compared to fan ducts.

5.0 REFERENCES

1. Dougherty, R. P., "Nacelle acoustic design by ray tracing in three dimensions", AIAA 96-1773, 1996.
2. Bielak G. W., Premo J. W., Hersh A. S., "Advanced Turbofan Duct Liner Concepts", NASA CR-1999-209002.
3. Premo, J., "The Application of a Time-Domain Model to Investigate the Impedance of Perforate Liners Including the Effects of Bias Flow", AIAA 99-1876, 1999.
4. Allard J. F., "Propagation Of Sound In Porous Media – Modelling Sound Absorbing Materials", 1993, Elsevier Science Publishers Ltd.
5. Kelly J. J., Betts J. F., Follet J. I., Thomas R. H., "Bias Flow Liner Investigation", VPI – 434487, Virginia Consortium of Engineering & Science University, Dec. 1999.
6. Gallman, J. M., Kunze, R., K., "Grazing Flow Acoustic Impedance Testing for the NASA AST Program", 2002-2447, 2002.
7. Yu, J., Kwan, H.W., Chiou, S., "Microperforate Plate Acoustic Property Evaluation", 99-1880, 1999.
8. Laser Micromachining for Sound Attenuation Nacelle Face Sheets", NCTA '98 Technical Report, NCTA-AS&T-BJC-983, Northrop Grumman Corporation Report, 1998.

Appendix 1 - Analysis Of ADP Model Fan Lining Test Data

INTRODUCTION

The NASA Advanced Subsonic Technology (AST) Noise Reduction Program has set a goal of a 50% improvement in nacelle acoustic liner effectiveness relative to 1992 levels. Analytical design studies have been conducted within the AST program to develop liner concepts to help achieve this goal. The objective of the program described below was to use the results of the above design studies to design liners for a specific fan/nacelle and demonstrate the resulting benefits.

The demonstration test took place in 1996. The fan used for this demonstration was a NASA Lewis 22 in. diameter Pratt Whitney (PW) Advanced Ducted Propeller (ADP) model fan rig with 18 blades and 45 stators. The model was equipped with fan duct acoustic linings designed by Boeing using the most advanced design technology available. Advanced inlet and fan case linings were designed by PW as well. A schematic of the fan rig is shown in Figure 1.

The test setup included special features designed to help extract detailed acoustic lining performance information, such as a barrier to shield the aft fan noise for inlet radiation measurements. The test matrix included a variety of lining configurations in the inlet, fan case and fan duct sections of the rig, including hardwall in each section, as illustrated in the schematic in Figure 1. Several different lining types were used in this test including single layer or single degree of freedom (SDOF), double layer or double degree of freedom (DDOF), and bulk liners. The single layer and double layer liners both had woven wire face sheets with the double layer also having a woven wire septum. Both of these liners were linear, meaning that the impedance is nearly independent of sound pressure level (SPL). The baseline for 1992 level comparison was a liner produced by Dynamic Engineering, Inc. (DEI) which approximately scaled the liners tested by PW in the ADP engine demonstrator test conducted in 1992. Three runs were made using the DEI liners: a run conducted in 1995 with a slightly different fan design, a primary run during this current test, and a re–run during the current test. PW specified the last re–run of the DEI liners as the standard for 1992 technology. Table 1 below lists the lining type and location for each configuration to be examined in this report.

Table 1: Test Configurations

Configuration	Treatment Type		
	Inlet	Fan Case	Fan Duct
1	HW	HW	HW
2	DEI	DEI	DEI
3	SDOF	DDOF	SDOF
4	DDOF	DDOF	DDOF
5	BULK	DDOF	DDOF
6	DDOF	HW	DDOF
7	HW	DDOF	HW

The interstage liner was not changed unless necessary since it required the most downtime to replace. The last two configurations listed allow for insight into the effectiveness of interstage liners. In addition to the normal far–field measurements for each configuration tested, several runs using an aft barrier were done to keep aft fan noise from contaminating the inlet radiated noise data (Configurations #1, #3-5). The aft barrier was placed parallel and offset from the exterior nacelle so as not to affect the flow in the tunnel around the engine model itself.

The aft fan liners consisted of six different liner sections, each with its own geometric constraints. The scope of this report is limited to analysis of the performance of the Boeing designed lining within the fan duct. Detailed descriptions of the Boeing designed fan duct linings and the design processes are contained in Ref. 1. The PW designed inlet and fan case linings are not included in this analysis.

Since a scale model was tested, the data was scaled up to a hypothetical full–sized engine. This "new" engine was chosen to fit on a Boeing 747 derivative described in Ref. 1. The conversion was from the 22″ Fan Rig model to a 130″ full–scale engine. PW used the scale factor to shift the frequencies to full–scale as well as distance corrections to radiate the levels to a 150′ polar arc. The effect of the scaling is to increase the amplitudes (SPL) at a given measurement distance by 20 log of the scale factor and to shift one-third octave frequency bands by -10 log of the scale factor.

ENGINE NOISE MODELING

The ADP model test data received from PW was already scaled to the full–size engine. Both one-third octave and narrow-band data were used by Boeing to create a noise model estimating the contributions of the inlet radiated fan broadband and tone noise and the aft duct radiated fan broadband and tone noise components. The data was sorted by increasing power setting, and the angles (for one-third octave data) interpolated to 20° to 160° in increments of 10° since the model scale data was not measured at these 10° increment angles. The angles used in the far–field were referenced to the midpoint of the ADP fan rig which is downstream of the fan itself. This causes an offset at 90° of

approximately 10° when compared with using the fan nozzle as the origin and extrapolating the data to 150 foot polar arc full scale; likewise, there is approximately 8° offset at 120° and approximately 4° offset at 140°. The scale factor for going from a 22″ fan to a 130″ fan is 5.91. This scale factor was used to scale the model N1C (corrected rpm) in the data file to reflect the full–scale N1C. The final pre–processing step was to unbandshare the fan tones in the one-third octave data. This process removes any portion of a fan tone which lies in adjacent bands and puts all the energy in one band. The data was then ready to go through the Boeing ENgine MODeling (ENMOD) Process.

Two additional assumptions were used in the modeling process for this data. First, it was assumed that there is no jet noise present in the test data. Pratt Whitney manipulated the scaled one-third octave data such that the low frequency and very high frequency noise was rolled off at 1.5 dB/octave band. The low frequency roll–off was performed to eliminate jet noise, and the high frequency roll–off was done to eliminate what was believed to be wind tunnel noise. Second, since the turbine and low pressure compressor flow was ducted aft of the test region, the test data consists of only fan tones and fan broadband noise. It should be noted that the model ADP fan rig runs only at subsonic conditions, therefore buzzsaw tones, which normally occur at high power conditions are not present in this test data. The wind tunnel flow was around 0.1 Mach number for the conditions used in the models.

The first step in the modeling process takes the one-third octave data and separates it into forward and aft components. This split is done on a directivity basis for each band where a computer program identifies the minimum SPL angle and initially defines this angle as the point where inlet and aft components are equal (see Fig. 2). Generic forward and aft directivity shapes, which were derived from engine data with barriers, are then applied to roll–off the inlet and aft spectra. The program also attempts to minimize the change in split point angle from one third octave band to the next. After completing this step, the forward and aft components are defined at each angle for each one-third octave band.

The next step involves separating out all of the fan tone harmonics. This is done using both 1/3 octave and narrow-band data. The computer program identifies the tone frequencies in the data through the use of the fan blade count and RPM as shown in Figure 5. The process first uses the one-third octave component defined previously to determine tone level by subtracting broadband noise estimated using adjacent bands from the 1/3 octave SPL. If there is no identifiable tone in the one-third octave data, the relative difference between the tone and broadband levels in the narrow-band is used (with correction for bandwidth) for the third octave component. The tone is then separated from the one-third octave band data resulting in identified tone and broadband components for both inlet and aft fan noise. Tones present in the data but not identified as fan harmonics are removed so that they are not included in the broadband component model. With this separation completed, the forward and aft components (tones and broadband) are summed to create the total one–third octave spectra again. The model is then complete.

The next step is to verify the model. This is done by comparing the measured one-third octave data with the modeled levels. If these two do not agree, some energy in the third octave bands was added or lost in the modeling process. This is generally not a problem as the computer program continually checks to confirm totals with original test data and makes changes as necessary. Also, the aft barrier data which was taken during the test for some configurations was directly compared with the inlet component from the forward and aft split. An inaccurate choice of the inlet and aft radiated fan noise split point is the most probable source of error.

This modeling process was repeated for each of the seven configurations listed in the Table 1. An example of the resulting model is shown in Figs. 2 to 4 for the hardwall configuration at the approach, cutback, and sideline conditions. Table 2 below shows the kinds of plots contained in the figures. These models can then easily be used to compute the attenuation due to the inlet, interstage, or aft liners for both tones and broadband for each configuration.

Table 2: Engine Model Component Definitions

Prefix	Component	Prefix	Component
N1C	Test Data	IN1	Model Inlet Fan Total
TOT	Model Total	FB5	Model Aft Fan Broadband
IB1	Model Inlet Fan Broadband	AF5	Model Aft Fan Total

There are some general observations which resulted from going through the process to create the noise models for each configuration. The first fan harmonic (2BPF) is fairly dominant throughout the configurations and is especially large at aft angles. This is quite evident in Figure 5 where the dashed lines represent the frequency for BPF and its harmonics and the triangle symbols denote where a tone was identified. As expected, BPF is cut–off and not readily identifiable in the narrowband data. The higher harmonics are present generally up to the third harmonic (4BPF). There were some problems in the data at certain angles. The double layer liner at the sideline power condition had bad data at 147° and 158° which is evident in model plots at 150° for successive power levels. In addition, there was no sideline power condition run for the hardwall fan case configuration (#6 in Table 1), and the baseline DEI liner run was not a complete power line although the three conditions of approach, cutback, and sideline were included in the data set.

The directivity split point between dominant inlet and aft fan noise normally was around 70° to 80°. The directivities for the ADP had two peaks with a distinct valley in between as shown in Figure 6 where the inlet component is represented by the circular symbols and the aft component by the square symbols. The solid line is the total and where the inlet and aft are equal define the split point. This distinct valley does not occur in every configuration (especially at higher power settings) which results in a 10° uncertainty in the split point choice. The split point was also confirmed by comparisons with the aft barrier data taken for certain configurations (hardwall, single layer, double layer, and bulk). For the high frequency bands (above band 30) the agreement was quite good. The lower frequencies however show a fairly large disagreement between the barrier data and the

inlet noise model results. Examples are shown in figure 7 -9 for the hardwall approach, cutback and sideline conditions. The reason for this discrepancy is not known. Bands 21 and 22 were corrected for jet noise by PW using the 1.5 dB/octave roll off. However bands 23-25 also show a significant disagreement. If jet noise and its associated roll–off is responsible for the apparent contamination of the inlet data in the low frequencies one would expect the problem to worsen with increased power setting. This does not seem to be the case. In any case, caution should be used in calculating inlet liner low frequency attenuation.

LINING ATTENUATION OF AFT RADIATED FAN NOISE

Since Boeing was contracted to design the aft fan duct liners for the ADP model test, only the aft fan attenuations were calculated and compared with the pre–test predictions in this report. There were four different aft fan duct liners tested: hardwall, Boeing single layer, Boeing double layer, and a DEI liner. The attenuations for the aft liners can be calculated by comparing several different configurations to extract the effect of the aft liners. The DEI liner was specified as the 1992 technology standard to be compared against the current liners. The differences between the single and double layer liners also give an idea of how much improvement is possible using current technology.

Fully Treated Nacelle Aft Attenuations

Attenuations for the basic configurations (#2–5 in Table 1) were calculated by simply taking the desired treated configuration SPLs and subtracting them from the fully hardwall case SPLs (#1 in Table 1). Attenuations were calculated with the aft fan broadband noise models described above and are shown in Figures 10–21 for the four basic treated configurations (#2–5 in Table 1). These attenuations all contain the effects of the fan case liner and thus cannot be directly compared to the pre–test predictions which did not include this liner. The aft attenuations with the Boeing designed single layer liner fan duct (#3) are similar to those with the DEI single layer liners (#2) except the Boeing single layer liner fan duct configuration appears to show more high frequency attenuation than the DEI liner. Also the DEI liner peak attenuation is slightly larger than for the Boeing configuration at the cutback and sideline conditions. Note that the case liner was a single layer liner for the DEI linings and a double layer for the Boeing configuration. The Boeing double layer liner fan duct configuration (#4) appears to have slightly higher peak attenuation than the Boeing single layer fan duct configuration (#3) but the bandwidth of the double layer liner fan duct does not appear appreciably better then for the single layer liner fan duct. The aft attenuations for configuration #5, labeled the bulk absorber configuration in figs. 19-21, are expected to be essentially a repeat of configuration #4 since only the inlet liner is different. The peak attenuations appear to repeat well but there are bandwidth differences which are not understood. Configuration #5 shows poorer high frequency attenuation than configuration #4 for the approach and sideline conditions but slightly better high frequency attenuation at the cutback condition.

Aft PNLT Attenuations

The aft PNLT directivities and attenuations calculated by extrapolation of the noise models to the FAR conditions for approach, cutback and sideline for the design airplane are shown in figs. 22-24. Results are shown for the fully hardwall nacelle, the DEI liner nacelle, the Boeing single layer fan duct nacelle and the Boeing double layer liner nacelle. The Boeing designed liners showed significant improvement relative to the DEI liner. Also the Boeing double layer liner showed significant peak angle PNLT attenuation improvement relative to the Boeing single layer liner at cutback and takeoff.

Fan Duct Liner Attenuations

The last two configurations tested (#6-7 in Table 1) can be used to isolate the aft liner attenuations which were predicted during the design process. For the aft single layer liner, only one comparison can be made for attenuations while two different comparisons can be made for the aft double layer liner. These comparisons are shown in Table 3. In addition, the attenuation effects of the fan case liner on aft fan noise are isolated and examined as indicated in Table 3 even though no predictions for this attenuation were made by Boeing prior to the test.

Table 3: Comparisons for Attenuation Calculations

Attenuation	Inlet	Mid	Aft	Attenuation	Inlet	Mid	Aft
Fan Duct	HW	DDOF	HW	Fan Case	HW	HW	HW
	SDOF	DDOF	SDOF		HW	DDOF	HW
Fan Duct	HW	DDOF	HW	Fan Case	DDOF	HW	DDOF
	DDOF	DDOF	DDOF		DDOF	DDOF	DDOF
Fan Duct	HW	HW	HW				
	DDOF	HW	DDOF				

The aft fan duct liner prediction comparisons are shown in Figures 25-30 using the aft fan broadband noise models and calculated according to Table 3 above. The plots for the fan duct attenuations are marked according to whether the fan case was hardwall or treated. The data are compared to predictions made for bands 27–38.

The attenuations for the Boeing designed single layer fan duct liner are shown in Figures 25-27. At approach, the predicted levels are 2–3 dB higher than measured; at cutback they are close to the measured attenuations; and at sideline, the predicted levels are well below the measured data except at the very aft angles. The measured peak attenuation frequency is generally one or two bands lower than the predictions; however, the general shape and bandwidth of the predictions agree quite well with the measured values. The shift in peak attenuation may be due to off–design cavity depths of the liner due to the difficulties of production in model scale. The single layer predictions also show a distinct secondary peak at band 37 which is most likely a cavity resonance. This resonance is not consistently observed in the measured data.

Two independent comparisons can be made to calculate the measured attenuation for the double layer liner. The comparisons are shown in Figures 28-30. As for the single layer liner, the predicted double layer liner attenuations were higher than the measured data at the approach condition, agreed reasonably well with the measured data at the cutback condition and were significantly below the measured data at the takeoff sideline condition. The two measured attenuation calculations closely match each other below band 34; however, there are large differences seen in the higher bands where more attenuation is measured with the hardwall fan case than the treated fan case. The slope of the attenuation levels at the higher bands for the treated fan case seems to agree with the roll–off of the predicted attenuations. This is clearly seen at the cutback condition (Figure 29) where the attenuation levels at the higher bands with the hardwall fan case do not roll–off. Unfortunately, there was no takeoff sideline condition run for the hardwall fan case configuration. One interpretation of this data is that for the hardwall fan case configuration there is more energy in the higher order modes as the noise exits the case region into the fan duct than for the treated fan case configuration. This is consistent with the idea that the case liner will more strongly attenuate higher order modes. The Boeing prediction code assumes a modal energy distribution which is nearly constant until the modes approach cutoff where the energy per mode falls off rapidly. It is not known if this distribution more closely matches the hardwall or treated fan case situation at the entrance to the fan duct.

The standard process at Boeing uses a correction factor of 1.0 at approach, 0.8 at cutback, and 0.6 at sideline applied to the attenuations predicted with the duct propagation code. The 0.6 factor clearly made the predicted attenuations too low at the sideline condition. It appears that a correction factor of approximately 0.8 would better fit the data at all power conditions if the predictions are applied to the treated fan case reference noise levels. For a hardwall fan case the Boeing predictions with a 0.8 factor will under predict the higher frequency attenuations.

Sound power levels were calculated from the aft broadband noise models using SPL data from 90° to 140°. Sound power level attenuations were then determined by taking the delta between the same configurations listed in Table 3 for the fan duct double layer liner. Figure 31 shows a contour plot of the sound power level attenuations for both the treated and hardwall fan case comparisons over the entire power-line. The sound power attenuations confirm the same observations made previously. Clearly, the levels are very similar below band 33 for both comparisons. The peak power attenuation level of 7 dB is around band 30 in both cases, and the same increase in high frequency attenuation for the hardwall fan case is evident. Note that the sideline condition is not included in these plots due to missing data and/or bad data points in the spectra.

Single Layer Liner Attenuations vs. Double Layer Liner Attenuations

As shown in Ref. 1, Boeing expected a significant improvement in attenuation for the Boeing designed double layer liner fan duct compared to the Boeing designed single layer liner fan duct. Comparisons of the measured double layer - single layer differences with the pre-test predictions are shown in Figures 32-34. The pre–test predictions showed the

most improvement for the double layer liner over the single layer liner at the approach condition. The double layer liner did show consistent improvement between bands 25 and 30 as was predicted although generally the improvement was not as large as predicted (except for the sideline condition). The predicted high frequency attenuation improvement shown by the second peak centered around band 35 for the double layer liner however was not observed. In fact in the very high frequencies, bands 36-40, the single layer liner data showed more attenuation than the double layer liner data. The reason for this is not known. It should be pointed out, however, that there is no way of knowing what the actual liner impedances were at these high frequencies. Frequency bands 36-40 full scale actually covered the frequency range of approximately 21 kHz to 66 kHz in the model test. No demonstrated ability exists to measure liner impedance at these frequencies.

Fan Case Liner Attenuations

The effect of the fan case lining on the aft radiated noise is shown in Figures 35-37. Two sets of attenuation spectra are shown representing the last two sets of comparisons shown in Table 3 . The benefit of the case liner was smaller with the treated fan duct than with the hardwall fan duct In fact, the case lining appears to increase the high frequency noise with the treated fan duct. One would expect the fan case liner to be less effective with a lined fan duct than with a hardwall fan duct as is observed but the apparent noise increase at 90° and 100° is not consistent with the strong attenuation measured with the hardwall fan duct. Note that the larger high frequency case liner attenuation with the hardwall fan duct is consistent with the observation above that the fan duct lining was more effective with the fan case hardwall than with the fan case treated.

As with the fan duct, aft sound power attenuation levels were calculated for the fan case liner configurations and are shown in Figure 38. The contour shows quite clearly the larger high frequency attenuations associated with the hardwall fan duct.

Fan Tone Attenuations

The lining attenuations discussed in the above sections were all determined from the aft fan broadband noise models. The estimated aft fan duct radiated tone attenuations are shown in Figures 39-44 for the Boeing designed single layer and double layer aft fan ducts. Non–zero data points are only shown for those tones which could be clearly identified in both the hardwall and treated narrowband data, i.e. those tones not masked by the broadband noise floor. Also shown for comparison are the measured and predicted broadband attenuations discussed previously. It is clear that there are significant differences between the measured tone and broadband attenuations. Although there are some exceptions it appears that the overall tendency is for the tone attenuations to be larger than the broadband attenuations. As noted previously, the first fan harmonic is dominant in the aft arc for the hardwall spectra. These figures show that both liners have effectively attenuated this tone. The double layer liner, however, tends to attenuate more fan harmonics than the single layer liner. This is especially evident at the cutback condition where several fan harmonics have been attenuated. The cutback condition also shows much higher tone attenuation levels for the double layer liner than the single layer

liner. At approach and sideline however, the tone attenuations for the two liners are similar in magnitude. Also note that the blade passage tone does not appear in the measured tone attenuations because it has been cut–off as expected. The Boeing predictions more closely match the measured broadband attenuations than the tone attenuations.

CONCLUSIONS

The evaluation of the nacelle liners relative to the 1997 25% peak aft angle PNLT attenuation improvement goal shows that the Boeing fan duct liner designs met the goal. At the approach condition both the Boeing single and double layer liner fan ducts showed a very large improvement (230%) relative to the DEI liner. At cutback the Boeing double layer liner showed a 51% improvement relative to the DEI liner and a 35% improvement relative to the Boeing single layer liner. At sideline the Boeing double layer liner showed a 109% improvement relative to the DEI liner and 56% improvement relative to the Boeing single layer liner. Boeing considers the comparison of the Boeing designed single layer fan duct with the Boeing designed double layer liner fan duct a reasonable comparison of 1992 technology with current advanced liners with some concerns. The main concern is related to the constraints associated with model scale acoustic liner testing. Model scale testing of nacelle liners is not an established procedure. It is not possible to scale the full scale designs because of the small curvature radii in model scale systems, the strength limitations for a scaled sheet thickness and the manufacturing limitations associated with the small orifice holes used with nacelle liners. In addition it is not possible to verify that the liner built for the model test has the desired acoustic impedance. While care was taken to minimize these concerns by using woven wire resistance elements without perforated plate and careful manufacturing procedures, the lack of ability to confirm the design impedance is a major difficulty.

Relative to the Boeing single layer liner fan duct, the Boeing double layer liner showed consistent improvement between bands 25 and 30 as was predicted, although generally the improvement was not as large as predicted (except for the sideline condition). The high frequency attenuation improvement predicted for the double layer liner however was not observed. In fact, in the very high frequencies, bands 36-40, the single layer liner data showed more attenuation than the double layer liner data. It appears that the single layer liner high frequency attenuation was better than predicted. When the double layer liner fan duct was evaluated with a hardwall fan case its high frequency attenuation was found to increase. This can be interpreted in terms of modal attenuation. If the fan case has already attenuated the more easily attenuated modes the fan duct lining efficiency drops, because it must attenuate a larger percentage of more difficult to attenuate modes.

The double layer liner fan case attenuation measured with a hardwall fan duct showed more attenuation at the higher frequency bands than with the treated fan duct. This is also probably a modal effect. The fan case lining is not as important if another liner, the fan duct liner, is available to attenuate the same modes that the case attenuates. The apparent increase in noise by the fan case with the treated fan duct is not understood in light of its significant attenuation with a hardwall fan duct.

The standard process at Boeing uses a correction factor of 1.0 at approach, 0.8 at cutback, and 0.6 at sideline applied to the attenuations predicted with the duct propagation code. The 0.6 factor clearly made the predicted attenuations too low at the sideline condition. It appears that a correction factor of approximately 0.8 would better fit the data at all power conditions if the predictions are applied to the treated fan case reference noise levels.

There are some general observations which resulted from going through the process to create the noise models for each configuration. The first fan harmonic (2BPF) is fairly dominant throughout the configurations and is especially large at very aft angles. As expected, BPF is cut–off and not readily identifiable in the narrowband data. The higher harmonics are present generally up to the third harmonic (4BPF).

REFERENCES

1. Bielak G. W., Premo J. W., Hersh A. S., "Advanced Turbofan Duct Liner Concepts", NASA CR-1999-209002

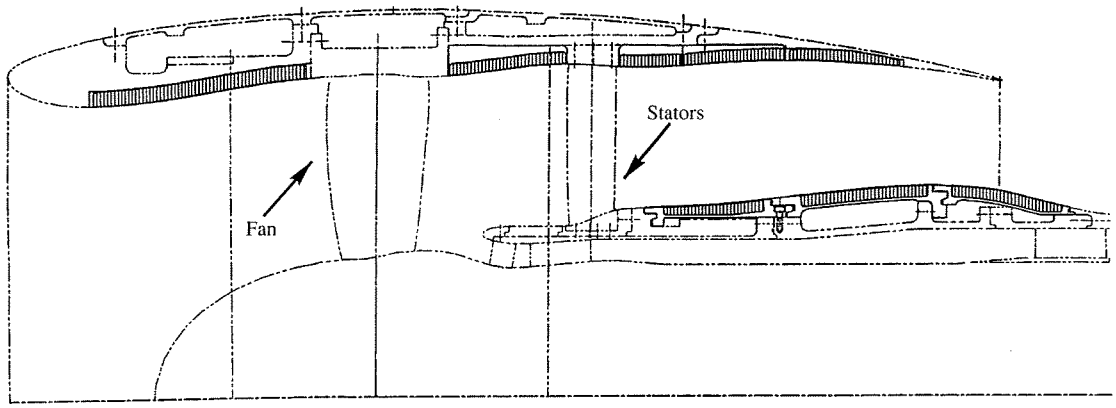

Figure 1: ADP Cutaway Schematic

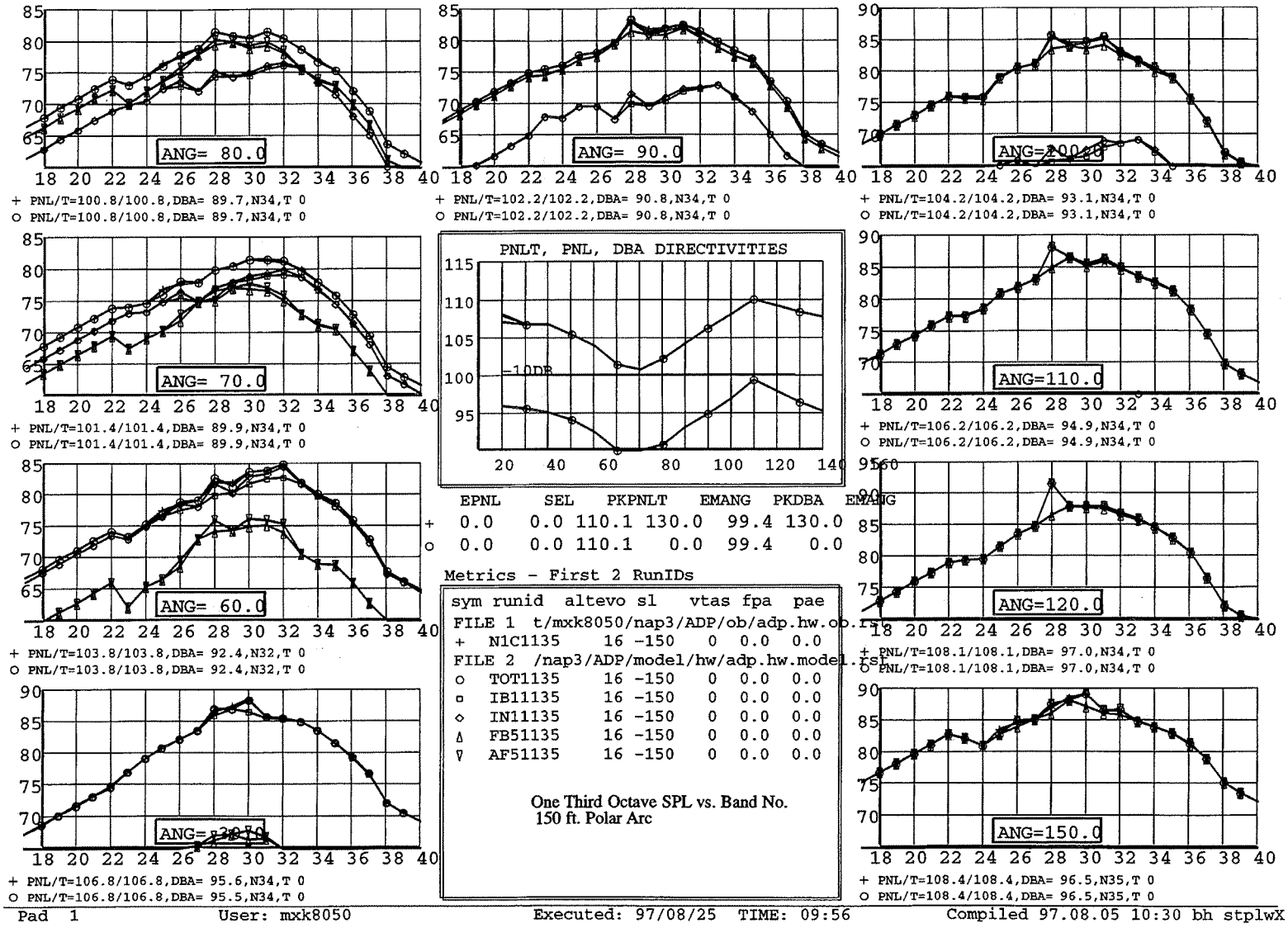

Figure 2: Hardwall Configuration at Approach Condition

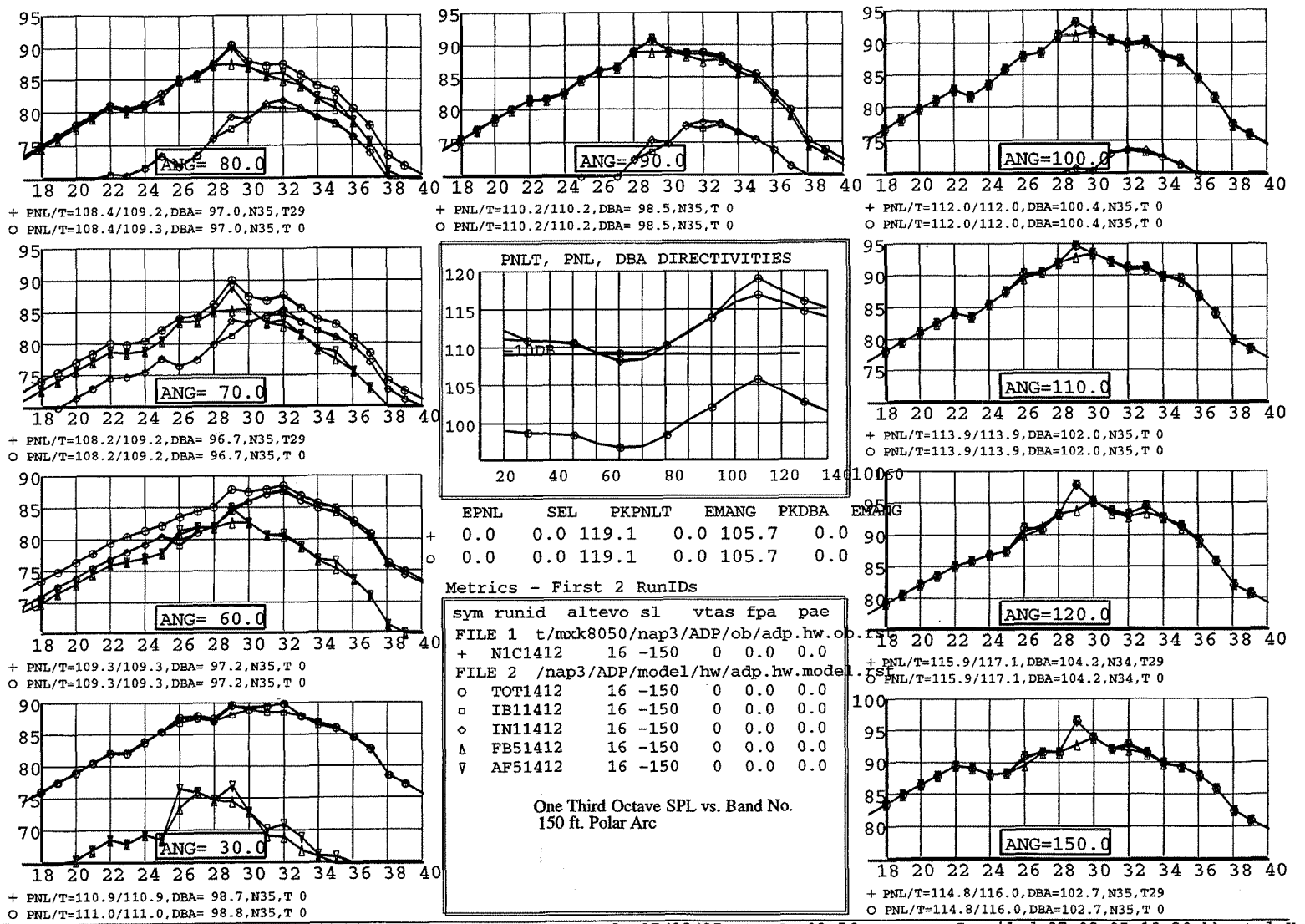

Figure 3: Hardwall Configuration at Cutback Condition

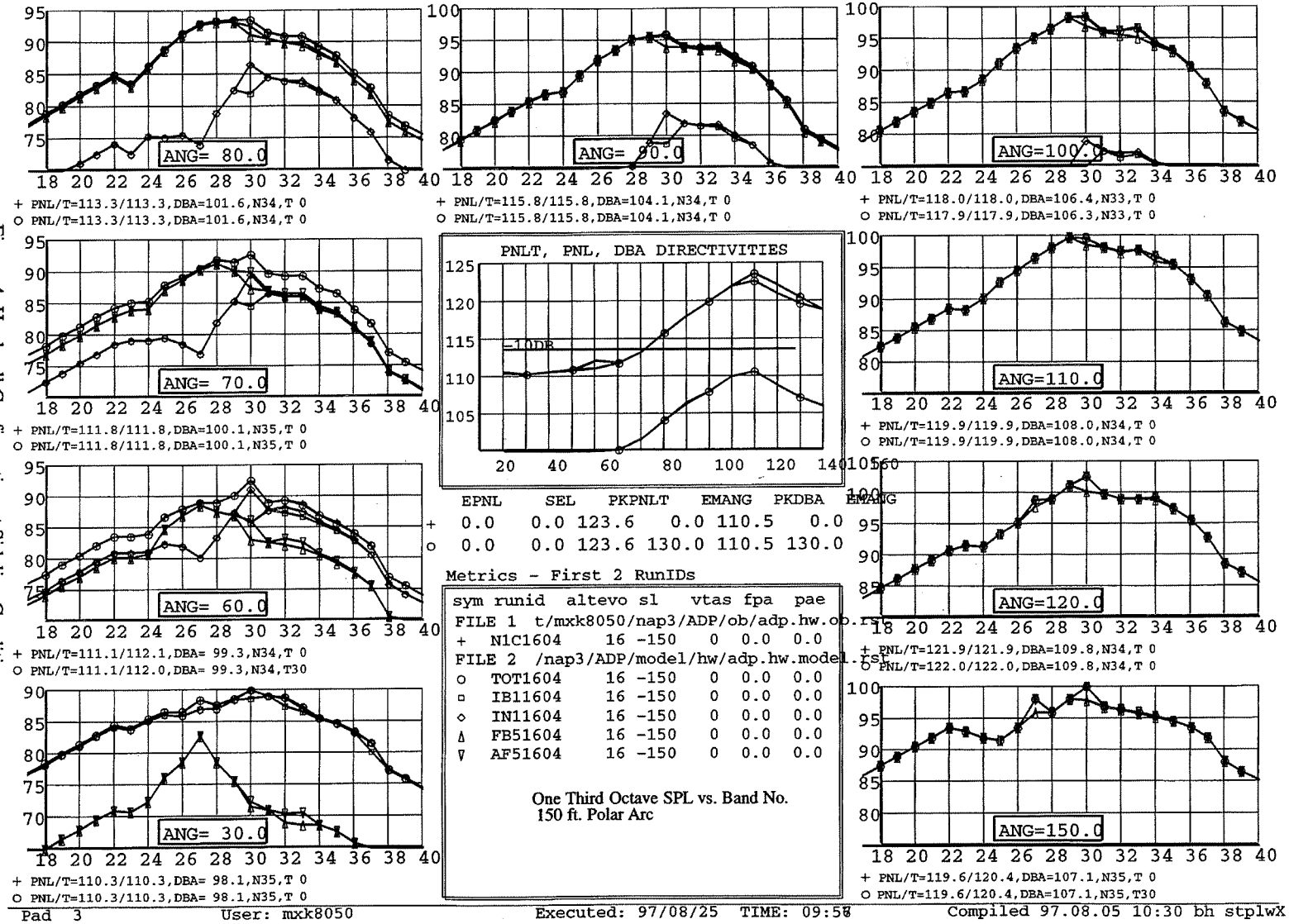

Figure 4: Hardwall Configuration at Sideline Condition

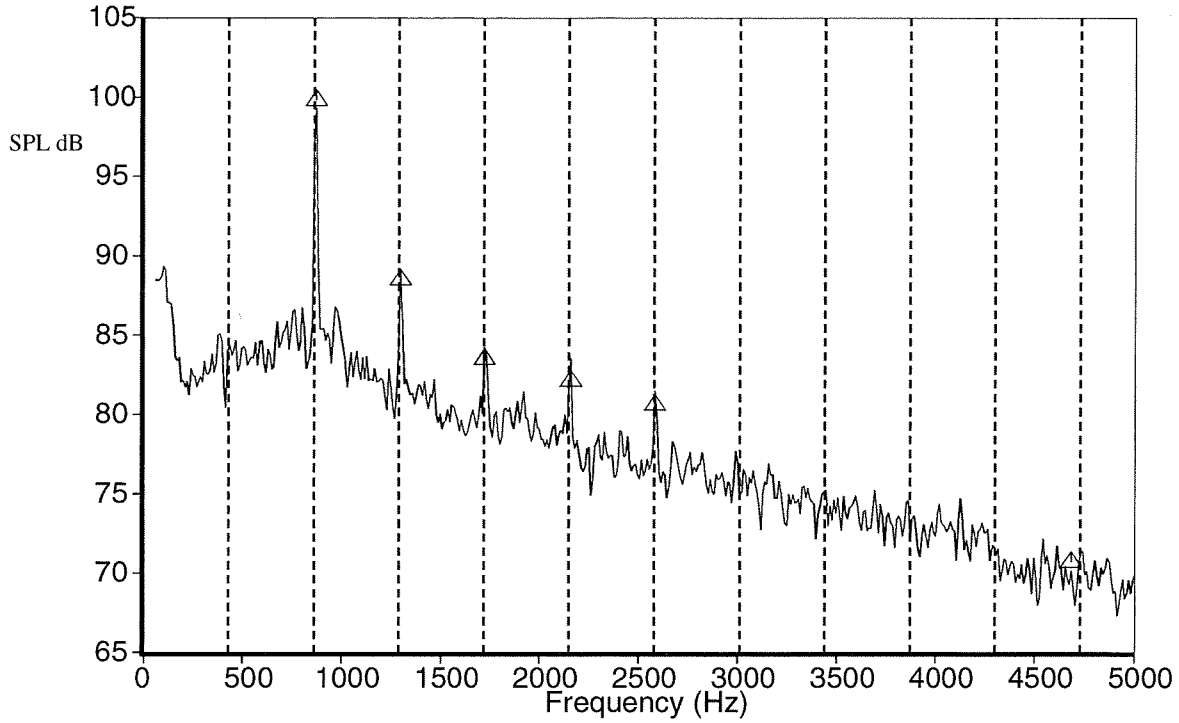

Figure 5: Hardwall Narrow-band Data at 130 deg for Cutback

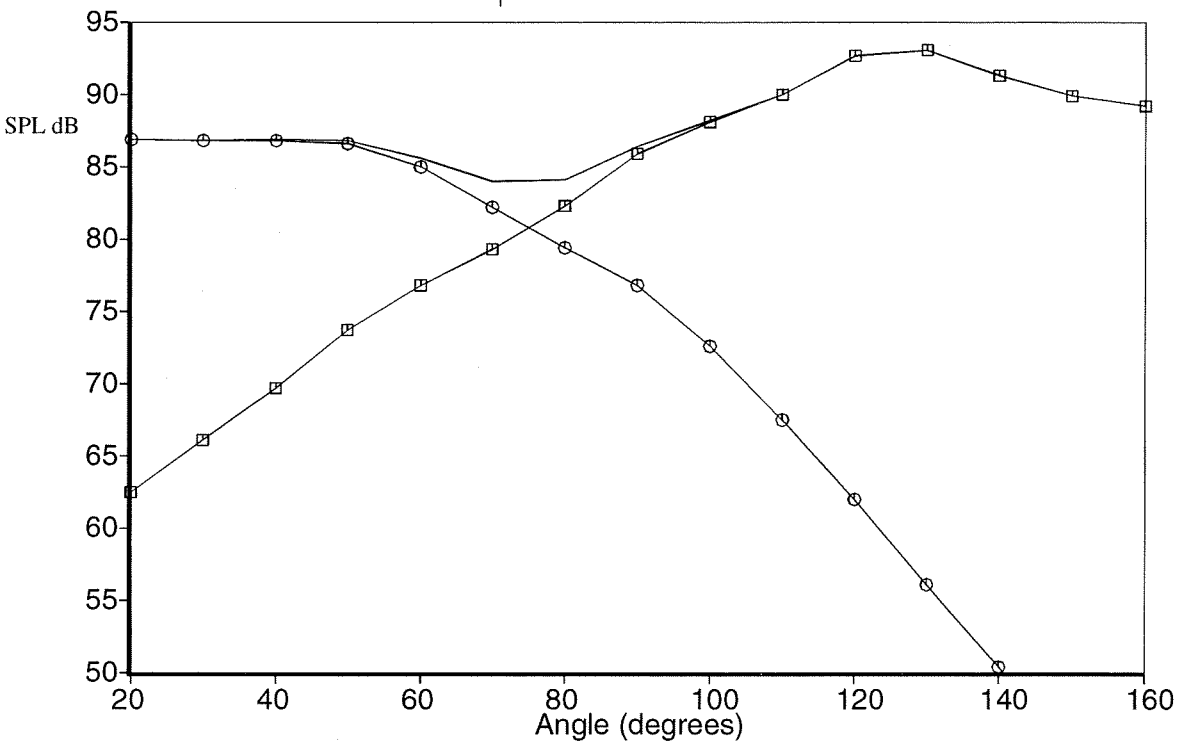

Figure 6: Hardwall Directivity for Band 34 at Cutback

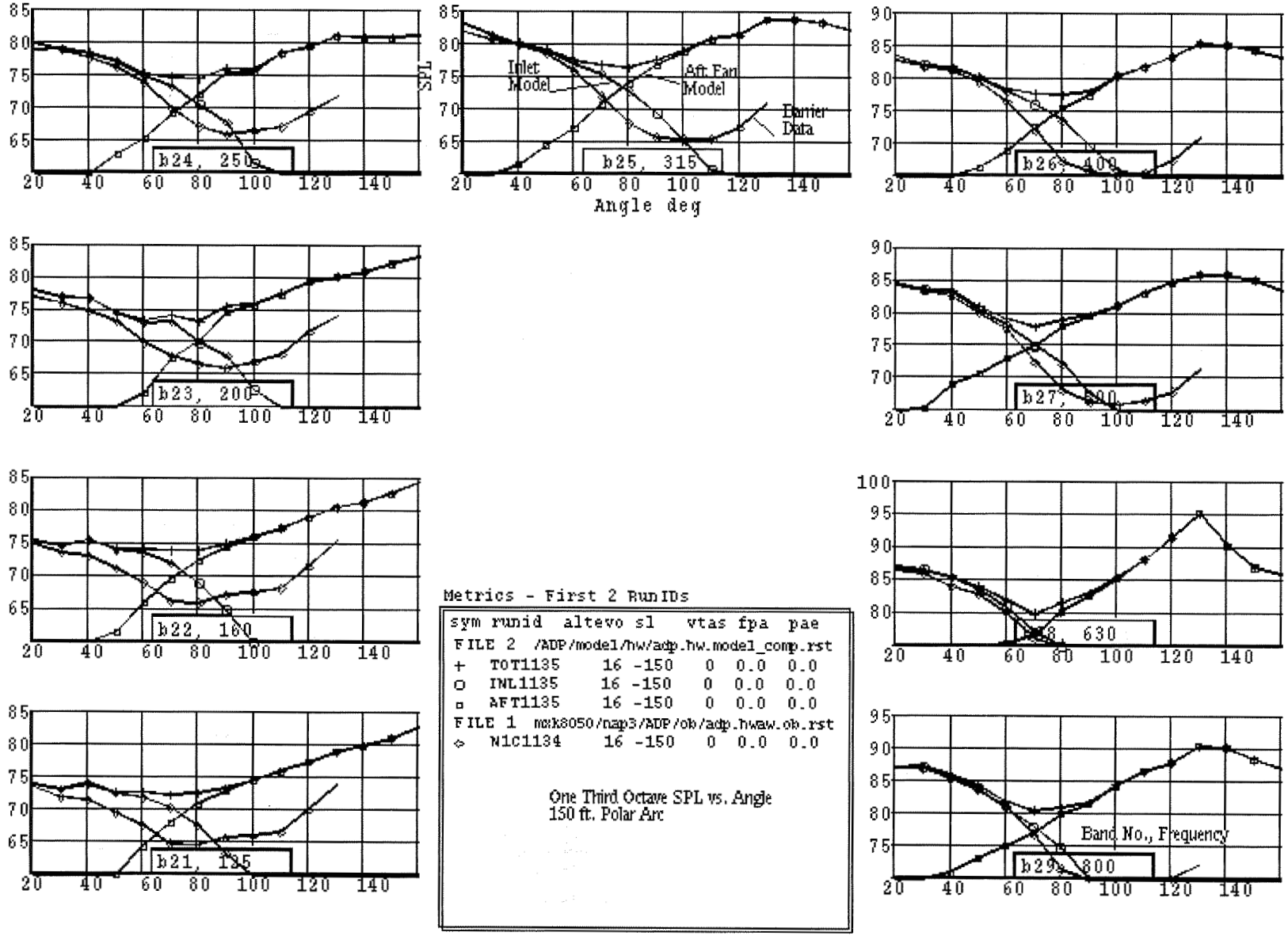

Figure 7: Hardwall Forward/Aft Split Comparison with Aft Barrier Data at Approach Condition

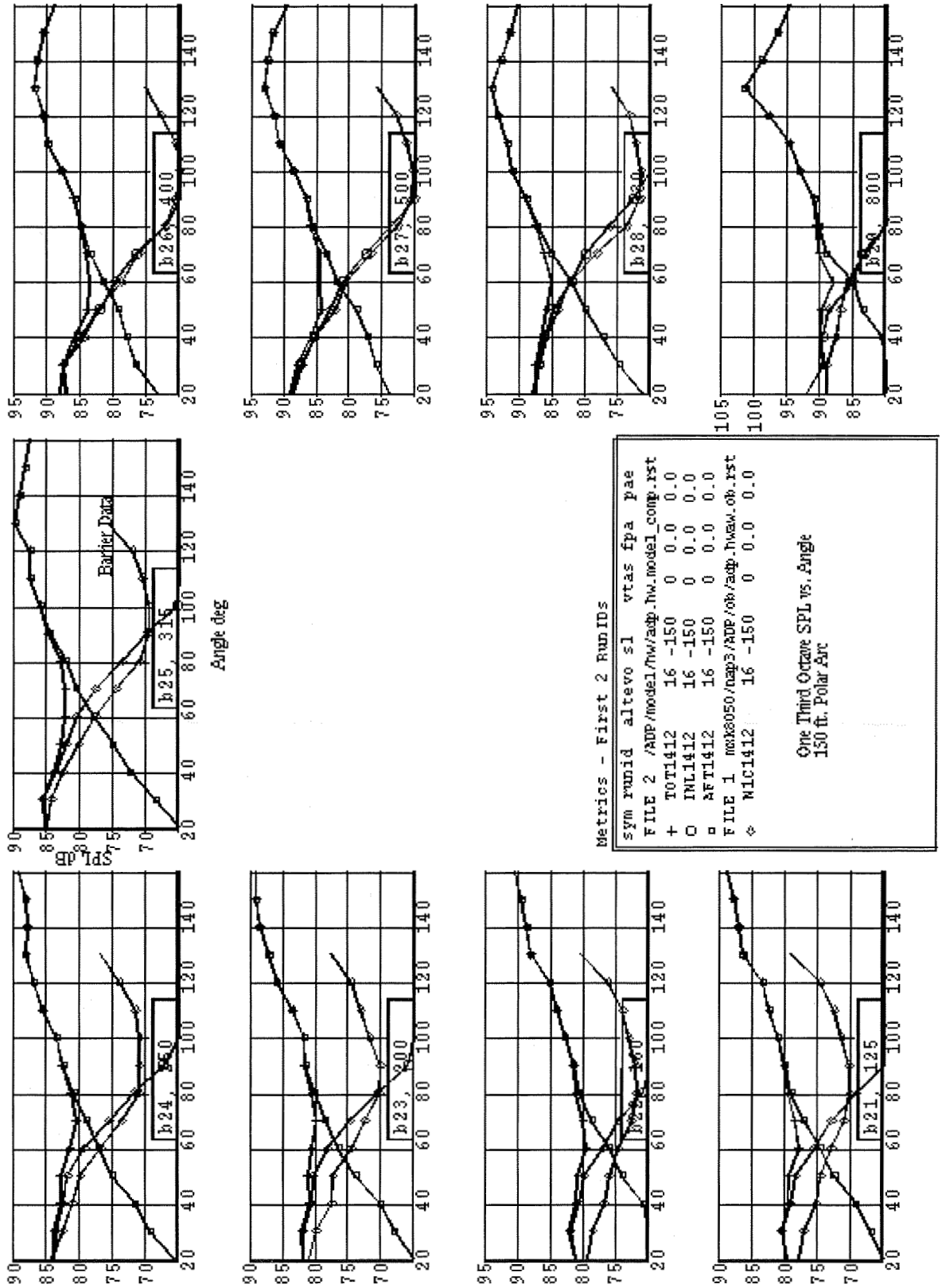

Figure 8: Hardwall Forward/Aft Split Point Comparison with Aft Barrier Data at Cutback Condition

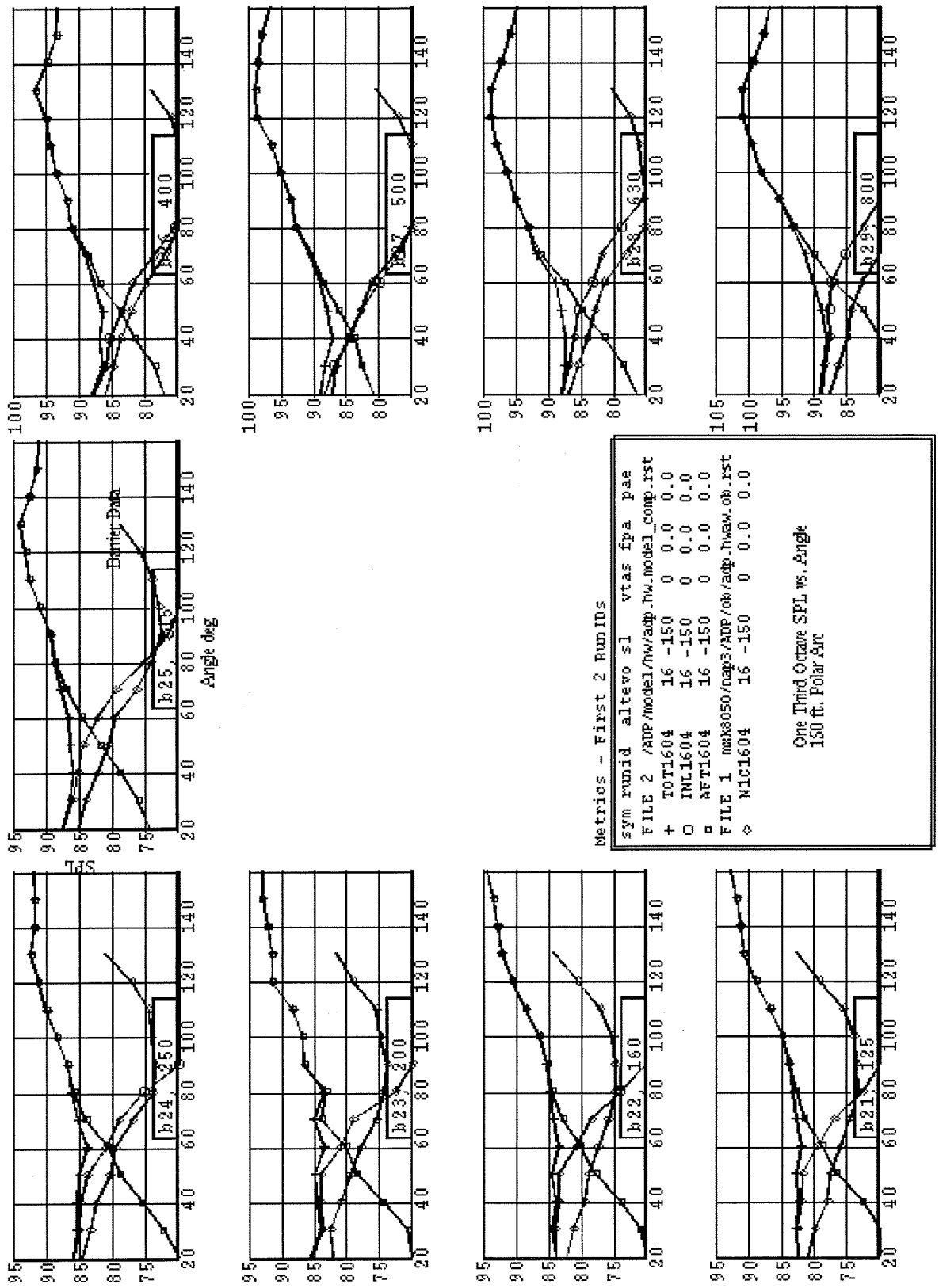

Figure 9: Hardwall Forward/Aft Split Comparison with Aft Barrier Data at Sideline Condition

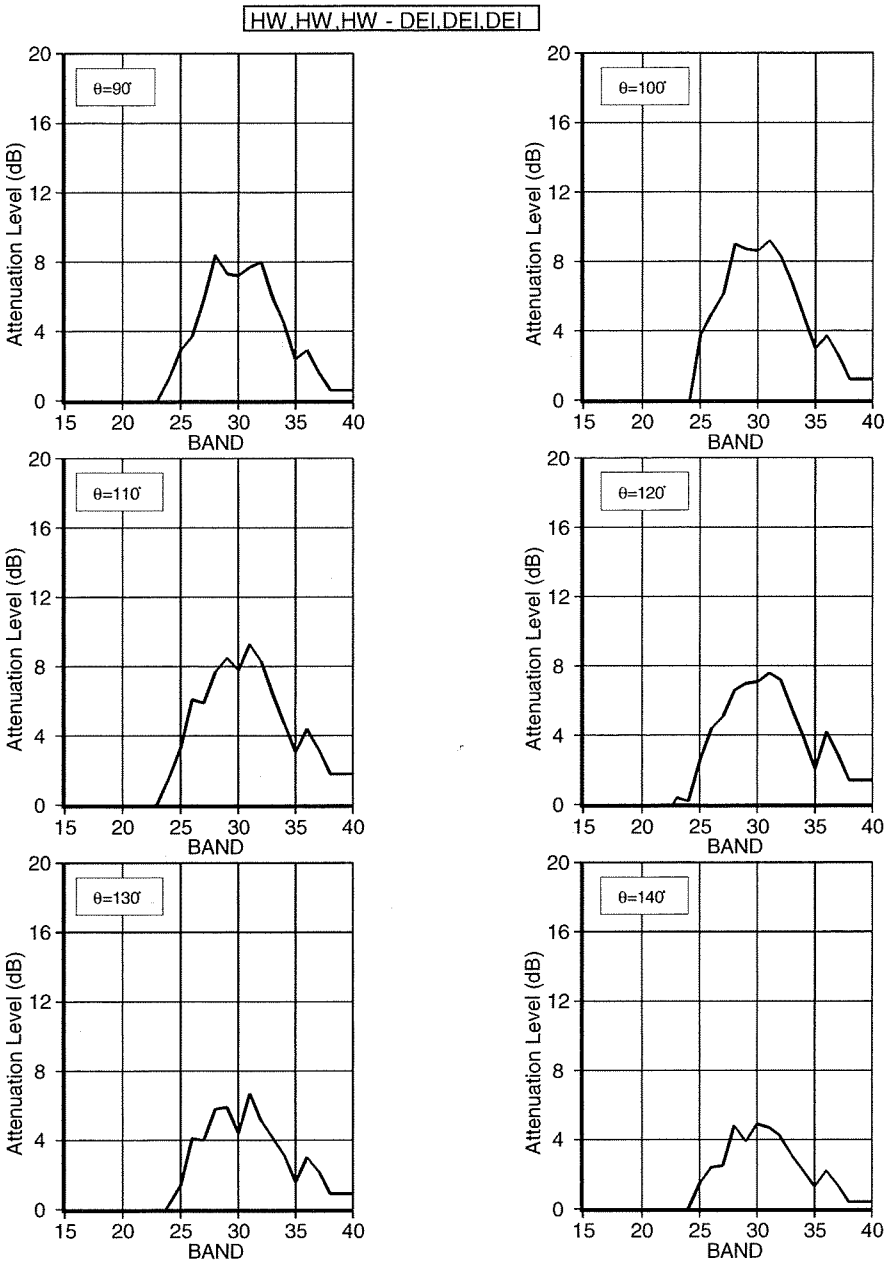

Figure 10: DEI Liner Aft Fan Broadband Attenuation at Approach

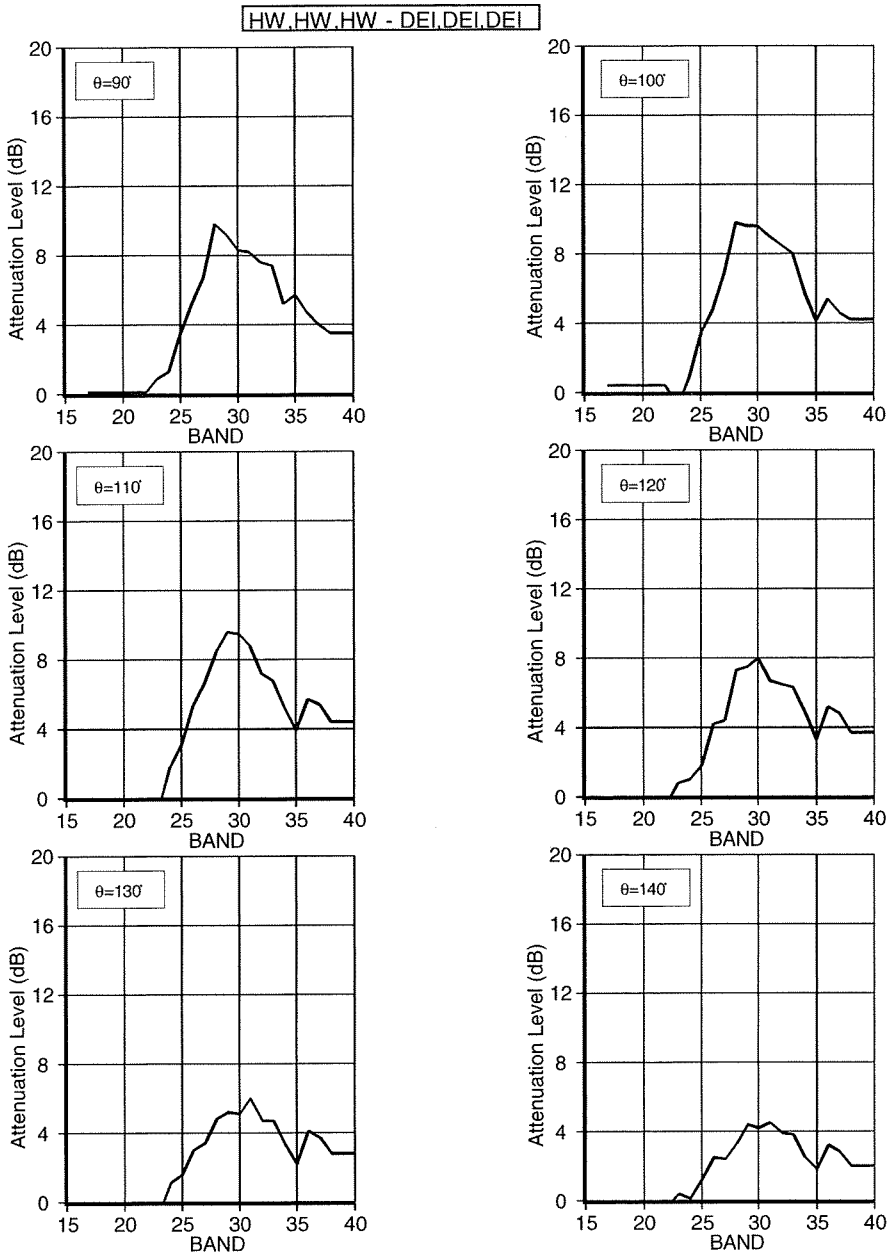

Figure 11: DEI Liner Aft Fan Broadband Attenuation at Cutback

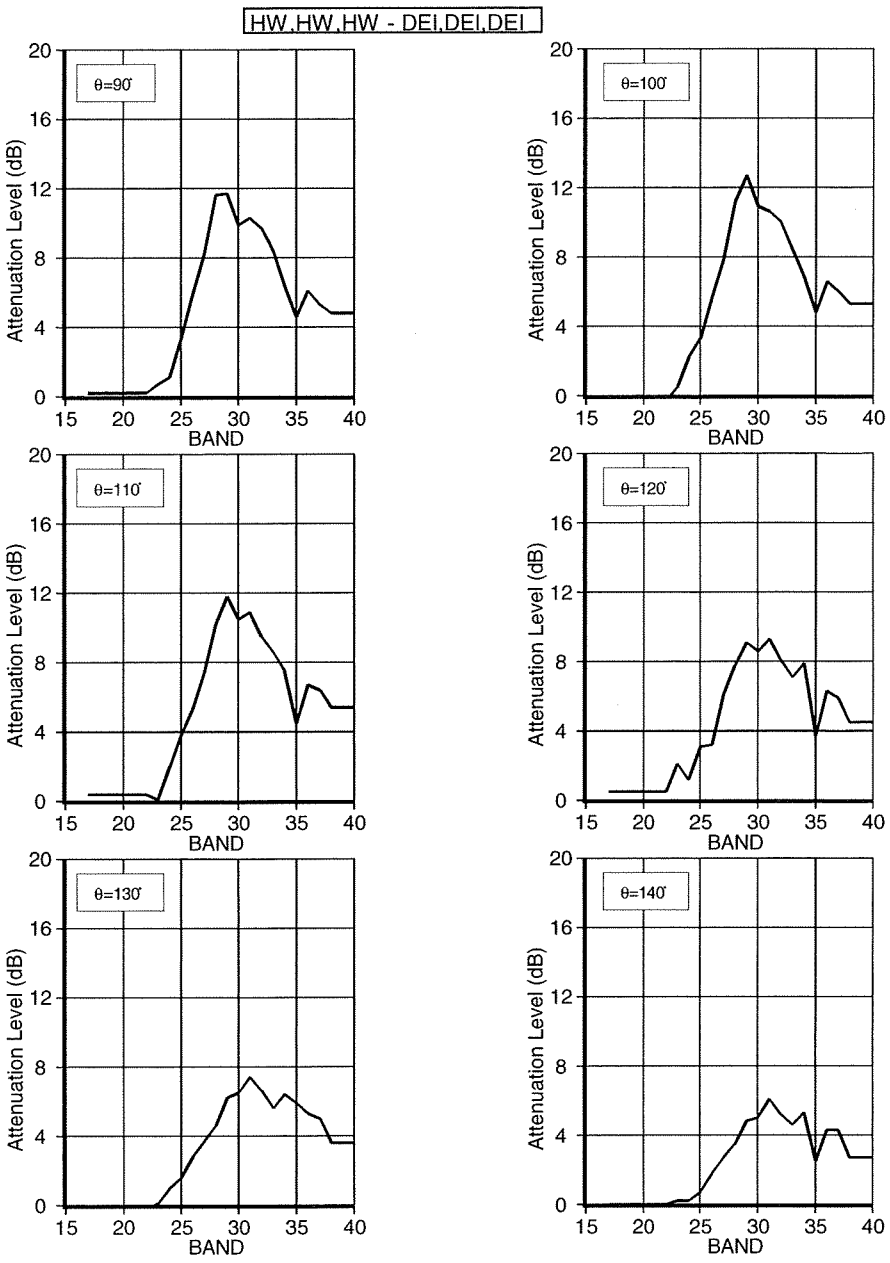

Figure 12: DEI Liner Aft Fan Broadband Attenuation at Sideline

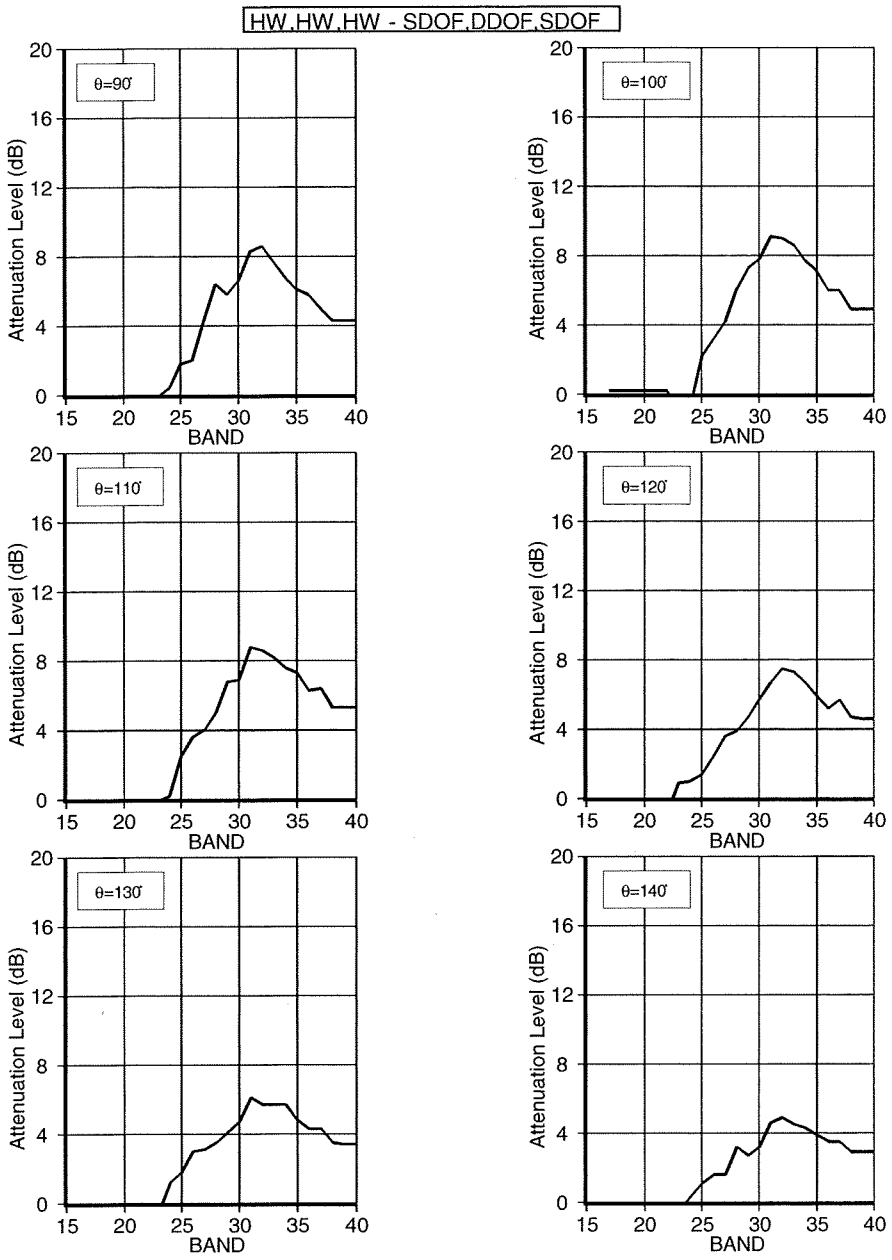

Figure 13: Single Layer Liner Aft Fan Broadband Attenuation at Approach

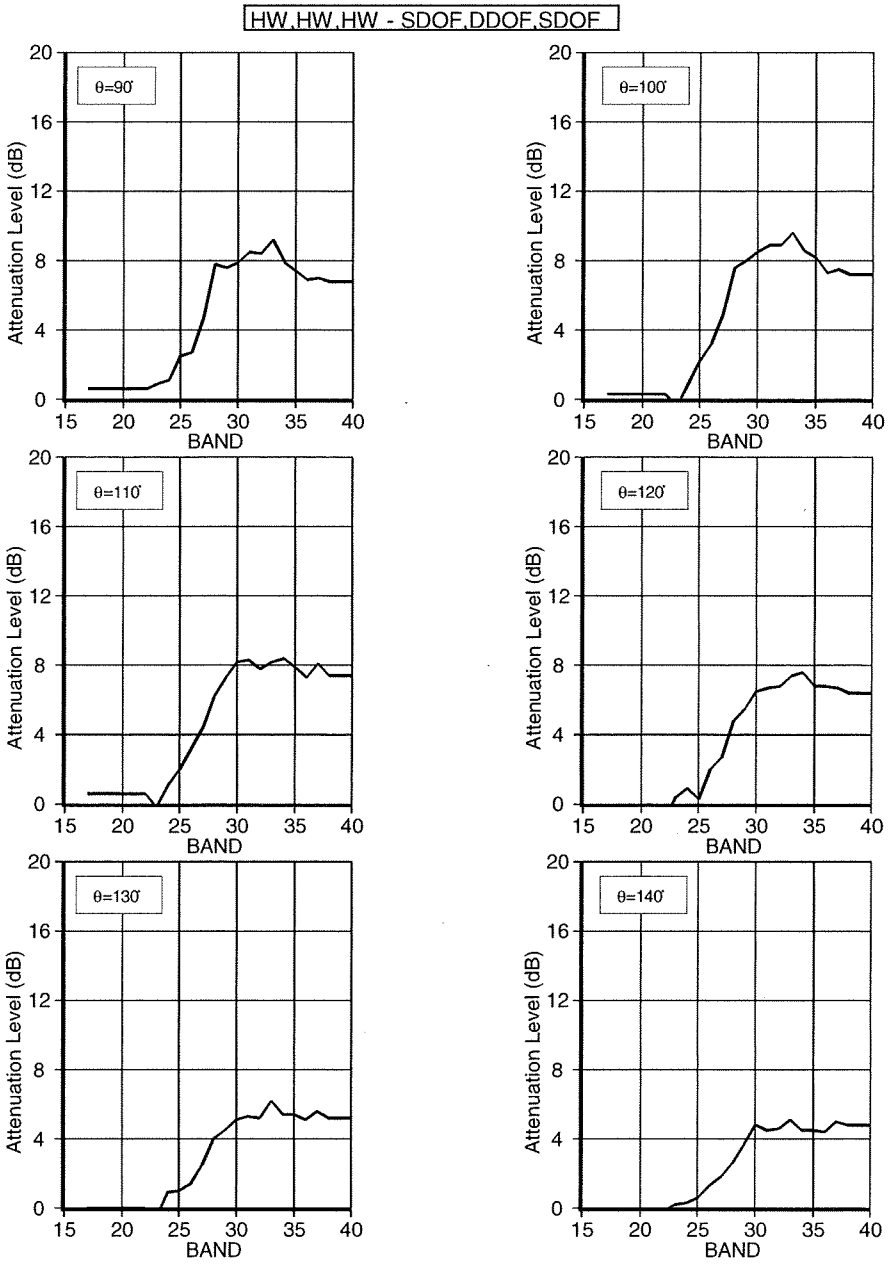

Figure 14: Single Layer Liner Aft Fan Broadband Attenuation at Cutback

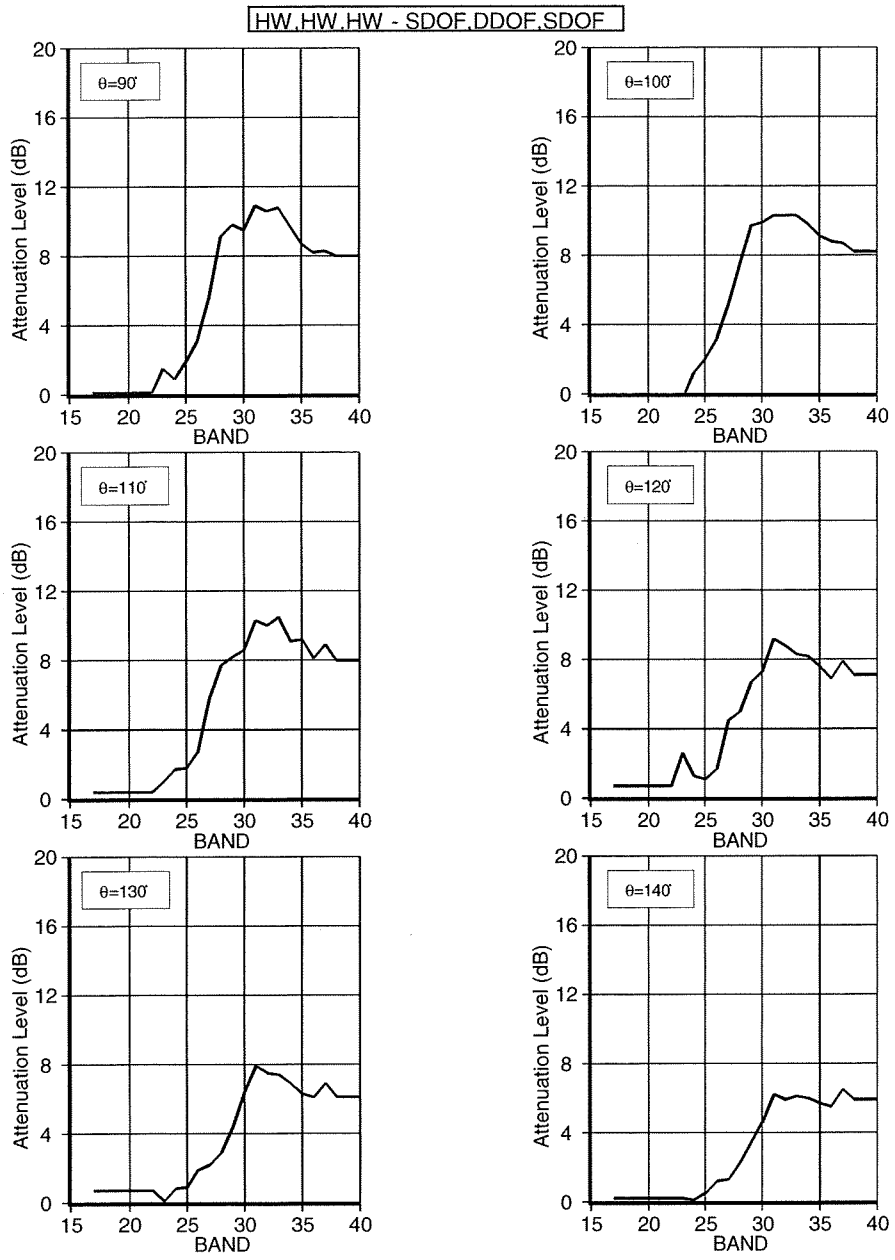

Figure 15: Single Layer Liner Aft Fan Broadband Attenuation at Sideline

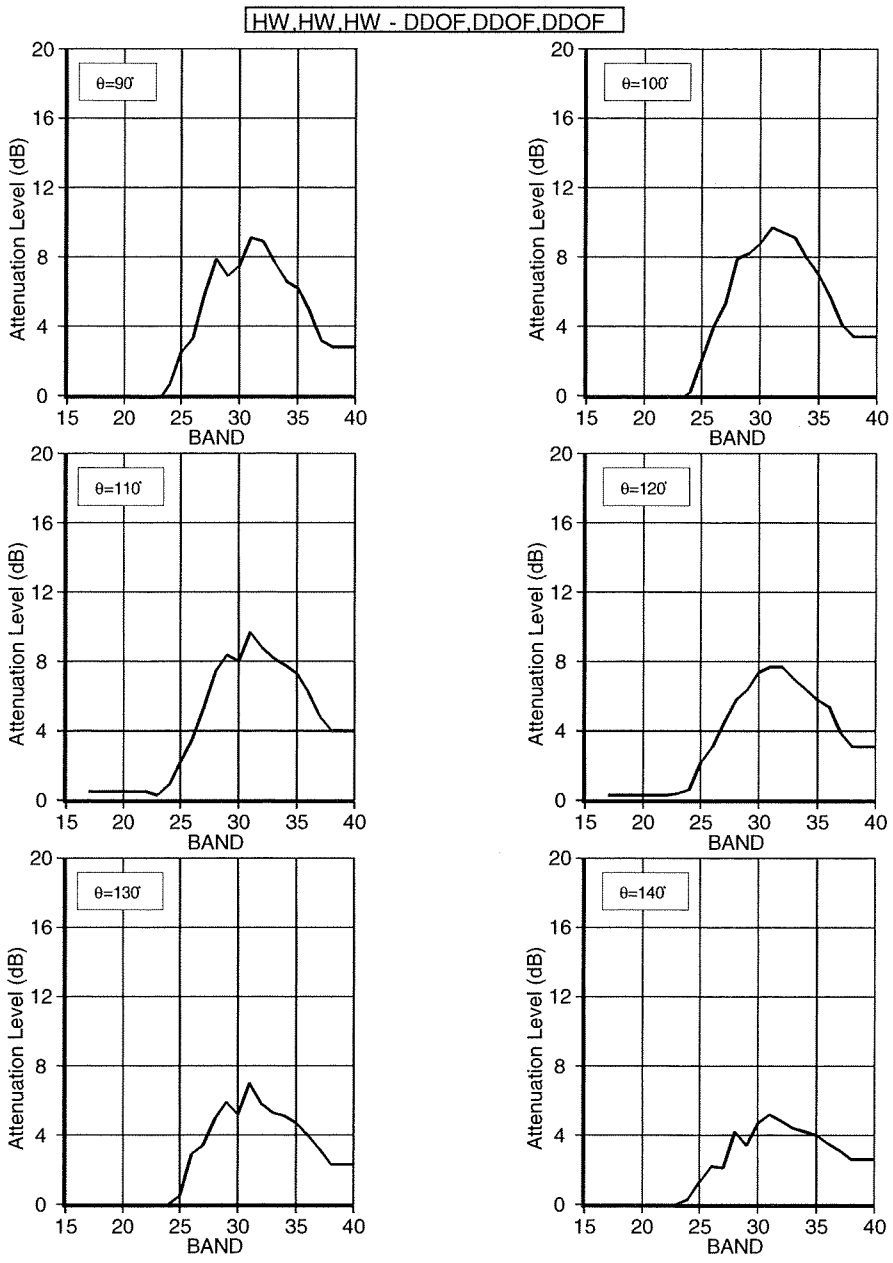

Figure 16: Double Layer Liner Aft Fan Broadband Attenuation at Approach

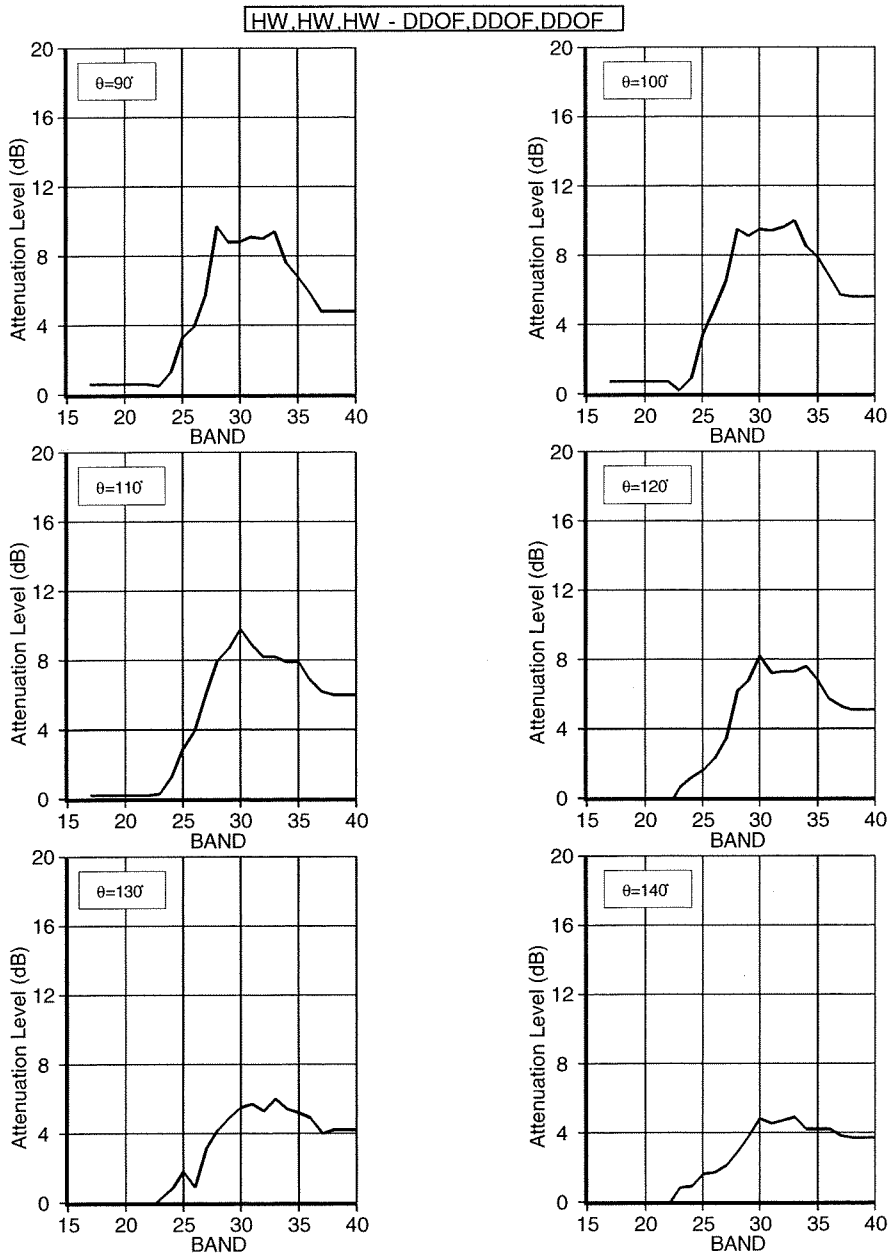

Figure 17: Double Layer Liner Aft Fan Broadband Attenuation at Cutback

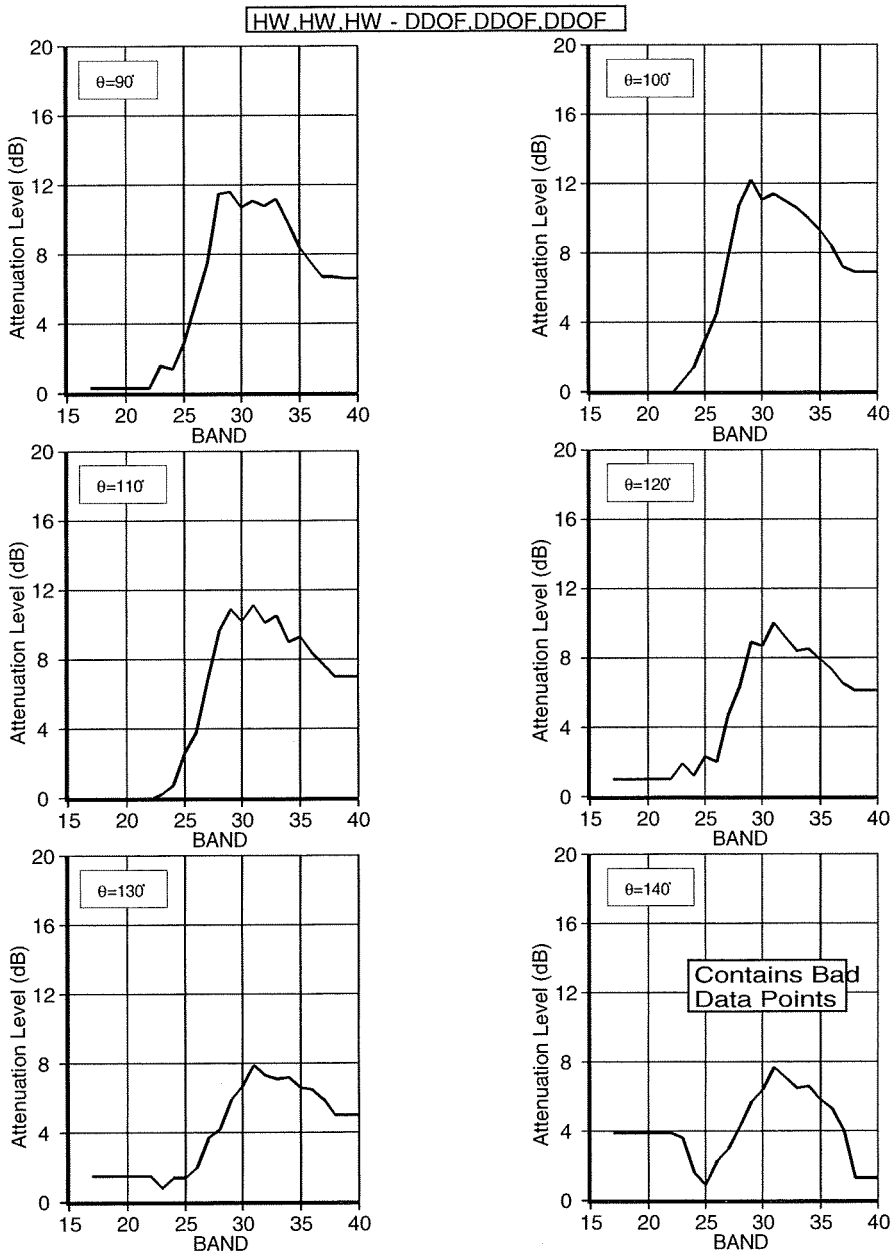

Figure 18: Double Layer Liner Aft Fan Broadband Attenuation at Sideline

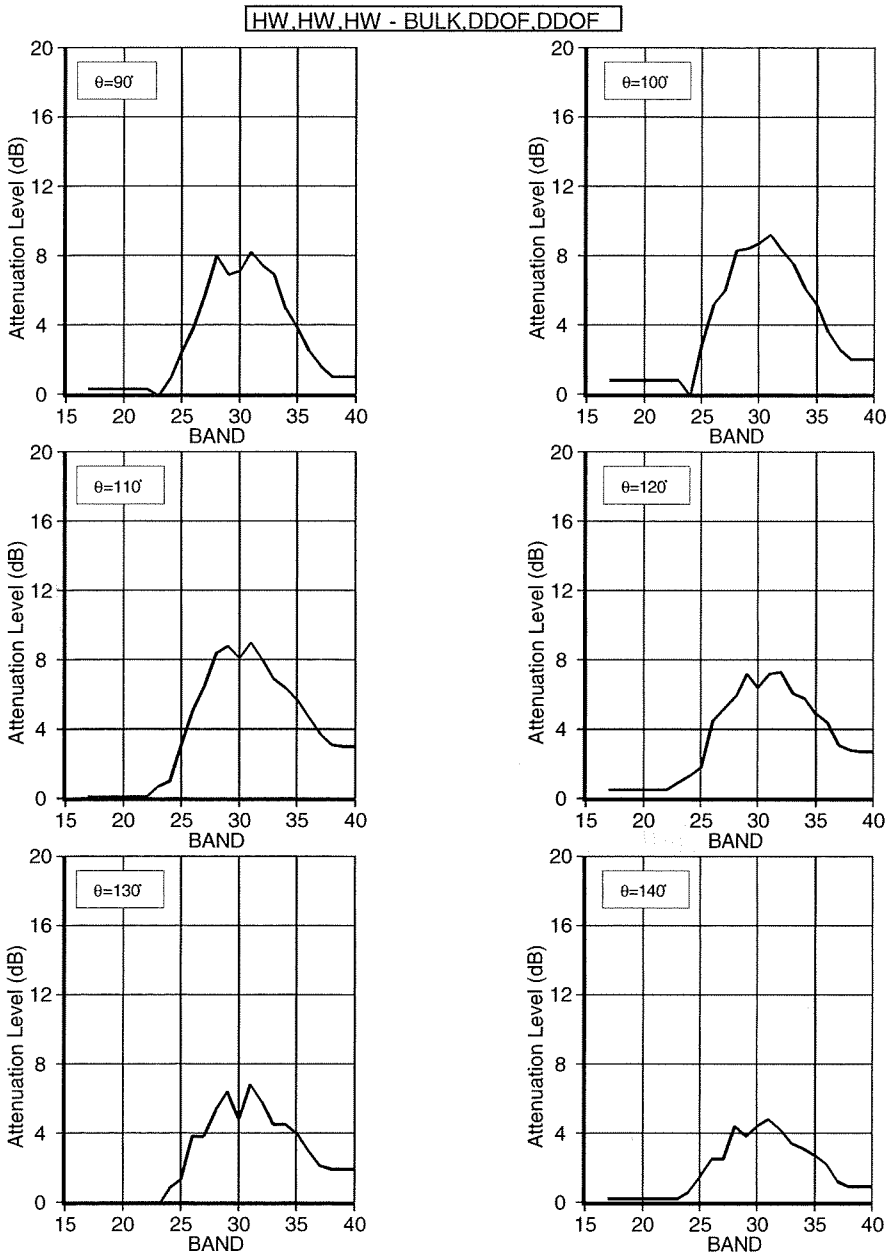

Figure 19: Bulk Absorber Aft Fan Broadband Attenuation at Approach

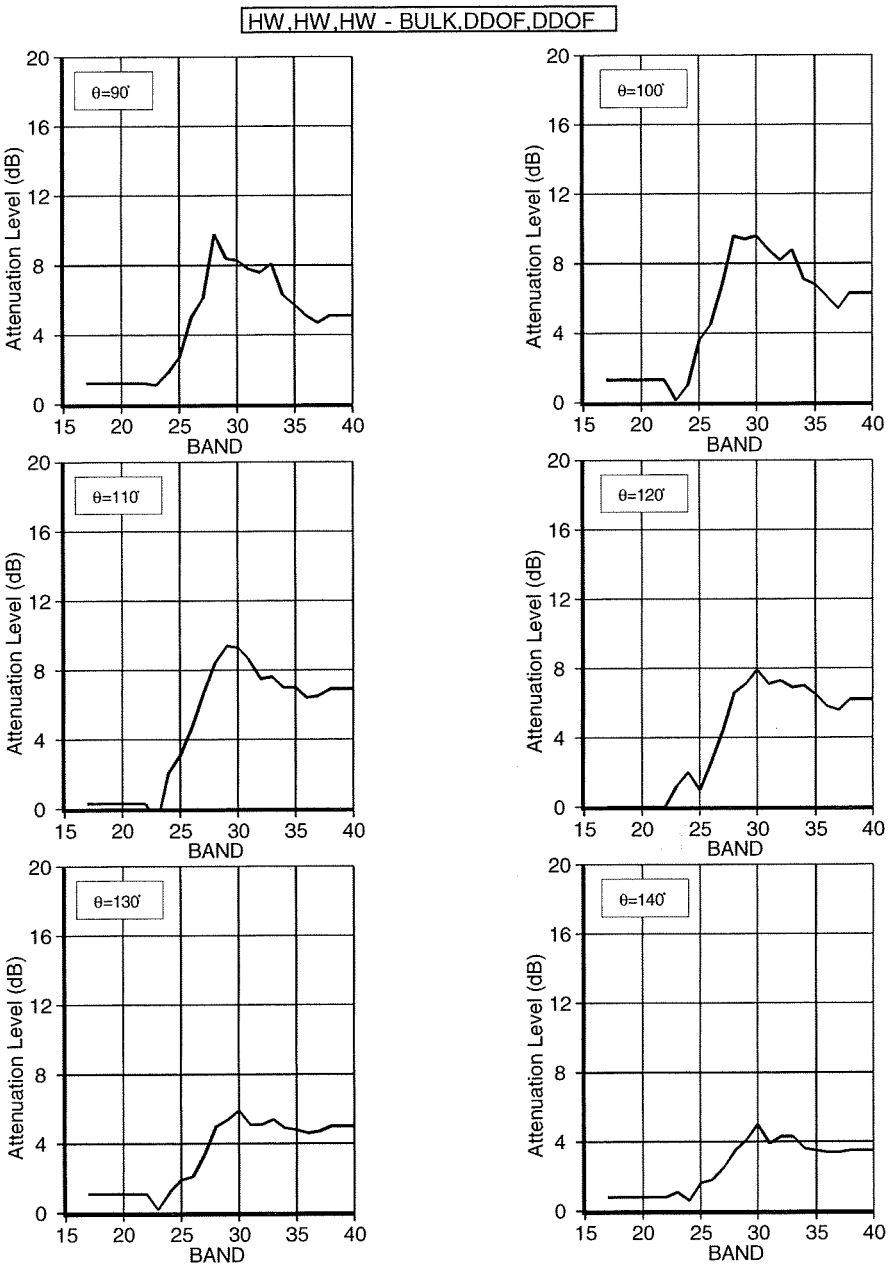

Figure 20: Bulk Absorber Aft Fan Broadband Attenuation at Cutback

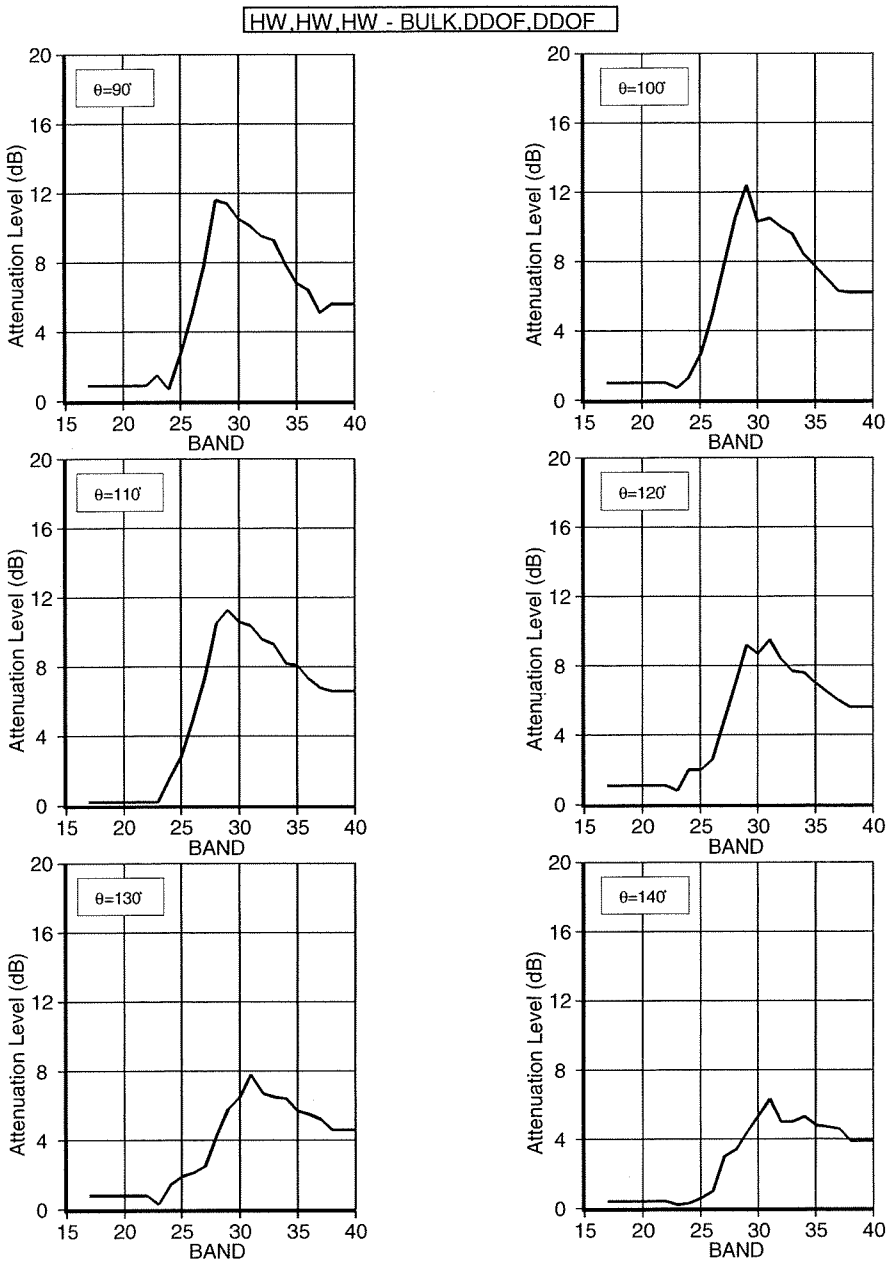

Figure 21: Bulk Absorber Aft Fan Broadband Attenuation for Sideline

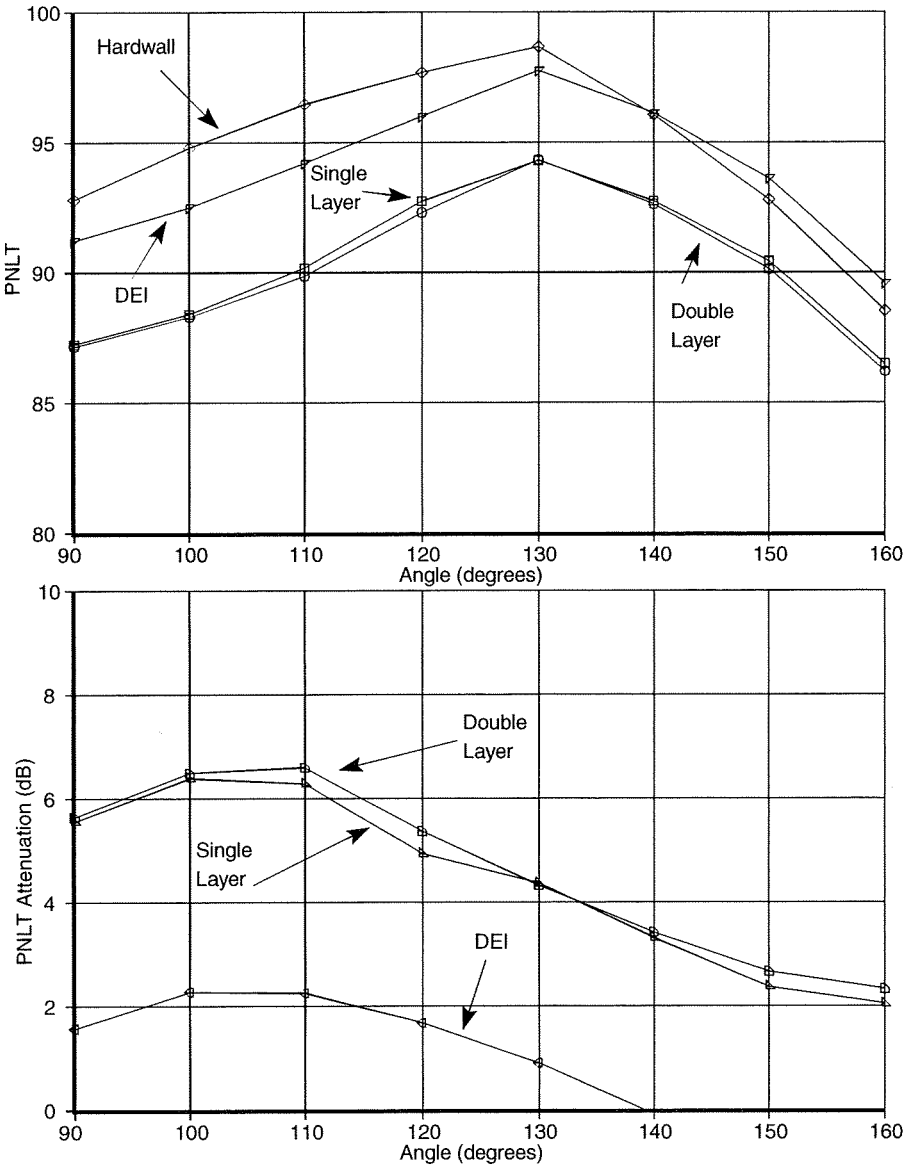

Figure 22: PNLT Calculations at Approach Condition

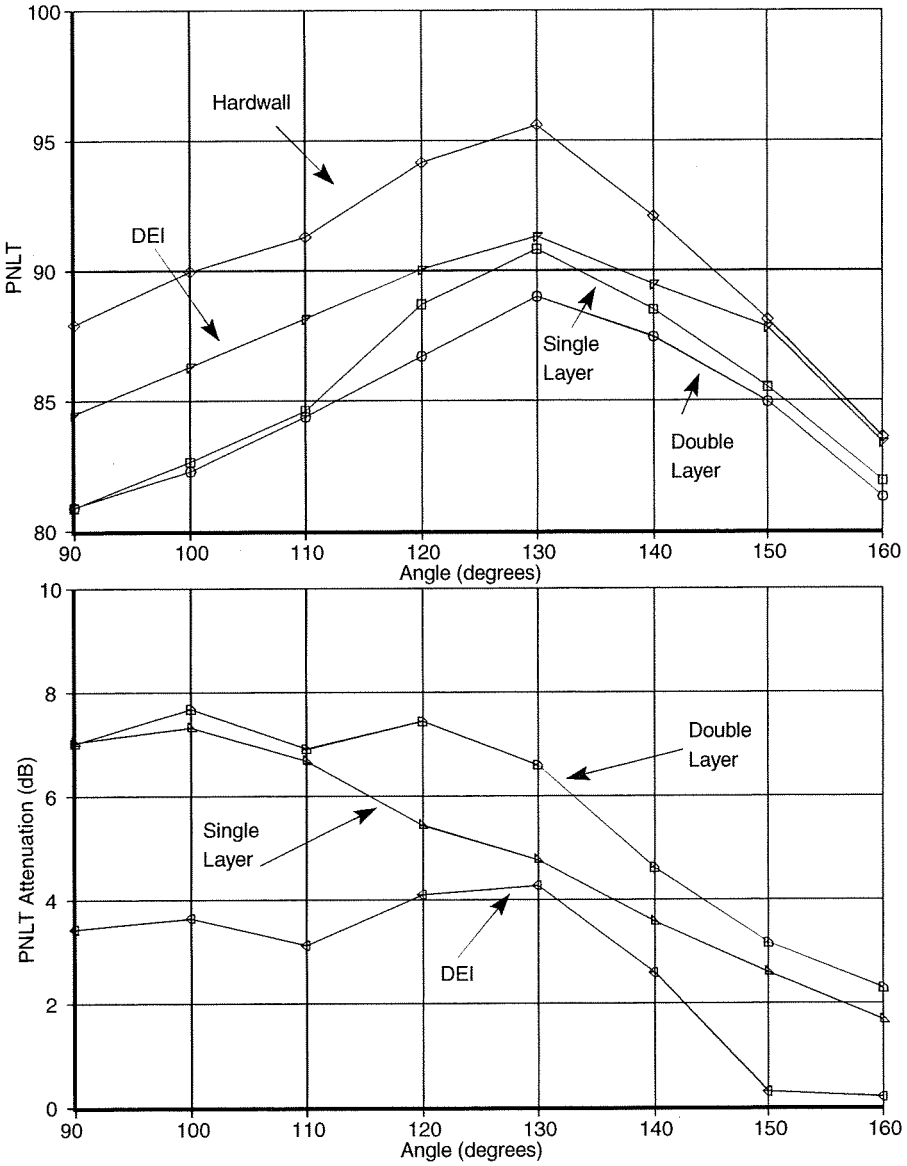

Figure 23: PNLT Calculations at Cutback Condition

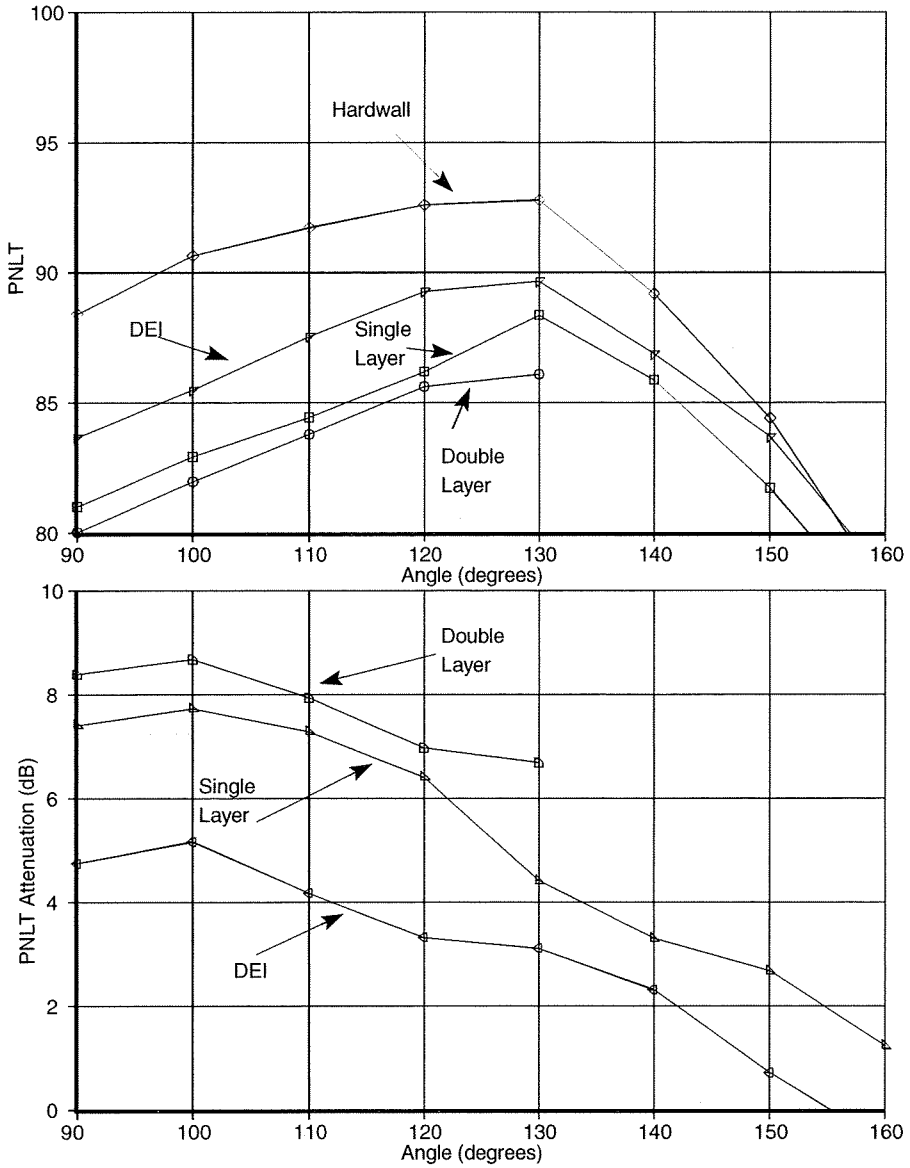

Figure 24: PNLT Calculations at Sideline Condition

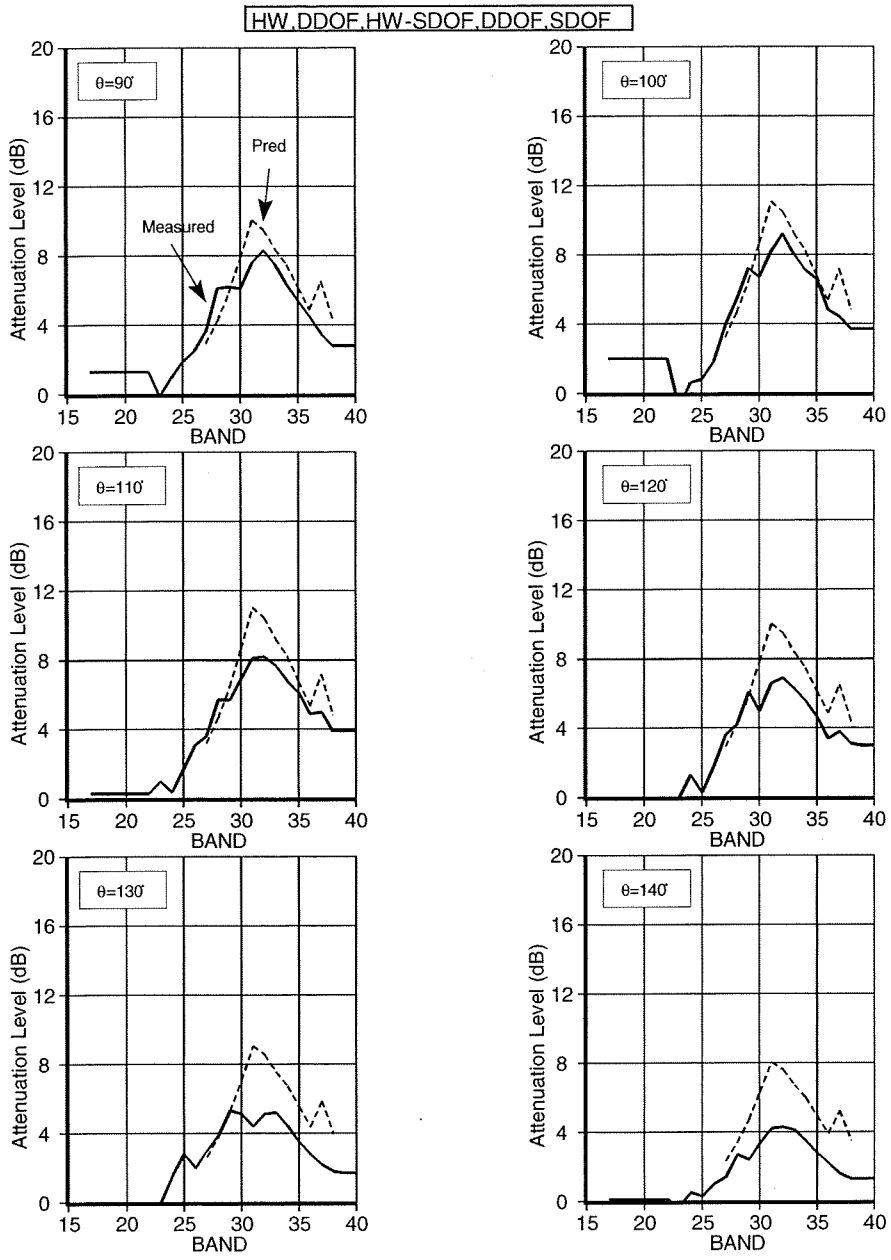

Figure 25: Single Layer Liner in Aft Fan Duct at Approach

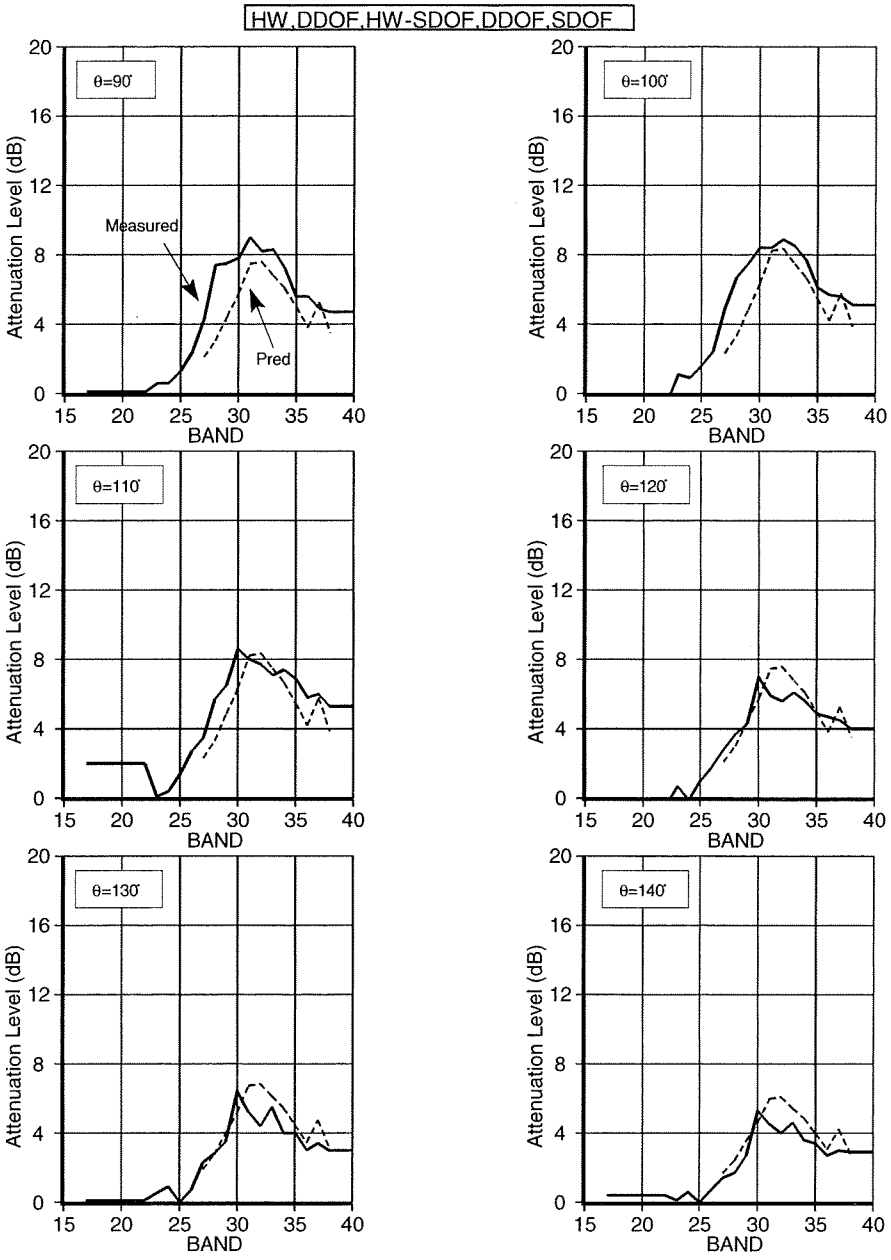

Figure 26: Single Layer Liner in Aft Fan Duct at Cutback

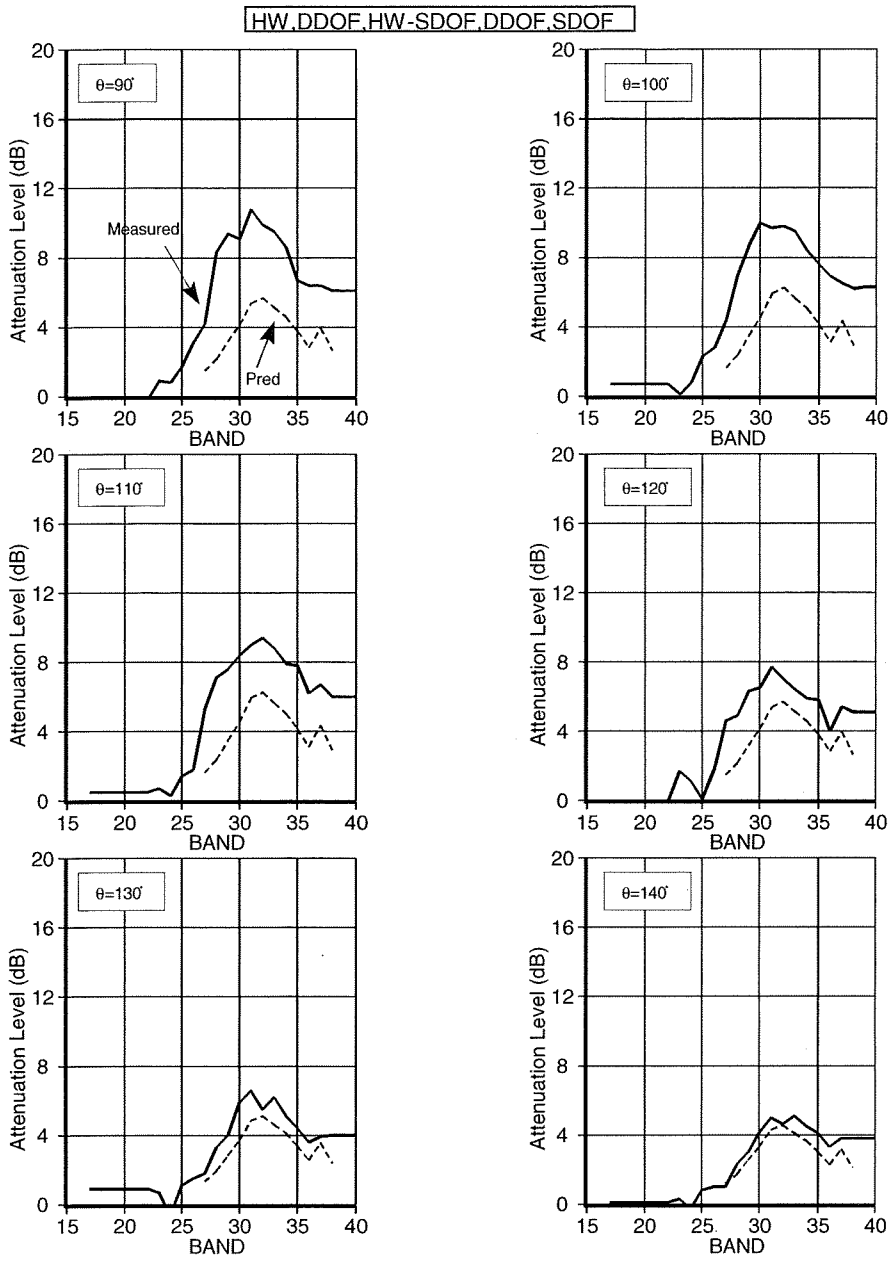

Figure 27: Single Layer Liner in Aft Fan Duct at Sideline

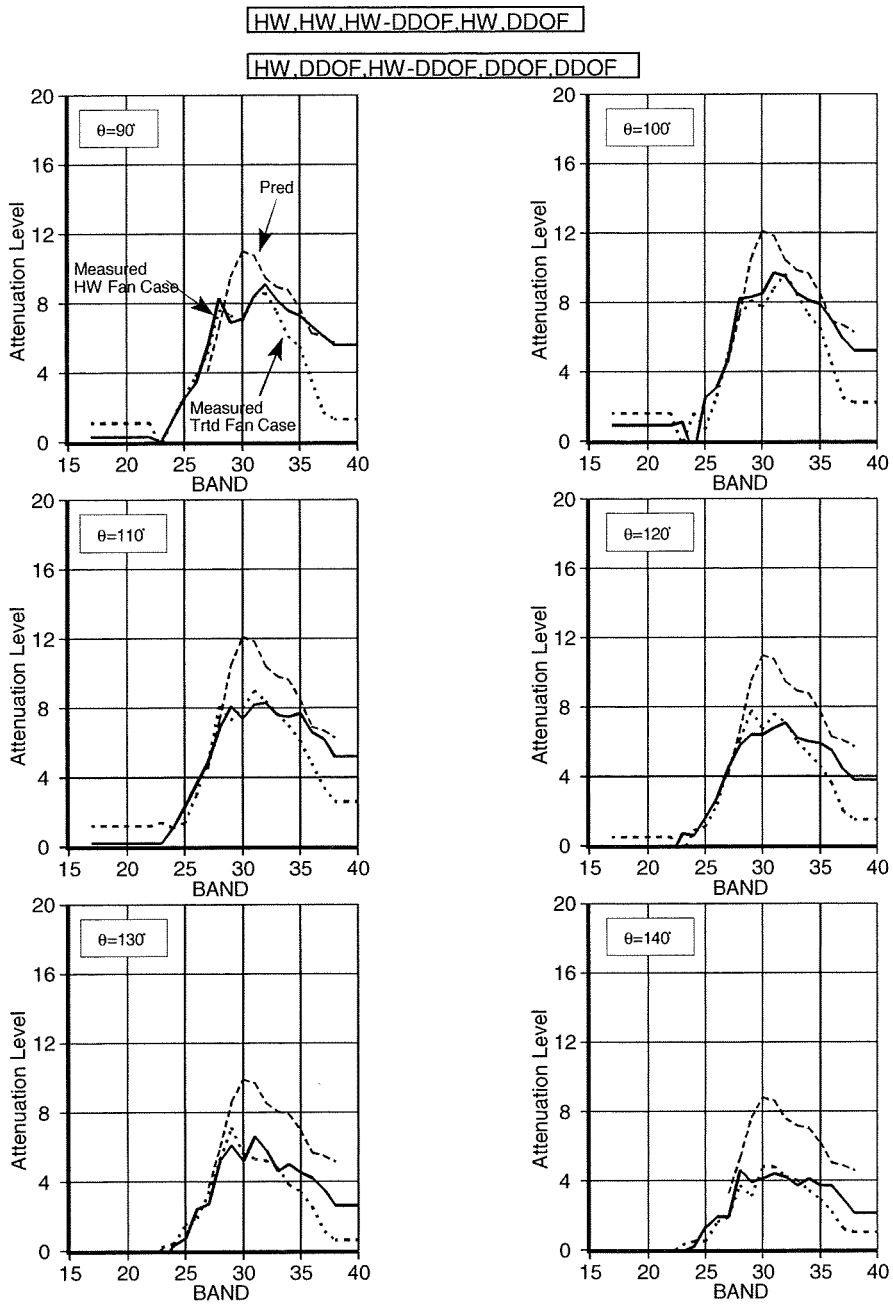

Figure 28: Double Layer Liner in Aft Fan Duct at Approach

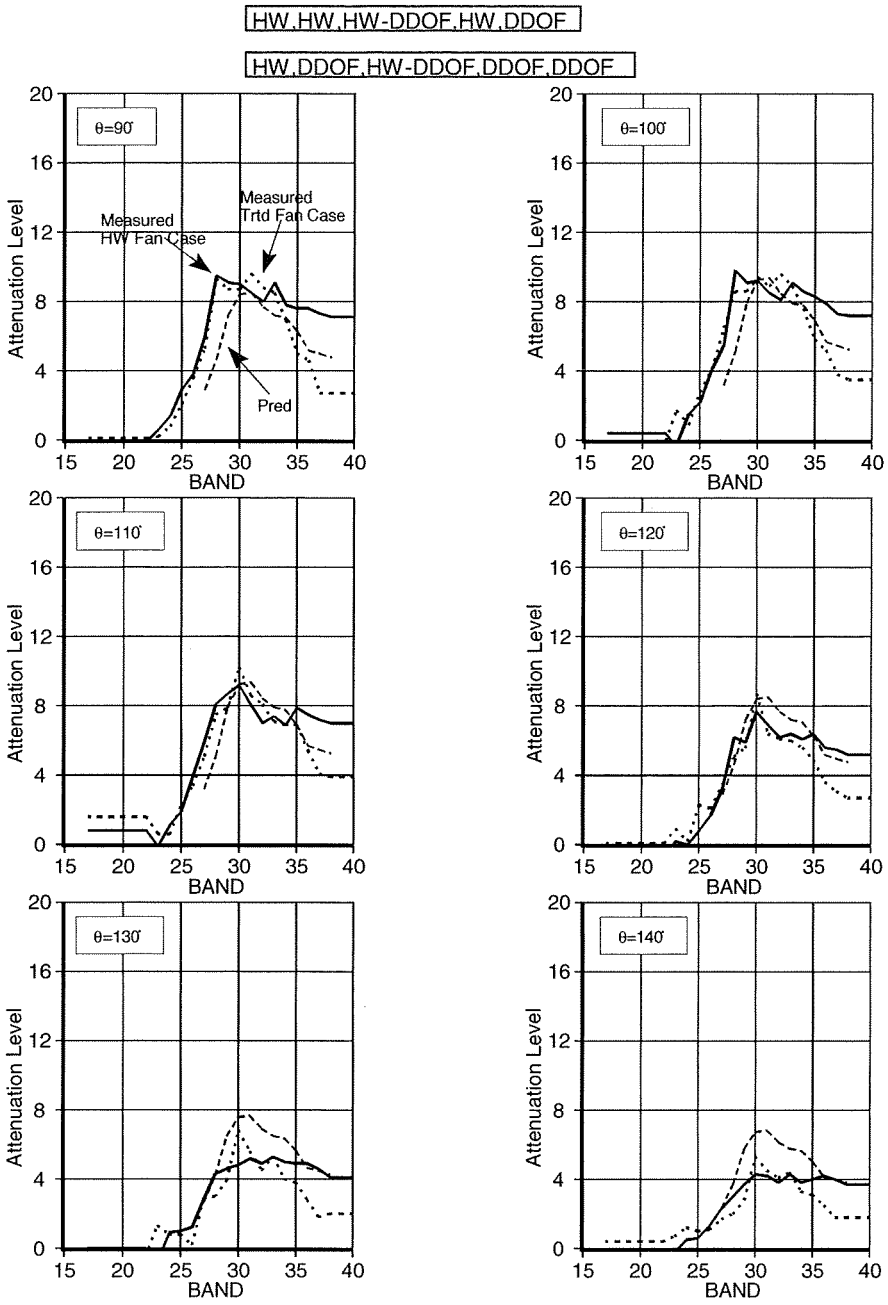

Figure 29: Double Layer Liner in Aft Fan Duct at Cutback

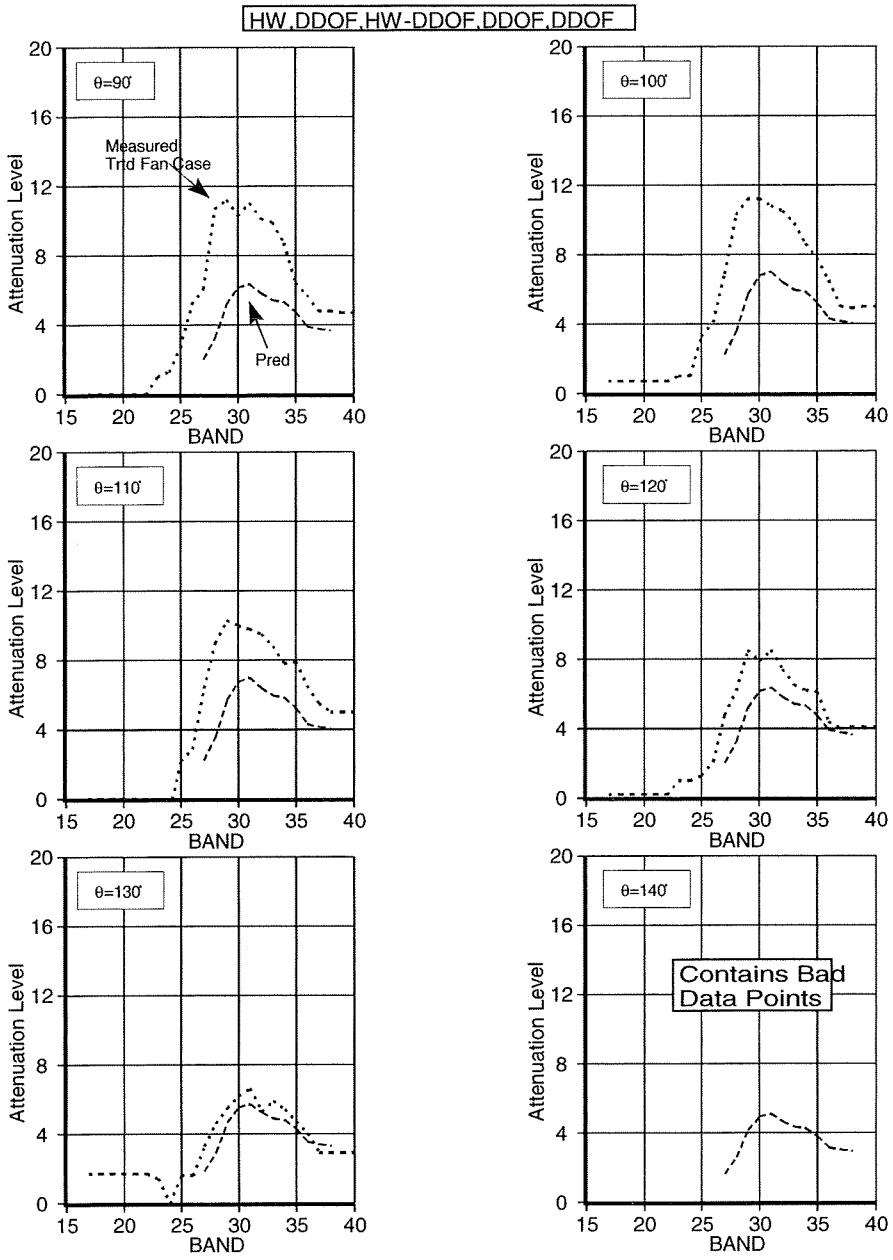

Figure 30: Double Layer Liner in Aft Fan Duct at Sideline

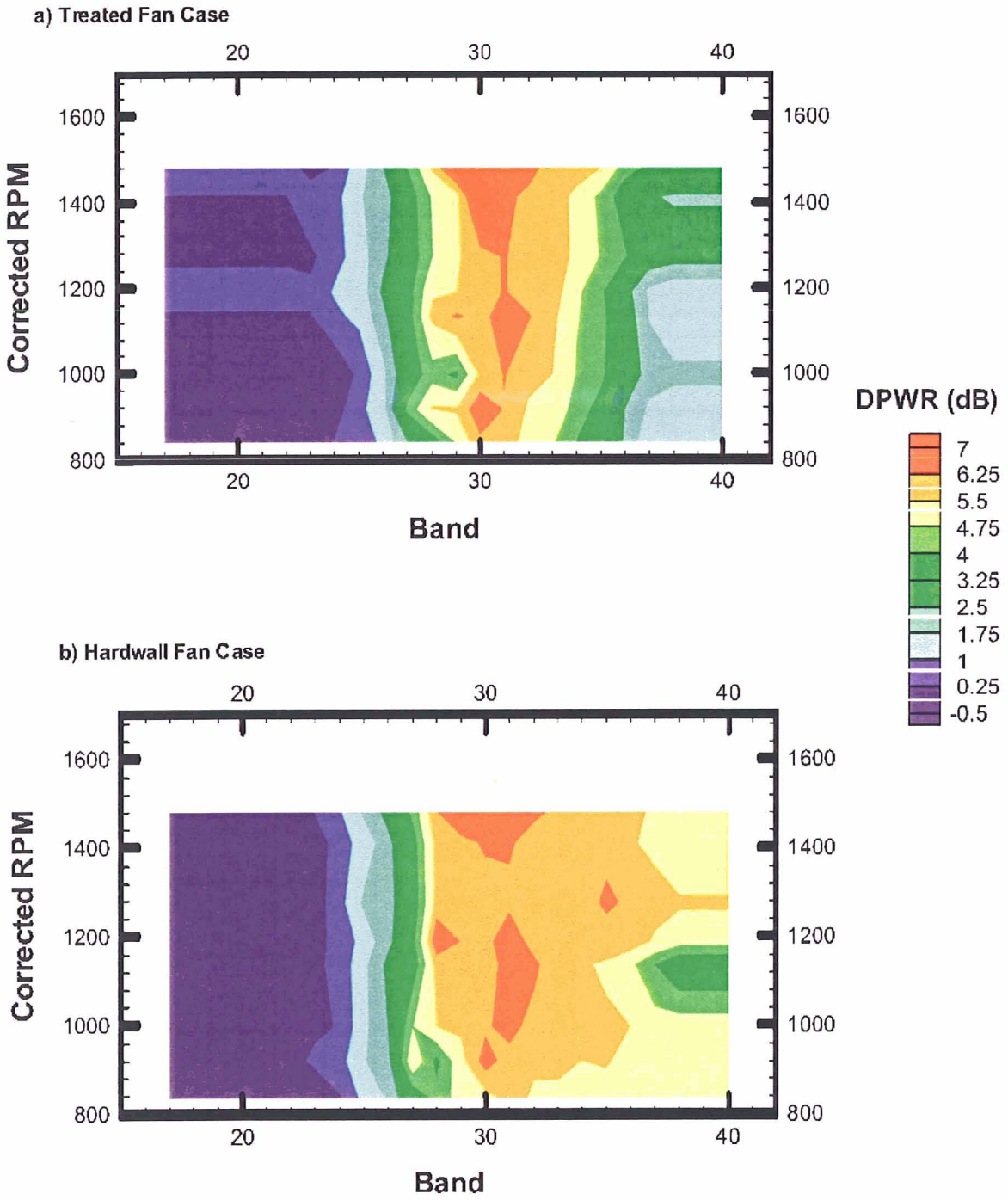

Figure 31: Aft Broadband Power Attenuations Double Layer Fan Duct Liner

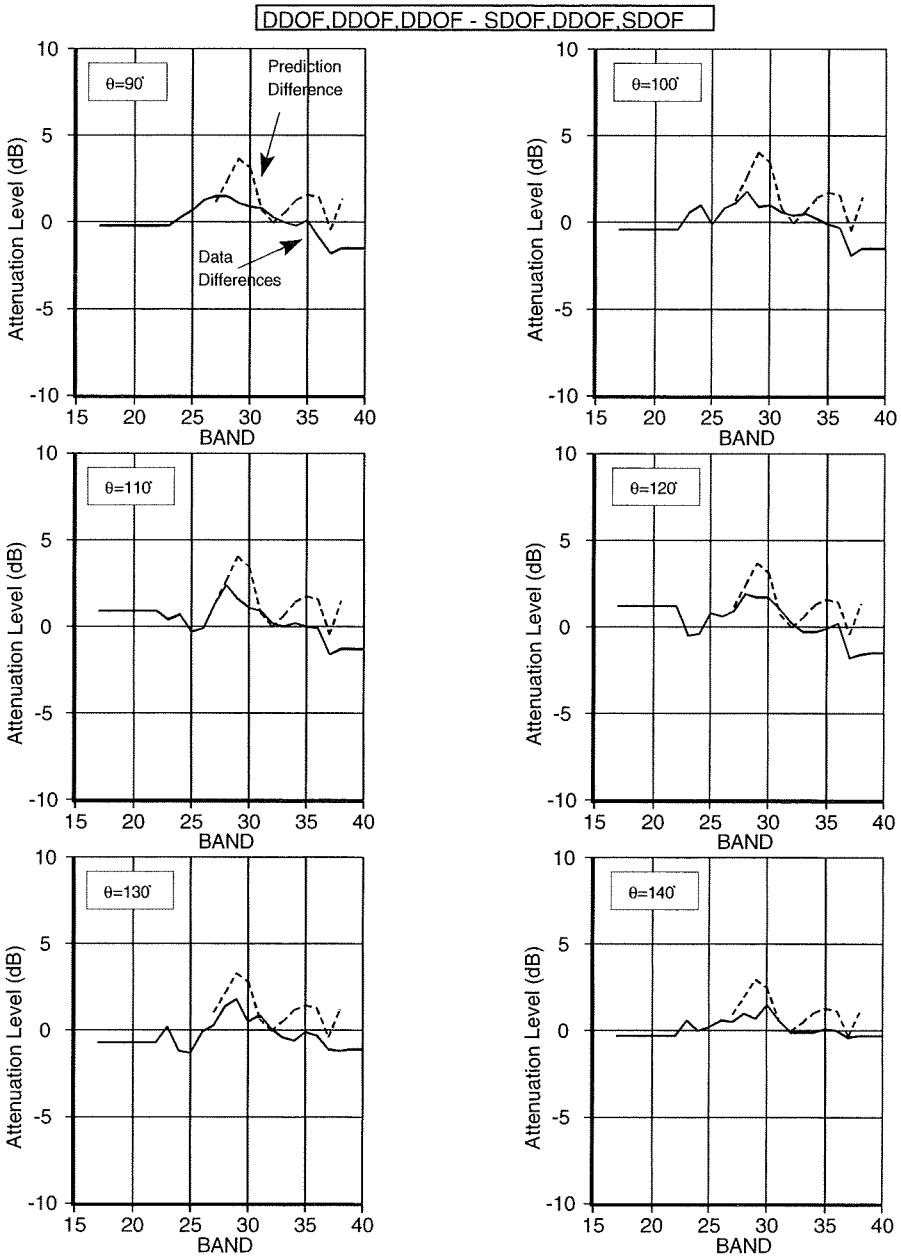

Figure 32: Single Layer and Double Layer Liner Comparison at Approach Condition

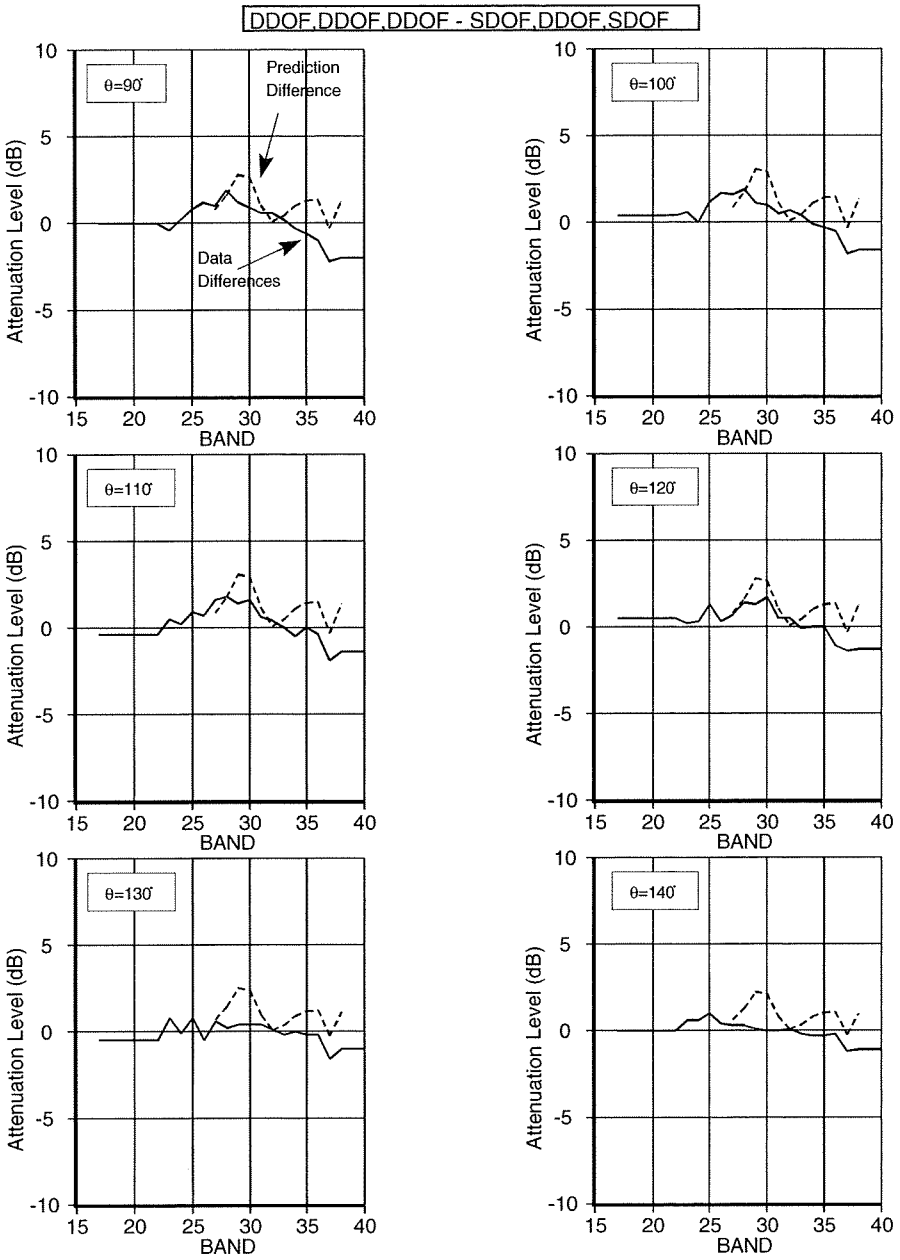

Figure 33: Single Layer and Double Layer Liner Comparison
at Cutback Condition

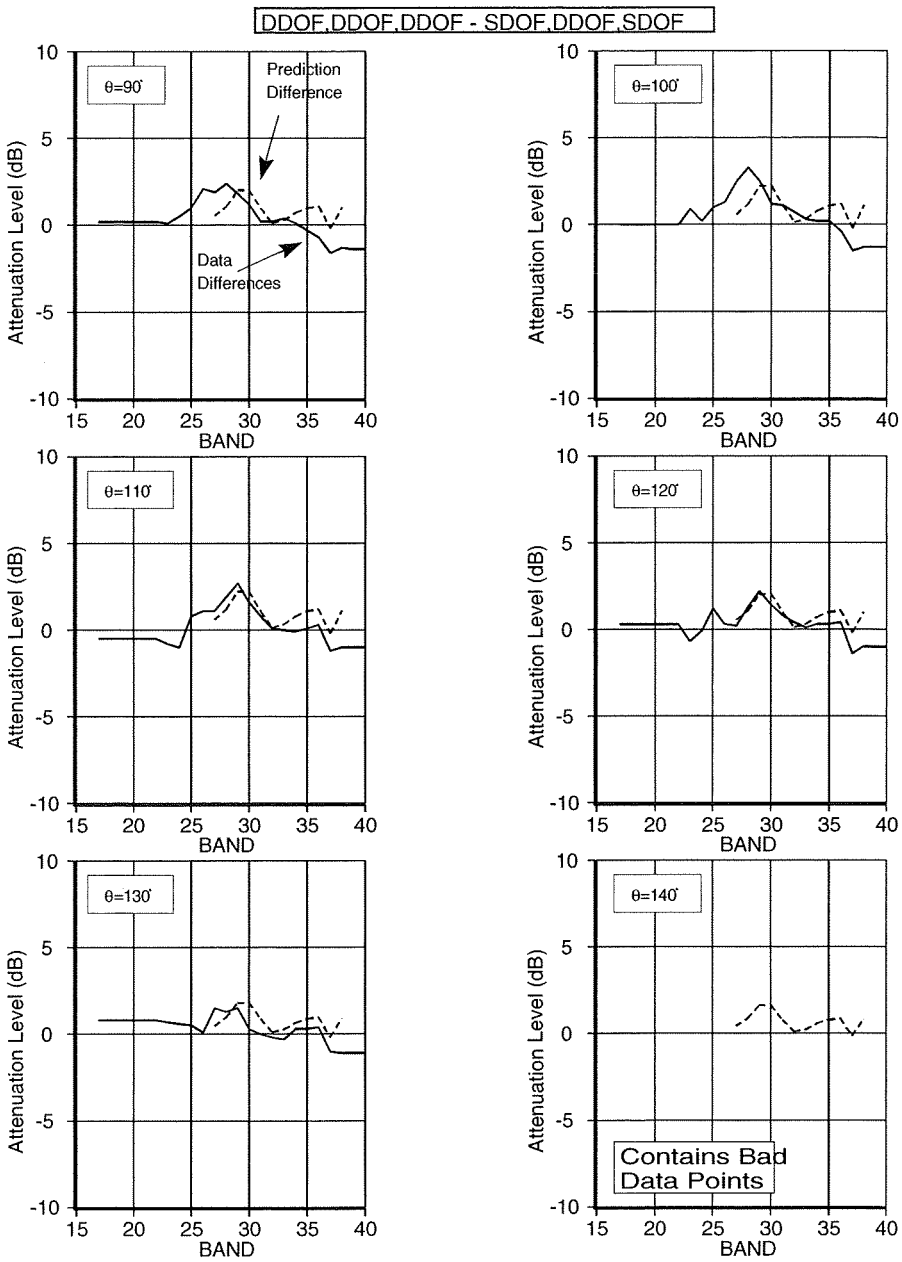

Figure 34: Single Layer and Double Layer Liner Comparison
at Sideline Condition

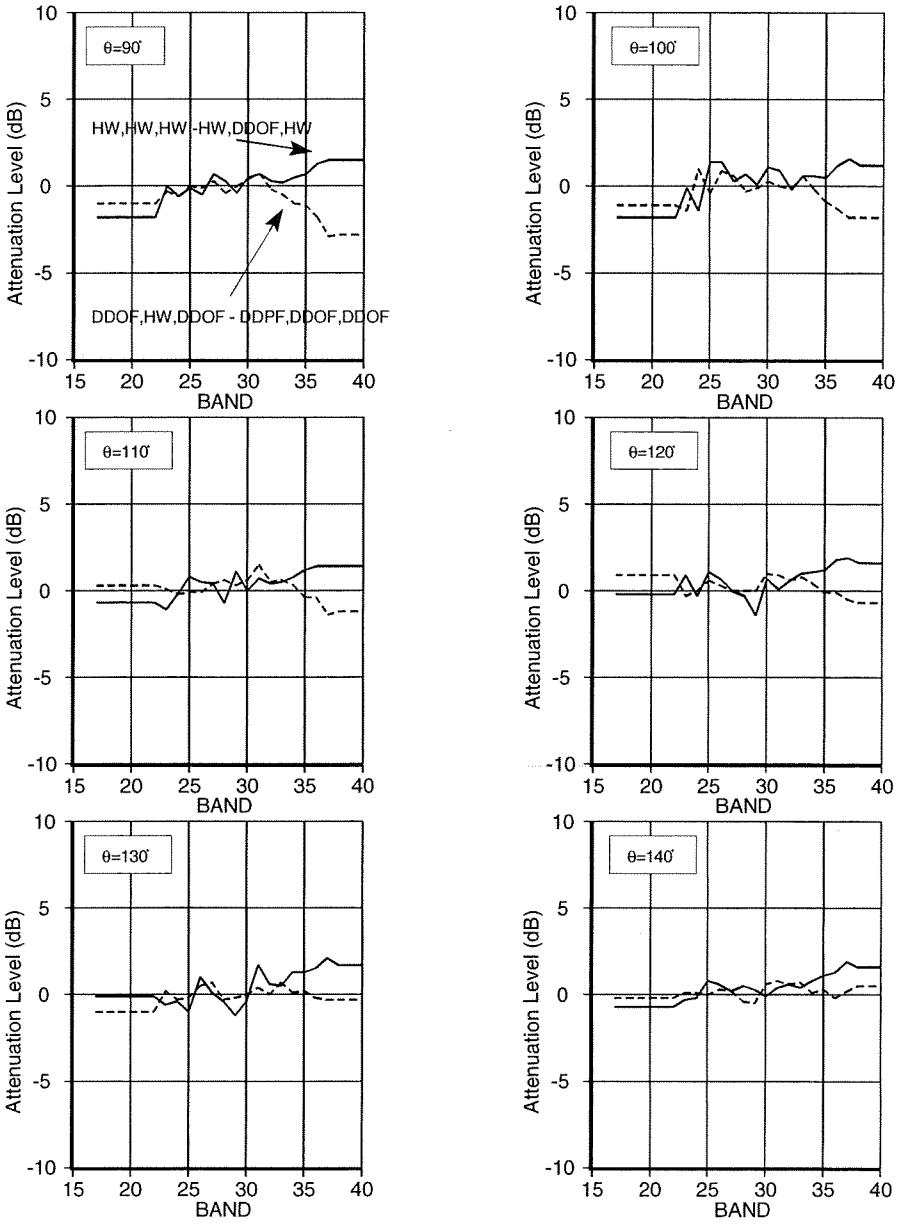

Figure 35: Fan Case Attenuations at Approach Condition

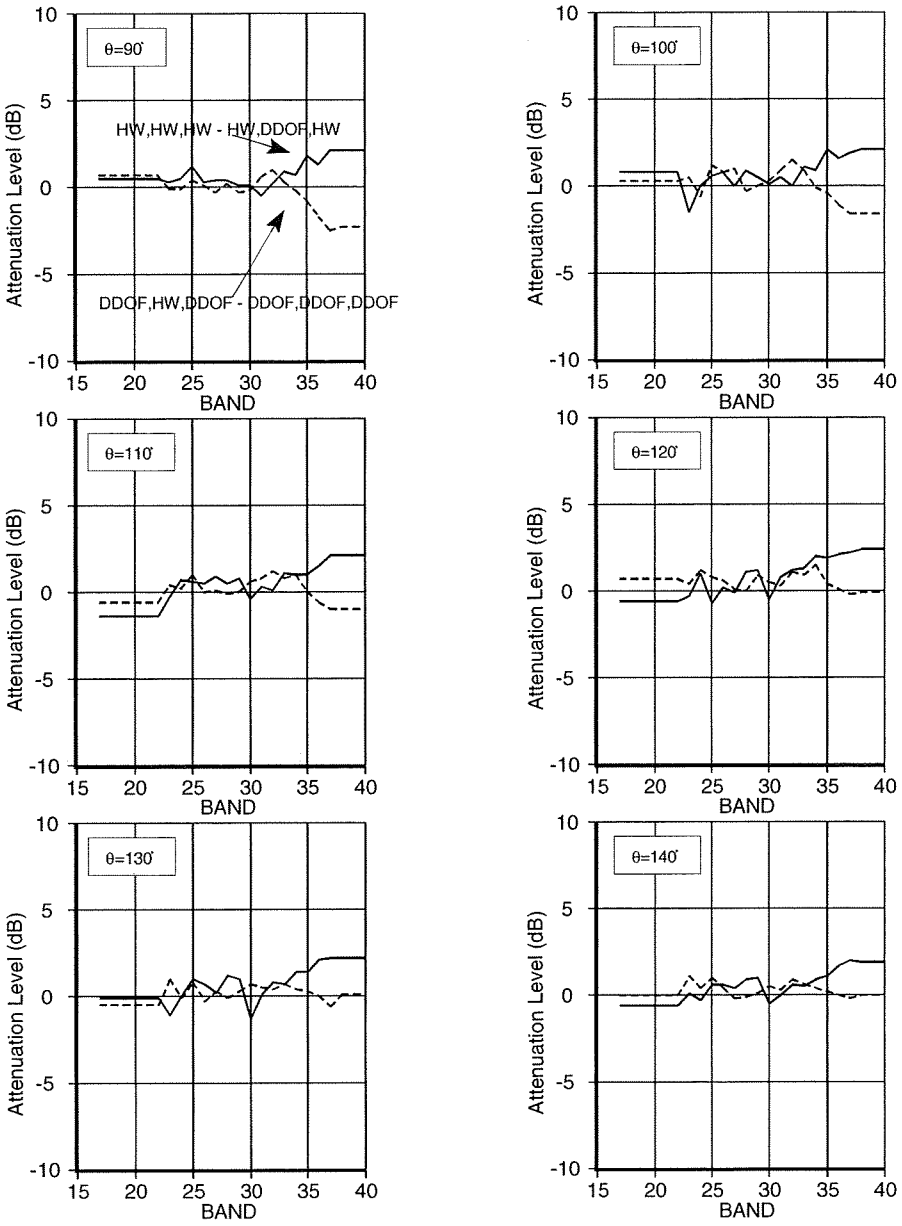

Figure 36: Fan Case Attenuations at Cutback Condition

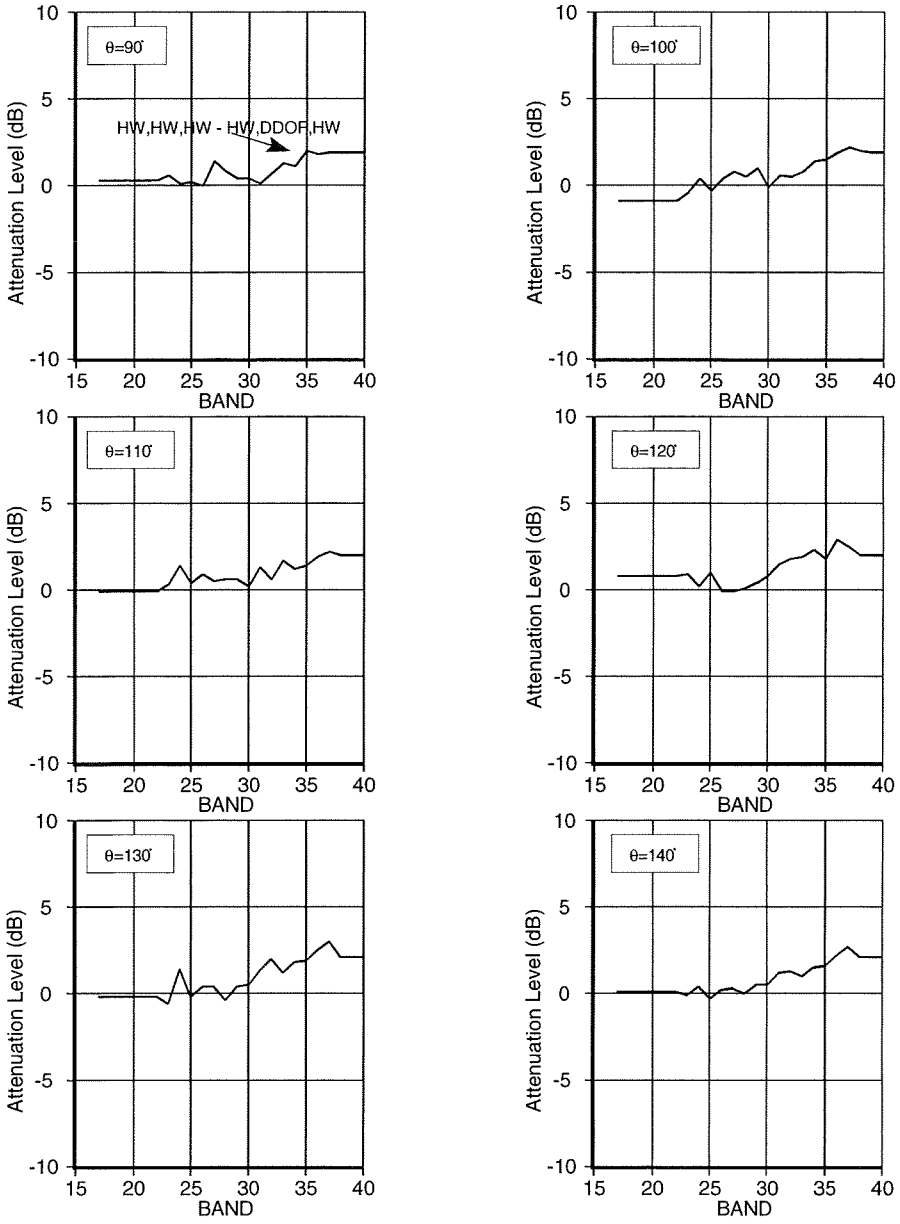

Figure 37: Fan Case Attenuations at Cutback Condition

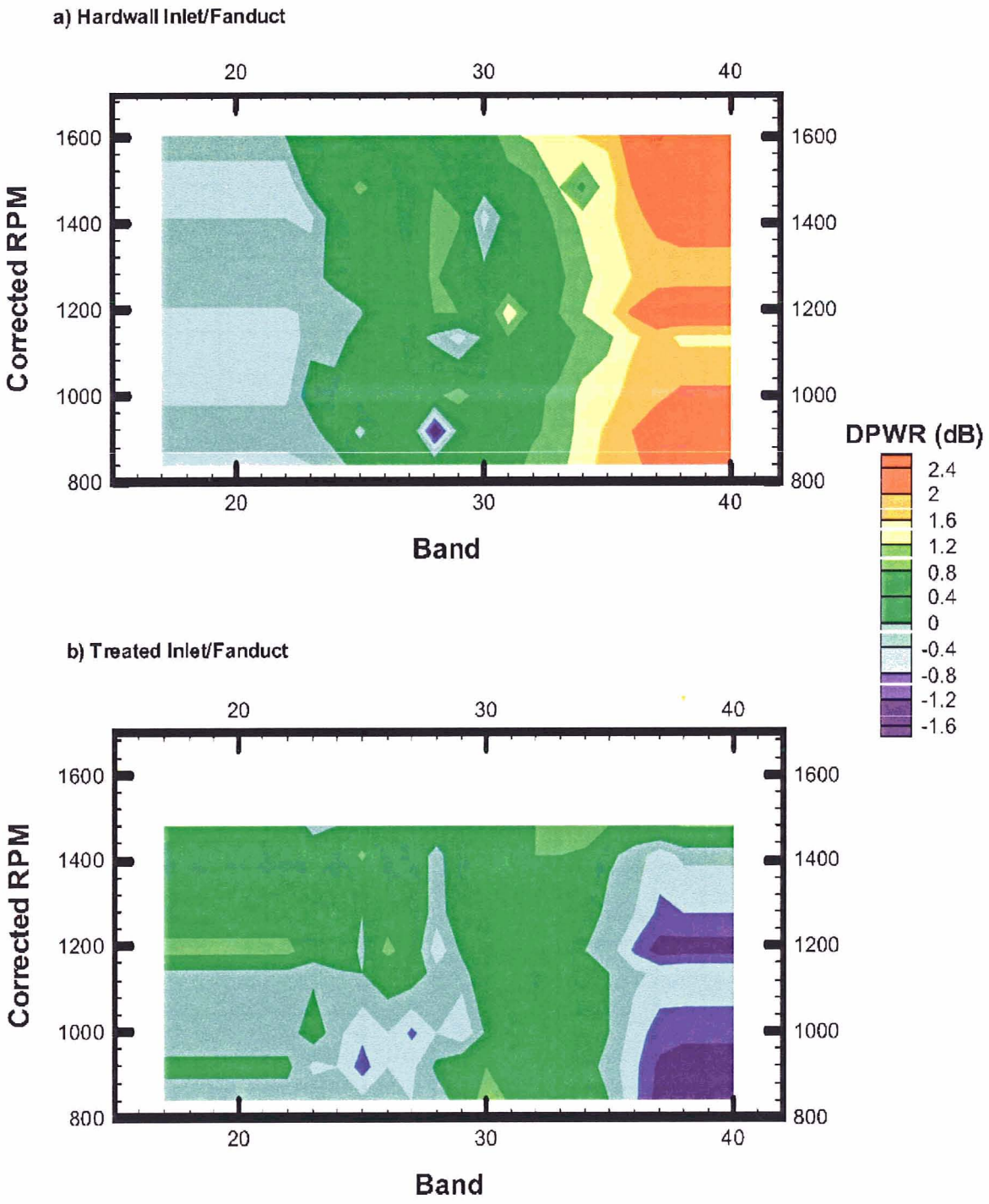

Figure 38: Aft Broadband Power Attenuations
Fan Case Liner

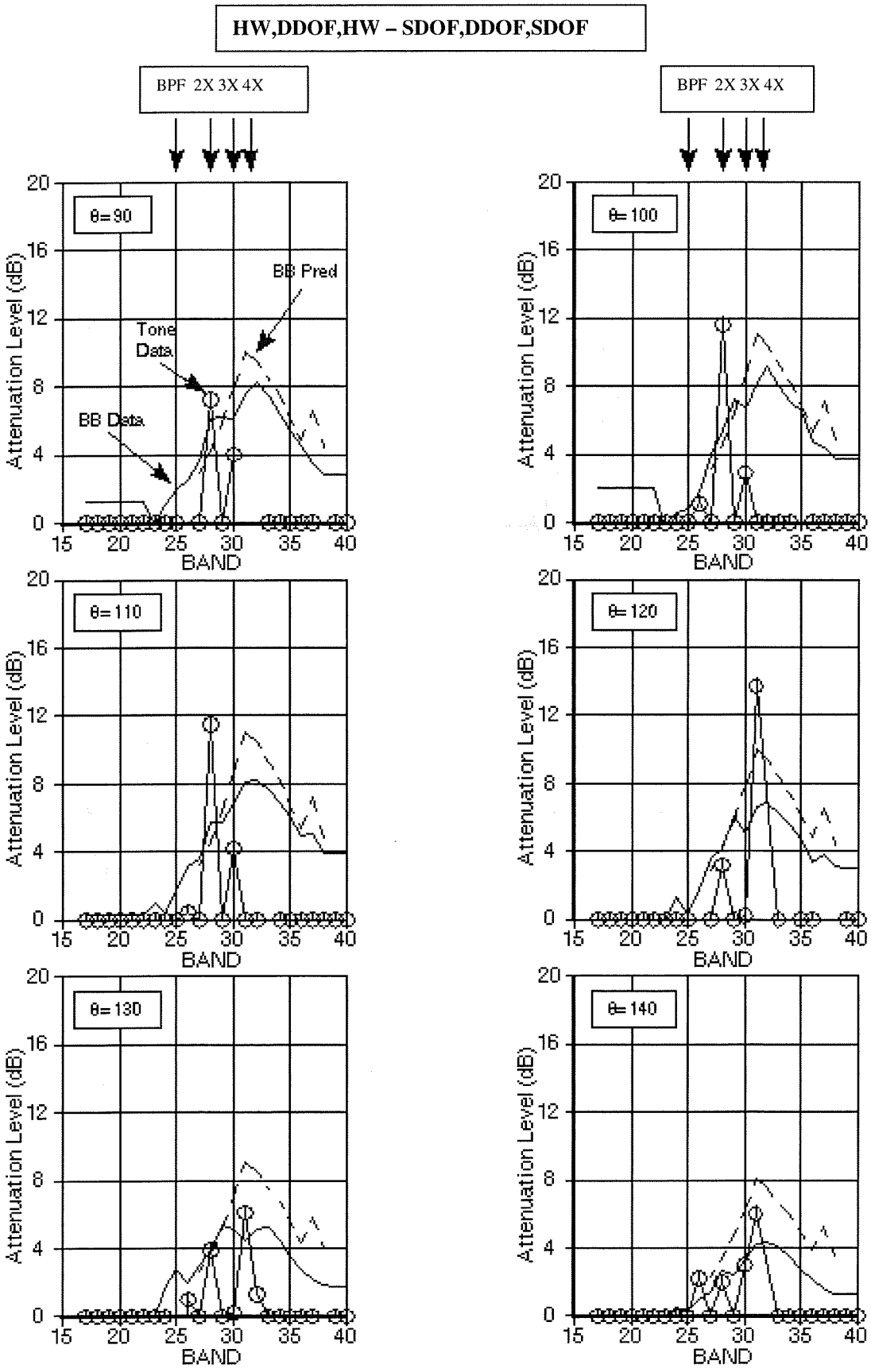

Figure 39: Aft Fan Tone and Broadband Attenuation for Single Layer Liner at Approach Condition

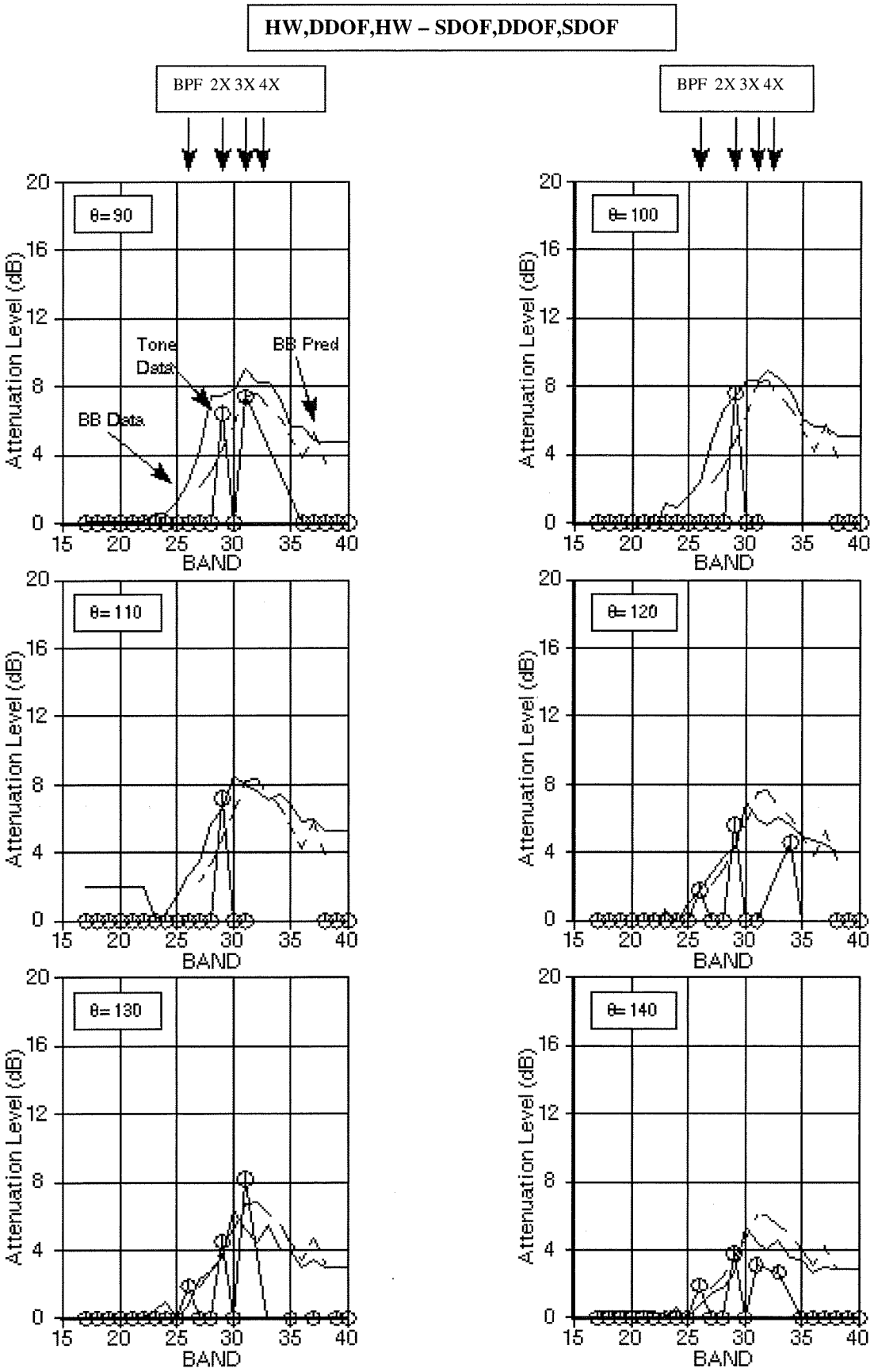

Figure 40: Aft Fan Tone and Broadband Attenuations for Single Layer Liner at Cutback Condition

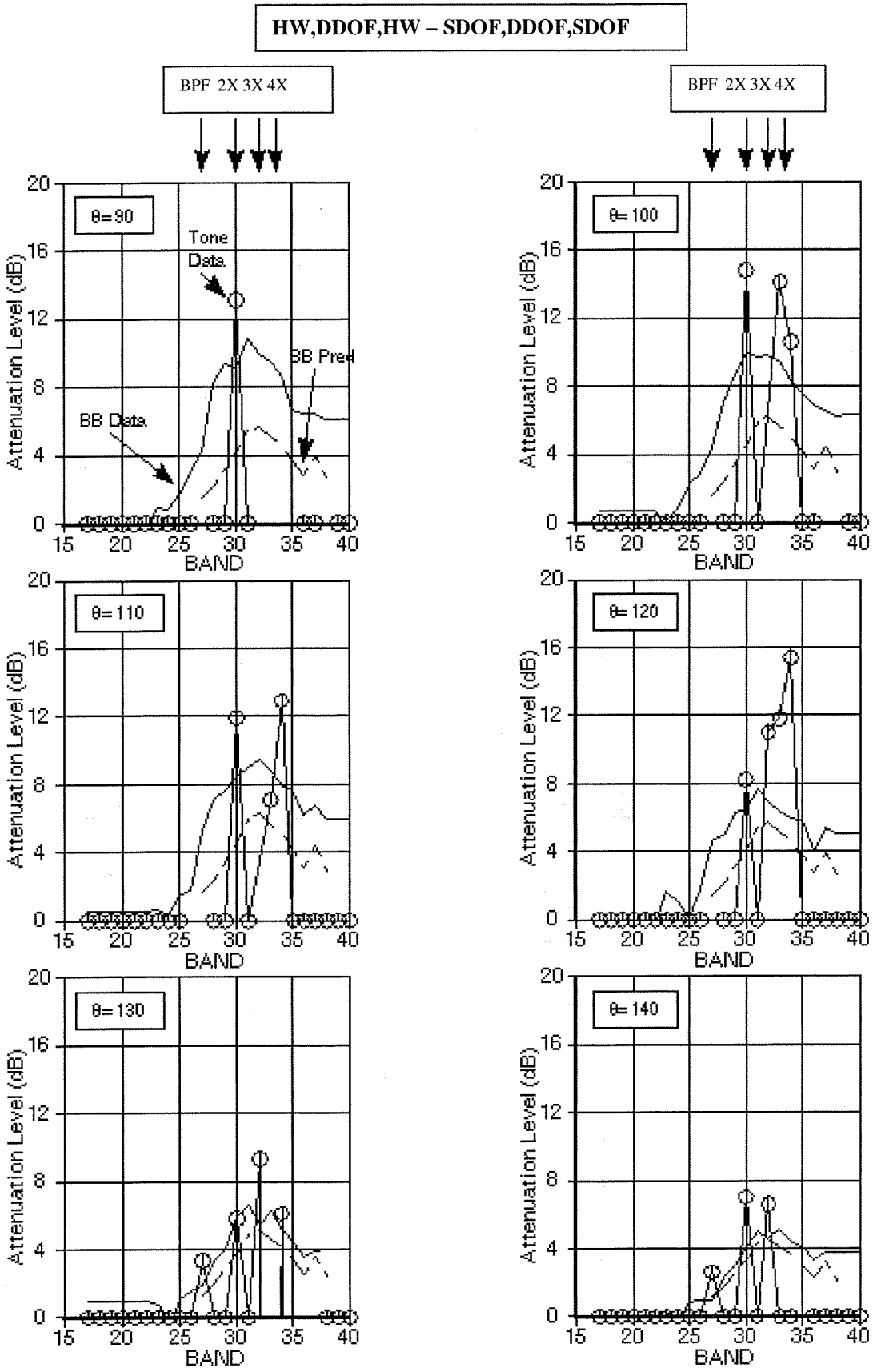

Figure 41: Aft Fan Tone and Broadband Attenuations for Single Layer Liner at Sideline Condition

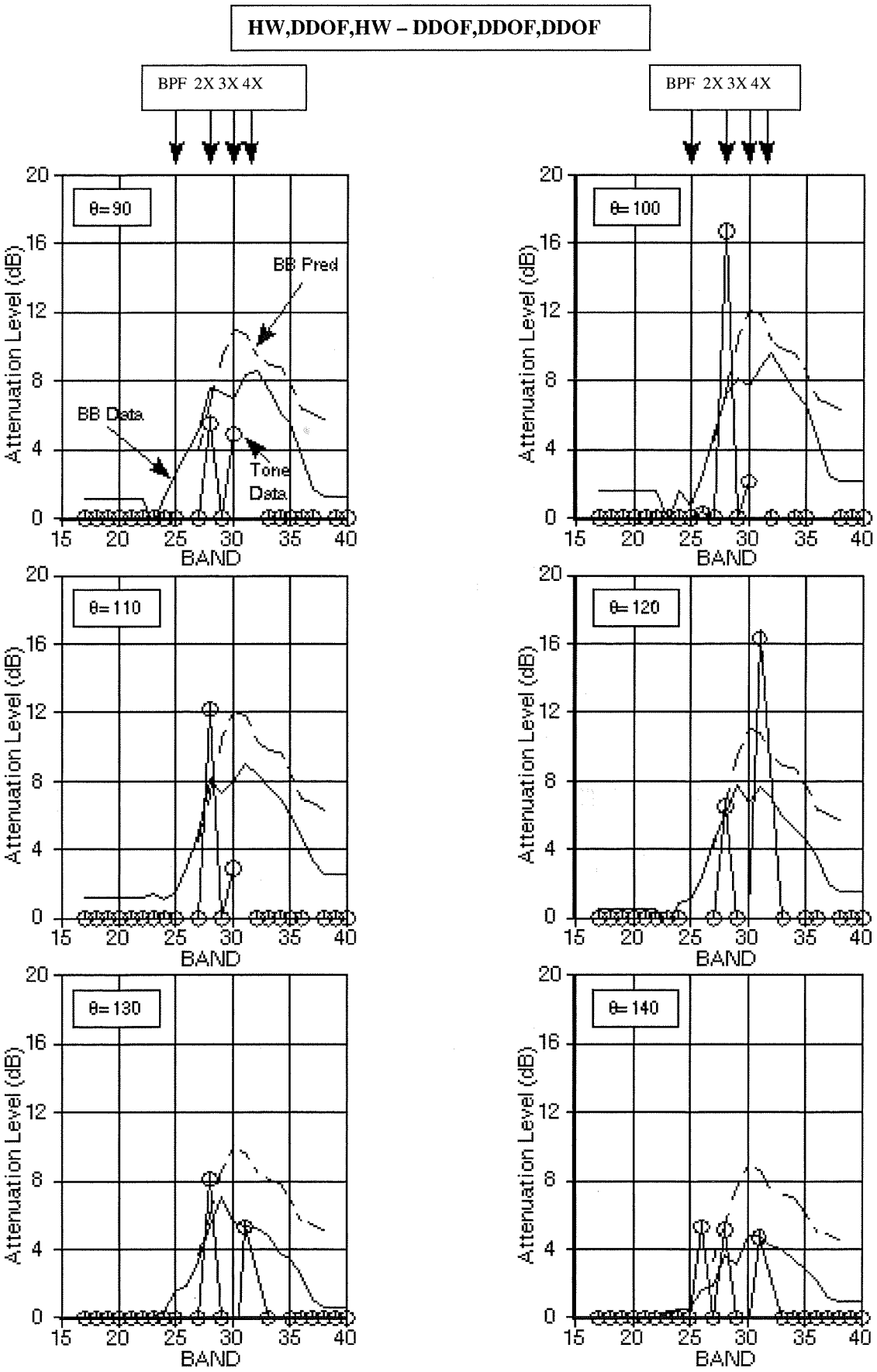

Figure 42: Aft Fan Tone and Broadband Attenuations for Double Layer Liner at Approach Condition

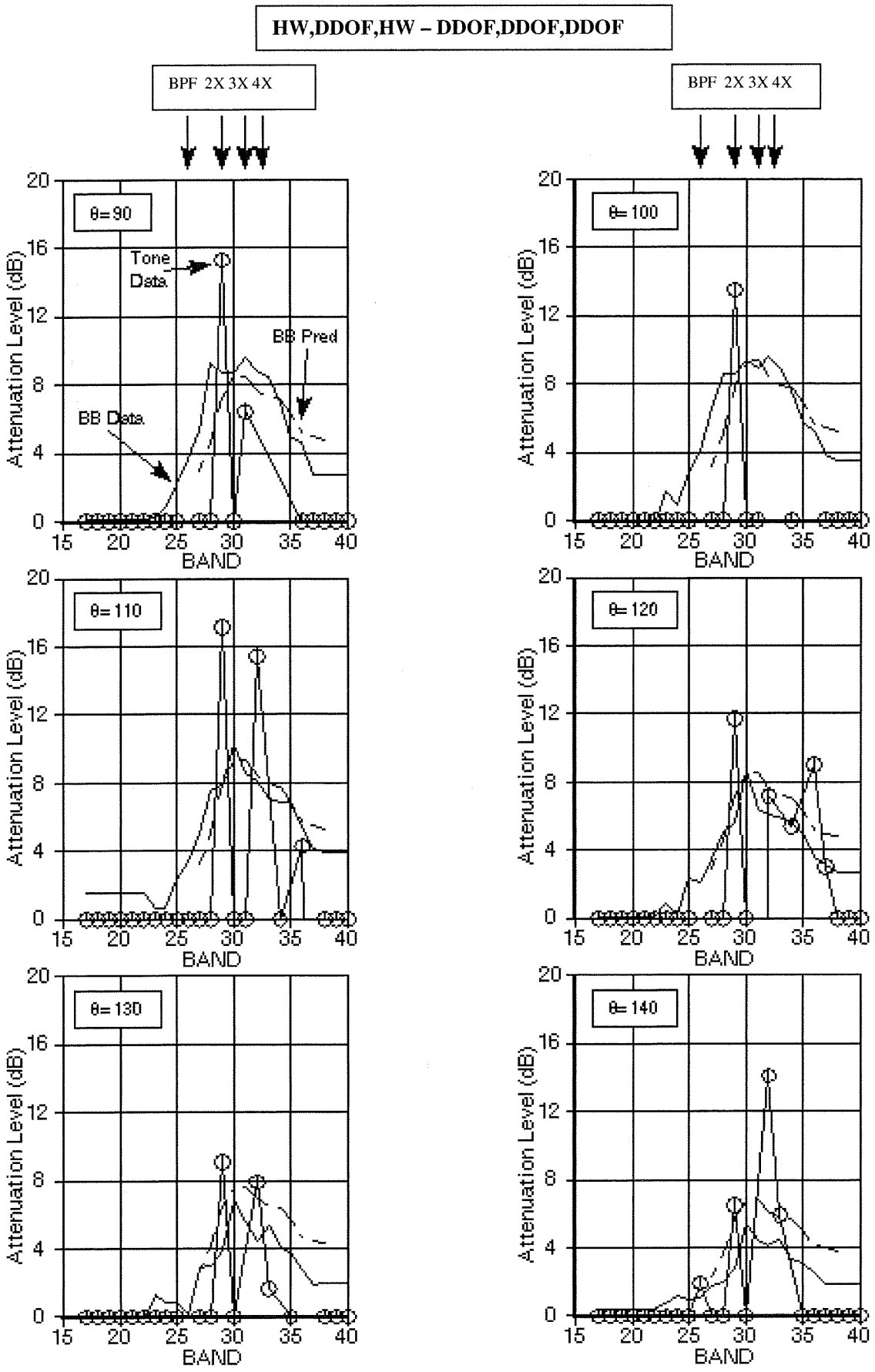

Figure 43: Aft Fan Tone and Broadband Attenuations for Double Layer Liner at Cutback Condition

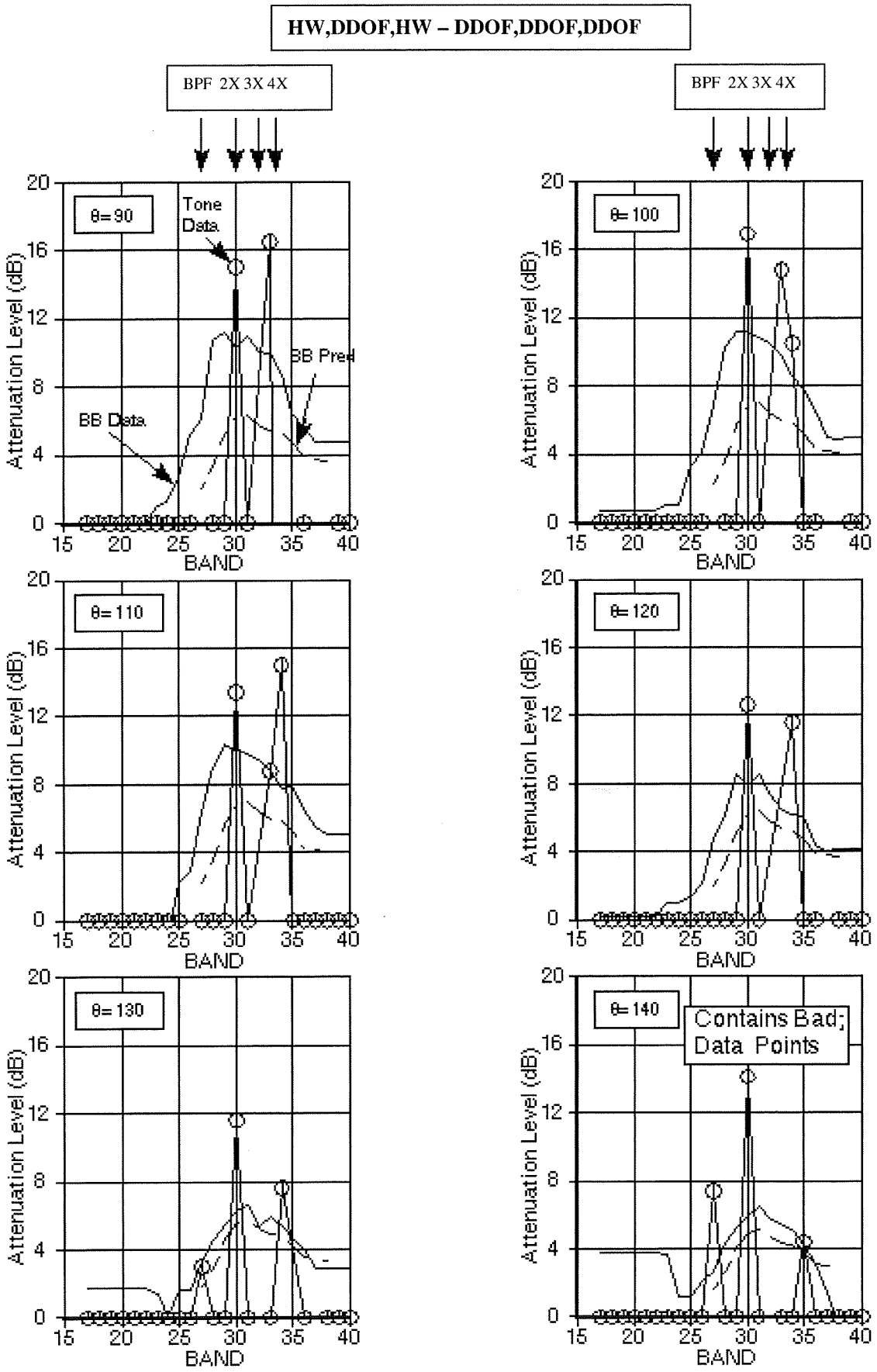

Figure 44: Aft Fan Tone and Broadband Attenuations for Double Layer Liners at Sideline Conditions

Appendix 2 - Grazing Flow Impedance Testing Of Bias Flow and High Temperature Liners

BACKGROUND

Grazing flow impedance testing was accomplished in late 1996 to investigate effects of acoustic lining impedance control through heating the acoustic lining or bias air flow through the acoustic lining. This report presents results of the data analysis accomplished to extract lining impedance from the test data and compares the results to pre-test predictions.

TEST PANEL CONFIGURATIONS

Bias Flow Double Layer Configuration

The bias airflow lining panel consisted of a double layer Helmholtz resonator configuration, with a 190 cgs Rayl @ 105 cm/s porous mesh skin replacing the standard impervious backing sheet. The bias airflow was introduced via a plenum chamber attached on the back side of the lining.

A schematic of the lining geometry is shown in Figure 1.

The lining geometric parameters are :

Face sheet: 14.7 % Percent open area.

Septum : 6.0 % Percent open area

Core depths- Face sheet to septum: 3.14"

Septum to back sheet 0.76"

Heated Double Layer Configuration

The heated lining panel was a standard double layer configuration with the impervious backing sheet replaced with a thick aluminum sheet. This aluminum backing sheet had slots machined in one side to accept electric heating rods. Thermocouples were installed during panel fabrication. These were located at four levels in the double layer, at six locations laterally, nominally in the centers of honeycomb cells. The levels were 1) just beneath the face sheet; 2 & 3) just above and just below the buried septum; and 4) at the lining interior surface of the heated aluminum backing sheet.

A schematic of the lining geometry is shown in Figure 1.

The lining geometry parameters are:

Face sheet: 6.9 Percent open area

Septum : 4.2 % Percent open area

Core depths- Face sheet to septum: 1.31"

Septum to back sheet 2.63"

TEST CONDITIONS

The test conditions included :

Up to four grazing flow Mach numbers – 0., .25, .35, and .5

Two sound levels – maximum achievable (approximately 160 dB) and nominally 10 dB down from maximum (approximately 150 dB)

Bias air flow – nominal 120 cm/sec average flow through the liner (M=.004), both pressure (air exiting the face sheet into the test duct) and vacuum (air entering the lining from the test duct)

Temperature – maximum heating not to exceed the 350 degree F limit of the liner bonding adhesive. Thermocouples at the heated backing sheet monitored for this condition.

TEST GEOMETRY

The high frequency grazing flow duct was used for all testing. The duct flow cross section is 2" x 2". The installed liners comprise the top wall of the test section. The microphone axial traverse data are taken over the 16" length of the test liners.

IMPEDANCE EXTRACTION ANALYSIS

The basic test measurement is the transfer function between a fixed (reference) microphone and a traversing microphone. The microphones are located in the duct wall opposite the installed liner. The reference microphone is located at the approximate start of the liner (the upstream end). The traverse microphone begins at the same axial position, and a transfer function is acquired over the length of the liner, in 0.2" increments.

Within the extraction process, any interim impedance (some 'guess' at the start of the process) is used together with duct conditions to obtain wave equation modal eigenvalues and propagation constants. Modal amplitude coefficients are obtained via imposing acoustic pressure and velocity matching over duct cross sections at the beginning and end of the liner. Additional conditions involved relate to source and duct exit conditions. The

source is assumed to be a plane wave for frequencies below second mode cut-on. Above cut-on, the second mode is included, and the complex modal amplitude leads to two more independent variables in the overall process. At the duct exit, a rho-c termination is currently assumed, leading to the absence of any upstream direction propagation downstream of the lining. In general, seven upstream propagating modes and seven downstream propagating modes are utilized in the three sections of the analysis – upstream hardwall, lined section, and downstream hardwall. This allows for the higher modes created at the hard/lined interfaces due to scattering, and these modes are necessary to satisfy matching near these interfaces. The special cases of the input source (upstream hardwall with one or two downstream modes) and the downstream hardwall section (rho-c termination leads to no upstream direction modes here) were discussed above.

With the modal amplitude coefficient solutions, a set of analytical transfer functions can be generated at the same locations and frequencies as the test data. Minimization of the residual (least squares) is then the control for the iteration process. The resultant final impedance, and the second incident mode amplitude coefficients for frequencies above cut-on, are the solution set.

ANALYSIS RESULTS – IMPEDANCE EXTRACTION

Bias Flow Panel

The impedance extraction results for the bias flow panel for the condition of bias flow into the back of the panel with an average speed of 120 cm/sec (M=.004) and exiting the face sheet into the duct (pressure case) are shown in Figure 2 for the maximum SPL condition with grazing flow Mach numbers 0., 0.25, 0.35, and 0.5. Figure 3 is for the same bias flow speed and direction for the minimum SPL condition with grazing flow Mach numbers 0., 0.2, and 0.5. Maximum SPL conditions were approximately 160 dB overall, with a spectrum comprised of a 1kHz. tone and resultant harmonics, superimposed on the flow noise. Minimum SPL conditions were a reduction in the tone level of approximately 10 dB relative to maximum conditions (OASPL of approximately 150 dB).

For the condition of bias flow from the duct into the face sheet with an average speed of 120 cm/sec (M=.004) and evacuated through the back sheet (vacuum case), the results for the maximum SPL are shown in Figure 4, for duct grazing flow Mach numbers 0., 0.24, 0.35, and 0.5. Results for the minimum SPL are given in Figure 5, for duct grazing flow Mach numbers 0., 0.2, and 0.5.

The bias flow panel was also tested under zero bias flow conditions. The maximum SPL data are shown in Figure 6 for duct Mach numbers 0., 0.24, and 0.5. Minimum SPL conditions are given in Figure 7 for duct Mach numbers 0 and 0.5.

Heated Panel

The heated panel results are shown in Figure 8. These results are for the panel heated to approximately 350 degree F, maximum SPL conditions, for grazing flow Mach numbers 0., 0.25, 0.35, and 0.5. The reduced SPL condition was only tested at Mach 0, and is shown in Figure 9. The maximum SPL condition from Figure 8 is included here to show the significant impact of sound level not only on the resistance magnitude, as expected, but also on the frequency characteristics of both resistance and reactance.

ANALYSIS RESULTS – PREDICTIONS AND DISCUSSION

Bias Flow Liner

The bias flow liner impedance measurements shown in figures 2-7 do not appear to show significant differences. The resistance values near 2000 Hz show the most changes but this is an anti-resonance region where the impedance measurements are most susceptible to error. Also there seems to be a trend for the reactance curves for the M=.5 grazing flow conditions to show lower values in the mid frequency range. Otherwise, in spite of changes in SPL by approximately 10 dB, grazing flow Mach numbers from 0-.5 and bias flow mean Mach numbers of 0 and .004 the impedance curves are remarkably similar. Fig.10 shows predictions of the bias flow liner impedance spectra for the test conditions with no bias flow using the Dean/Hersh prediction procedure of reference 1. While these predictions are similar to those measured they appear to show larger SPL and grazing flow dependence than the measurements. Fig. 11 shows the same predictions using the Boeing orifice impedance code. The Boeing code predictions show better agreement with the no-bias flow data with smaller SPL and grazing flow dependence.

Figs. 12-13 show predictions of the bias flow effects on the liner impedance spectra for the test conditions using the Dean/Hersh prediction procedure. The predictions show stronger bias flow effects than measured for the 150 dB SPL condition. Smaller effects are predicted at 160 dB as was measured. It is unfortunate that data was not measured for smaller SPL's. In fact, the concept for application of bias flow for nacelle linings being considered, is to use bias flow at the landing condition where the SPL's are of the order of 140 dB. Fig. 14 shows a prediction of the effect of bias flow on the test liner at 140 dB and the test bias flow Mach number of .004 using the Dean/Hersh procedure. A fairly large bias flow effect is predicted for no grazing flow with a lesser effect predicted with a grazing flow Mach number of .5.

Boeing now believes that using the Dean/Hersh impedance model to design a nacelle candidate bias flow liner for testing may have been premature. More fundamental testing aimed at accurate impedance modeling of the bias flow impact and its dependence on SPL and grazing flow for an individual resistance element should be done before a more complex double layer liner is designed. The Dean/Hersh impedance model may not be sufficiently accurate for designing a bias flow double layer liner. Also, as reported in

reference 2, the basis for the Boeing bias flow test liner design used a version of the Dean/Hersh impedance model with a code error. The above comparisons corrected this error and show similarities to the measured data but indicate that the model is still in need of improvement.

Elevated Temperature Liner

Unfortunately we were not able to determine the impedance at ambient temperature with the flow duct test data. A measurement with the normal incidence impedance tube at ambient temperature however was made with the SPL approximately 150dB. Also there was data measured at 150 dB in the flow duct at high temperature and zero grazing flow (fig.9) . If this data is compared with the ambient temperature normal incidence impedance tube data in fig. 15 one may get an estimate of the effect of increasing the lining temperature. The high temperature resistance appears to have decreased relative to the ambient temperature data as was predicted prior to the test. This is believed to be due to the reduced air density at the lining with increased temperature. The reactance change seen in figs. 9 and 15 associated with the lining temperature change is not understood. The anti-resonance seen in the ambient temperature impedance tube data would be expected to move to higher frequency by the ratio of the square root of the temperature as appears to be the case but the sign change of the reactance is not predicted. Fig. 15 shows predictions of the effect of grazing flow and elevated temperature for the test liner at 150 dB. The predictions show the reduced resistance and reactance shift and also show a reduced effect of grazing flow at the higher temperature. Although the data is not totally clear, fig.8 does not appear to show a resistance change with grazing flow as predicted but this is data measured at 160 dB where we have seen a small dependence on grazing flow with the bias flow liner.

CONCLUSIONS

At high SPLs, 160 dB and 150 dB, the tested bias flow liner impedance did not show a strong dependence on changes in SPL, grazing flow up to M=.5, or bias flow up to average M=.004. The small SPL and grazing flow dependence is predicted by the Boeing impedance model. The Dean/Hersh impedance model predicts stronger dependence on SPL, grazing flow and bias flow than was measured. The value of the test data is significantly compromised due to the lack of lower SPL data. Background noise restricted the testing to high SPLs. Testing of more basic liners, single layers, is needed to develop better impedance modeling before a complex nacelle lining design is again attempted.

The high temperature liner test was not conclusive because of the lack of reference data at ambient temperature. Limited data was measured at ambient temperature with a normal incidence impedance tube which indicated that the liner resistance was reduced with increased temperature as predicted. The reactance change observed with this data, however, was not understood.

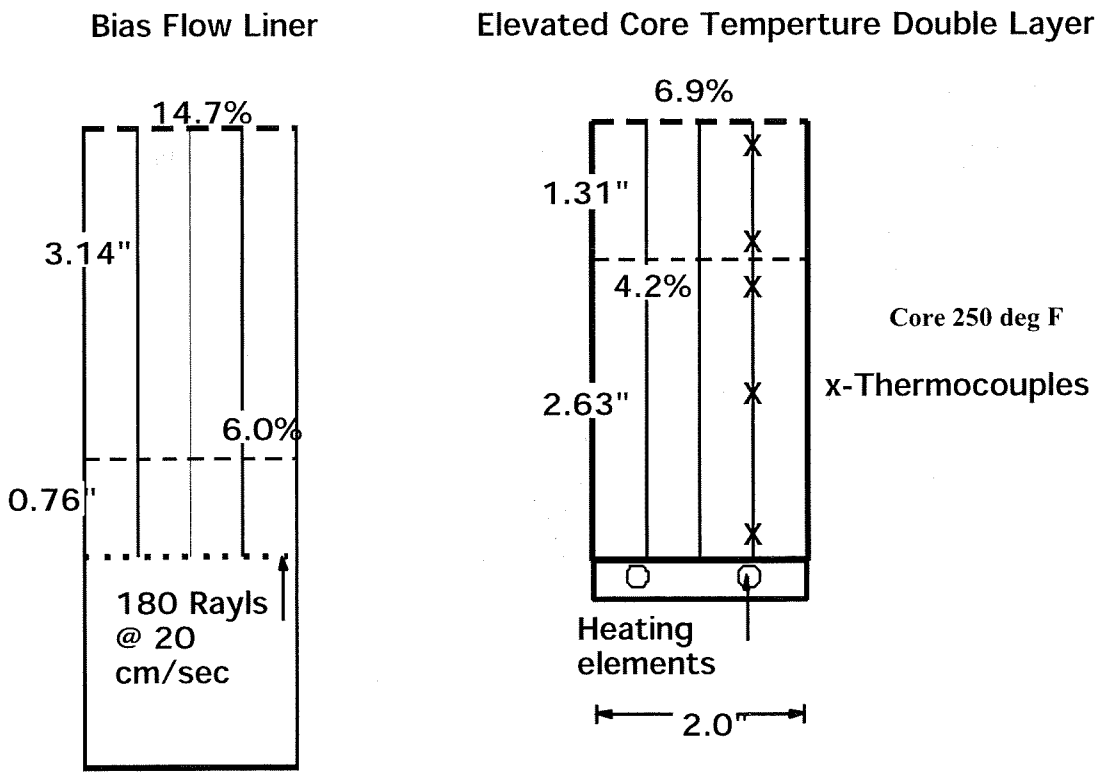

Figure 1: Adaptive Liner Test Designs

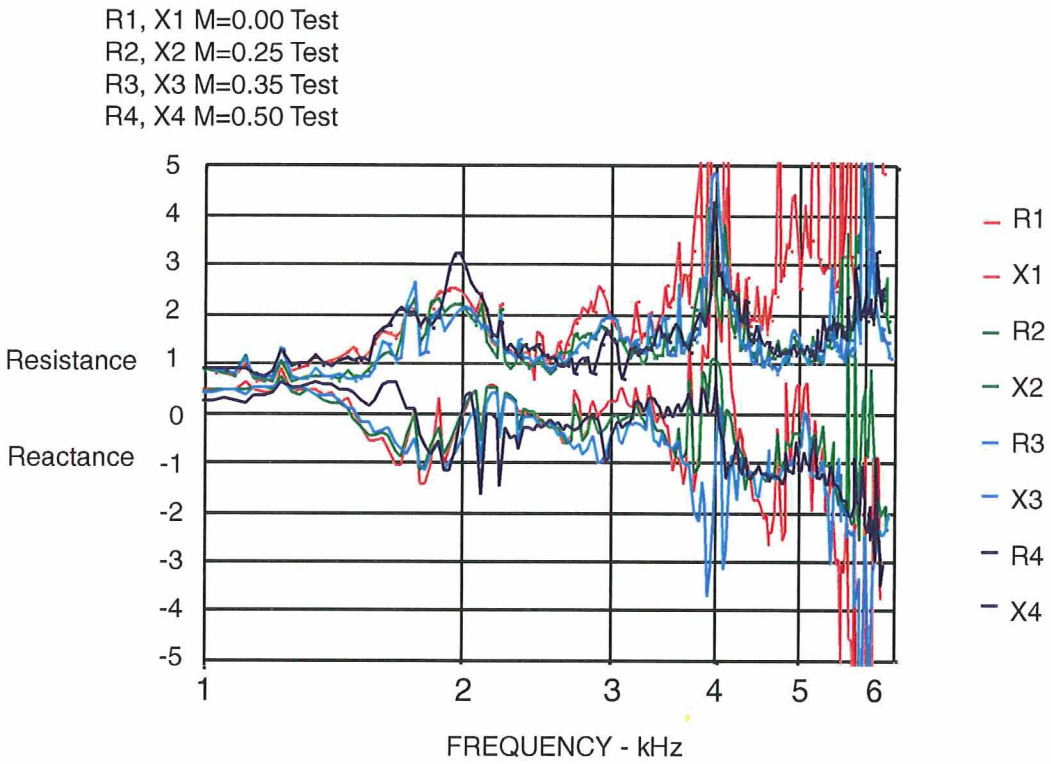

Figure 2: Bias Flow Panel, Pressure Condition, Max SPL

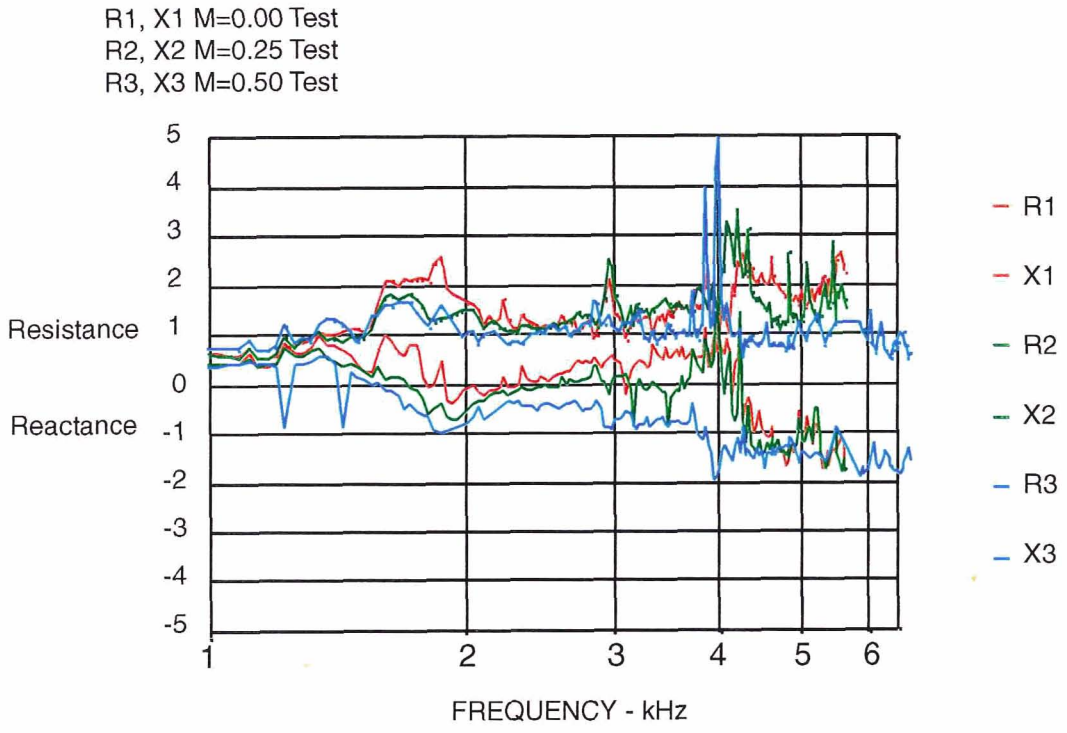

Figure 3: Bias Flow Panel, Pressure Condition, Min SPL

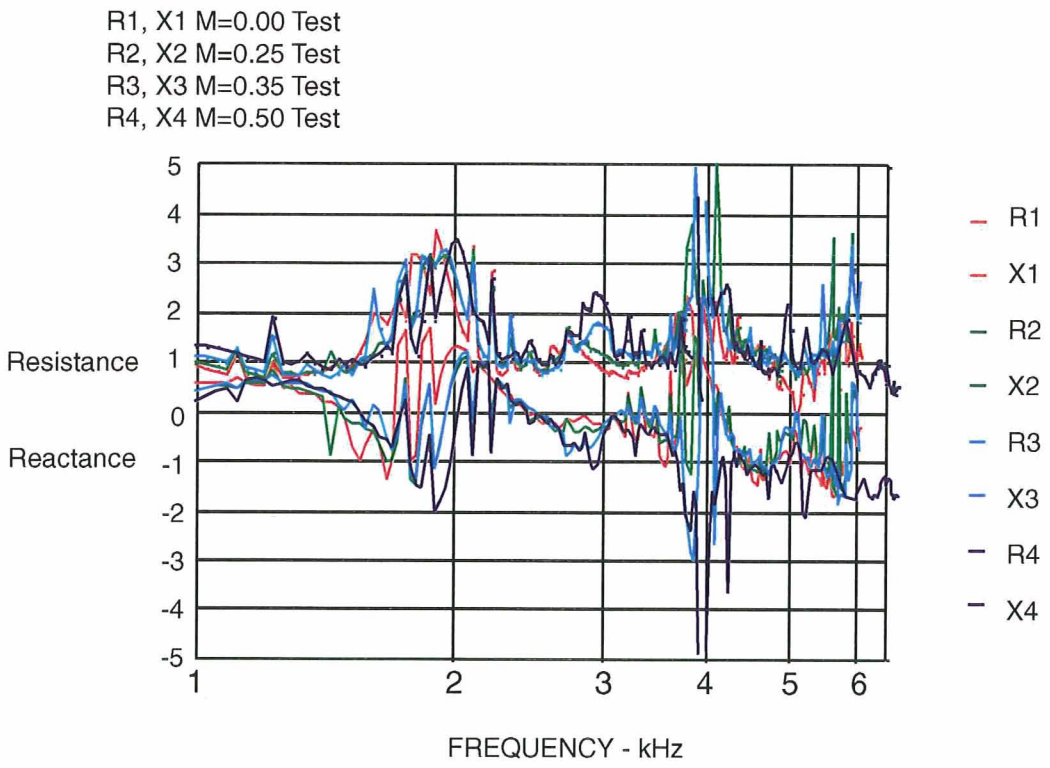

Figure 4: Bias Flow Panel, Vacuum Condition, Max SPL

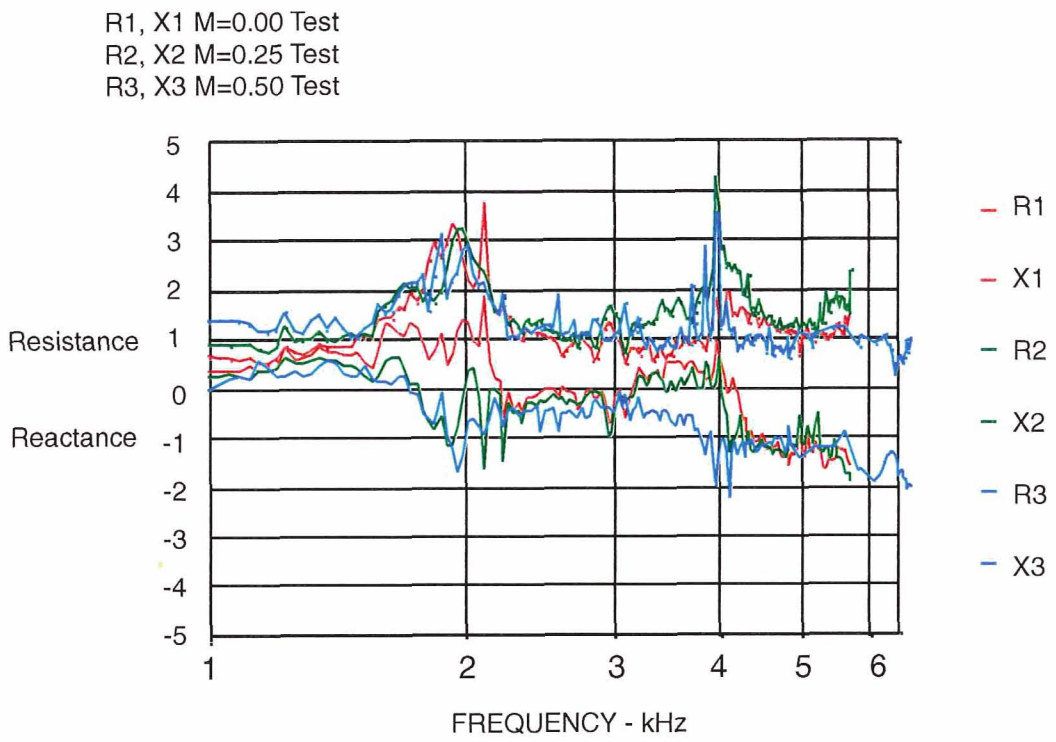

Figure 5: Bias Flow Panel, Vacuum Condition, Min SPL

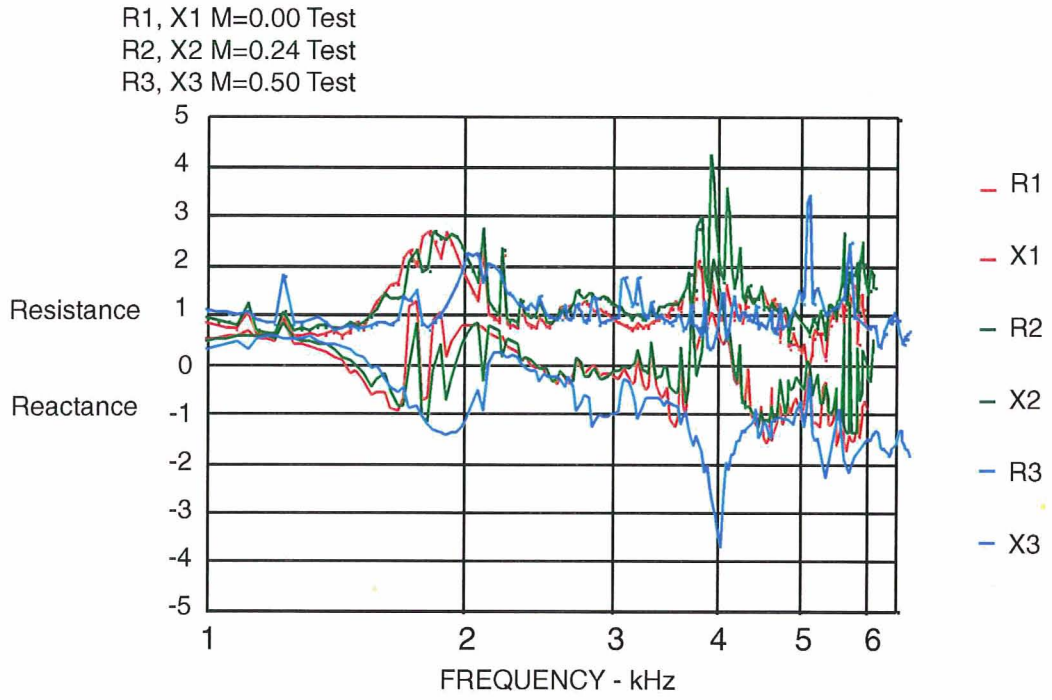

Figure 6: Bias Flow Panel, No Bias Flow, Max SPL

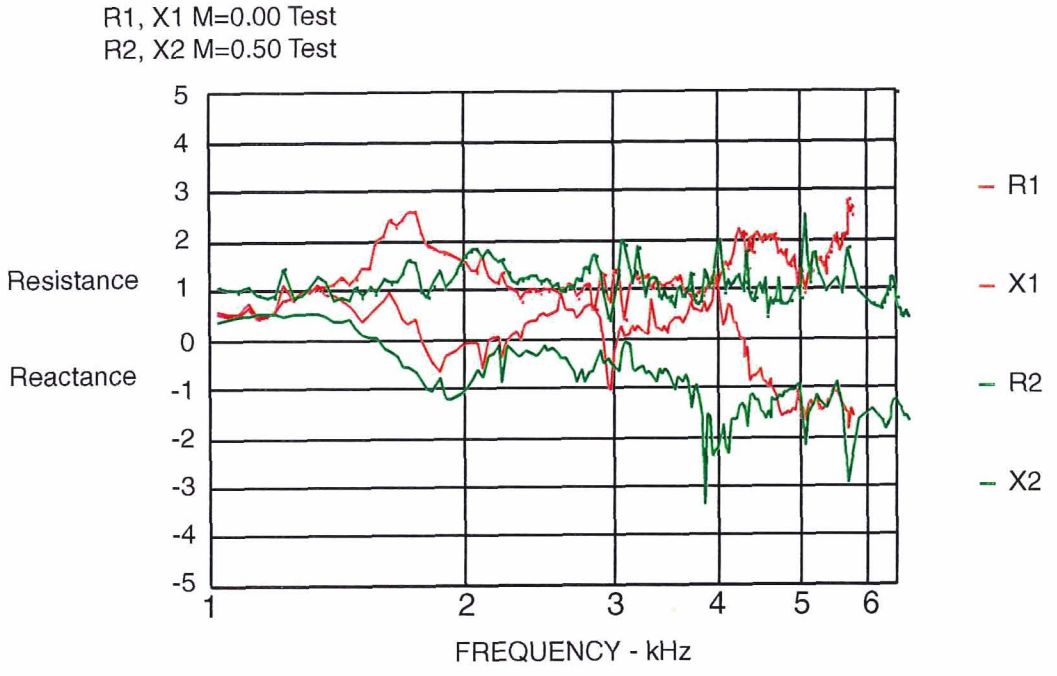

Figure 7: Bias Flow Panel, No Flow, Min SPL

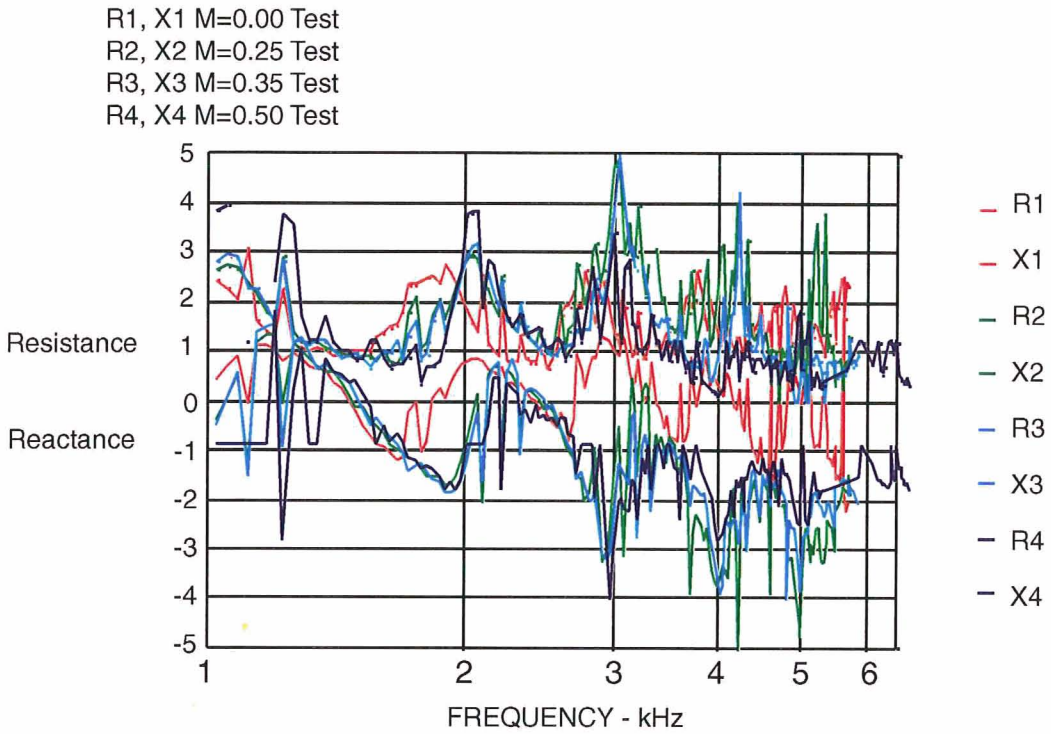

Figure 8: Heated Panel, With Heat, Max SPL

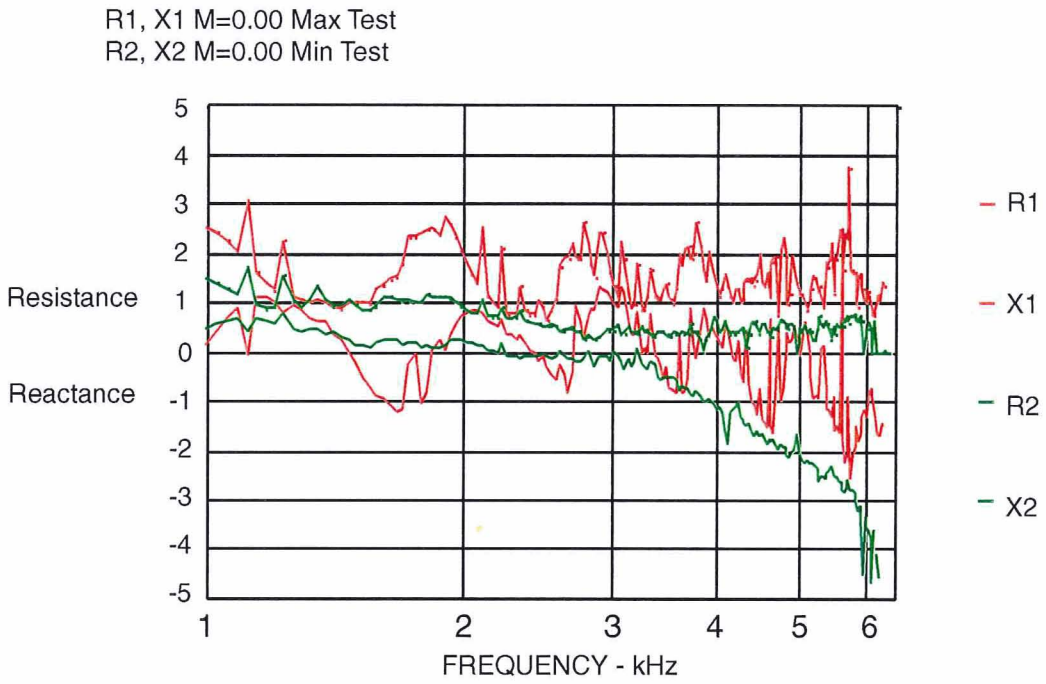

Figure 9: Heated Panel, Mach 0, Max vs. Min SPL

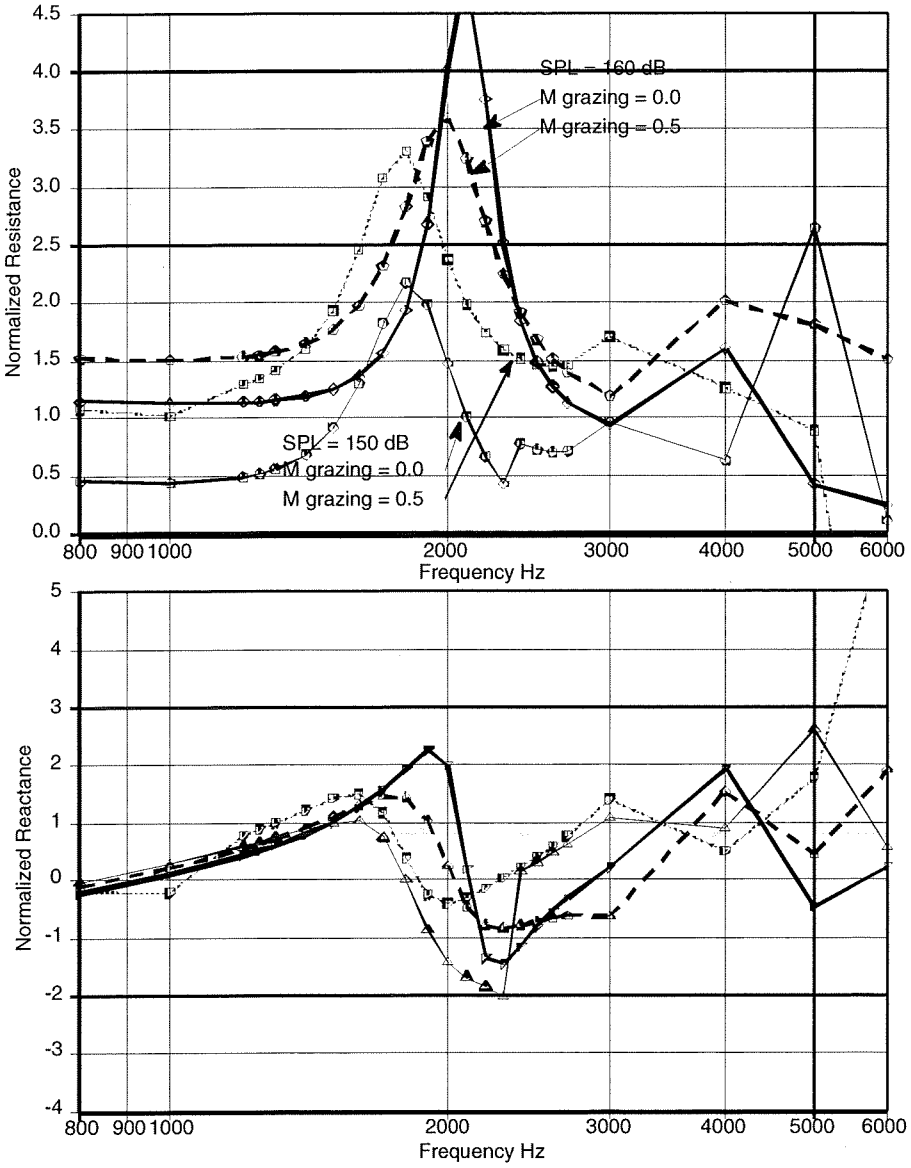

Fig. 10 Bias Flow Acoustic Liner Impedance Predictions With Dean/Hersh Procedure – No Bias Flow

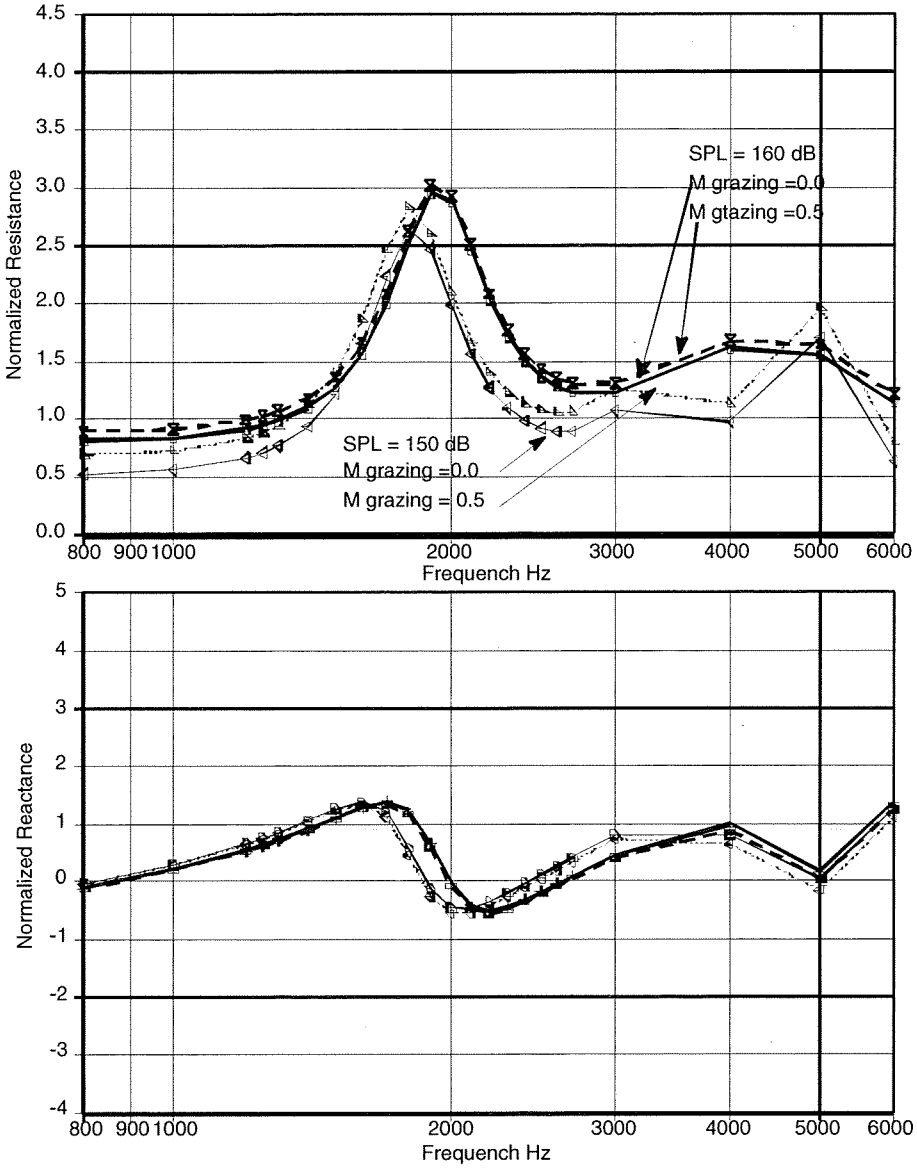

Fig. 11 Impedance Predictions For Bias Flow Test Liner With Boeing Orifice Impedance Models – No Bias Flow

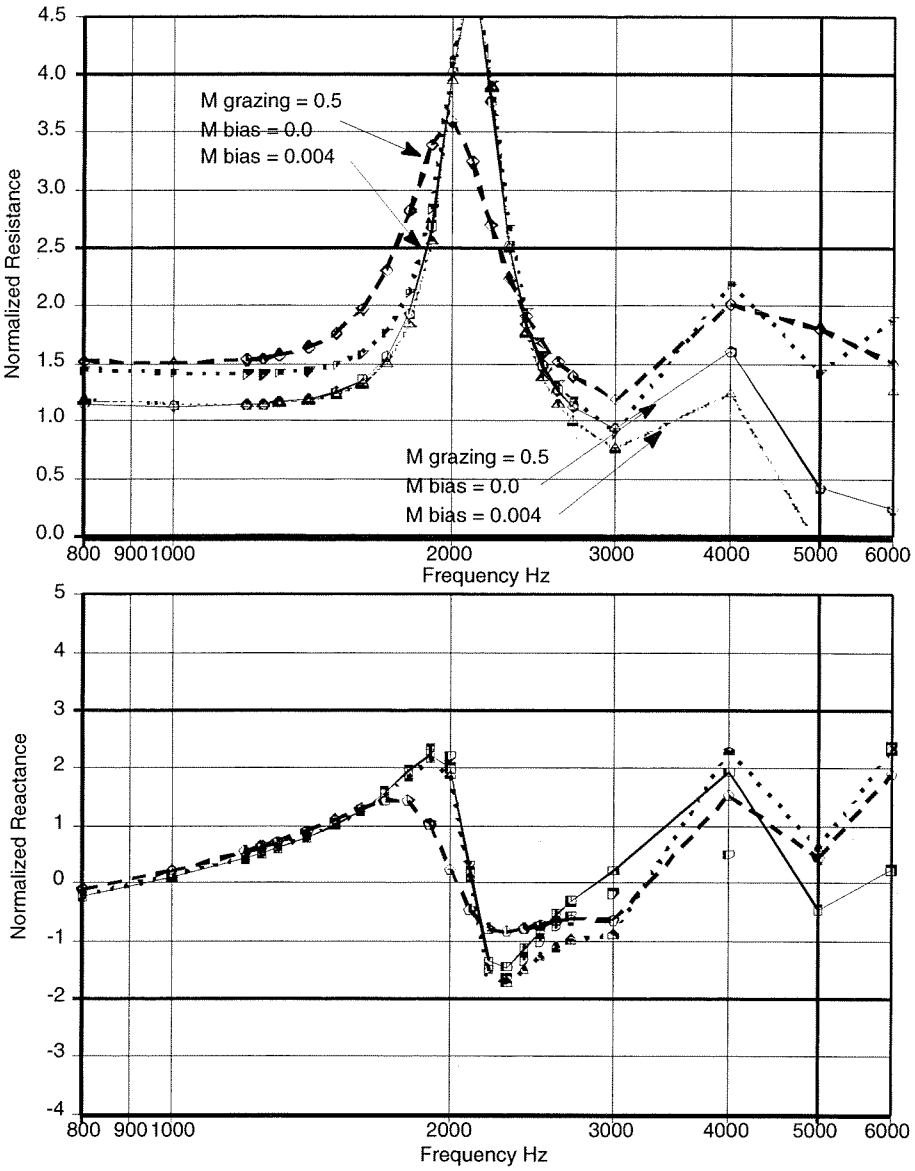

Fig. 12 Bias Flow Liner Predicted Impedance Dean/Hersh Impedance Model Effect of Bias Flow At SPL = 160 dB

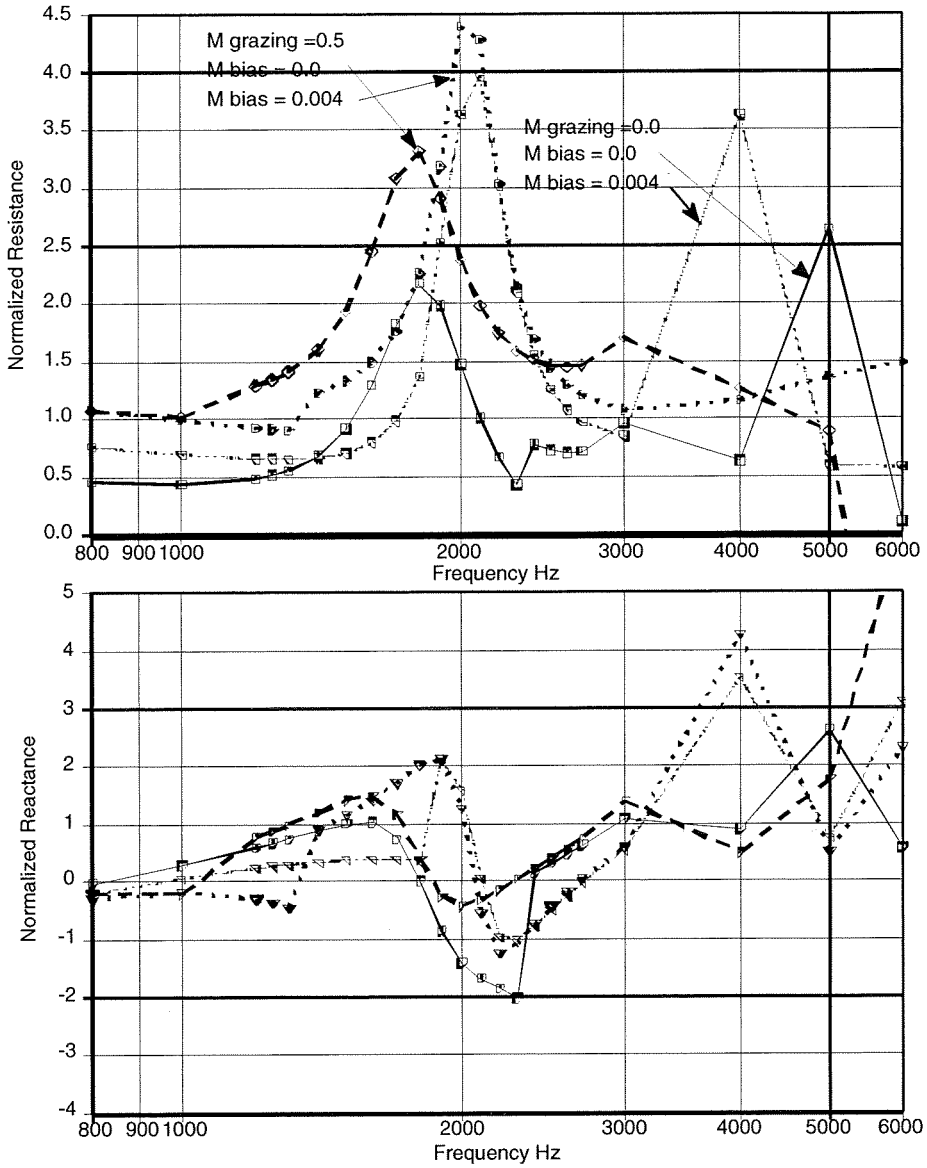

Fig. 13 Bias Flow Liner Predicted Impedance Dean/Hersh Impedance Model Effect Of Bias Flow At SPL = 150 dB

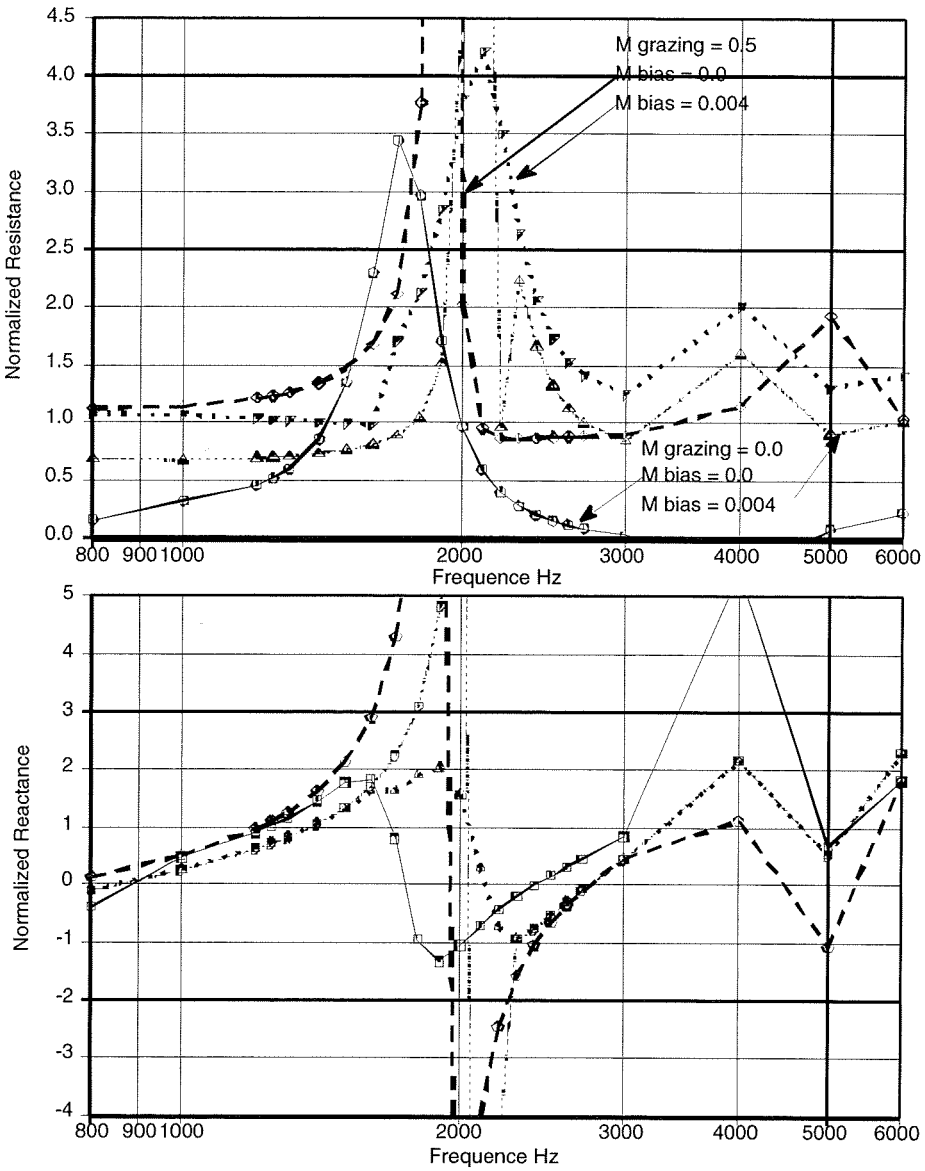

Fig. 14 Bias Flow Liner Predicted Impedance Dean/Hersh Impedance Model Effect Of Bias Flow At SPL = 140 dB

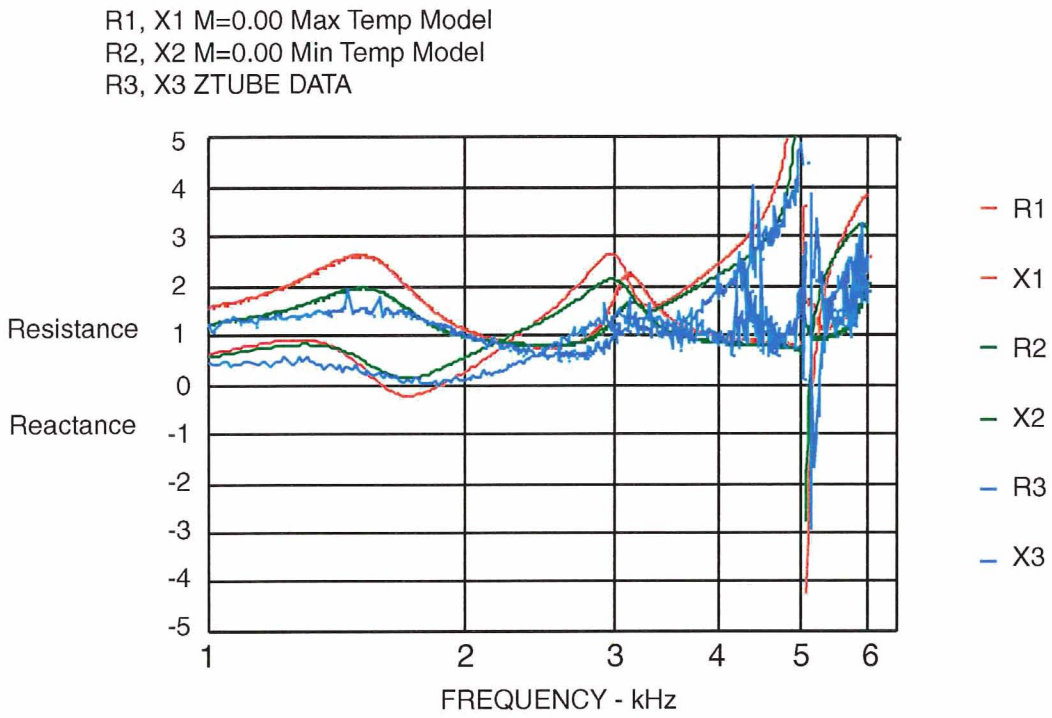

Figure 15: Heated Panel Impedance Tube Data vs. Model

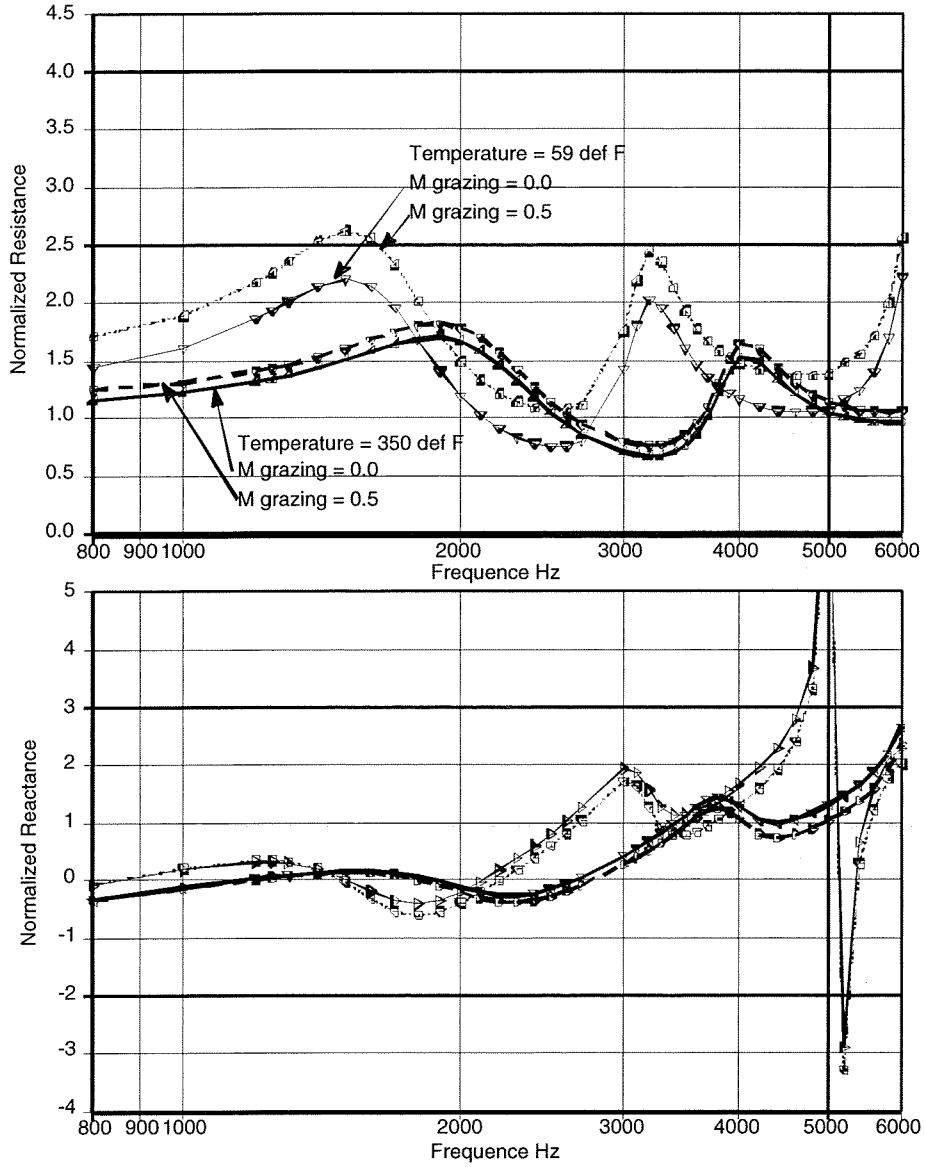

Fig. 16 High Temperature Liner Impedance Prediction Boeing Prediction Model Effect Of Temperature At SPL = 150 dB

Appendix 3 - Acoustic Testing of Scaled Micro-Perforated Sheets

1. INTRODUCTION

The aircraft industry's current interest in using Helmholtz resonators constructed with cavity-backed micro-diameter orifices to achieve linear or near linear sound absorbing liners motivated the development of a preliminary design, one-dimensional impedance model. The intent of the model is to provide the aircraft engine nacelle liner designer with a reasonable accurate, yet simple means of specifying resonator geometry to achieve desired wall impedance in aircraft engine applications. An experimental investigation was conducted to measure the effects of faceplate thickness-to-orifice diameter ratio, SPL and grazing flow speed on the impedance of Helmholtz resonators. The effects of grazing flow boundary-layer thickness were not investigated. The measurements were used to calibrate unknown empirical parameters derived in the one-dimensional impedance model.

2. MODEL DERIVATION

The derivation of the impedance prediction model is based on applying conservation of unsteady mass and vertical momentum flux across the control volume of the resonator orifice configuration sketched in Figure 1. During the inflow half-cycle, the acoustic volume flow entering the resonator orifice through the upper control surface is denoted by $u_{oN}S_{oN}$. The quantity $u_{vcN}S_{vcN}$ represents the sound particle volume flow exiting the control volume lower surface, where S_{vcN} represents the so-called "vena contracta" area. The volume flow VS_{VN} represents the grazing volume flow deflected into the resonator cavity by the driving sound pressure field P_D. The quantity H_N represents the orifice lumped element inertial length. The faceplate thickness is denoted by τ, the cavity depth by L_{cav} and the cavity cross-sectional area by S_{cav}.

The in-flow model shown in Figure 1 is valid only during the half-cycle when the incident acoustic velocity is pumped into the resonator cavity - it is not valid during the other half-cycle when the acoustic velocity is ejected from the resonator cavity. The restriction of the model to the in-flow half-cycle is not unduly limiting because the particle volume flow pumped into and out-of the resonator cavity must be constant over a dynamically steady-state sound period. Thus an empirical solution over the in-flow half-cycle should result in an empirical solution over the entire cycle.

Conservation of Mass. Assuming $H_N << \lambda$, the conservation of mass flux within N perforate control volumes (all assumed equal) may be written[1],

$$Nu_{vcN}S_{vcN} = NVS_{VN} + Nu_{0N}S_{0N} \tag{1}$$

Equation (1) shows that to first-order, the pumping of volume flow into and out-of a resonator orifice is governed by unsteady, incompressible motion. This makes sense because acoustic changes can occur only over scale lengths on the order of an acoustic wavelength.

Conservation of Vertical Momentum. The conservation of momentum in the vertical direction may be written,

$$\begin{aligned} &\rho_o(NS_{oN})H_N\frac{du_{vcN}}{dt} + \rho_o[u_{vcN}^2(NS_{vcN}) - u_{oN}^2(NS_{oN})] = \\ &P_D(NS_{oN}) - P_{cav}(NS_{oN}) - \tau_{wN}(NS_{wN}) \end{aligned} \tag{2}$$

The various terms in Eq. (2) are described below:

- The first term on the left-hand-side (LHS) represents the rate of increase of momentum stored in the control volume. The lumped element inertial length

parameter H_N is unknown and must be determined experimentally. The quantity NS_{0N} represents the open area of the N orifices.

- The second term on the LHS represents a Bernouilli type of nonlinear increase in momentum flux across the control surfaces S_{0N} and S_{vcN}.
- The first term on the right-hand-side (RHS) represents the incident acoustic driving force acting on the control surface area NS_{0N}.
- The second term on the RHS represents the cavity restoring force acting upon the fluid entering the resonator cavity.
- The third term on the RHS represents the momentum loss from frictional wall shear stresses τ_{WN} distributed over the face-plate thickness wetted area $S_{WN} = \pi d_N \tau$.

Model Simplifications. The non-linearity of Eq. (2) prevents an analytic solution. It must be solved numerically to achieve a dynamically steady-state solution, followed by a Fourier transform to calculate the fundamental harmonic velocity component. Although this procedure is numerically straightforward, it greatly complicates the design of sound absorbing liners. Since the goal of this effort is to derive a reasonable accurate, but simple impedance model, the following *six* simplifications are introduced to derive an analytic solution.

Discharge Coefficient. The *first* simpification introduces an acoustic discharge coefficient, C_{DN} and a grazing flow deflection coefficient, C_{VN} defined as

$$C_{DN} \equiv \frac{S_{vcN}}{S_{oN}}; \qquad C_{VN} \equiv \frac{S_{VN}}{S_{oN}} \tag{3}$$

The parameter C_{DN} governs the average sound particle volume flow rate entering the resonator cavity. It is the acoustic equivalent to the discharge coefficient concept used in steady-state pipe flow[2,3]. The parameter C_{VN} governs the steady-state grazing flow volume flow rate deflected into the resonator orifice. Substituting Eqs. (1) and (3) into Eq. (2) results in the following simplification,

$$\begin{aligned} &\rho_o(NS_{oN})H_N \frac{du_{vcN}}{dt} + N\rho_o S_{oN}[C_{DN}(1-C_{DN})u_{vcN}^2 + 2C_{DN}C_{VN}Vu_{vcN}] = \\ &NS_{oN}(P_D - P_{cav}) - NS_{wN}\tau_{wN} \end{aligned} \tag{4}$$

In deriving Eq. (4), steady-state terms associated with the deflection of the grazing flow into the cavity were ignored and only acoustic terms retained. It is intuitively clear that at low values of SPL, resonator non-linear resistive losses become negligibly small. Under these conditions, the non-linear term *(1-C_{DN})* should also become negligibly small. Test data, presented later, shows that indeed $C_{DN} \rightarrow 1$ when SPL becomes small.

Cavity Pressure. The *second* simplification assumes that the cavity pressure can be accurately modeled by solving the one-dimensional wave equation resulting in the following expression,

$$P_{cav} = -i\rho_0 c_0 \sigma C_{DN} \cot\left(\frac{\omega L_{cav}}{c_0}\right) u_{vcN}; \qquad \sigma \equiv \frac{NS_{0N}}{S_{cav}} \tag{5}$$

Non-Linearity. The *third* and *fourth* simplifications address the non-linearity of Eq. (2). These simplifications are based upon the experimental findings of Ingard and Ising[4]. Near resonance and at high SPL, Ingard and Ising used hot-wires to measure the amplitudes of higher harmonic velocity components. Test data showed that the higher harmonic velocity

components were small relative to the fundamental. This permits the replacement of the nonlinear term $\left(\hat{u}_{vcN}e^{i\omega t}\right)^2$ with the approximate expression,

$$\left(\hat{u}_{vcN}e^{i\omega t}\right)^2 \cong \left[\hat{u}_{vcN}\right]^2 e^{i\omega t} \tag{6}$$

It also permits the following harmonic relationship between u_0 and P_0,

$$u_{vcN}(t) = \hat{u}_{vcN}\exp\left(i\omega t + \theta_p\right) \tag{7}$$

where θ_p is an unknown phase shift between u_{vcN} and P_D. If sound frequencies are restricted to be at or very near resonance, then $\theta_p \approx 0$. To simplify the notation, the symbol (^) is deleted in the remainder of this report and it is understood that only acoustic amplitudes are considered.

Equation (6) forces the nonlinear velocity term u_{vcN}^2 to oscillate harmonically. Physically, this can be interpreted as the loss of higher harmonic acoustic energy - most of the harmonic acoustic energy is retained. Since we are interested in using micro-diameter orifice liners to achieve linear or near linear sound absorbing liners, this simplification is reasonable.

Viscous Scrubbing Losses. The *fifth* simplification addresses the wall shear stresses τ_{wN} and assumes that they are generated by steady-state and unsteady viscous scrubbing losses. A simple model, based upon dimensional analysis, is proposed. Steady-state shear stresses are assumed to be proportional to $\mu_o C_{DN}u_{vcN}/\delta_{avN}$ where δ_{avN} is an orifice faceplate averaged boundary-layer thickness and $C_{DN}u_{vcN}$ is an orifice area averaged acoustic particle velocity. Because δ_{avN} is unknown, it is assumed to be proportional to d_{0N} so that steady-state shear stresses are proportional to $\mu_o C_{DN}u_{vcN}/d_{0N}$. Acoustic shear stresses are derived assuming "Stokes-like" axially uniform diffusion of vorticity over the orifice thickness so that it is proportional to $\mu_o C_{DN}u_{vcN}\sqrt{\omega/\nu}$. With these assumptions, the wall shear stress τ_{wN} is written,

$$\tau_{wN} = \left(K_{ssN} + K_{acN}\sqrt{\frac{\omega d_{oN}^2}{\nu}}\right)\frac{\mu_o}{d_{oN}}C_{DN}u_{vcN} \tag{8}$$

where K_{ssN} and K_{acN} are unknown parameters that must be determined experimentally.

Resistance/Reactance De-Coupling. The *sixth* and final simplification is introduced to achieve a simple, practical solution to Eq. (4). This simplification is motivated by the impedance measurements shown in Figure 2 for a resonator constructed with a faceplate thickness-to-orifice diameter ratio, $\tau/d_{0N} > 1$. The measurements show resistance increases dramatically and reactance decreases moderately with grazing flow speed. These measurements suggest that a resistance model can be derived that is *de-coupled* from the effects of reactance. Because of the relatively modest effect of grazing flow speed on reactance, well-known lumped element reactance equations are used, modified to account for the effects of grazing flow speed and SPL, to model reactance. In Section 3, empirical corrections will be used to generalize the resistance and reactance models over a wide range of frequencies below and above resonance.

Substituting Eqs. (5 - 8) into Eq. (4) and dividing by $N\rho_o S_{oN}$ yields

$$C_{DN}(1-C_{DN})u_{vcN}^2+\left[2C_{VN}V+\frac{4\nu_o\tau}{d_{oN}^2}\left(K_{ssN}+K_{acN}\sqrt{\frac{\omega d_{oN}^2}{\nu_0}}\right)\right]C_{DN}u_{VCN}$$
$$+i\left[\omega H_N-c_0\sigma\cot(kL_{cav})\right]C_{DN}u_{VCN}=\frac{P_D}{\rho_0} \tag{9}$$

Tuned Resistance. Near resonance, the real part of Eq. (9) simplifies to,

$$C_{DN}(1-C_{DN})u_{vcN}^2+\left[2C_{DN}C_{VN}V+4\frac{\nu_o\tau}{d_{oN}^2}\left(K_{ssN}+K_{acN}\sqrt{\frac{\omega d_{oN}^2}{\upsilon_0}}\right)\right]u_{vcN}=\frac{P_D}{\rho_o} \tag{10}$$

The solution to Eq. (10) is

$$u_{vcN}=\sqrt{\frac{P_D}{\rho_0 C_{DN}(1-C_{DN})}+\left[\frac{\alpha'}{2C_{DN}(1-C_{DN})}\right]^2}-\frac{\alpha'}{2C_{DN}(1-C_{DN})} \tag{11}$$

where α', introduced to simplify notation, is defined as

$$\alpha'\equiv\left[2C_{DN}C_{VN}V+4\frac{\nu_o\tau}{d_{oN}^2}\left(K_{ssN}+K_{acN}\sqrt{\frac{\omega d_{oN}^2}{\nu_o}}\right)\right] \tag{12}$$

With some modest algebra, the following tuned resistance ($R_{res} \equiv P_D/u_{cav}$) of resonators constructed with N circular orifices backed by a common cavity is derived,

$$\frac{R_{res}}{\rho_0 c_0}\equiv\frac{P_D}{\rho_0 c_0 u_{cav}}=\frac{P_D}{\rho_0 c_0\sigma C_{DN}u_{vcN}}=\sqrt{\left(\frac{1-C_{DN}}{C_{DN}}\right)\frac{P_D}{\rho_0 c_0^2\sigma^2}+\left(\frac{\alpha}{2\sigma c_0}\right)^2}+\frac{\alpha}{2\sigma c_0} \tag{13}$$

where α is defined as,

$$\alpha=C_{DN}C_{VN}V+\left(\frac{\tau\nu_0}{d_{0N}^2}\right)\left(K_{ssN}+K_{acN}\sqrt{\frac{\omega d_{0N}^2}{\nu_0}}\right) \tag{14}$$

In deriving Eq. (14), the coefficients 2 and 4 in Eq. (12) were absorbed into the parameters C_{VN}, K_{ssN} and K_{acN}.

Linear Resistance. Combining Eqs. (13) and (14) and assuming $V = 0$ and SPL low, resonator viscous resistive losses may be approximated as,

$$\frac{R_L}{\rho_o c_o}=\frac{1}{\sigma}\left(\frac{\nu_o}{c_o d_{oN}}\right)\left(\frac{\tau}{d_{oN}}\right)\left[K_{ssN}+\sqrt{\frac{\omega d_{oN}^2}{\nu_o}}\;K_{acN}\right] \tag{15}$$

Since at low SPL, resistance is independent of SPL and de-coupled from reactance at all frequencies, Eq. (15) is not restricted to frequencies near resonance.

Equation (15) can be further simplified by assuming that the resonator face-sheet open area is constant, independent of number of orifices. This leads to the following relationship between single and multiple orifice face-sheet configurations,

$$NS_{0N}=N\frac{\pi d_{0N}^2}{4}=S_{01}=\frac{\pi d_{01}^2}{4}\rightarrow d_{0N}=\frac{d_{01}}{\sqrt{N}} \tag{16}$$

Substituting Eq. (16) into Eq. (15) results in the following simplification,

$$\frac{R_L}{\rho_o c_o} = \frac{1}{\sigma}\left(\frac{\nu_o}{c_o d_{01}}\right)\left(\frac{\tau}{d_{01}}\right)\left[\; NK_{ssN} + \sqrt{N\frac{\omega d_{01}^2}{\nu_o}}\;\; K_{acN}\right] \tag{17}$$

Equation (17) shows that steady-state shear stresses are proportional to N and the acoustic shear stresses are proportional to $\sqrt{N}$. This suggests that resonators constructed with sufficently large numbers of orifices such that $N >> (K_{acN}/K_{ssN})^2(\omega d_{oN}^2/\nu_0)$ will have resistive losses that are nearly constant, insensitive to frequency and sound amplitude!

It is of interest to compare the *steady-state* resistive losses predicted by Eq. (17) for the case $N = 1$ to the *steady-state* losses predicted from fully-developed laminar pipe flow[2,3],

$$\frac{R_{fd}}{\rho_o c_o} = \frac{32}{\sigma}\left(\frac{\nu_o}{c_o d_{01}}\right)\left(\frac{\tau}{d_{01}}\right) \tag{18}$$

Comparing these expressions yields $K_{ssN} = 32$. Thus, it is reasonable to assume that $K_{ssN} \rightarrow 32$ for resonators constructed such that $\tau/d_{01} > 1$. Combining Eqs. (13-17), the final expression for the resonator-tuned resistance is written,

$$\frac{R_{res}}{\rho_o c_o} = \sqrt{\left(\frac{1-C_{DN}}{C_{DN}}\right)\left(\frac{P_D}{\rho_o c_o^2 \sigma^2}\right) + \left(\frac{C_{VN}}{2\sigma}M + \frac{R_L}{2\rho_o c_o}\right)^2} + \left(\frac{C_{VN}}{2\sigma}M + \frac{R_L}{2\rho_o c_o}\right) \tag{19}$$

Observe that when $M = V/c_o$ is large, $R_{res}/\rho_0 c_0 \rightarrow C_{VN}M/\sigma$.

Reactance. The derivation starts from the following well-known lumped element (low SPL) expression for the reactance of a single orifice Helmholtz resonator,

$$\frac{X}{\rho_o c_o} = \frac{\omega d_{e1}}{\sigma c_o} - \cot(kL_{cav}) \tag{20}$$

For resonators constructed with shallow depth cavities, Ingard[5] derived the following approximate expression for the orifice inertial length parameter d_{e1},

$$d_{e1} = \tau + \frac{0.85 d_{o1}}{1 + 0.625\sqrt{\sigma}} \tag{21}$$

Motivated by the data shown in Figure 2 and the suggestion by Ingard and Ising[4] that nonlinear orifice jetting reduces orifice end correction, a simple reactance model is proposed by replacing d_{e1} in Eq. (20) by an unknown inertial length parameter H_N,

$$\frac{X}{\rho_o c_o} = \frac{\omega H_N}{\sigma c_o} - \cot(kL_{cav}) \tag{22}$$

Here H_N is a function of orifice number, resonator geometry, SPL, frequency and grazing flow speed. Empirical solutions for H_N are presented below in Section 3.

3. EXPERIMENTAL PROGRAM

An experimental program was undertaken to provide a data base in order to generate empirical curve-fits of the five unknown parameters K_{ssN}, K_{acN}, C_{DN}, C_{VN} and H_N. These parameters are assumed to be independent of time and hence frequency. Table I below defines the parameters of six multiple orifice resonator configurations used to derive curve-fits to the above parameters where the subscript N denotes the number of orifices enclosed by a cavity. The bold numbers of the N = 36 resonator denotes a deeper cavity depth relative to the other cavities. Detailed impedance measurements of the six resonator configurations were obtained using Dean's two-microphone method[6].

Table I. Summary of Small Diameter Resonator Geometries

N	d_N (inches)	τ (inches)	τ/d_{oN}	L_{cav} (inches)	S_N/d_{oN}	σ
1	0.375	0.500	1.333	0.850	NA	0.035
4	0.188	0.500	2.667	0.850	2	0.035
9	0.125	0.500	4.000	0.850	2	0.035
16	0.094	0.500	5.333	0.850	2	0.035
36	**0.063**	**0.500**	**8.000**	**1.000**	**2**	**0.035**
64	0.047	0.500	10.667	0.850	2	0.035

3.1 Determination of Parameters K_{ssN}, K_{acN}, C_{DN}, C_{VN} and H_N

Empirical curve-fits to the above parmeters were obtained by dividing them into low SPL, high SPL and grazing flow parts. The following notation is introduced to distinguish low from high SPL values of H_N. The subscript L denotes linear or low values of SPL, the subscipt NL denotes non-linear or high values of SPL. Thus H_{LN} denotes the low SPL values of the inertial length parameter and H_{NLN} denotes its corresponding high SPL values. Finally, the notation H_{NV} is introduced to account for the effect of grazing flow. The frequencies at which resonance occurs as a function of SPL and grazing flow are denoted as F_{LN}, F_{NLN} and F_{NV}.

Linear Parameters K_{ssN} and K_{acN}. When SPL is low and/or orifice diameter is sufficiently small that $\tau/d_{oN} >> 1$, viscous scrubbing losses become very large relative to non-linear and grazing flow resistive losses. Under these conditions, resonator resistance is approximated by Eq. (17). Hersh, Walker and Celano[7] derived the following expression for the parameter K_{ssN},

$$K_{ssN} = 13 + 10.23\left(\frac{\tau}{d_{oN}}\right)^{-1.44} \tag{23}$$

Equation (23) shows that resonators constructed with very small values of τ/d_o have viscous scrubbing resistive losses that are much larger than fully-developed pipe flow resistive losses. These results are consistent with orifice entry and exit boundary-layer thicknesses that are *less* than orifice radius. *Conversely,* resonators constructed with large ratios of τ/d_o have resistive losses substantially less than the fully developed pipe flow valued of K_{ssN} = 32. This was not expected and is not understood. The derivation of the fully developed pipe flow resistance model assumes that entry flow effects are negligible. For steady state laminar flow, pipe entry lengths as long as 150 - 300 pipe diameters have been measured[2,3]. These very long entry lengths suggest that three-dimensional effects ignored in the derivation of fully-developed

laminar resistance model may play an important role in explaining the data. For example, instantaneous laminar separation bubbles formed near the orifice entry during inflow could explain why the asymptotic behavior of $K_{ssN} < 32$. Here, the orifice wetted area shear stresses in the laminar separation bubble would be opposite to the wall stresses on the remaining orifice wetted area thereby reducing the net stress and hence K_{ss}.

The data shown in Figure 3 was used to derive the following curve-fit to the parameter K_{acN},

$$K_{ac} = 7.56\left(\frac{\tau}{d_{oN}}\right)^{-0.288} - 0.375\left(\frac{\tau}{d_{oN}}\right) + 0.033\left(\frac{\tau}{d_{oN}}\right)^{2} \tag{24}$$

Linear Parameter F_{LN}. The effect of orifice number on resonator tuned frequency is displayed in Figure 4 for the resonator configurations shown in Table I. By normalizing the data as shown, the following curve-fit was derived,

$$\frac{F_{LN}}{F_{L1}} = 1.086\exp\left[-0.5\left|\left(\frac{N-34}{43.6}\right)\right|^{6.67}\right] \tag{25}$$

Here F_{LN} represents the tuned, low SPL, frequency for a resonator constructed with N orifices normalized by the tuned frequency for a resonator constructed with a single orifice (F_{L1}) and having the same open area. Equation (16) connects the dimensions of the N orifices to an equivalent open area single orifice.

Linear Parameter H_{LN}. The effect of orifice number on resonator inertial length parameter can be calculated from Eqs. (22) and (25). At resonance, H_{LN} becomes

$$H_{LN} = \frac{\sigma c_o}{\omega_{LN}} \cot\left(\frac{\omega_{LN} L_{cav}}{c_o}\right) \tag{26}$$

where $\omega_{LN} = 2\pi F_{LN}$. The RHS of Figure 5 shows that the model predicts reasonable accurately the low SPL, zero grazing flow impedance data for the resonator configurations described in Table I.

Nonlinear Frequency F_{NLN}. Although it is difficult to see, the reactance data displayed in Figure 2 shows the resonator tuned frequency to decease with increasing SPL in accord with the earlier measurements by Ingard and Ising[4]. The nonlinear tuned frequency is plotted in Figure 6 as a function of faceplate thickness and sound pressure amplitude for the resonator configurations of Table I. F_{NLN} was correlated in terms of the ratio of the following acoustic velocity parameters, $\omega_{LN} H_{LN}$ and $[P_{pk}/\rho_0]^{1/2}$, where $P_{pk} = \sqrt{2}P_D$ represents the incident sound pressure peak value,

$$V_{non} \equiv \sqrt{\frac{P_{pk}}{\rho_o (\omega_{LN} H_{LN})^2}} \tag{27}$$

The parameter V_{non} is important because $\omega_L H_{LN}$ characterizes the effects of resonator geometry and $[P_{pk}\rho_0]^{1/2}$ characterizes the effect of sound pressure amplitude on the acoustic behavior of Helmholtz resonators.

The data shown in Figure 6 suggest that the effects of orifice number and hence the ratio of faceplate thickness-to-orifice diameter are small. The following curve-fit of F_{NLN} was derived, normalized by $F_{LN,}$,

$$\frac{F_{NLN}}{F_{LN}} = 1 + 0.04\left[1 - \exp\left(-16V_{non}^2\right)\right] \tag{28}$$

where F_{LN} is defined by Eq. (25).

Non-Linear Inertial Length Parameter H_{NLN}. The inertial length parameter H_{NLN} was determined from experimental data by setting the reactance X = 0 (resonance) in Eq. (22) yielding

$$H_{NLN} = \frac{\sigma c_0}{2\pi F_{NLN}} \cot\left[\frac{2\pi F_{NLN} L_{cav}}{c_0}\right] \tag{29}$$

where F_{NLN} is defined by Eq. (28).

A computationally simpler way to calculate H_{NLN} is shown in Figure 7. Here H_{NLN}/H_{LN} is plotted in terms of the ratio F_{NLN}/F_{LN} for the resonator configurations of Table I. The data shows that at $H_{NLN}/H_{LN} \rightarrow 1$ when $F_{NLN}/F_{LN} \rightarrow 1$ which occurs when SPL becomes low as shown in Figure 6. Conversely at high SPL, H_{NLN}/H_{LN} decreases with SPL and is insensitive to faceplate thickness-to-orifice diameter ratio. The following correlation of H_{NLN}/H_{LN} in terms of F_{NLN}/F_{LN} was derived,

$$\frac{H_{NLN}}{H_{LN}} = \left[1 + 2.05\left(\frac{F_{NLN}}{F_{LN}} - 1\right)\right]^{-1} \tag{30}$$

Non-Linear Discharge Coefficient Parameter C_{DN}. Setting V = 0 in Eq. (19), the resonator tuned resistance becomes

$$\frac{R_{res}}{\rho_0 c_0} = \frac{R_L}{2\rho_0 c_0} + \sqrt{\left(\frac{1 - C_{DNres}}{C_{DNres}}\right)\frac{P_{inc}}{\rho_0 c_0^2 \sigma^2} + \left(\frac{R_L}{2\rho_0 c_0}\right)^2} \tag{31}$$

With R_{res} and R_L measured, Eq. (31) can be solved for the discharge coefficient parameter C_{DNres} at resonance resulting in the expression,

$$C_{DNres} = \frac{1}{1 + \Psi_{res}}; \qquad \Psi_{res} \equiv \frac{\frac{R_{res}}{\rho_0 c_0}\left(\frac{R_{res}}{\rho_0 c_0} - \frac{R_L}{\rho_0 c_0}\right)}{\frac{P_{pk}}{\rho_0 c_0^2 \sigma^2}} \tag{32}$$

The effects of SPL and resonator geometry on C_{DNres} was determined at resonance from experimental data using Eq. (32). The effect of faceplate thickness and SPL on C_{DNres} is shown in Figure 8. Observe that that $C_{DNres} \rightarrow 1$ *as SPL* $\rightarrow 0$. The following curve-fit to C_{DNres} was derived,

$$
\begin{aligned}
C_{DNres} &= \frac{1+a_{res}V_{non}^2+b_{res}V_{non}^2}{1+c_{res}V_{non}^4} \\
a_{res} &= 20.77+83\exp\left[-\left|\left(0.33\frac{\tau}{d_{oN}}-1.46\right)^{1.627}\right|\right] \\
b_{res} &= 2.70*10^4+2.61*10^5\exp\left[-\left|\left(0.27\frac{\tau}{d_{oN}}-1.25\right)^{1.8}\right|\right] \\
c_{res} &= 3.61*10^4+4.04*10^5\exp\left[-\left|\left(0.28\frac{\tau}{d_{oN}}-1.26\right)^{1.541}\right|\right]
\end{aligned}
\tag{33}
$$

The rather complicated curve-fit of the effect of frequency on the discharge coefficient data was also derived,

$$
C_{DN}=\frac{C_{DNres}+a_{cd}f_{non}^2}{1+b_{cd}f_{non}^2+a_{cd}f_{non}^2}; \qquad f_{non}\equiv\frac{f_{NL}}{f}-1 \tag{34}
$$

where

$$
a_{cd}=a_{1cd}+a_{2cd}\exp\left(-a_{3cd}V_{non}\right)
$$

$$
\begin{aligned}
a_{1cd} &= 18.81\frac{\tau}{d_o}-57.11\sqrt{\frac{\tau}{d_o}}\left[1-\exp\left(-0.18\frac{\tau}{d_o}\right)\right] \\
a_{2cd} &= \exp\left\{\frac{33.5\left(\frac{\tau}{d_o}\right)-78\left(\frac{\tau}{d_o}\right)^2+131\left(\frac{\tau}{d_o}\right)^3+917\left(\frac{\tau}{d_o}\right)^4}{1+148\left(\frac{\tau}{d_o}\right)^4}\right\} \\
a_{3cd} &= 43.2\frac{\tau}{d_o}-147.1\sqrt{\frac{\tau}{d_o}}\left[1-\exp\left(-0.19\frac{\tau}{d_o}\right)\right]
\end{aligned}
\tag{35}
$$

and

$$
b_{cd}=\frac{b_{1cd}+b_{2cd}V_{non}}{1+b_{3cd}V_{non}}
$$

$$
b_{1cd}=\frac{-3.44-0.182\frac{\tau}{d_o}}{1+0.342\frac{\tau}{d_o}}; \quad b_{2cd}=\frac{18.23+1.33\frac{\tau}{d_o}}{1+0.151\frac{\tau}{d_o}}; \quad b_{cd3}=\frac{38}{1+1.3*10^{-7}\left(\frac{\tau}{d_o}\right)^2} \tag{36}
$$

Grazing Flow Parameter C_{VN}. The grazing flow parameter C_{VN} was calculated from experimental data as a function of grazing flow speed, SPL, cavity geometry and number of orifices. The analysis of the data was substantially simplified by assuming that C_{DN} was independent of the grazing flow. Physically, this ignores the complexity of non-linear

interaction between the sound pressure field and the grazing flow. This interaction is highly three-dimensional and beyond the scope of the one-dimensional model.

Restricting the frequencies to resonance, the following expression for C_{VNres} was derived from Eq. (19),

$$C_{VNres} = \frac{\sigma}{M}\left[\left(\frac{R_v - R_L}{\rho_0 c_0}\right) - \left(\frac{R_o}{R_v}\right)\left(\frac{R_o - R_L}{\rho_0 c_0}\right)\right] \tag{37}$$

where R_v denotes resistance measured at a function of grazng flow speed, M denotes grazing flow Mach number, R_o denotes resistance in the absence of grazing flow and R_L denotes linear resistance. The results of applying Eq. (37) to the data are shown in Figure 9. The data was correlated in terms of the parameter $[\rho_o V^2/P_{pk}]^{1/2}$. Figure 9 shows that when $[\rho_o V^2/lP_{pk}]^{1/2} \geq 10$, C_{VNres} asymptotically appraches a maximum that is dependent upon the ratio τ/d_{oN}. Further, the asymptotic value of C_{VNres} decreases with increasing τ/d_{oN}.

The following curve-fit of the data shown in Figure 9 was derived,

$$C_{VNres} = a\left\{1 - \exp\left[-b\left(\frac{\rho_o V}{P_{pk}}\right)^2\right]\right\} \tag{38}$$

where

$$a = 0.016 + 0.224 exp\left[-0.036\left(\frac{\tau}{d_{oN}}\right)^2\right]$$

$$b = 0.012 + 0.0021 \exp\left[-0.012\left(\frac{\tau}{d_{oN}}\right)^4\right] \tag{39}$$

Grazing Flow Tuned Frequency and Inertial Length Parameters F_{NV} and H_{NV}. The effect of grazing flow on the the resonator tuned frequency F_{NV} and the inertial length parameter H_{NV} are plotted in Figures 10 and 11 respectively. A close examination of Figure 10 shows that the tuned frequency of the single orifice configuration was the most sensitive to grazing flow, increasing by almost 20% relative to its non-grazing flow, low SPL value. The tuned frequencies of the remaining resonators, constructed with N ≥ 4, were insensitive to grazing flow. The following, rather complicated, curve-fit of the resonators tuned frequencies was derived,

$$\frac{F_{NV}}{F_{LN}} = 1 + 0.2\left[1 - \exp\left(-55.12x^2\right)\right]; \quad x \equiv \frac{\left(\frac{P_{pk}}{\rho_o V_{non}^2}\right)^{0.115}\left(\frac{P_{pk}}{\rho_o c_o^2} + M^2\right)^{0.425}}{\left(\frac{\tau}{d_{oN}}\right)} \tag{40}$$

The inertial length parameter H_{NV} is determined from experimental data by setting the reactance X = 0 (resonance) in Eq. (22) yielding

$$H_{NV} = \frac{\sigma c_0}{2\pi F_{NV}} \cot\left[\frac{2\pi F_{NV} L_{cav}}{c_0}\right] \tag{41}$$

where F_{NV} is defined by Eq. (40).

A computationally simpler way to calculate H_{NV} is shown in Figure 11. Here H_{NV}/H_{LN} is plotted in terms of the ratio F_{NV}/F_{NL}. The data shows that at $H_{NV}/H_{LN} \rightarrow 1$ when $F_{NV}/F_{NL} \rightarrow 1$ which occurs when SPL and grazing flow become small as shown in Figure 10. Conversely at high SPL and high grazing flow speeds, H_{NV}/H_{LN} decreases as shown. The following curve-fit of H_{NV}/H_{LN} was derived,

$$\frac{H_{NV}}{H_{LN}} = \left[1 + 2.2\left(\frac{F_{NV}}{F_{LN}} - 1\right)\right]^{-1} \tag{42}$$

3.2 Model Predicted vs. Measured Impedance

The empirical curve-fits of five parameters K_{ssN}, K_{acN}, H_N , C_{DN}, *and* C_{VN} were used to predict the impedance of the resonators of Table I. Since the curve-fits derived for these parameters were based upon the impedance measurements of these resonators, it is reasonable to expect good agreement between model predicted and measured impedance. This will be shown to be true. The model needs to be validated by comparing its prediction to other impedance measurements published in the open literature.

The comparisons between predicted and measured impedance are displayed in Figures 12 - 14. The zero grazing flow data, summarized in Figures 12(a-f), show that non-linear Bernouilli resistive losses occur over the entire orifice number range even for the N = 64 (τ/d_{64} = 10.67) configuration, although the effect of SPL is substantially less than at lower values of N. The data shows that reactance is insensitive to the effects of SPL. The model predicts both resistance and reactance quite accurately over the entire frequency, SPL and orifice number range tested.

The effects of grazing flow on resistance are displayed in Figures 13(a-f). The grazing flow resistance data is not understood. The data shows inconsistent trends with frequency - it increases and/or decreases with frequency. Although this behavior suggests that the measurements may not be accurate and shoud be repeated, we believe the measurements may be accurate near resonance. The measurements do suggest, nontheless, that the effects of grazing flow are small for resonators constructed with $\tau/d_{oN} > 9$.

The effects of grazing flow on reactance are displayed in Figures 14(a-f). The data shows that reactance is fairly insensitive to orifice number and SPL and only moderately sensitive to grazing flow. The model predicted reactance is in good agreement with data.

4. CONCLUDING REMARKS

The model satisfactorily predicted the effect of orifice number, SPL and uniform grazing flow on the impedance of multiple orifices backed by a common cavity. The effects of boundary-layer thickness was not studied. These findings, however, are valid only for the single orifice-to-orifice spacing of $S_N/d_N = 2$. The effect and hence the importance of relative spacing has not been studied. In a effort to at least to identify the importance of relative spacing, two resonators with N = 25 were constructed with spacings of $S_{25}/d_{25} = 1$ and 3 as summarized in Table II below. The $S_{25}/d_{25} = 1$ spacing was as close as practical (without orifices merging) and the $S_{25}/d_{25} = 3$ spacing as far as practical (to avoid cavity wall interaction effects). The effect of array spacing on resistance is displayed in Figure 15 and the corresponding effect on reactance is displayed in Figure 16.

Figure 15 contains four graphs. The LHS graphs labeled "a" and "b" compare the effects of array spacing for SPL = 120/140 dB at V = 0. These graphs show a negligible effect of spacing on resistance. In contrast, the RHS graphs labeled "c" and "d" show a large effect of array spacing on resistance at V = 80 m/s. Figure 16 shows that the corresponding effect of array spacing on reactance is much less dramatic. The data shows clearly, however, that increasing array spacing decreases orifice inertial reactance. The decrease appears to be insensitive to grazing flow speed and SPL. *These tests show clearly that the effects of orifice spacing with grazing flow have an important on resonator resistance. Further tests are required to establish a larger data base to better understand the effects of orifice array spacing.*

Table II. Resonator Used in Array Spacing Tests

N	d_{oN} (inches)	τ (inches)	L_{cav} (inches)	S_N/d_{oN}	σ
25	0.075000	0.50	0.85	**1.0**	0.035
25	0.075000	0.50	0.85	**3.0**	0.035

The above test program was conducted with the orifice arrays orientated perpendicular to the incident grazing flow. A test was conducted to measure the effects of rotating the array 45^0 with respect to the grazing flow. Test results, displayed in Figures 17 and 18, show that the effects of resonator orientation have only a small affect upon resonator resistance and reactance. This suggests that orifice interaction in the form of upstream wake impingment can be ignored for grazing flow speeds below 80 meters/second.

The effects of orifice spacing and orientation with respect to grazing flow are important issues that were not included as part of this study. The limited data show, however, that orifice spacing is important and the effects of array orientation to grazing flow may be important at grazing flow speeds in excess of 80 meters/second. Their effects should be understood and incorporated into a liner design prediction code. Finally, as mentioned earlier, the model should be validated by comparing it to impedance data in the open literature.

The authors acknowledge the insightful and important contributions made by Mr. Gerald Bielak of the Boeing Commercial Aircraft Company.

REFERENCES

1. Temkin, S. *Elements of Acoustics*, John Wiley & Sons, pg. 179, 1981.
2. ASME. *Fluid Meters - Their Theory and Applications.* ASME, 1959.
3. Schlichting, H., *Boundary-Layer Theory,* McGraw-Hill Book Company, pgs 176-178, 78-80,560, 1968.
4. Ingard, U. and Ising, H., "Acoustic Non-Linearity of an Orifice", JASA, Vol. 42, No. 1. 6-17. 1967.
5. Ingard, U., "On the Theory and Design of Acoustical Resonators", JASA, V. 25, pp. 1037-1062, 1953.
6. Dean, P. D., "An In-Situ Method of Wall Acoustic Impedance Measurement in Flow Ducts", JSV, Vol. 34, No. 1, p. 97, 1974.

7. Hersh, A. S., Walker, B. E., and Celano, J. W., " Helmholtz Resonator Impedance Model. Part 1. Non-Linear Behavior", submitted to AIAA Journal, October, 2001.

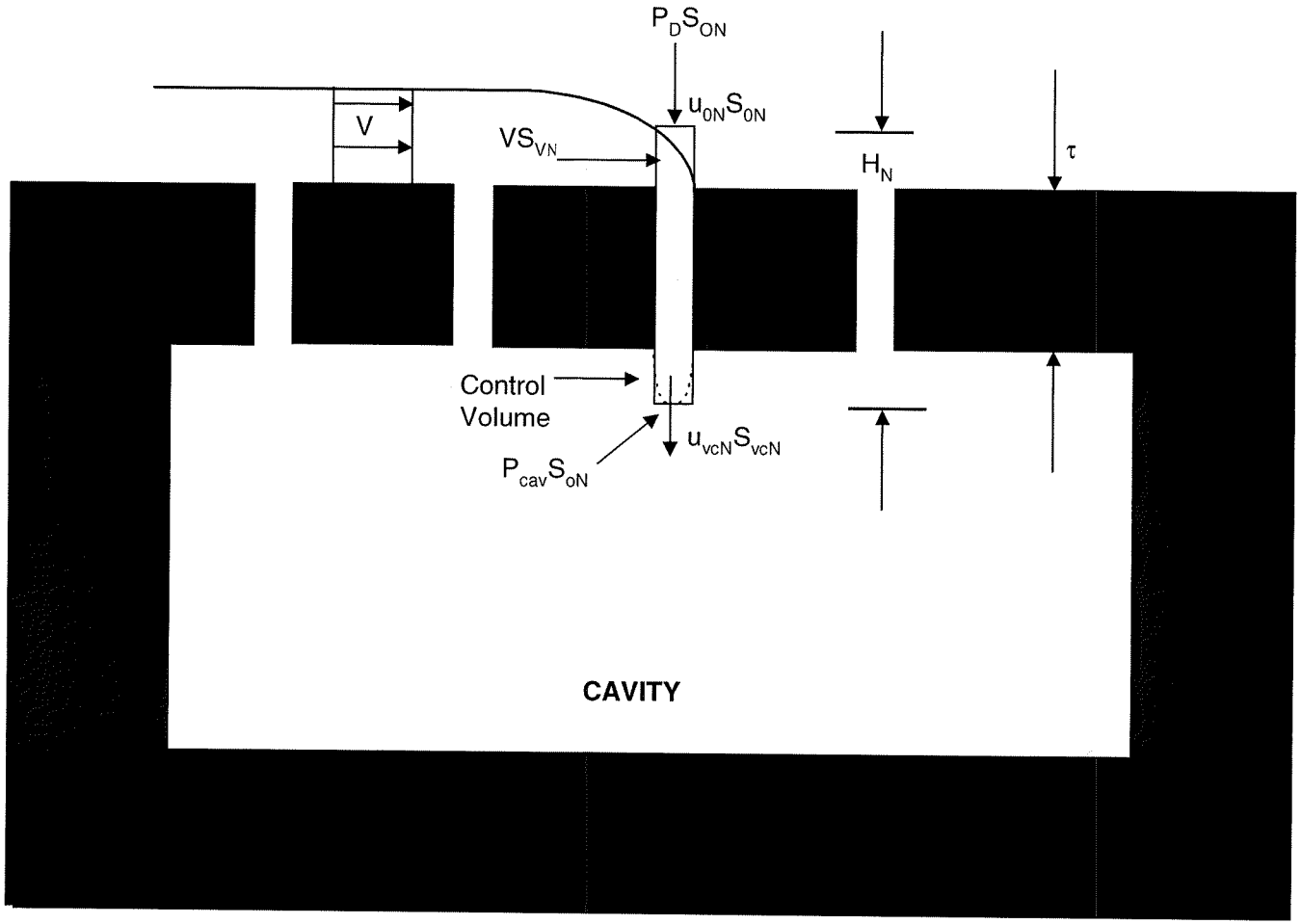

Figure 1. Control Volume Used in Model Derivation

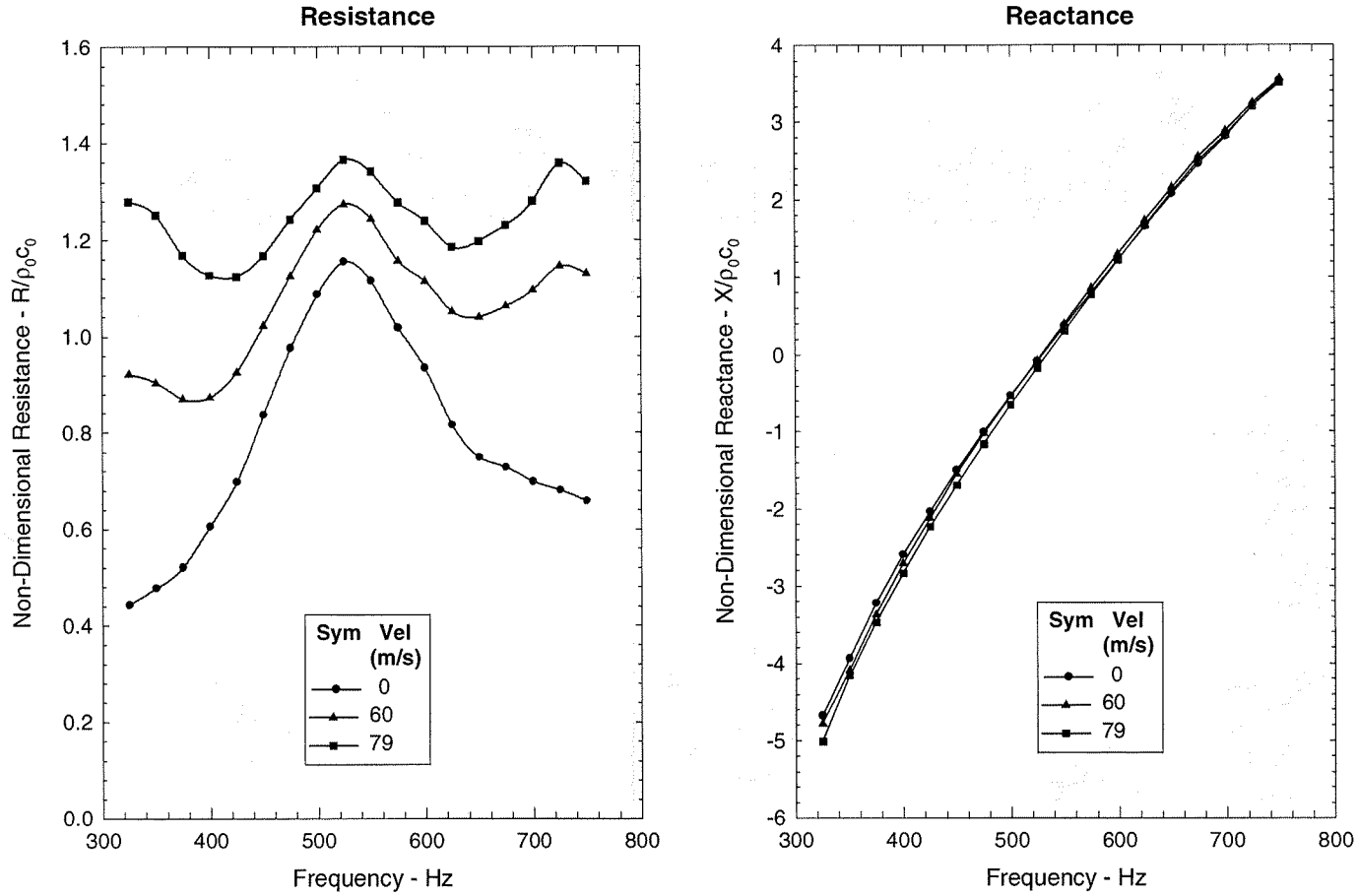

Figure 2. Effect of Grazing Flow on Impedance of N = 9 Orifice Resonator: SPL = 140 dB, d_{ori} = 0.125-in., τ = 0.5-in., D_{cav} = 2.0-in., L_{cav} = 0.85-in.

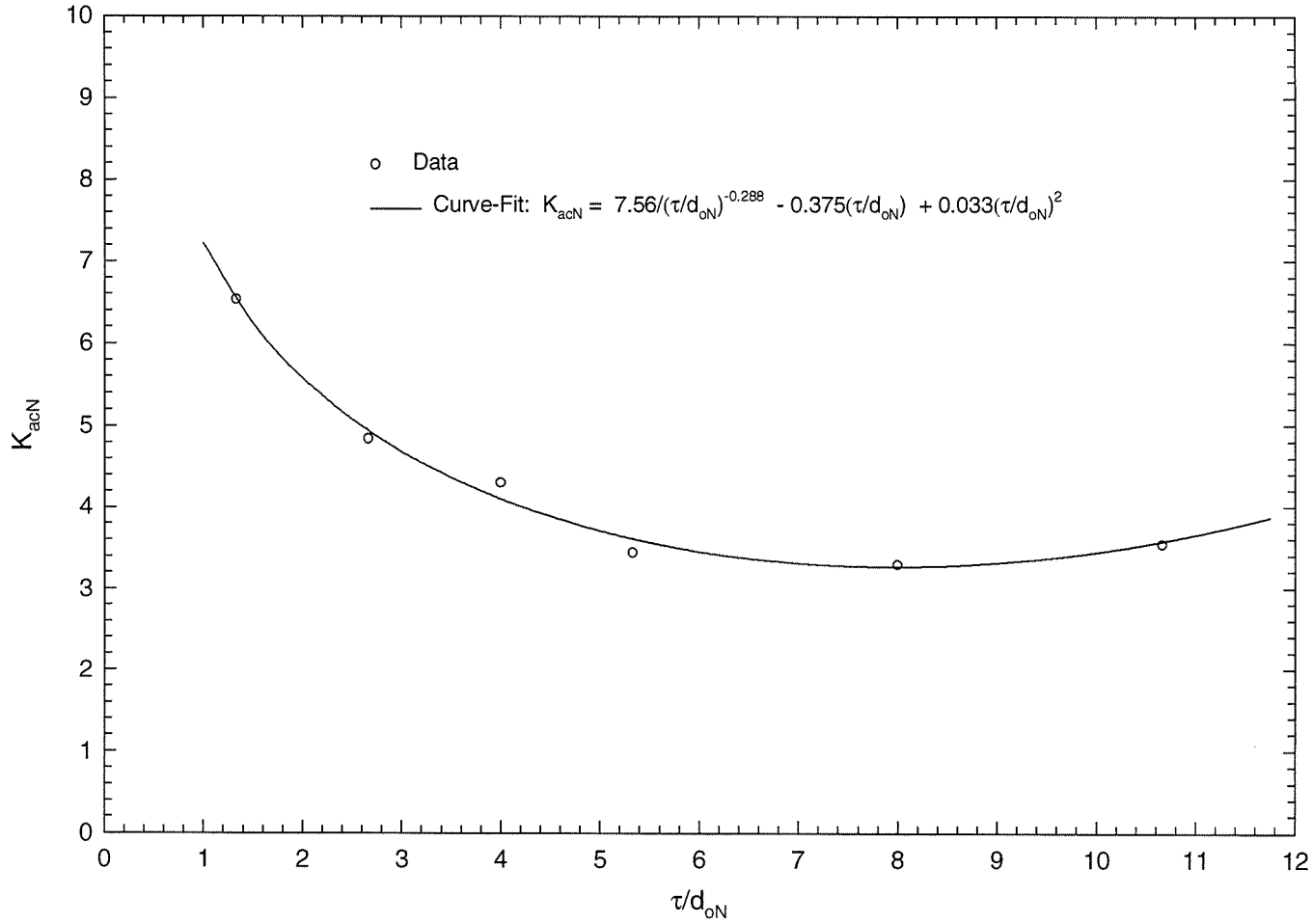

Figure 3. Curve-Fit of Parameter K_{acN}

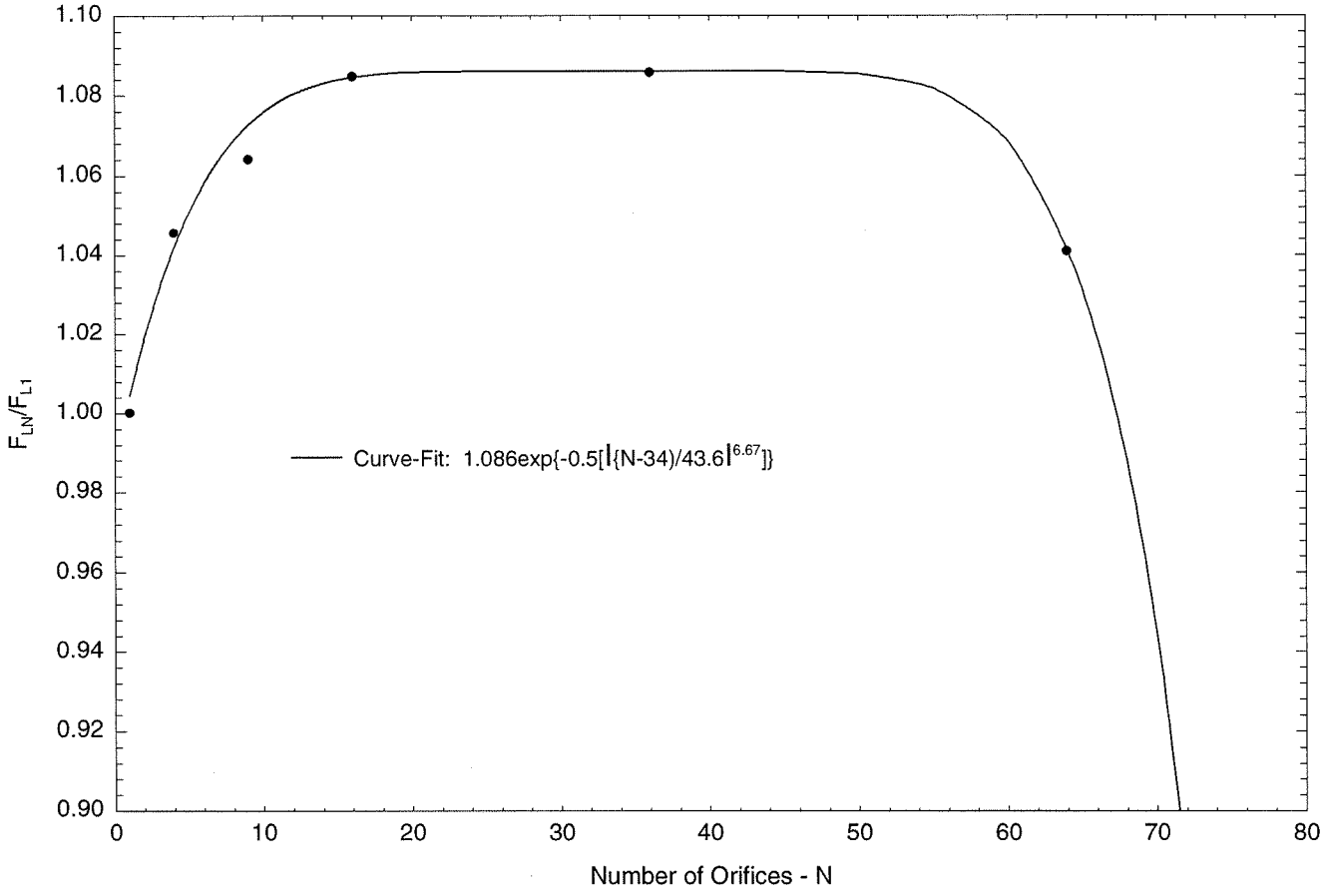

Figure 4. Effect of FacePlate Thickness-to-Orifice Diameter on Resonator Tuned Frequency

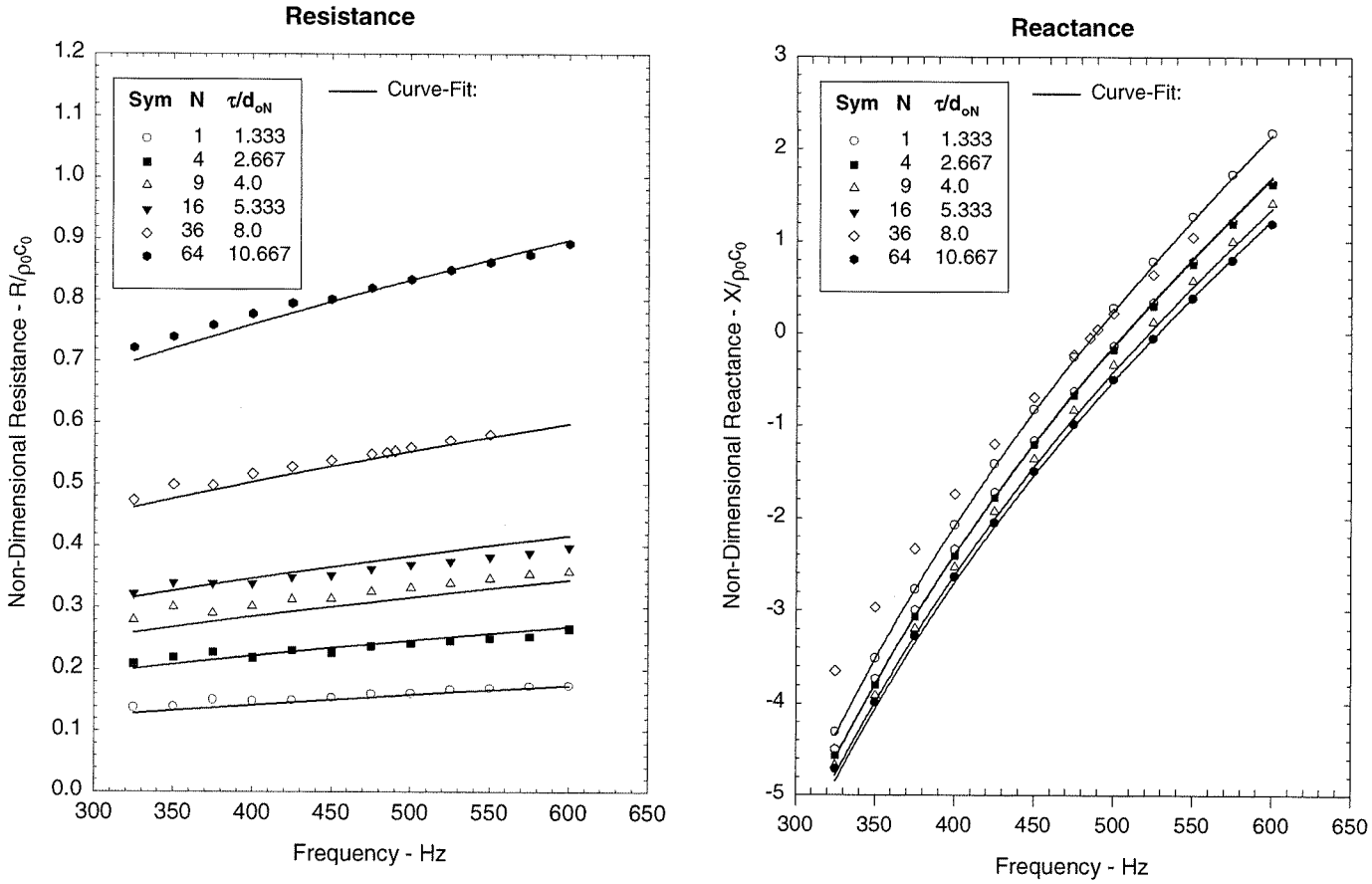

Figure 5. Measured and Predicted Effect of Orifice Number on Resonator Linear Impedance: SPL = 80 dB, V = 0

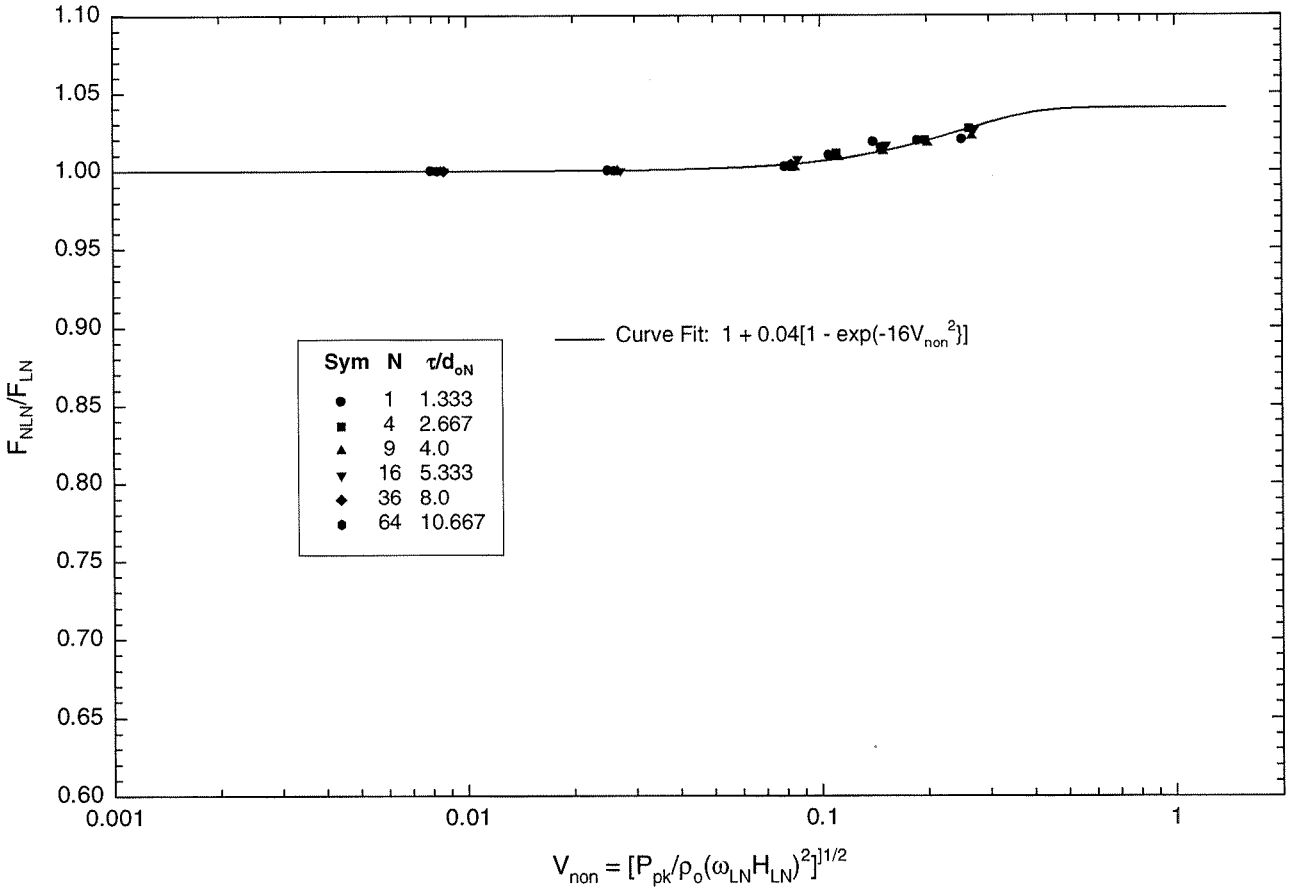

Figure 6. Effect of SPL and Orifice Number on Resonator Tuned Frequency; V = 0, $S_N/d_N = 2$

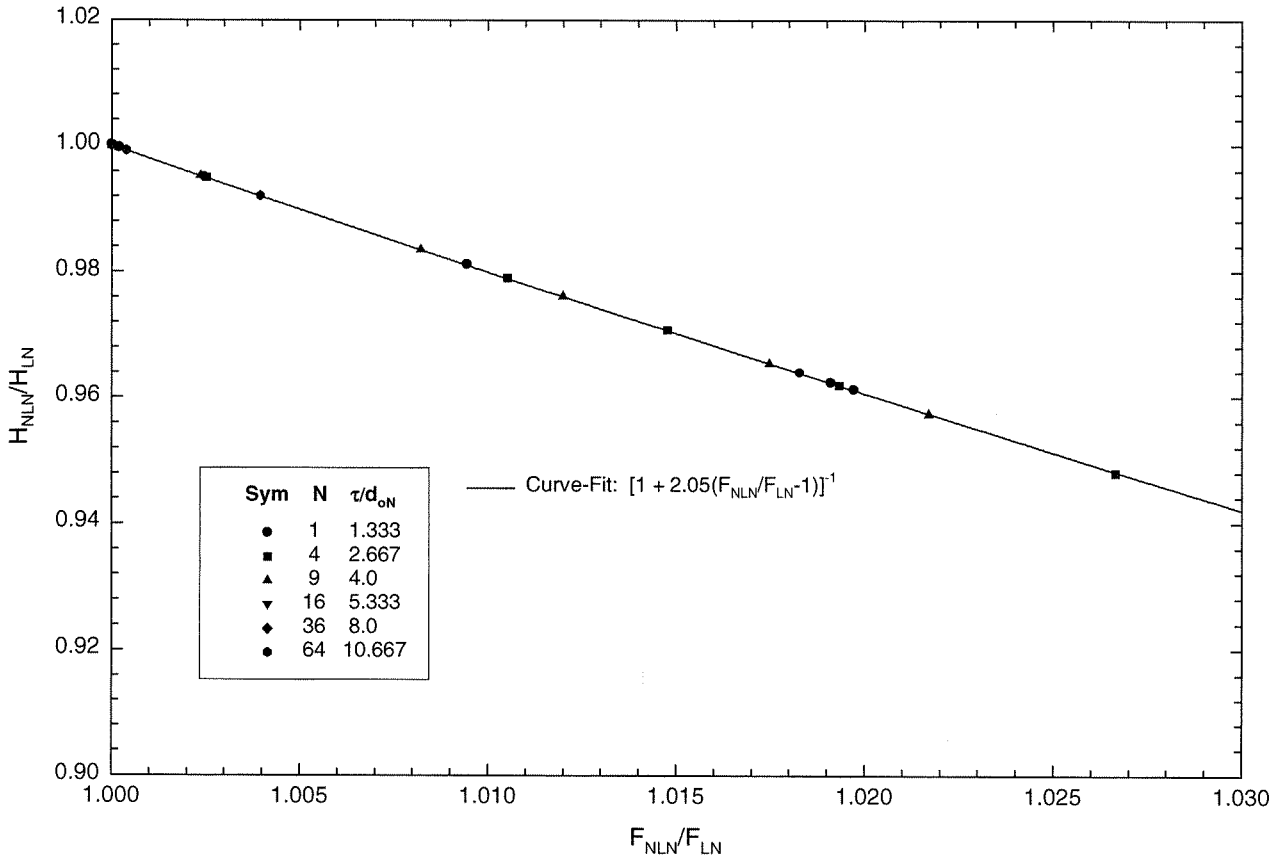

Figure 7. Correlation of Non-Grazing Flow Inertia Length Parameter in Terms of Tuned Frequency Parameter

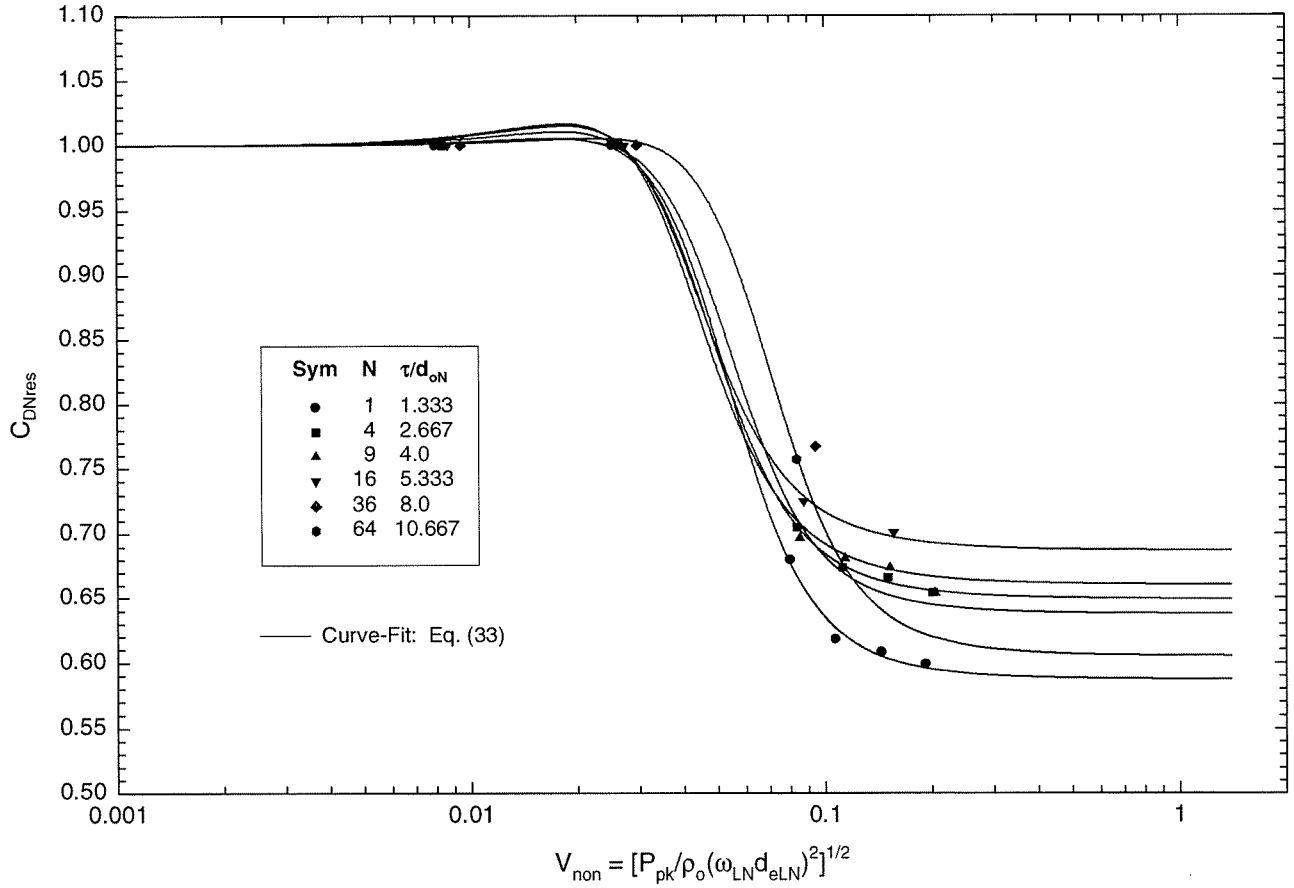

Figure 8. Effect of Orifice Number on Resonator Tuned Discharge Coefficient: V = 0, $S_N/d_N = 2$

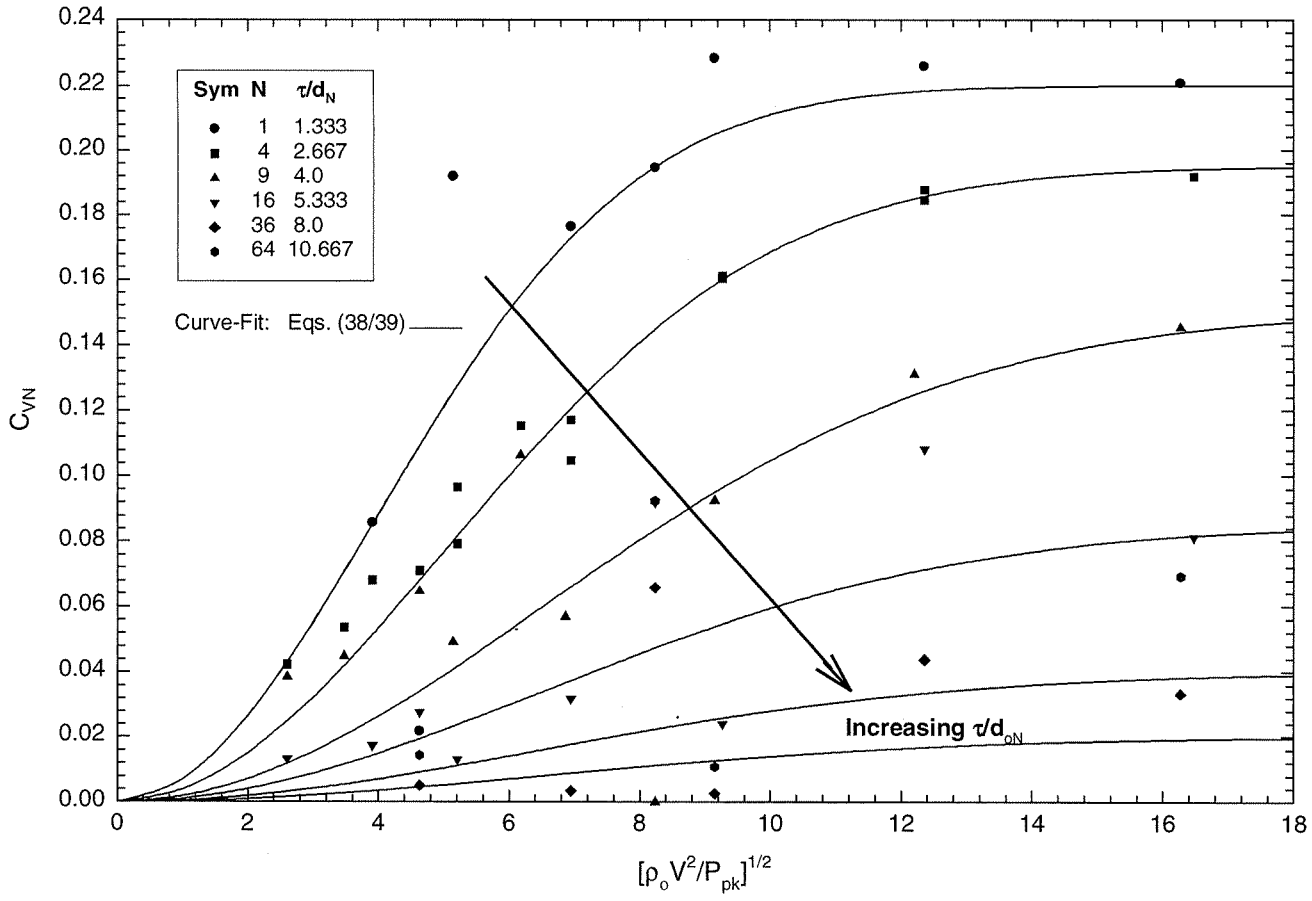

Figure 9. Effect of Orifice Number and Grazing Flow on Resonator Grazing Flow Parameter C_{VN}

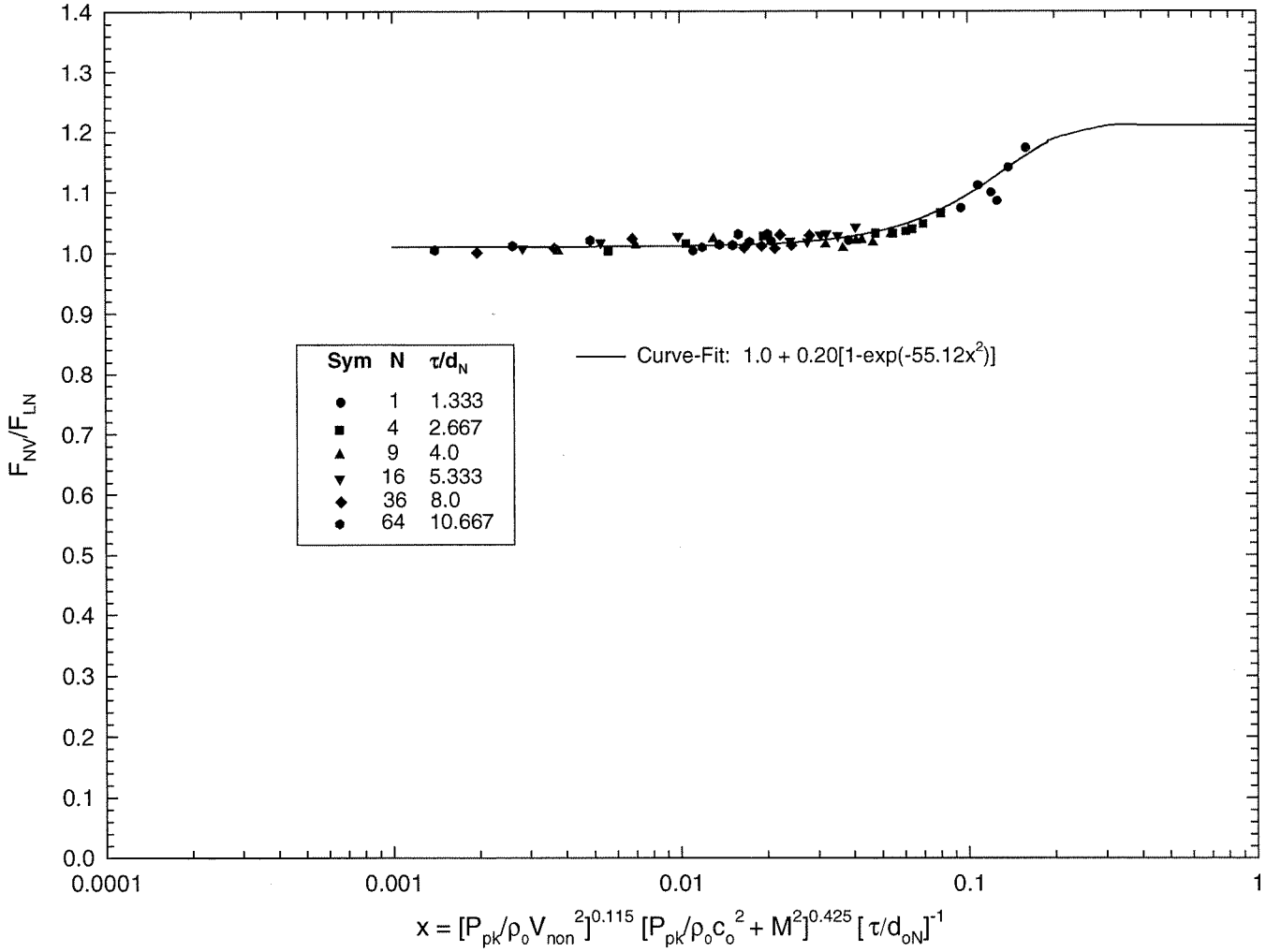

Figure 10. Effect of Orifice Size, SPL and Grazing Flow on Resonator Tuned Frequency

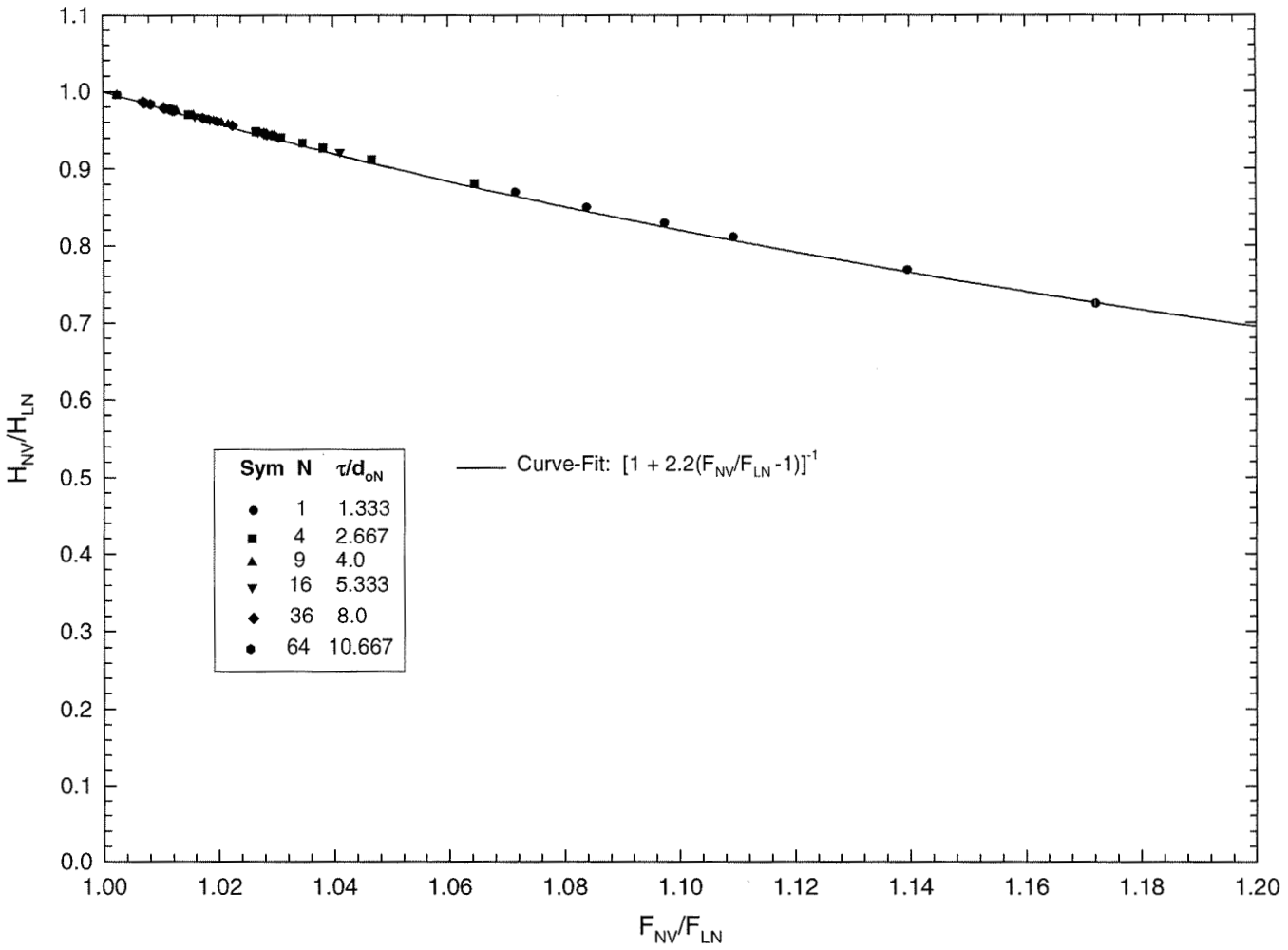

Figure 11. Correlation of Inertial Length Parameter in Terms of Tuned Frequency Parameter

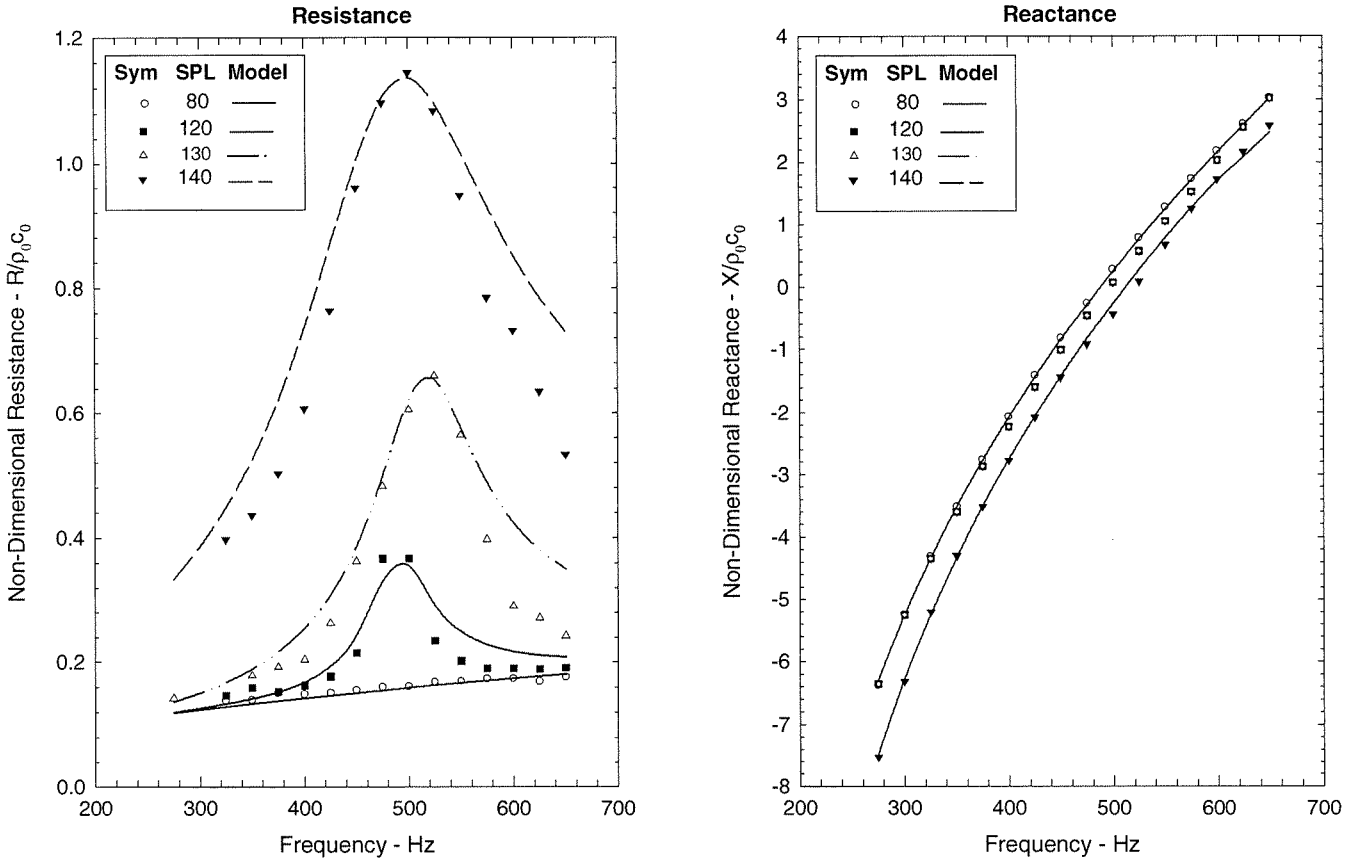

Figure 12a. Measured and Predicted Impedance of N = 1 Resonator Configuration: V = 0 and $S_N/d_{oN} = 2$

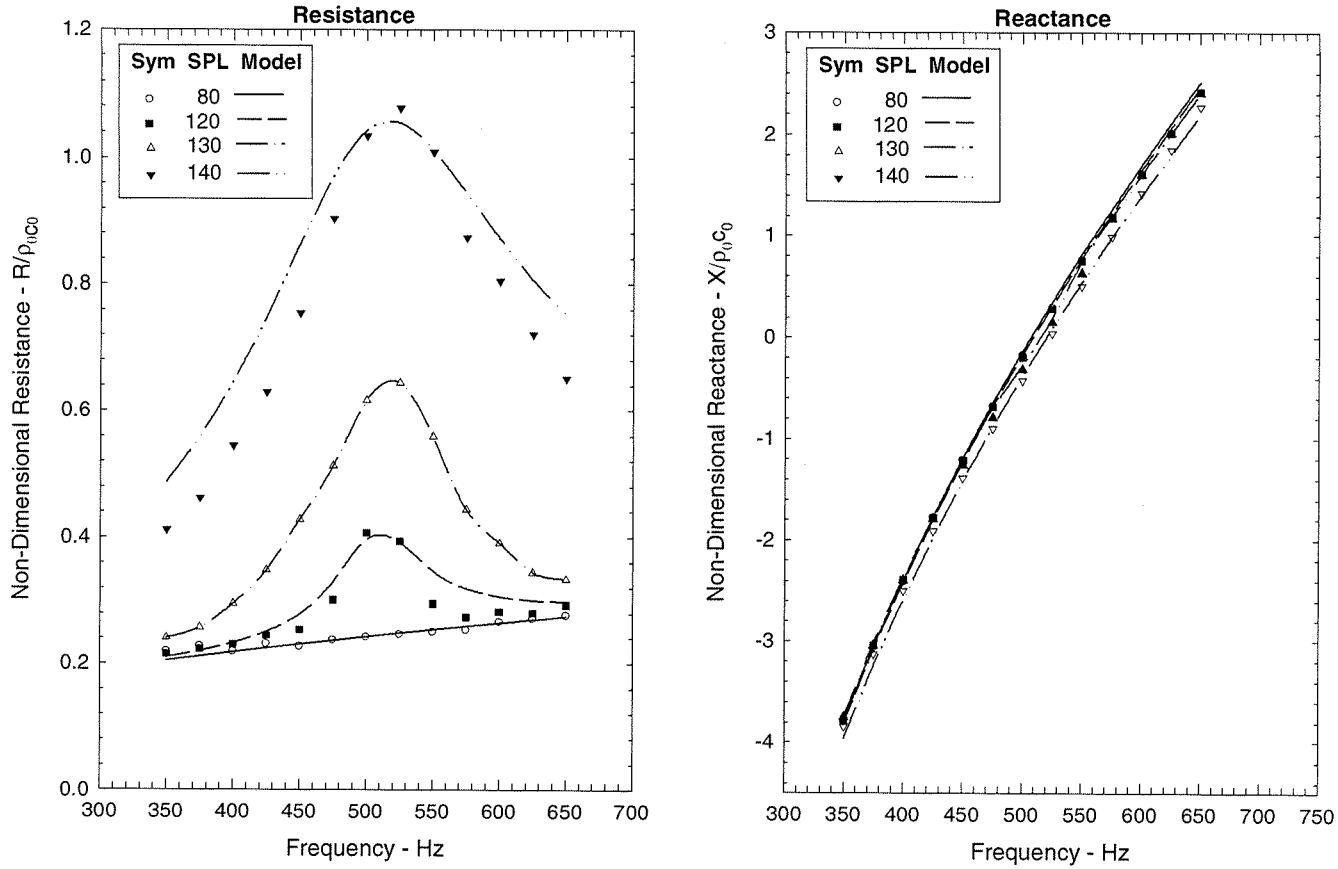

Figure 12b. Measured and Predicted Impedance of N = 4 Resonator Configuration: V = 0 and $S_N/d_{oN} = 2$

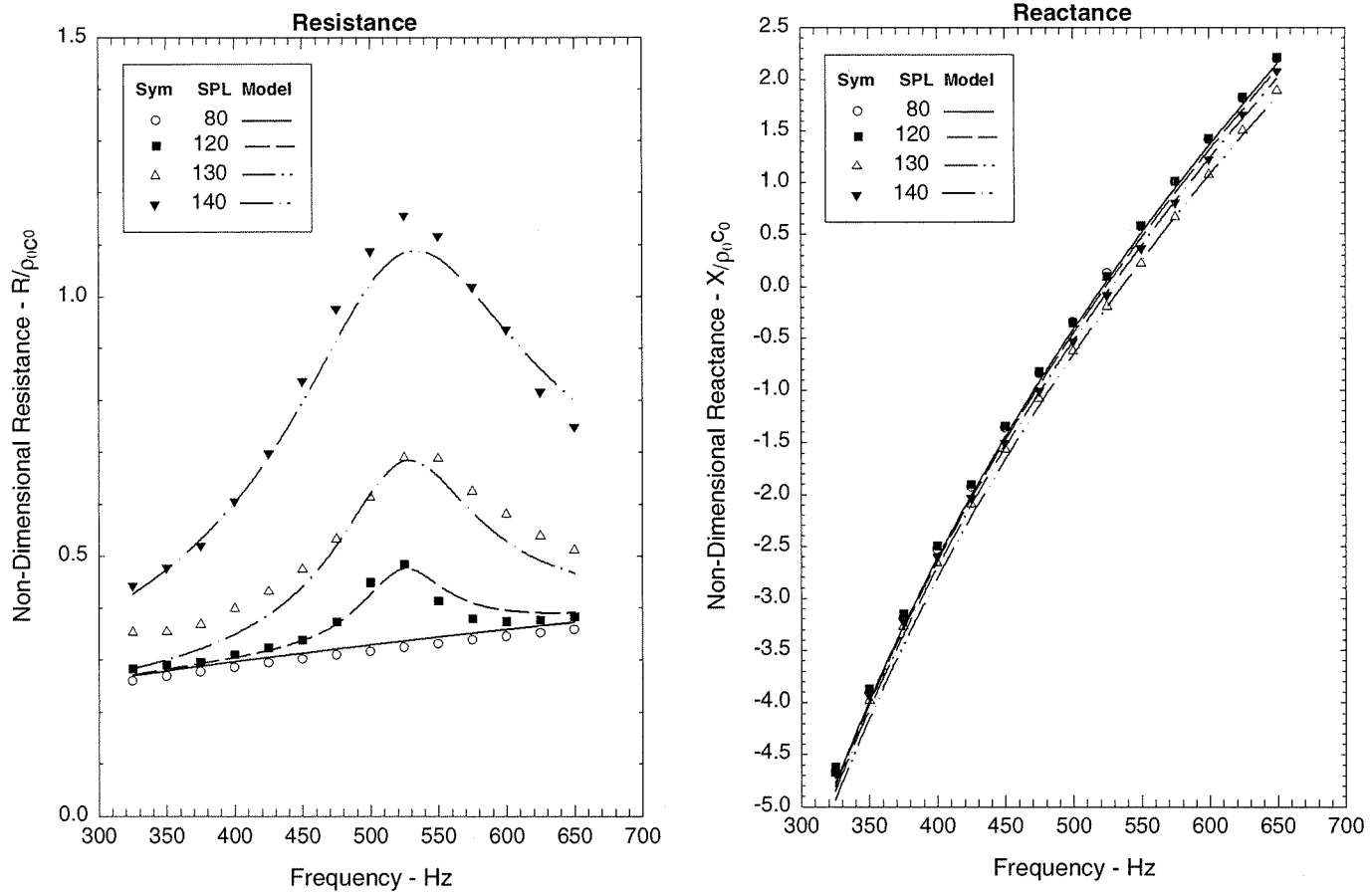

Figure 12c. Measured and Predicted Impedance of N = 9 Resonator Configuration: V = 0 and $S_N/d_{oN} = 2$

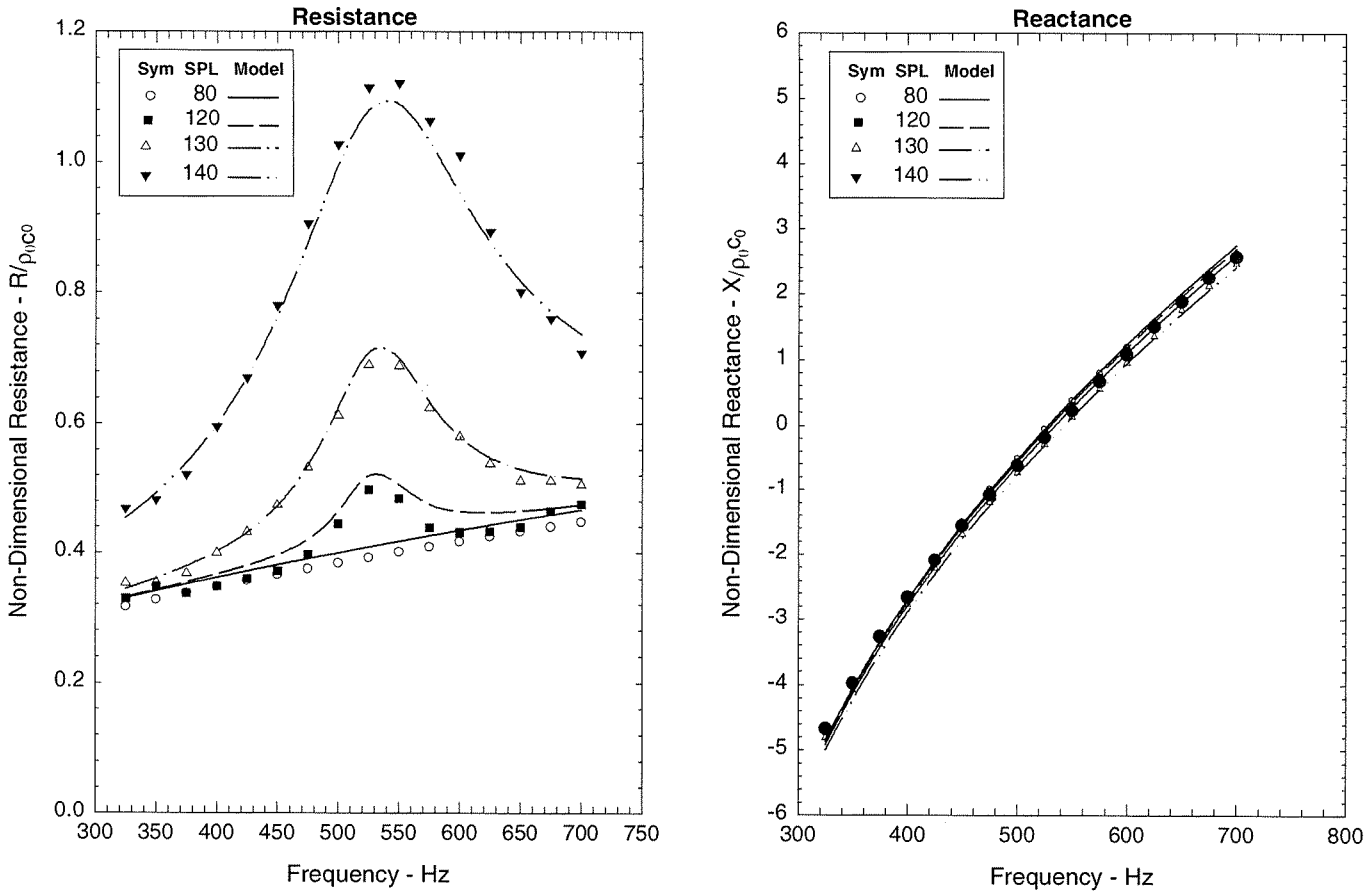

Figure 12d. Measured and Predicted Impedance of N = 16 Resonator Configuration: V = 0 and $S_N/d_{oN} = 2$

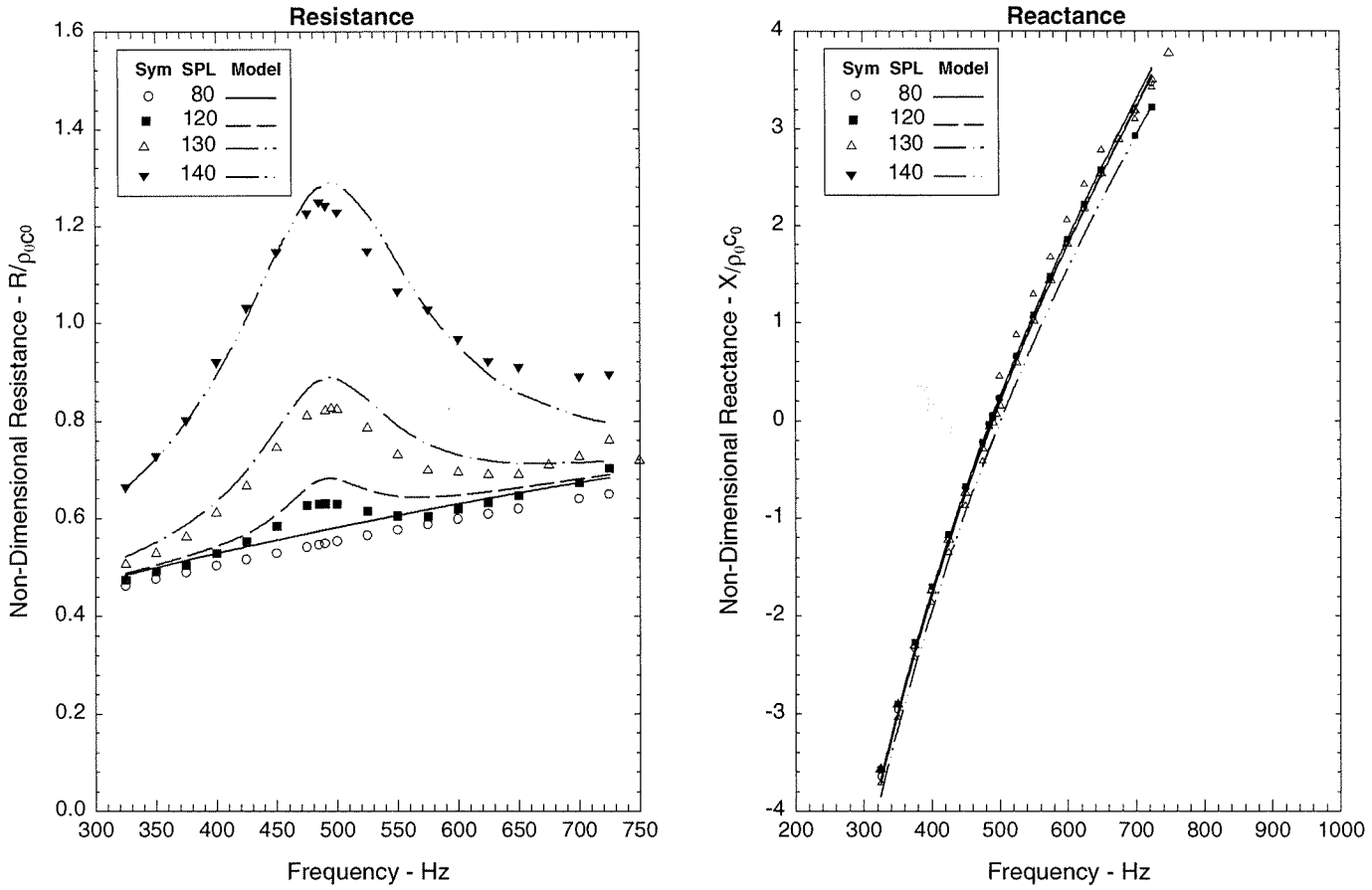

Figure 12e. Measured and Predicted Impedance of N = 36 Resonator Configuration: V = 0 and $S_N/d_{oN} = 2$

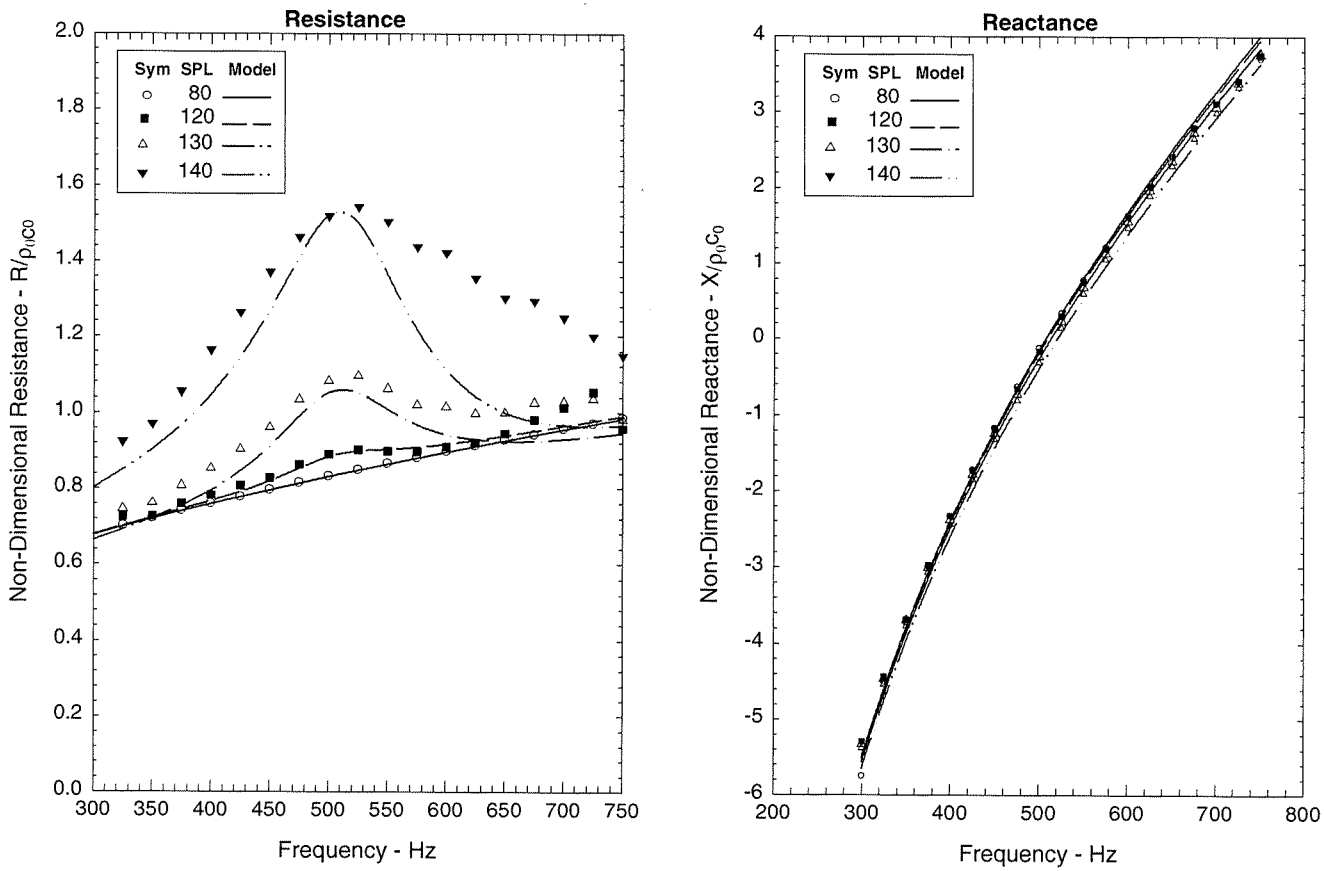

Figure 12f. Measured and Predicted Impedance of N = 64 Resonator Configuration: V = 0 and $S_N/d_{oN} = 2$

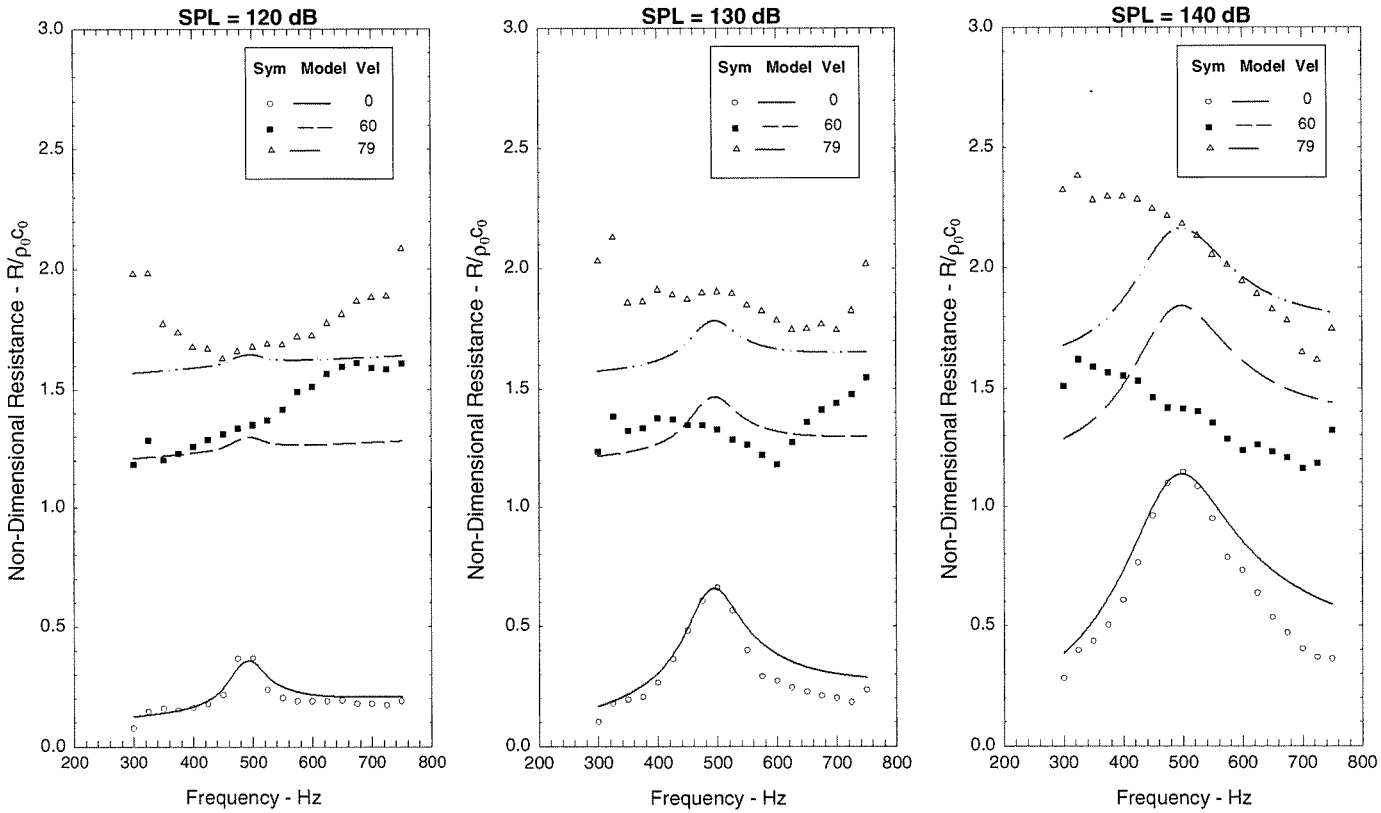

Figure 13a. Measured and Predicted Effect of Grazing Flow on Resistance of N = 1 Resonator

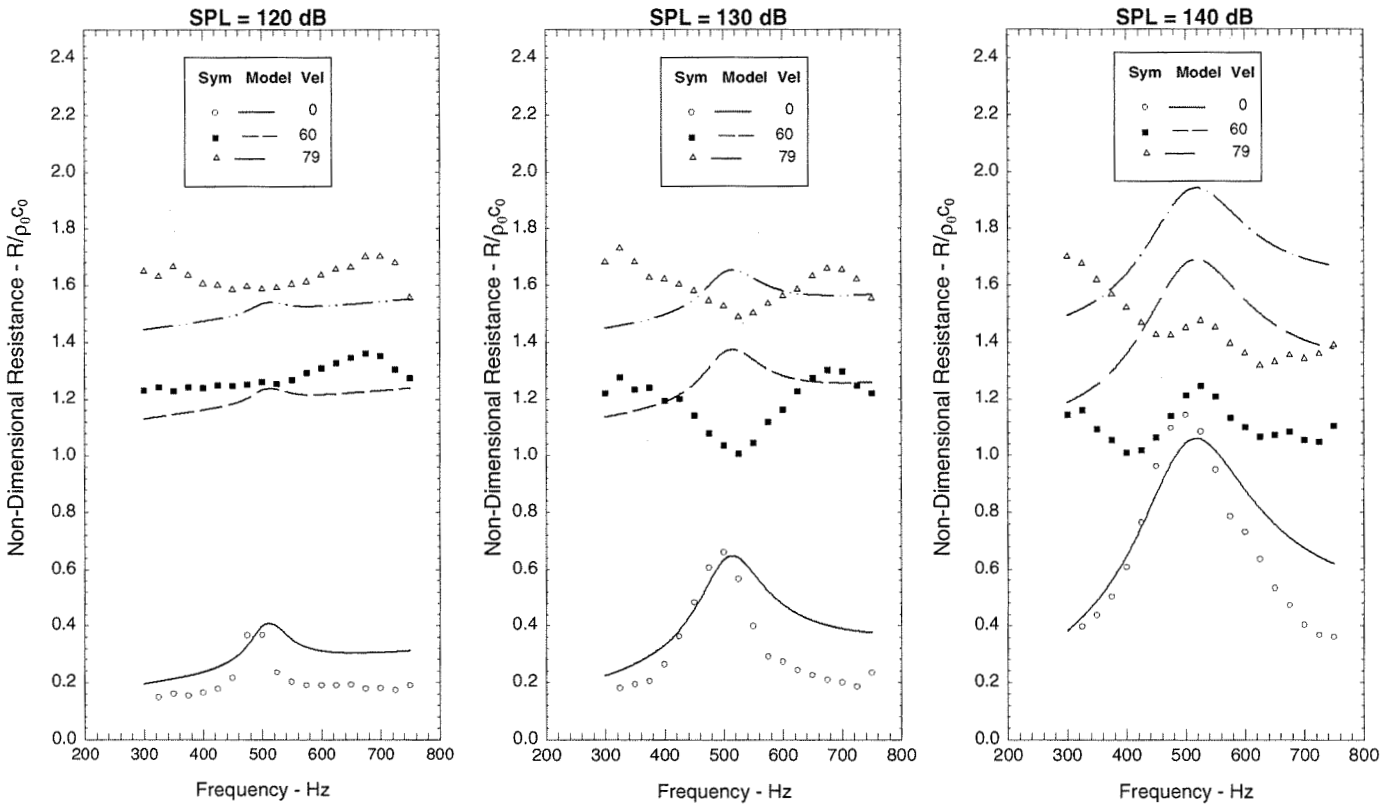

Figure 13b. Measured and Predicted Effect of Grazing Flow on Resistance of N = 4 Resonator

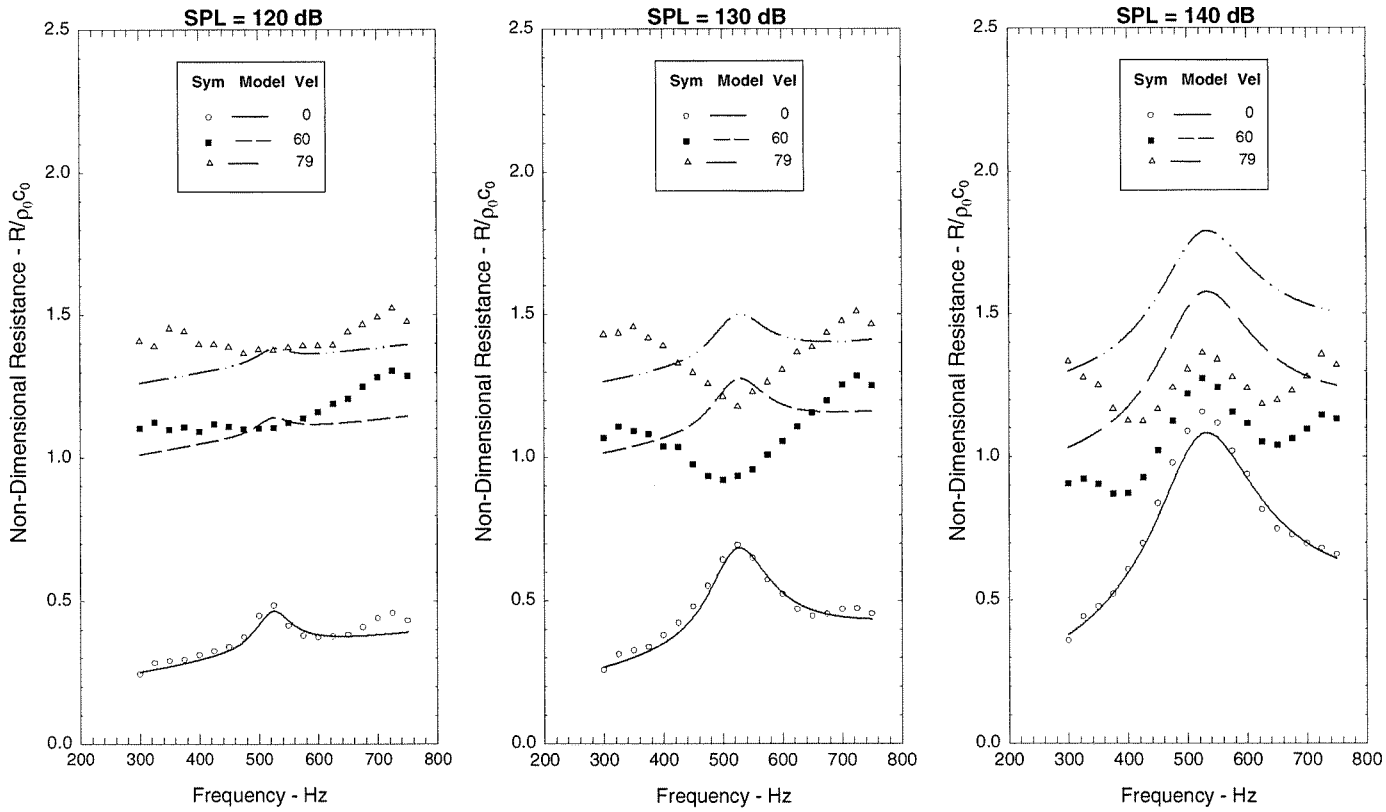

Figure 13c. Measured and Predicted Effect of Grazing Flow on Resistance of N = 9 Resonator

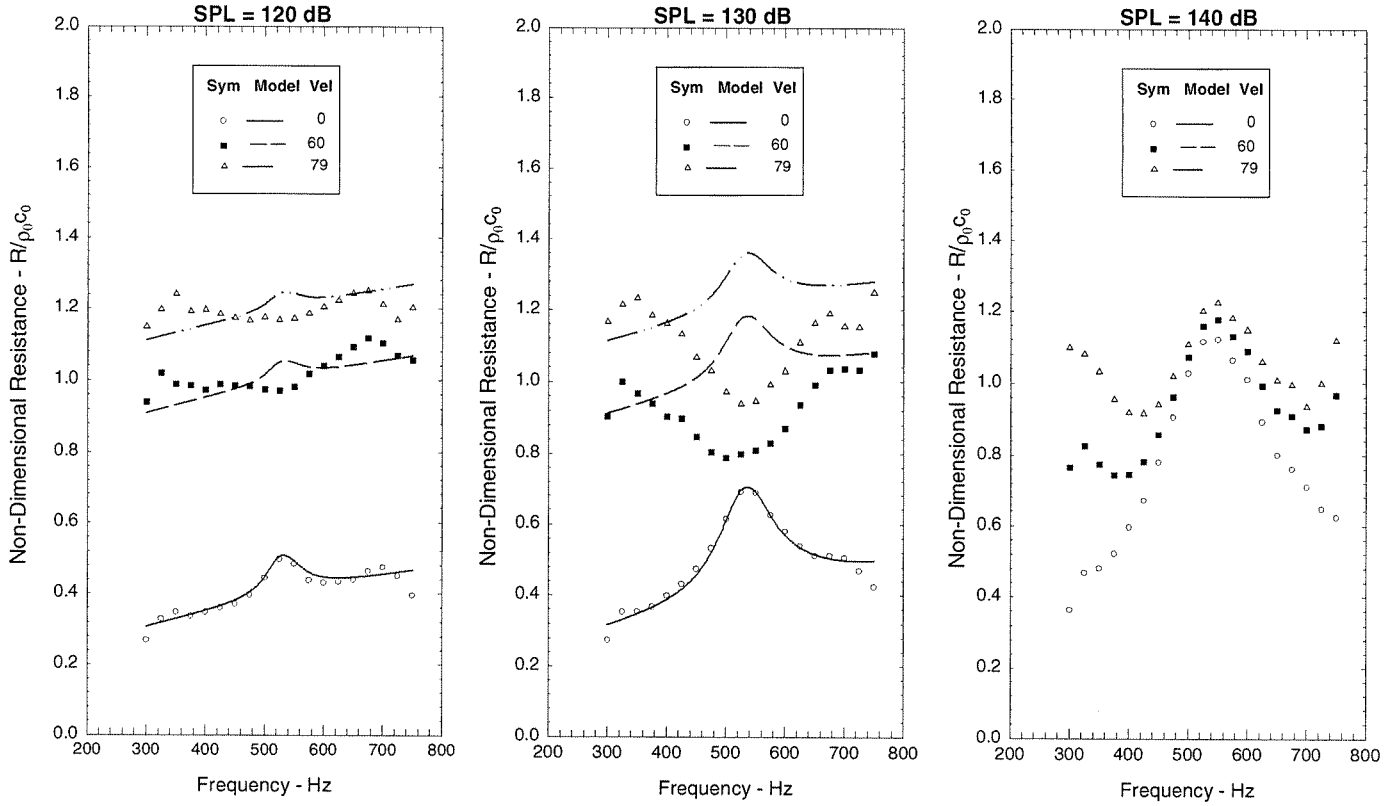

Figure 13d. Measured and Predicted Effect of Grazing Flow on Resistance of N = 16 Resonator

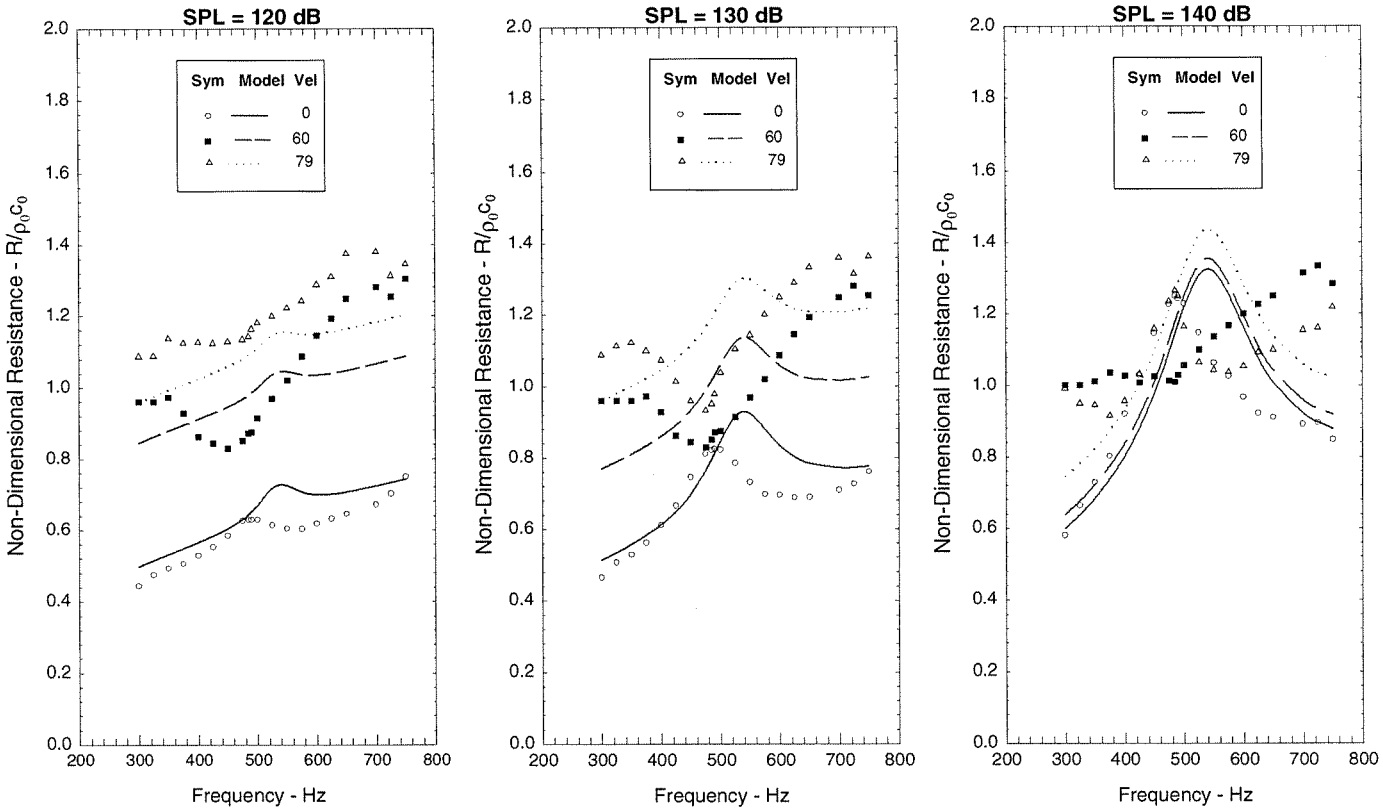

Figure 13e. Measured and Predicted Effect of Grazing Flow on Resistance of N = 36 Resonator

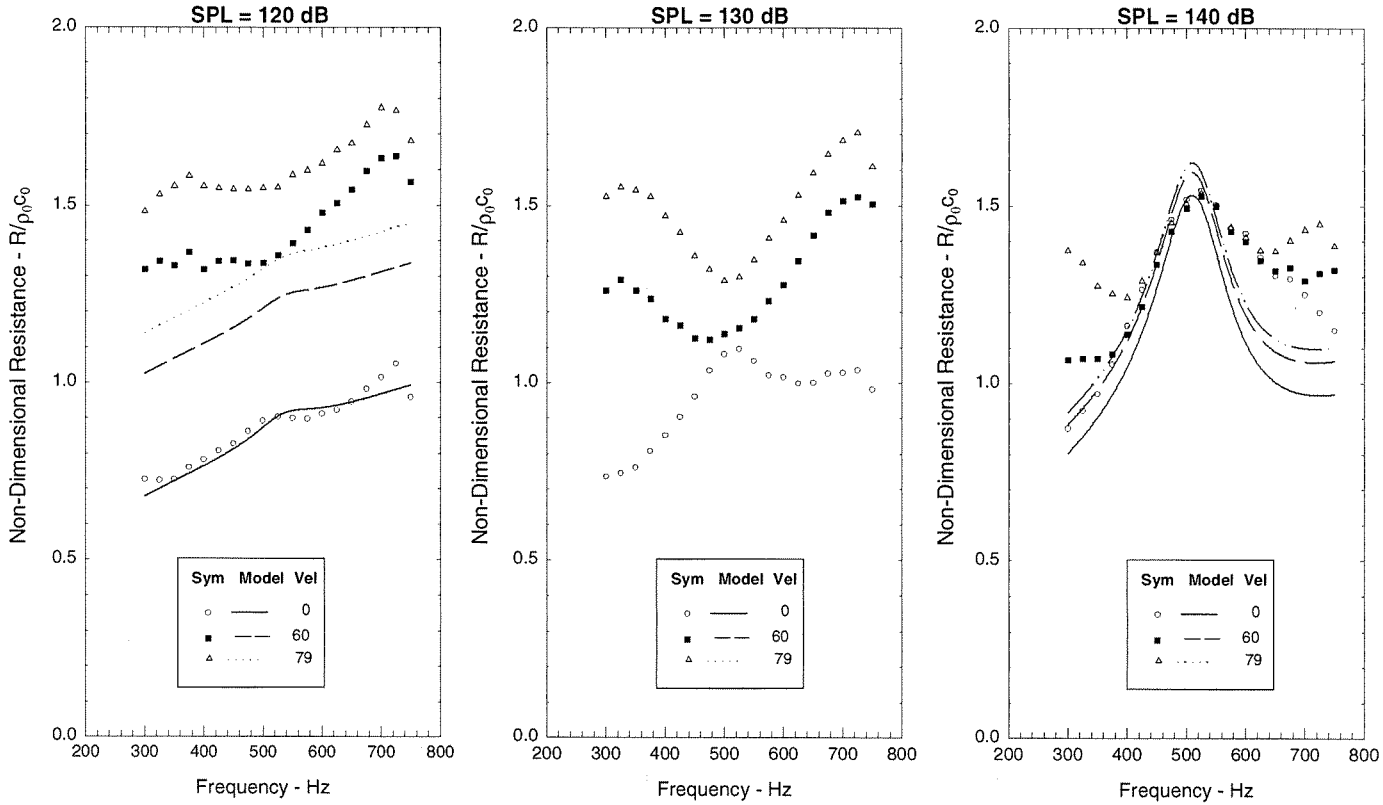

Figure 13f. Measured and Predicted Effect of Grazing Flow on Resistance of N = 64 Resonator

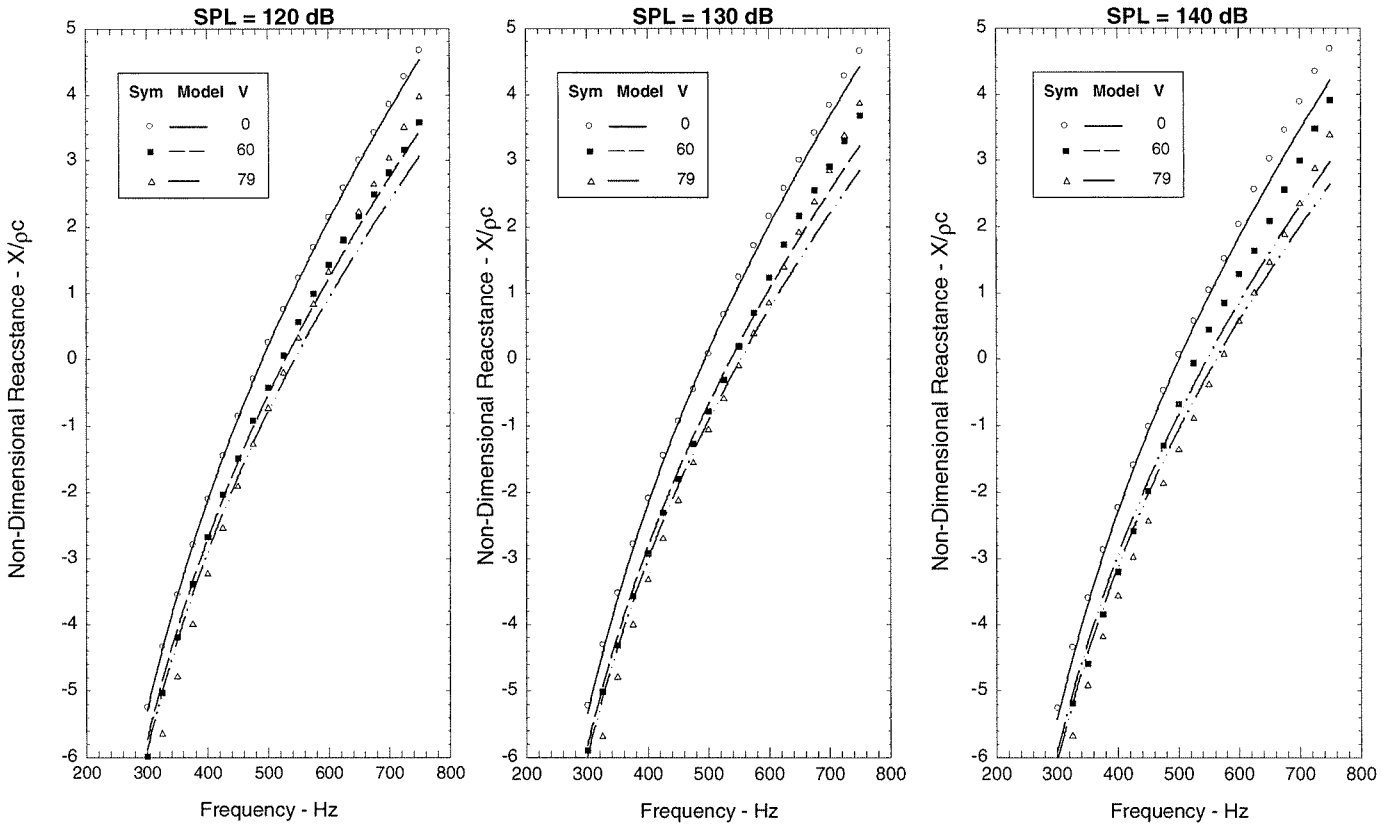

Figure 14a. Measured and Predicted Effect of Grazing Flow on Reactance of N = 1 Resonator

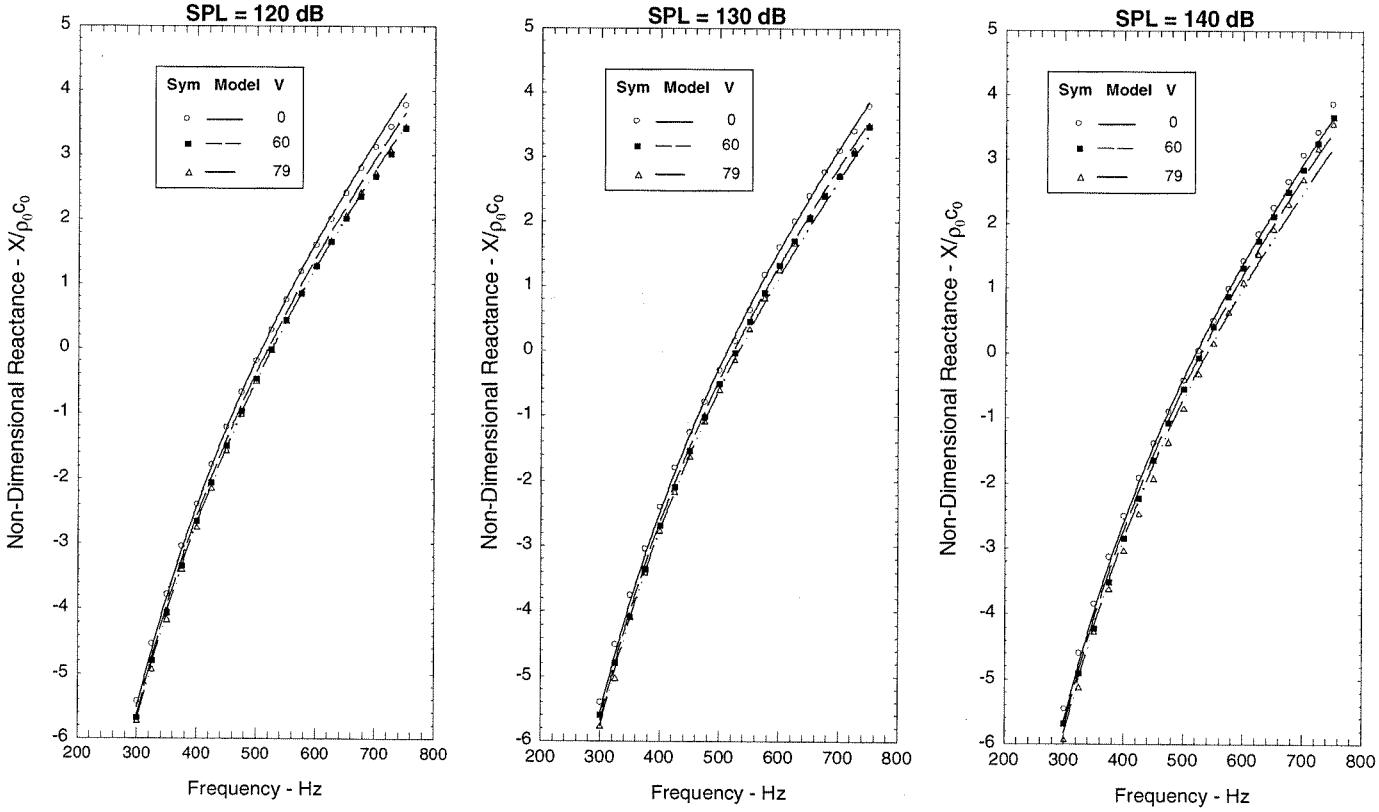

Figure 14b. Measured and Predicted Effect of Grazing Flow on Reactance of N = 4 Resonator

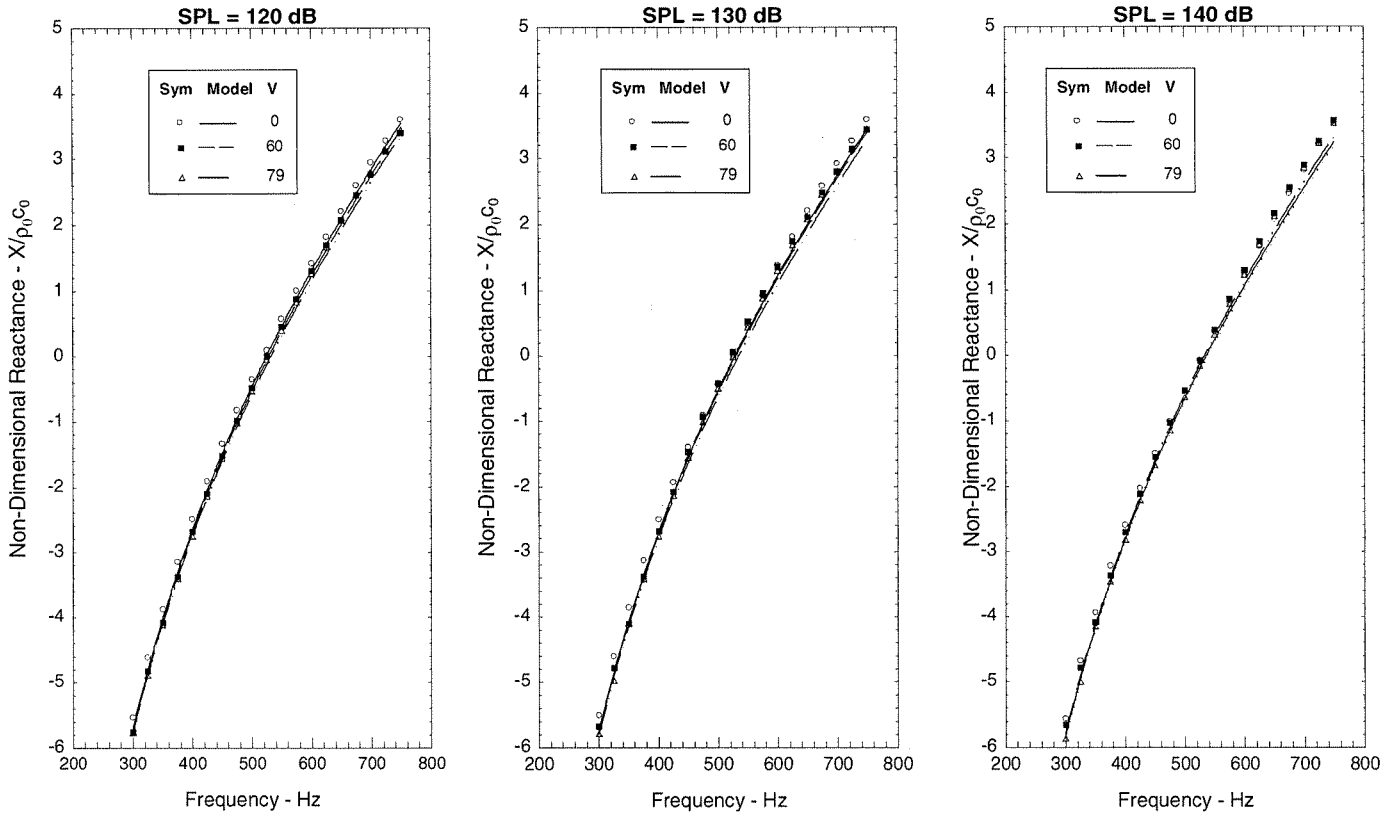

Figure 14c. Measured and Predicted Effect of Grazing Flow on Reactance of N = 9 Resonator

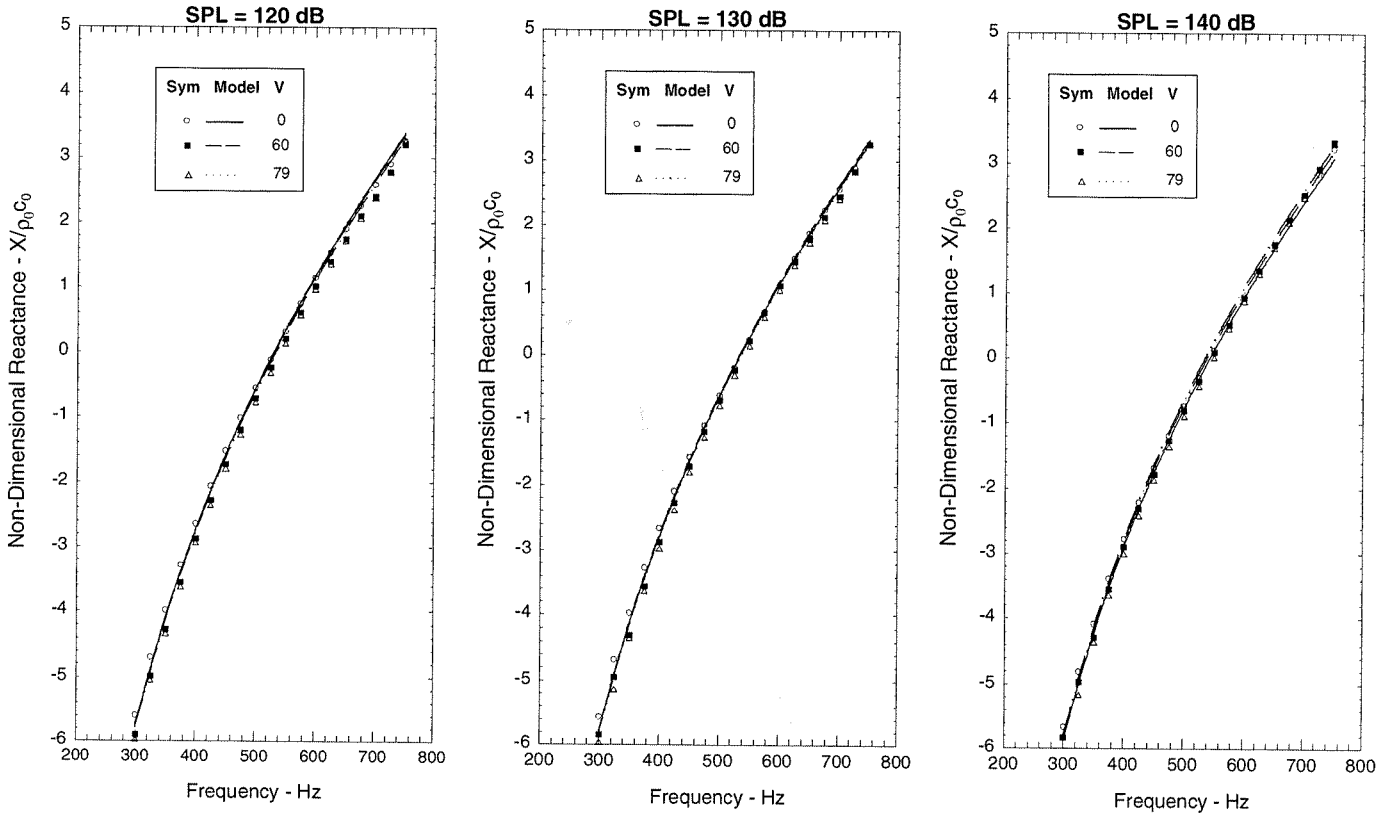

Figure 14d. Measured and Predicted Effect of Grazing Flow on Reactance of N = 16 Resonator

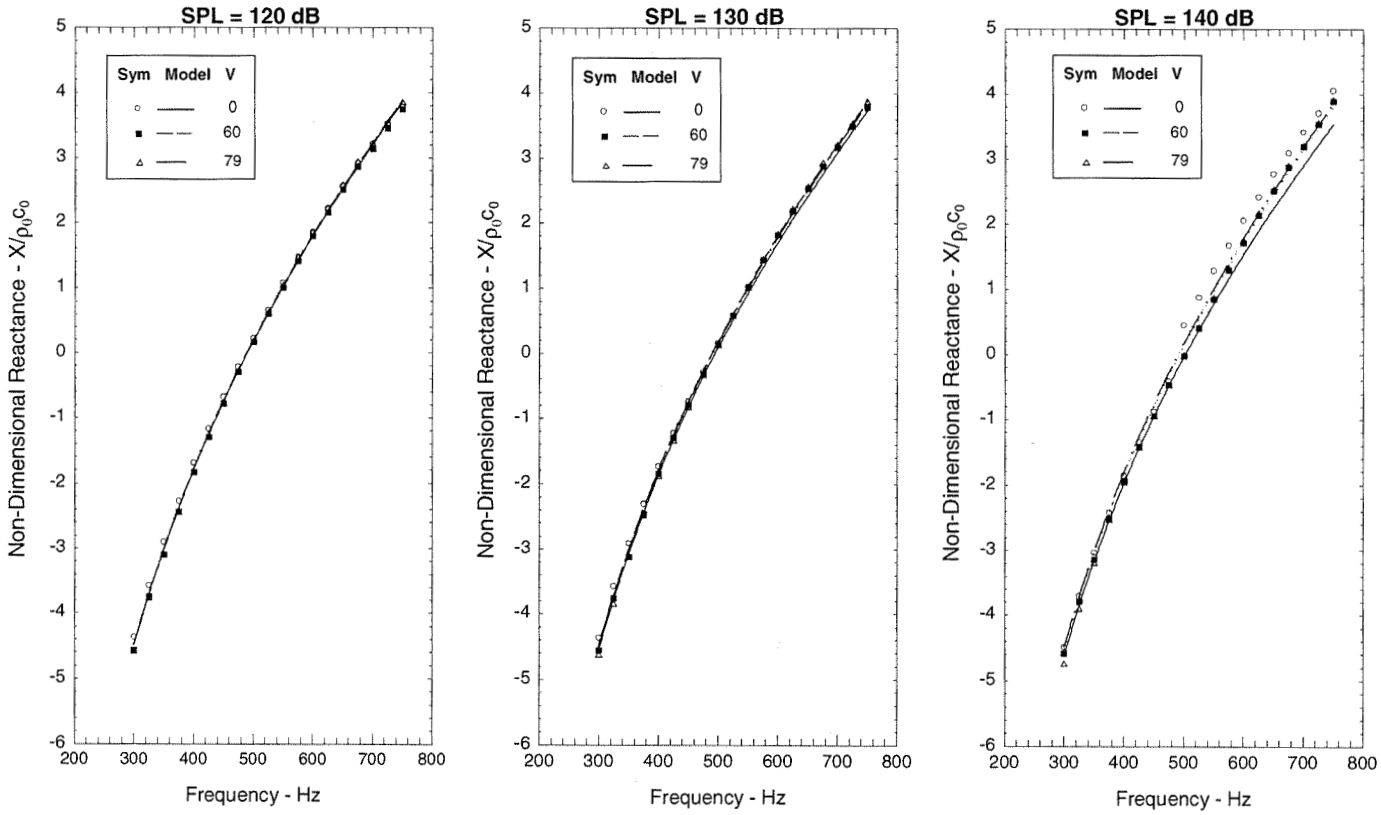

Figure 14e. Measured and Predicted Effect of Grazing Flow on Reactance of N = 36 Resonator

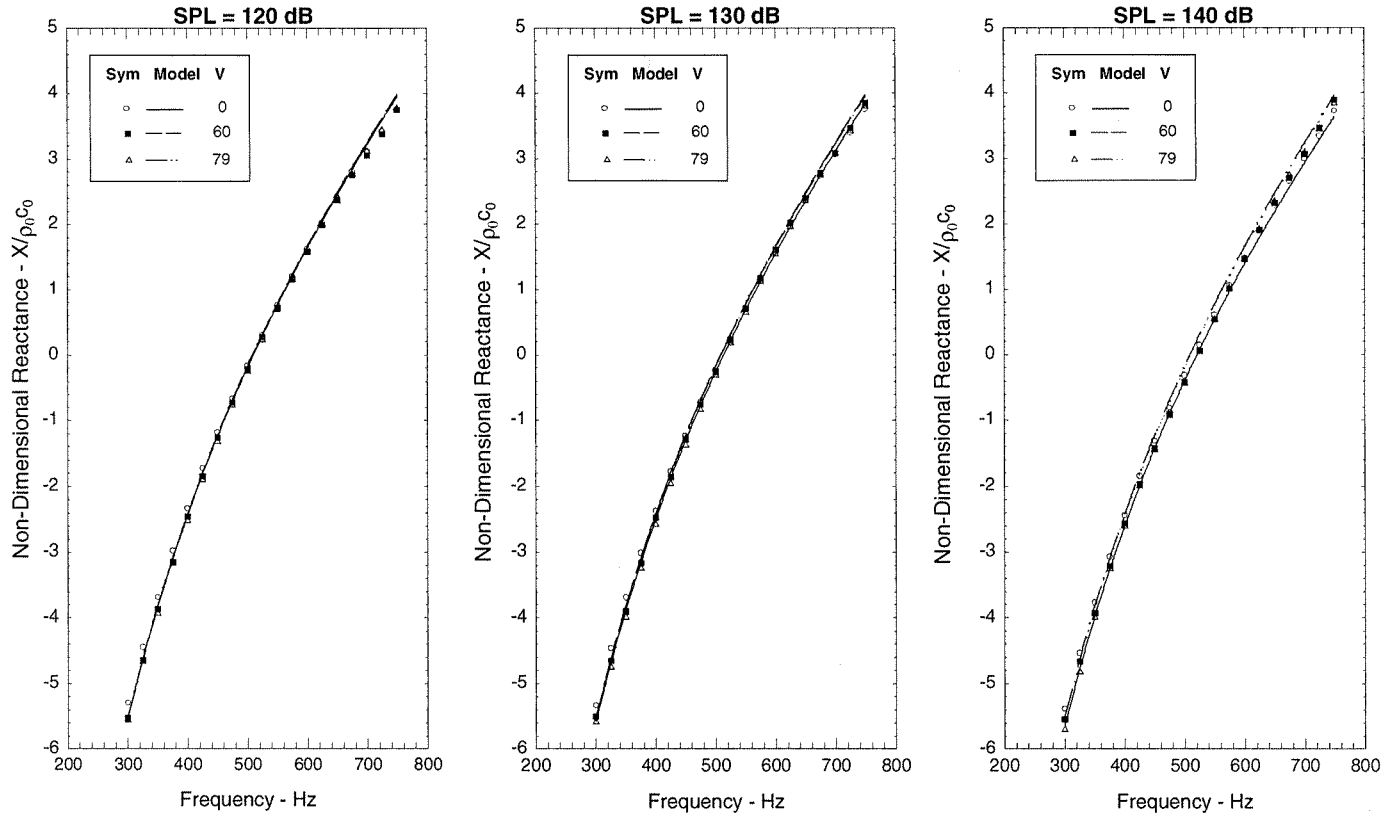

Figure 14f. Measured and Predicted Effect of Grazing Flow on Reactance of N = 64 Resonator

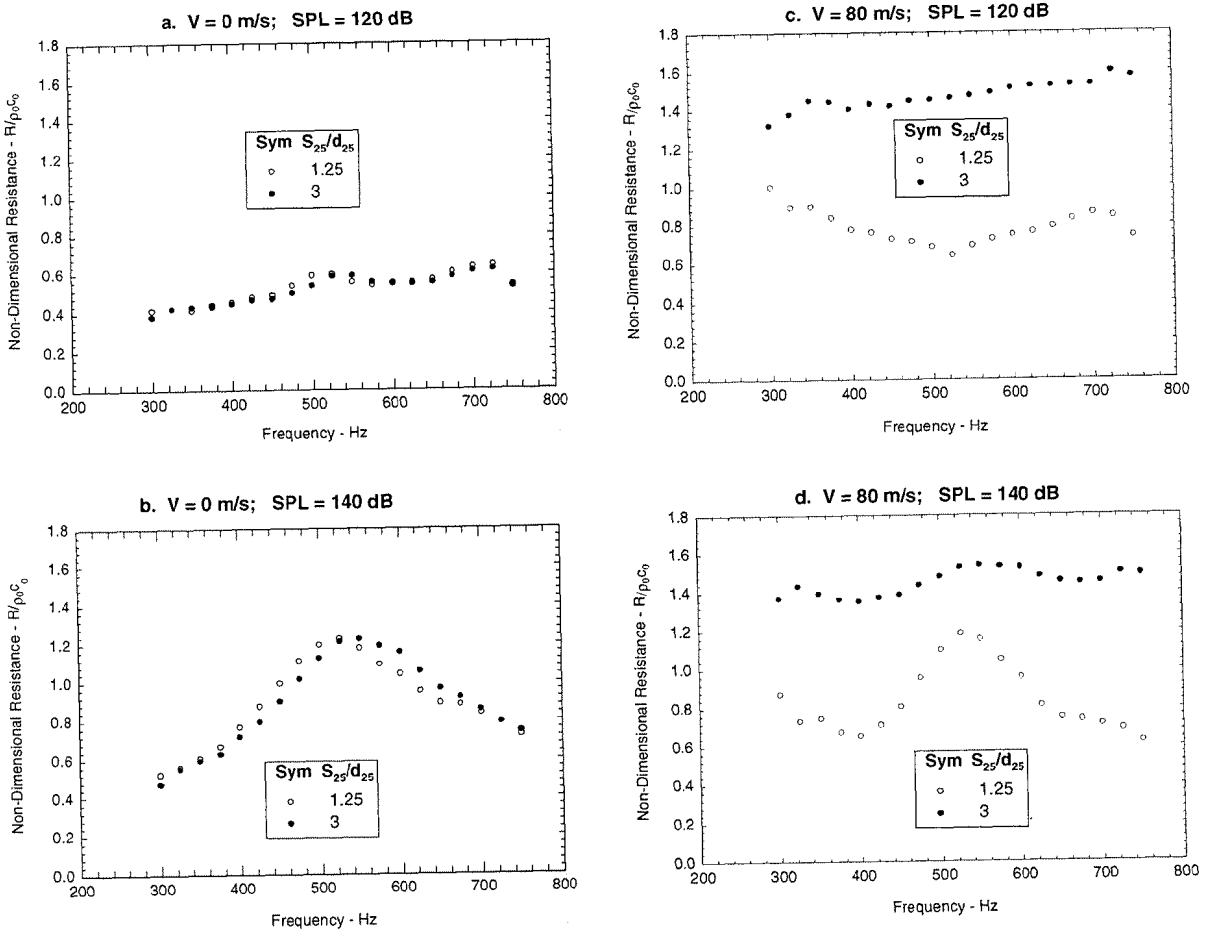

Figure 15. Effect of Array on Resistance of N = 25 Resonator

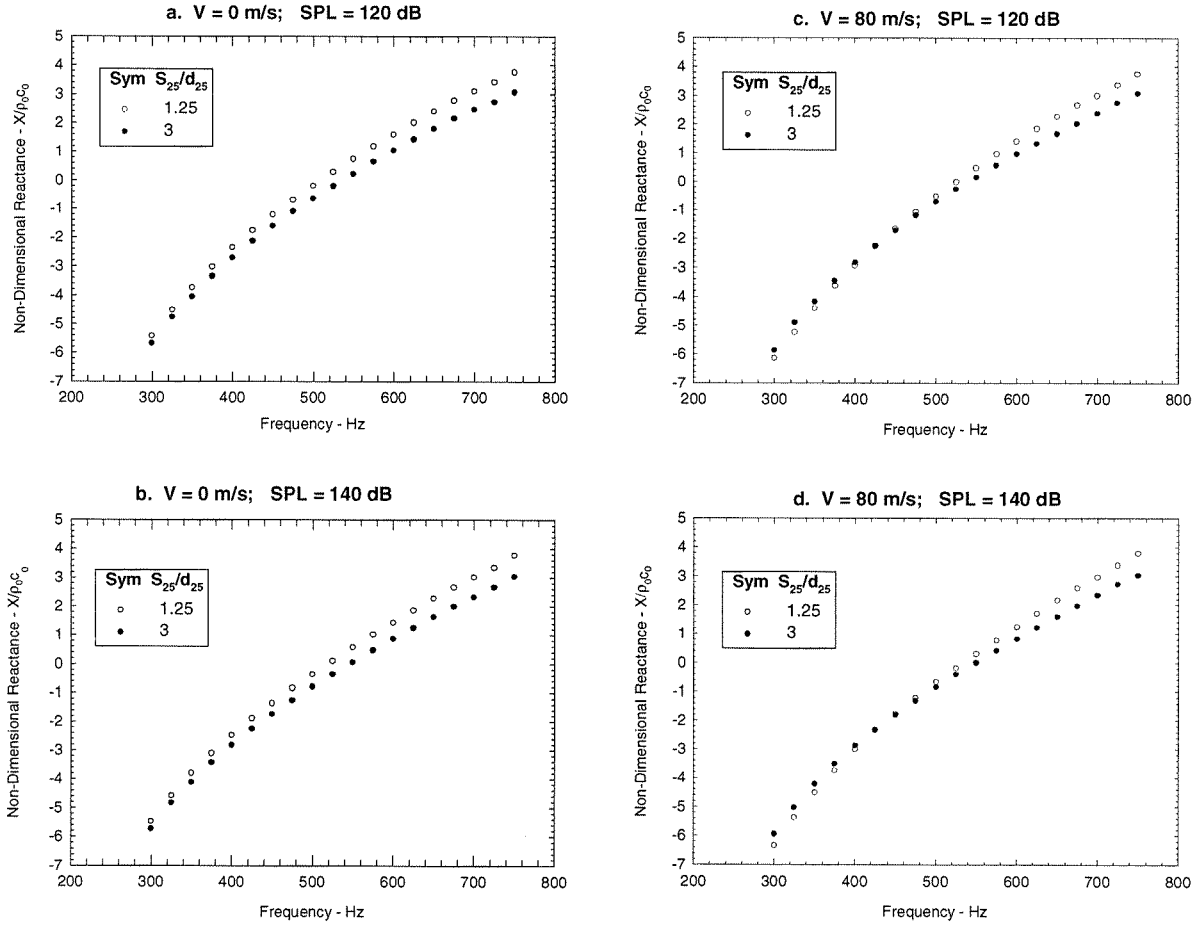

Figure 16. Effect of Array Spacing on Reactance of N = 25 Resonator

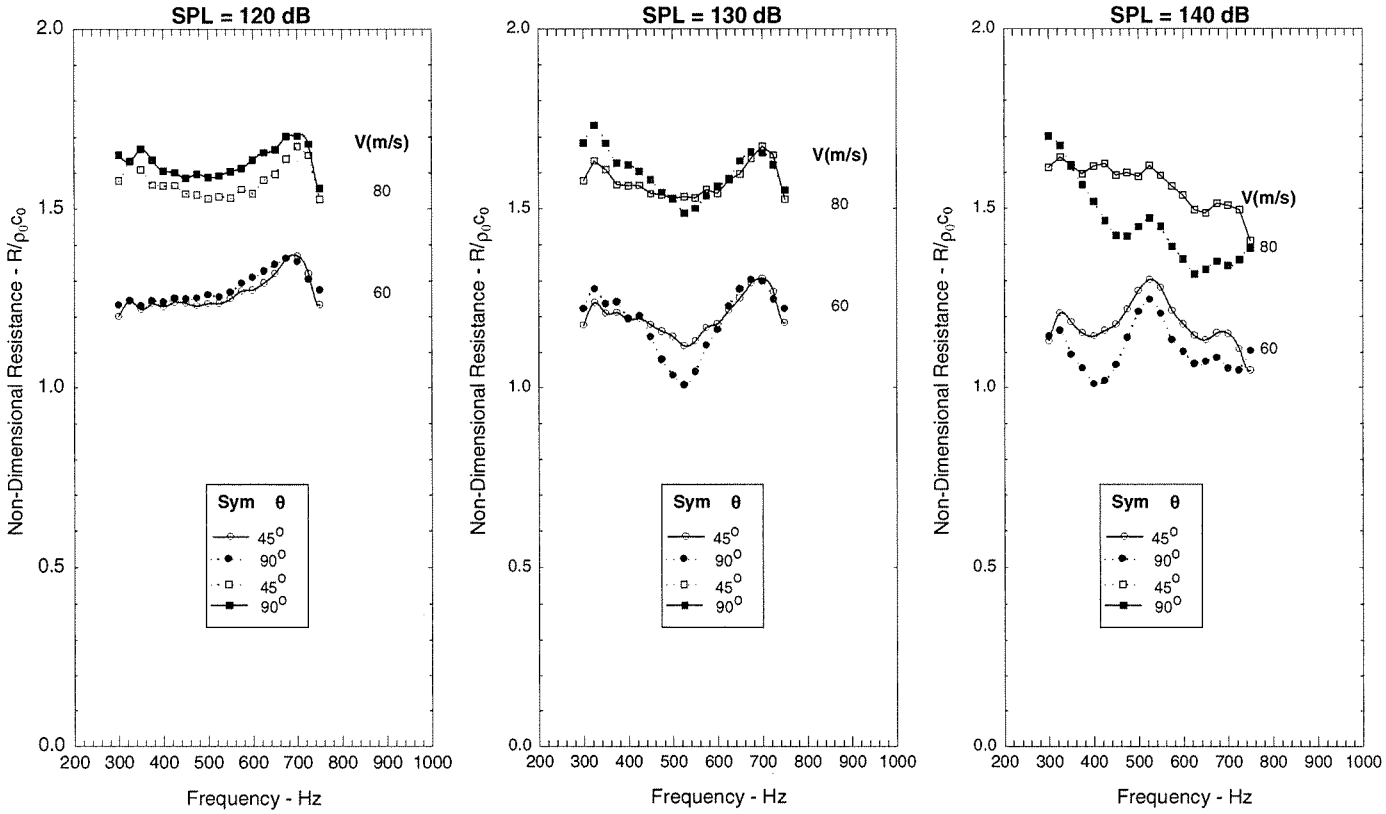

Figure 17. Effect of Rotating Array 45^0 on Resistance of N = 4 Resonator Configuration

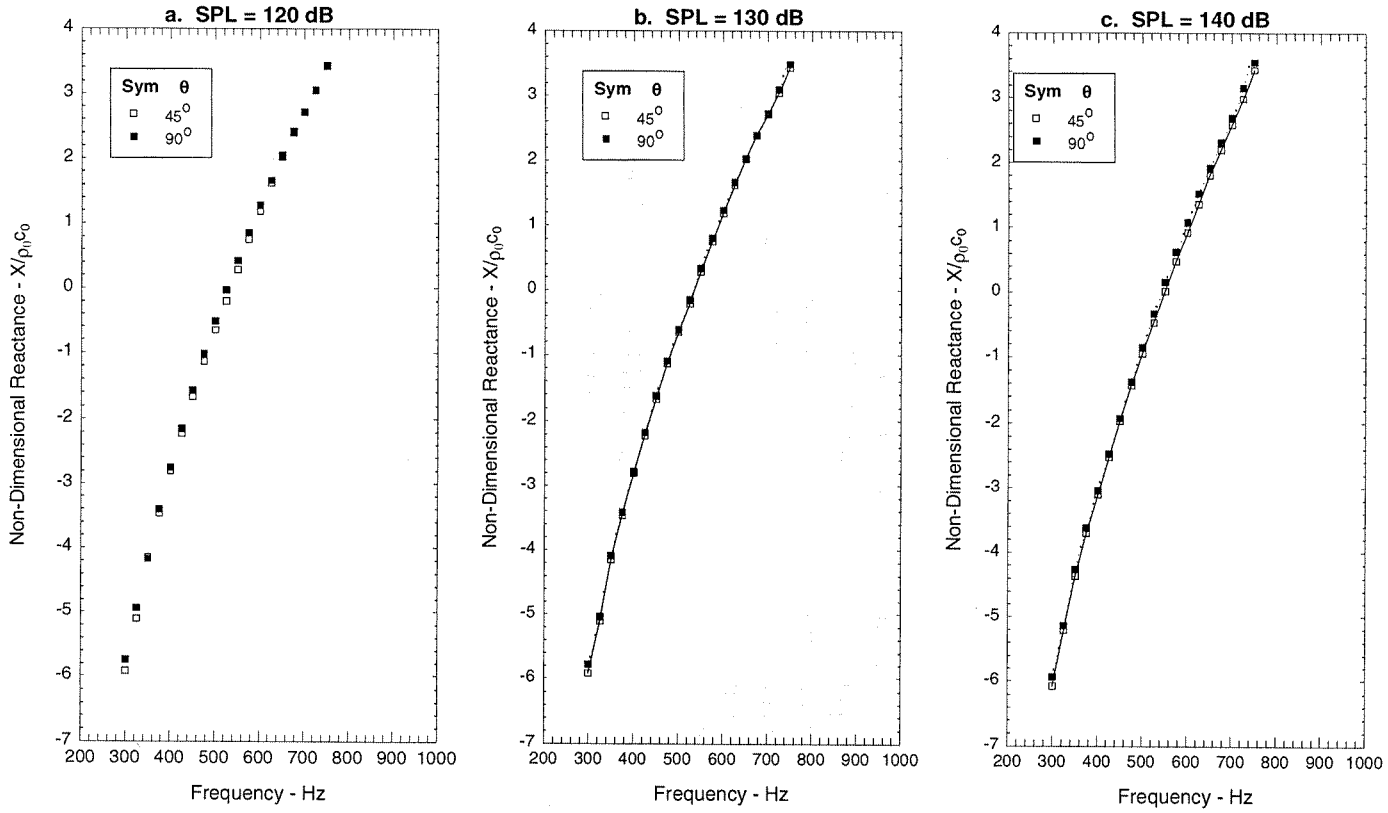

Figure 18. Effect on Rotating Array 45^0 on Reactance of N = 4 Resonator Configuration: V = 80 m/s

Appendix 4 - Extended Reaction Lining Study

INTRODUCTION.

Current nacelle acoustic liners are designed around the assumption of local reaction. That is, the impedance at a given point on the liner only responds to the acoustic and flow conditions in its immediate vicinity (with the region small compared to the acoustic wavelength). This assumption has been shown to hold for presently installed liners which are typically made up of a face sheet and one or more layers of honeycomb cells.

A correctly designed single layer locally reacting liner will provide the best possible attenuation for a single mode at the design frequency. The attenuation bandwidth can then be increased by adding additional layers, but the locally reacting liner can only be optimized for one mode (or incidence angle).

The purpose of this study is to investigate the potential for attaining additional improvements in attenuation, relative to the locally reacting case, by allowing acoustic propagation inside the liner. In a duct, a phase difference exists between neighboring cells. The phase difference is a function of incidence angle (effectively mode number at a given frequency, as each mode can be thought of as striking the liner at a different incidence) and the spatial separation between cells. This phase difference leads to a varying pressure distribution down the two neighboring cells, which, in turn, will drive the 'in-liner' propagation for acoustically connected cells.

The ideal outcome would be for any additional attenuation gains attained by extended reaction to compensate for the replacement of mesh facing sheet single layer liners with more durable perforated facing sheet liners. Locally reacting mesh liners have better (broader) attenuation profiles than perforate liners.

The questions investigated by this work are two-fold, with the common goal of designing a test to investigate the most promising extended reaction designs. These are,

1. Does the extended reaction concept exhibit any potential for liner optimization for more than one mode, given that different modes will have different phase relationships between neighboring cells (because of their differing incidence angles)?

2. Is there a potential for increased attenuation bandwidth?

Two approaches have been adopted. The first involves the validation and investigation of two codes designed to predict the impedance of an experimental configuration, with two cells linked by a resistive element, and the phase of the source to each being independently controlled. These codes can then be used to model a finite length non-locally reacting liner, where, as previously stated, a phase difference exists between neighboring cells.

The second study is being performed using the Boeing liner optimization and duct attenuation program (MELO). The code is being used to investigate the modal duct

attenuation of various configurations of extended reaction liners, with downstream propagation only.

NORTHROP-GRUMMAN DOUBLE IMPEDANCE TUBE STUDY.

Test Setup

Northrop-Grumman has designed a dedicated test to investigate the acoustic behavior of non-locally reacting cells, using a concept suggested by Ron Olsen of Boeing. They have constructed a double impedance tube arrangement which can determine the acoustic impedance of two neighboring cells with the common wall linked via a resistive mesh. The cell samples are 1.5" square and 1.42" deep. Fig 1 shows a sketch of the set-up.

The SPL and phase of the sound incident on each cell can be independently controlled. A phase difference in the incident sound at each cell leads to a pressure difference across the common wall, varying with frequency. This pressure gradient will drive sound through the common wall resistive layer, leading to a change in the surface impedance of each cell.

Test Results.

Northrop-Grumman has supplied impedance data (as a function of frequency and phase difference) for three configurations. All three have 40 cgs Rayl face sheets. The configurations are,

1. Hard common wall.
2. 40 cgs Rayl common wall.
3. 80 cgs Rayl common wall.

The raw data are plotted in figs 2 to 9 for the cases with the resistive common walls. A positive phase difference indicates that cell 1 leads cell 2. For ease of interpretation of the sensitivity to phase angle, the raw data has been plotted at 20° intervals.

Inspection of the plots provides a high degree of confidence in the data quality. This is observed via the consistent trends of the data between the 40 cgs Rayl and 80 cgs Rayl common wall samples as a function of frequency and phase difference.

The 40 cgs Rayl common wall liner has zero reactance (a resonance) at ~ 2100Hz, at zero phase (where the liner behaves as if it is locally reacting). At 1000Hz, the cell 1 resistance shows almost no variation with phase angle, whereas the cell 2 resistance increases by ~0.6ρc at a phase angle of 60°. A small shift in frequency to 800Hz results in a significant change in the impedance behavior with phase, probably associated with an anti-resonance.

At 800Hz, the zero phase or "locally reacting" resistance measured for both cells shows a sizeable jump from that expected, i.e. ~1.78ρc instead of .96ρc (i.e. 40 cgs Rayls). The

resistance measurement is much more susceptible to error near anti-resonance so the validity of the 800 Hz data is somewhat questionable.

However, even though the 'baseline' (i.e zero phase or locally reacting) value of ~1.78ρc is high, there is still a significant systematic variation in impedance with phase angle at 800 Hz. Cell 1 and cell 2 exhibit opposing trends in resistance - cell 1 resistance decreases from the baseline level to ~1.35ρc at 60°, whereas cell 2 increases rapidly to ~13ρc at the same phase angle. Hence, if these effects are real, and not resulting from experimental inaccuracies, the predictions may be able to pick it up. Prediction/measurement agreement under these conditions (with the rapid fluctuations) would verify both the data and the predictions. This question is addressed in **Impedance Predictions** section.

At frequencies above the resonance, e.g. at 4000Hz, the resistance of cell 1 increases by ~0.4ρc and the resistance of cell 2 varies to a much smaller degree (actually reducing by ~0.15ρc). This is somewhat opposite behavior to that at around 800Hz.

The 800Hz data still easily exhibit the most phase-sensitive trends. Unfortunately, it becomes progressively more difficult to test at lower frequencies to see if these trends are continued. This may be worth further inspection by attempting perhaps 600Hz. Hopefully, any inaccuracies in the data will not mask the trends of impedance with phase angle.

The reactance data exhibit a different trend to that for the resistance, in that there is little or no effect with phase at the higher frequencies (i.e. typically above 3000Hz), with an increasing sensitivity as frequency reduces. Below the resonance frequency, there is an appreciable change in reactance with phase for both cells. At 1000Hz, the reactance of cell 1 increases by ~0.7ρc at 60°, whereas the cell 2 reactance decreases by ~1.2ρc at the same phase angle. Again, a small shift to the lower frequency of 800Hz has a dramatic effect. Cell 1 exhibits similar but slightly larger magnitude phase behavior as that for 1000Hz. However, cell 2 varies extremely rapidly with phase, to the point that reactance goes through a large negative value at 40° , before quickly reversing in sign to go positive above ~60° and then continuing to go further positive at higher phase angles (not shown). This is associated with a rapid change in the resistance at this frequency.

The 80 cgs Rayl common wall data (figs 6 to 9) show the same trends (with frequency and phase angle) as the 40 cgs Rayl data. The variations in impedance, however, are reduced for a given phase angle. This is consistent with intuitive expectations where, in the limit of increasing common wall resistance, a hard wall is reached and the liner reverts to the locally reacting case.

In general, in order to attain a greater bandwidth at low frequency, a less negative reactance is preferred. Therefore, on first inspection, the results from this impedance test are not very promising. Certainly, from 1kHz to 2 kHz the cell 2 behavior is in the wrong sense in that the reactance gets more negative as the phase difference increases. The picture is more complex with these liners, though, in that resistance also varies with phase angle and frequency. In general resistance varies little with frequency for single layer locally reacting linear liners, thereby making reactance the most flexible design parameter

in obtaining an impedance match. Further investigation is required, following validation of the prediction routines, to see if,

1. the impedance change of one cell favorably outweighs that of the other cell.

2. the behavior is different for a larger number of linked cells.

3. the variation of impedance with phase can be exploited to achieve a better match to the optimum impedance for more than one mode (incidence angle) at a given frequency.

Impedance Predictions.

Two impedance computer models have been constructed for prediction of the double impedance tube data. The first of these, Zmatrix, was developed by Fred Hutto of Boeing, while working at Northrop-Grumman. The second is an extension to the existing Boeing impedance prediction code, Ymod, and was developed by Bielak and Premo. Both codes were used to predict impedance as a function of phase angle for the discrete frequencies tested by Northrop-Grumman (800Hz and 1,2,3,4KHz).

The two models use the 'lumped element' technique to model an acoustic lining. This treats each element of a liner separately (e.g. face sheet, cavity) and, assuming plane wave propagation, solves a matrix equation for nodal pressures and particle velocities. Both codes allow propagation between two neighboring cells with a variable phase difference (and SPL) between the sources.

As previously stated, the variation in phase at the face sheet leads to varying spatial pressure distributions down into the two cells. This variation is modeled by splitting the cavity into a number of sub-cavities. Five sub-cavities have been used in these models but, in the limit, there will be a continuous pressure distribution down each cell.

Figs 10 to 19 show the impedance predictions against the raw data for the 40 cgs Rayl common wall. The unconnected points represent the data and are plotted at the actual phase angles tested between the drivers, not interpreted values as in the previous section. The predicted degree of variation in impedance with phase is in broad agreement with the data, for both models, i.e., limited variation around the resonance (e.g. 2,3kHz) and larger variations away from the resonance. However, although qualitatively good, the quantitative agreement is not.

Note that the agreement with the models would be better if the impedance tube measured resistance was at the nominal value of 1ρc. This is the DC flow resistance value but was measured higher at some frequencies (~ 1.8ρc at 800Hz and ~1.2ρc at 1KHz) by the impedance tube with a cavity backing. This phenomena has been discussed earlier. At higher frequencies, the impedance tube measured value was nearly equal to the DC flow resistance value of 1ρc.

At 800Hz, Ymod predicts little variation in impedance with phase angle. However, impedance varies significantly with phase for both cells (in particular, cell 2) and especially at the higher phase angles. At this frequency, Zmatrix agrees with the data much better than Ymod, predicting a much larger excursion in resistance and reactance than the latter. Zmatrix predicts a negative shift in cell 2 reactance with increasing phase angle followed by a sign reversal at ~90°. Though underpredicting the severity of the measured data behavior, the ability of Zmatrix to predict this general trend lends weight to the confidence in the low frequency data. The cell 1 impedance, while varying to a much lesser extent than cell 2, is also better predicted by Zmatrix.

At 1KHz, Zmatrix also shows the better agreement with the data. At 2KHz and 3KHz, both methods predict the data to an acceptable degree of accuracy. At 4KHz, Ymod provides the better prediction.

To summarize, both methods exhibit potential. However, the first question which needs to be addressed is why the models differ in their estimations. This is particularly true at low frequencies (≤ 1000Hz). Some investigations have been carried out but will require further work. Once this discrepancy is clarified, the best model (or either if they agree), could be used to try to exploit the behavior with phase angle for acoustic advantage. Also, the observed reactance behavior at low frequencies and for a larger set of connected cells remains to be fully addressed. In order to perform the former task, validation of one of the models is important, given the lower limit of the tube is ~800Hz.

MELO STUDY

Introduction.

MELO (Multi-Element Liner Optimizer) is a liner optimization and duct attenuation calculation program developed by Boeing. The program will optimize a given liner construction to attain the maximum attenuation of the modes propagating downstream in a given duct geometry.

The purpose of this part of the extended reaction study is to investigate the attenuation of various non-locally reacting geometries and compare them to what is achievable with locally reacting liners. MELO has initially been used to look at two rectangular duct geometries. The first was 5cm x 20cm (height x length), the second 50cm x 200cm. Primarily, only the lowest order mode propagates (cut-off frequency is ~ 3400Hz) for the smaller duct. Running the code, for this geometry, enabled familiarity to be gained and confidence to be established in the predictions for extended reaction configurations.

The second geometry is more representative of a full scale bypass duct application. Given the large L/H of most bypass ducts, higher order modes are generally well attenuated and lining optimization tends to focus on maximizing the attenuation of the lowest order mode. Hence, when considering bypass ducts, the emphasis for extended reaction liners will be on achieving greater bandwidth rather than multi-modal attenuation. Inlets should be studied with multi-modal optimization.

The prime target for this study is to evaluate the potential attenuation gains achievable with extended reaction liners in a fan duct. This will be achieved by validating MELO. With this in mind, a duct propagation test was devised. For convenience of manufacture and analysis, this was a 2-D test and was performed by Northrop Grumman. Once validated, MELO can then be used for full scale applications.

Initial MELO studies

Predicted Attenuations.

A single layer, locally reacting, linear liner was chosen as a datum. For convenience, this liner was optimized for attenuation of the lowest order mode at 2000Hz. The exercise was then repeated for the larger duct geometry.

In addition to the locally reacting liner, the following cross-section of extended reaction configurations were also assessed,

1. 4% open area perforated core (i.e. 4% POA).
2. 8% open area perforated core (8% POA).
3. 1cm flute @ 0° to the duct axis. A flute here is used to describe a channel within the liner.
4. 1cm flute @ 90° to the duct axis (essentially locally reacting, given a constant phase and amplitude across the duct).
5. 1cm flute @ 45° to the duct axis.
6. 40 cgs Rayl/cm bulk absorber.
7. 80 cgs Rayl/cm bulk absorber.
8. 40 cgs Rayl/cm bulk absorber, locally reacting.

The results presented here are for non-locally reacting liners having the same depth and face sheet resistance as the locally reacting liner. Further studies have optimized the individual extended reaction designs for test in the 2-D flow duct.

5 cm Duct.

The locally reacting datum liner for this duct is a single layer liner with a 9.9 cgs Rayl linear face sheet and a core depth of 3.8cm. The attenuation comparison for the lowest order mode is plotted in fig 20. The y-axis has been limited to 30dB, in order to identify the bandwidth behavior more easily.

The results for this duct provide confidence in the MELO predictions, in that,

1. The locally reacting liner provides the best attenuation at the design frequency, 2KHz (the liner was designed with the Cremer optimum impedance at this frequency).

2. As expected, the attenuation characteristics of the flute at 90° to the duct axis approximate those of the datum liner.

3. The bulk absorber shows a broad attenuation bandwidth, with the locally reacting bulk absorber performing slightly better in this respect. This is consistent with expectations. It is worth noting that the bulk liner attenuation peaks at ~4000Hz and significantly exceeds the locally reacting attenuation, which dips at the anti-resonance at this frequency.

4. The 4% POA perforated core produces attenuation levels closer to the locally reacting case than the 8% POA core. In the limit (i.e. 0% POA), they would be identical.

5. As the flute angle becomes more aligned with the duct axis, the observed attenuation decreases.

In addition,

6. Although the peak attenuation of the 4% and 8% perforated core liners was lower than for the locally reacting liner, both comfortably exceed 30dB and the attenuation away from the design frequency improved.

50cm duct.

The locally reacting datum liner for this duct is a single layer liner with a 118 cgs Rayl linear face sheet and a core depth of 1.1cm. This duct has multiple modes propagating. Figs 21 to 23 show the modal attenuation for modes 1 to 3. As expected, the higher order modes are more efficiently attenuated (note that mode 3 is cut-off at 500 and 630Hz). When comparing the lowest order mode attenuation spectra for both ducts, some points are notable,

1. The attenuation characteristics are different because the behavior depends on λ/H. H has increased by a factor of 10 for the larger duct. When the wavelength becomes small relative to the duct height, a significant degree of beaming occurs and the wall amplitudes are reduced.

2. The bulk absorbers do not provide the same relative gains in attenuation bandwidth especially at high frequencies ($\geq$ 3150Hz). However, their attenuation levels are much closer to the locally reacting levels around the tuned frequency and are almost symmetrical about this frequency.

In addition, in the larger duct where multiple modes propagate,

3. The attenuation spectra retain a fairly constant profile from mode to mode. The peak is shifted up by $1/3^{rd}$ octave as mode number increases.

4. As the perforated core POA increases, the attenuation peak reduces and moves to higher frequencies.

5. As the flute angle, of the fluted core, moves towards the duct axis (i.e. towards 0°), the attenuation peak also reduces and shifts to higher frequencies.

These predictions do not provide convincing evidence for any improvements in attenuation from the extended reaction liners modeled using MELO, except from the increased bandwidth observed from the bulk liners, but primarily for the 5cm duct. However, these liners were all assessed with the face sheet resistance and cell depth of the optimized single layer locally reacting liner. A full optimization, for example, on perforated core POA, flute angle and bulk absorber density should lead to more promising results.

This study satisfied its objective of assessing the general behavior of the MELO predictions. Finally, bandwidth comparisons should be made against a double layer locally reacting liner, the liner type most commonly installed for enhanced bandwidth. These studies are discussed later where MELO predictions are computed for 'real' fan duct applications.

Duct Propagation Test

Introduction

MELO has been used initially to evaluate the attenuation behavior of extended reaction configurations. This code has not been validated against test data for these liners. Hence, a duct propagation test is necessary in order to assess the accuracy of the attenuation predictions.

It is known that MELO performs better for a 2-D rectangular duct. Hence, a 2-D duct propagation test will most easily investigate the accuracy of the predictions. In addition, a 2-D duct is easily manufactured and the modal attenuation analysis is greatly simplified (because, in one plane, only the lowest order mode exists).

Liner and Test Definition

Fig 24 shows a schematic of the test set-up. The lined duct dimensions were chosen to represent a typical fan duct. The duct height at 22" was chosen to conveniently mount the four speaker horns necessary for the combined requirements of a broadband source and tones with a preferred modal content. The lined duct length of 3' gives an L/H of 1.64. A higher L/D would compromise the overall length of the device, given the size of the anechoic chamber. The duct width was chosen at 1.3" to be shallow enough to ensure the acoustic pressure didn't vary in that plane over the frequency range of interest (500Hz to 4000Hz).

The exponential horns on the speakers are designed to give a cut-off frequency well below 500Hz. Fibreglass wool is placed in the horns to reduce the interference between them. A mic is also inserted in each horn to ensure consistency in level between runs.

The samples, both locally reacting and extended reaction, were constructed from wire mesh facing sheets and, if applicable, wire mesh walls. Given the goal of replacing wire mesh single layer liners with perforate liners, the latter were not used because the relatively low duct SPLs would drive down the facing sheet POA, leading to unacceptably high facing sheet mass reactance.

The purpose of the test is to fully validate the MELO code, so it was desirable to design a range of samples which would cover the full spectrum of the concept. MELO was used to optimize locally reacting and extended reaction mesh single layer liners for maximum OASPL attenuation and maximum PNLT attenuation of a typical mid-twin wide chord cutback spectra at 110°. The optimized locally reacting and extended reaction liners designed have been simplified for ease of manufacture and are listed in table 1. These liners present a satisfactory cross-section of liners to explore the concept of extended reaction fully and are adequately different to hopefully be able to easily distinguish the attenuation spectra.

Two types of measurement are proposed for the samples. In the first phase of testing, insertion loss measurements will be performed by taking a log average of the SPLs of the far-field mics in the anechoic chamber, and subtracting this from a similar measurement for either a datum sample or a hard wall test section. This can then be used to validate MELO predictions of the overall attenuation for all propagating modes.

The second phase of testing will depend on the outcome of the insertion loss measurements. If these show promise, modal measurements will be made. This will entail using 4 rows of 12 mics inserted 5" from the start and end of the lined section (i.e. 2 pairs of 2 rows). These are needed to identify the modal content of forward and aft radiated sound. The speakers can be driven in specific combinations of phase relationship to preferentially excite a given mode. The measurements will provide further information on the mode-by-mode (and hence incidence-dependent) attenuation, which MELO is also able to predict.

Table 1 Optimized Samples

Sample #	DC Flow Resistance (cgs Rayls)	Depth (cm)	Common Wall Resistance (cgs Rayls)
1	50	3.2	20
2	90	3.2	Hard (i.e locally reacting)
3	50	3.2	40
4	50	3.2	0 (i.e. no cells)
5	50	3.2	Hard

Notes:

- Samples 1 and 2 approximate the MELO optimized output
- Sample 1 - Max PNLT attenuation, extended reaction
- Sample 2 - Max PNLT attenuation, local reaction
- Samples 3,4, 5 - Additional samples to complete a parametric set

Attenuation Predictions

Fig 25 shows the MELO attenuation predictions for the samples listed in table 1. As expected from their parametric nature, the attenuation profile varies substantially from sample to sample. The predictions indicate that the difference in profiles should make it possible to measure the influence of extended reaction. The 'optimized' (approximate, as samples are a parametric set) extended reaction liner has a 0.51dB increase in PNLT attenuation over the optimized locally reacting liner.

An attempt was also made to optimize extended reaction liners, both mesh and perforate for a 'real' application, i.e. with flow. The attenuation predictions are shown in fig 26. The PNLT attenuation gains exhibited for mesh extended reaction liners over mesh locally reacting liners with zero flow, are reduced substantially with a grazing flow Mach number of 0.51 (now 0.22dB instead of 0.51dB). However, the gain from extended reaction is of the same order as the gain of the mesh over the perforate (single layer) facing sheet.

Unfortunately, the gain from extended reaction shown for mesh liners does not carry through for perforates. At M =0.51, perforate extended reaction liners do not show any attenuation gain over local reaction (and hence this liner plot is superfluous).

The extended reaction single layer mesh lining PNLT attenuation still lies well below the double layer capabilities, which are 1.12dB (perforate) and 1.31dB (mesh) higher.

These predictions, which will be evaluated fully following the duct propagation test, indicate that extended reaction will not exhibit any significant potential for 'real' applications in the fan duct (nil gain for perforates). However, this is not necessarily true for inlets, where multiple modes are propagating. The wavefronts are also more normal to the liner. Hence, the gain in attenuation can be expected to be greater than for fan ducts (given extrapolation from M =-0.51 through M=0.0 to positive Mach numbers). This will be investigated to see if any gains in the inlet justify the incorporation of extended reaction liners.

CONCLUSIONS AND RECOMMENDATIONS.

This report has detailed the status of the extended reaction study. The objective is to investigate the concept thoroughly through the validation of MELO with a 2-d duct propagation test scheduled at Northrop Grumman. Then the validatd code can be used for assessment of these liners for 'real' applications.

Early work concentrated on the validation of three prediction schemes, two of which are aimed at understanding the fundamental process of propagation between cells while the other optimizes extended reaction configurations for maximum attenuation in a given duct geometry.

The two double cell prediction schemes show good qualitative agreement with the Northrop-Grumman experimental data but need further investigation. The predictions for this unique 2 cell arrangement show the largest phase-dependent effects at low frequency.

A 2-D duct propagation test has been defined for the evaluation of the MELO extended reaction prediction capability. This were performed by Northrop Grumman in October 1998. A group of liners were designed to cover the full spectrum of extended reaction wall resistances. The test data in general agreed well with the predicted spectral variations for the different samples except that the attenuation magnitudes were about half the predicted values. The reason for this discrepency is not known.

Preliminary predictions for fan ducts do not show large attenuation gains from extended reaction designs over locally reacting liners, with the only benefits being observed for wire mesh face sheets and connecting cavity walls.

Studies should continue to investigate the variations in impedance with mode order (effectively phase angle) to identify if potential exists to optimize for more than a single mode, as currently occurs with present locally reacting liners. This will be more easily qualified for an inlet, as opposed to a fan duct, where higher order modes are less well attenuated.

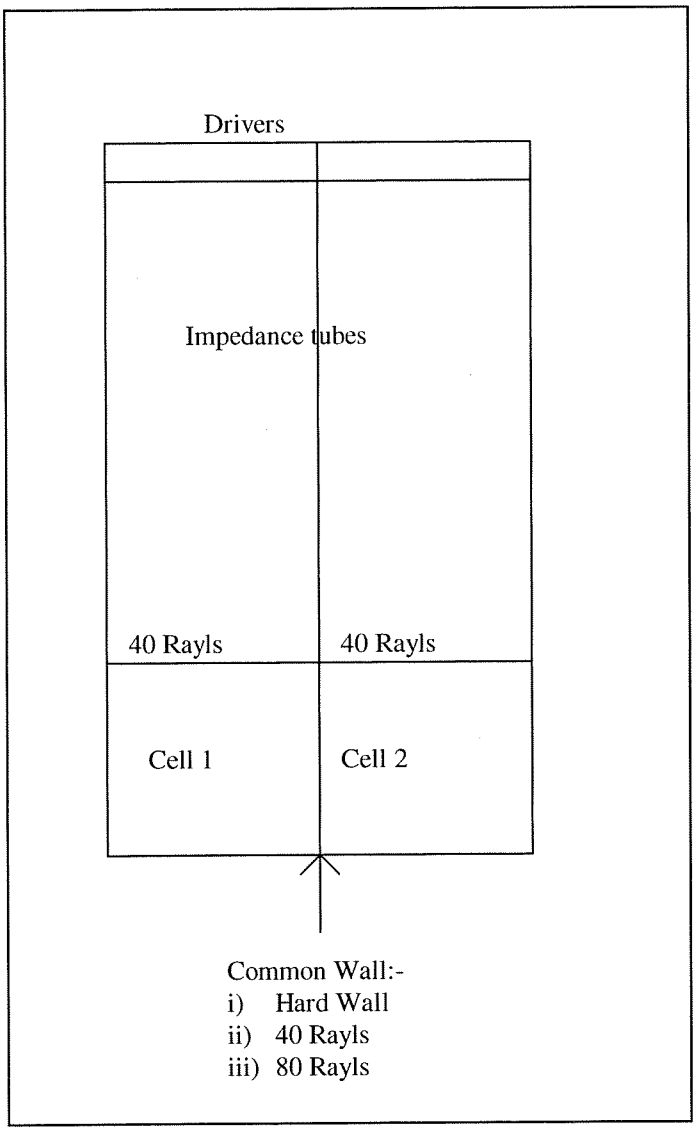

Fig. 1 Schematic of double impedance tube.

Fig. 2 Double Impedance Tube Resistance, 40 Rayl Face Sheet and Wall, Cell 1

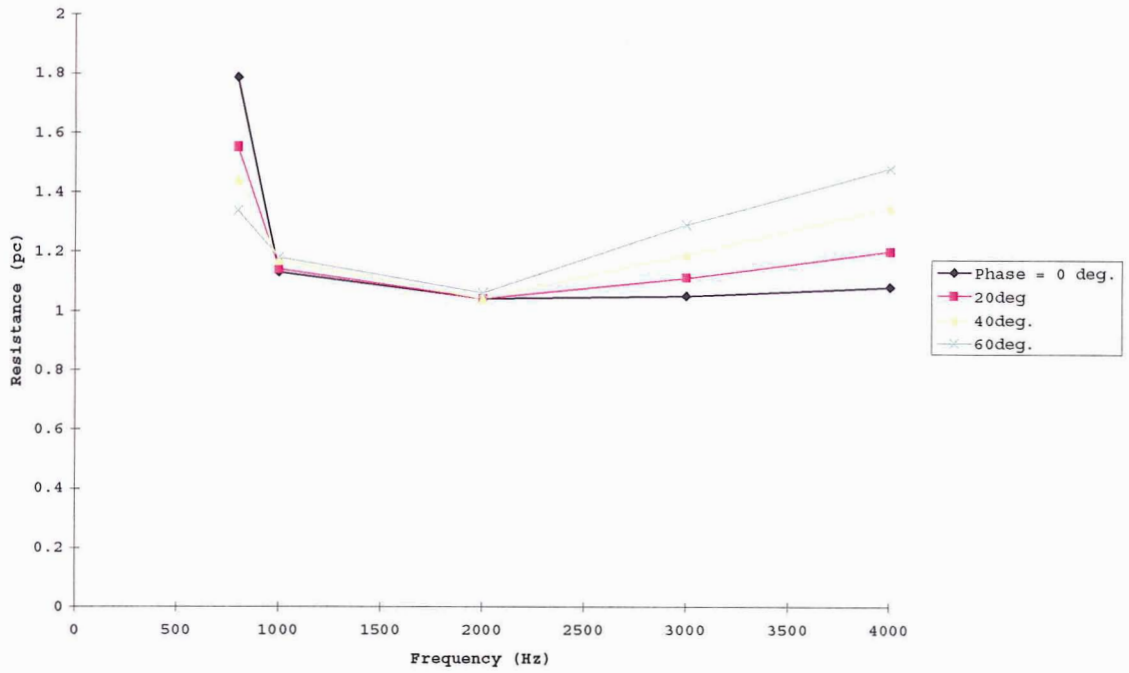

Fig. 3 Double Impedance Tube Resistance, 40 Rayl Face Sheet and Wall, Cell 2

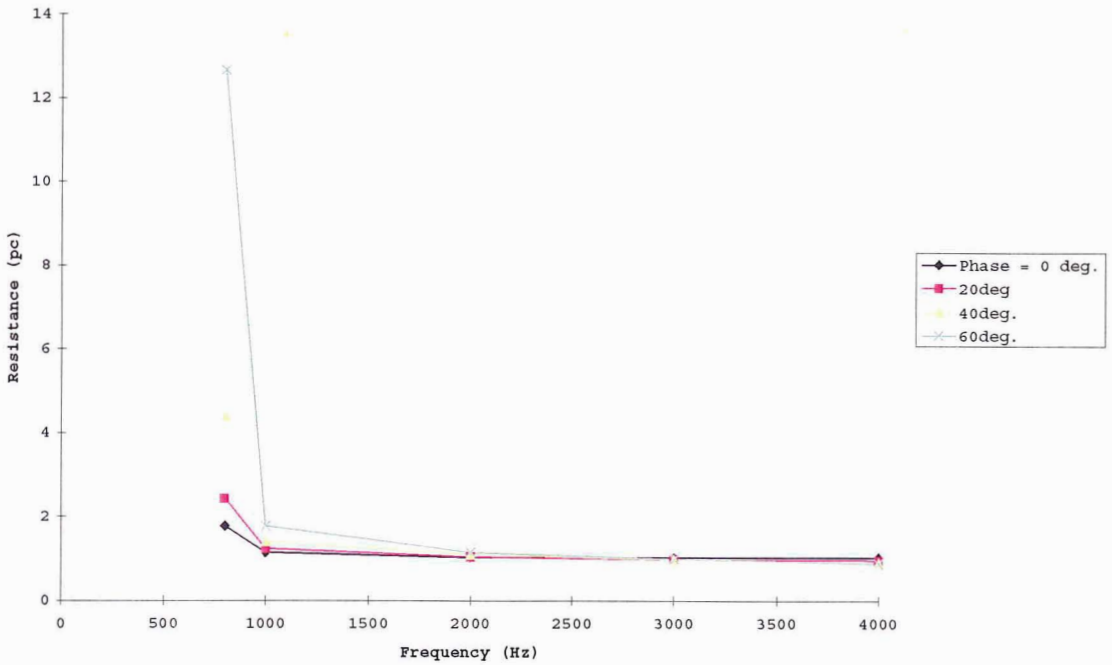

Fig. 4

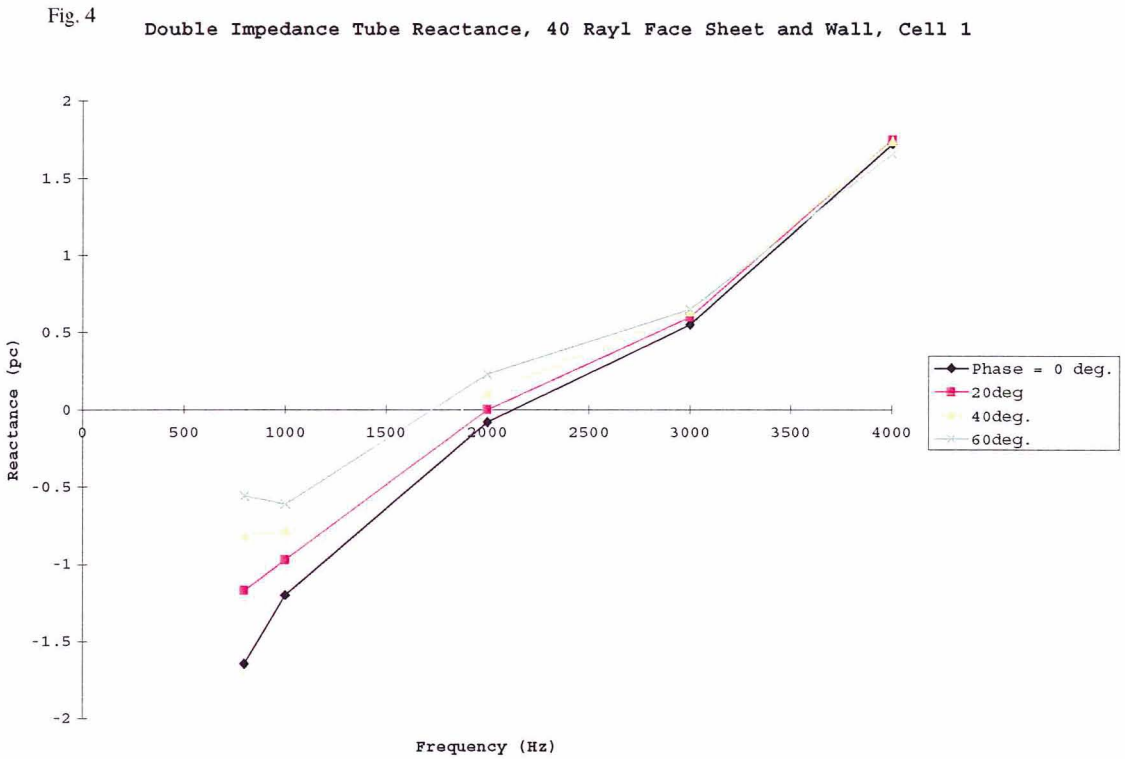
Double Impedance Tube Reactance, 40 Rayl Face Sheet and Wall, Cell 1
Reactance (pc)
Frequency (Hz)
Phase = 0 deg.
20deg
40deg.
60deg.

Fig. 5

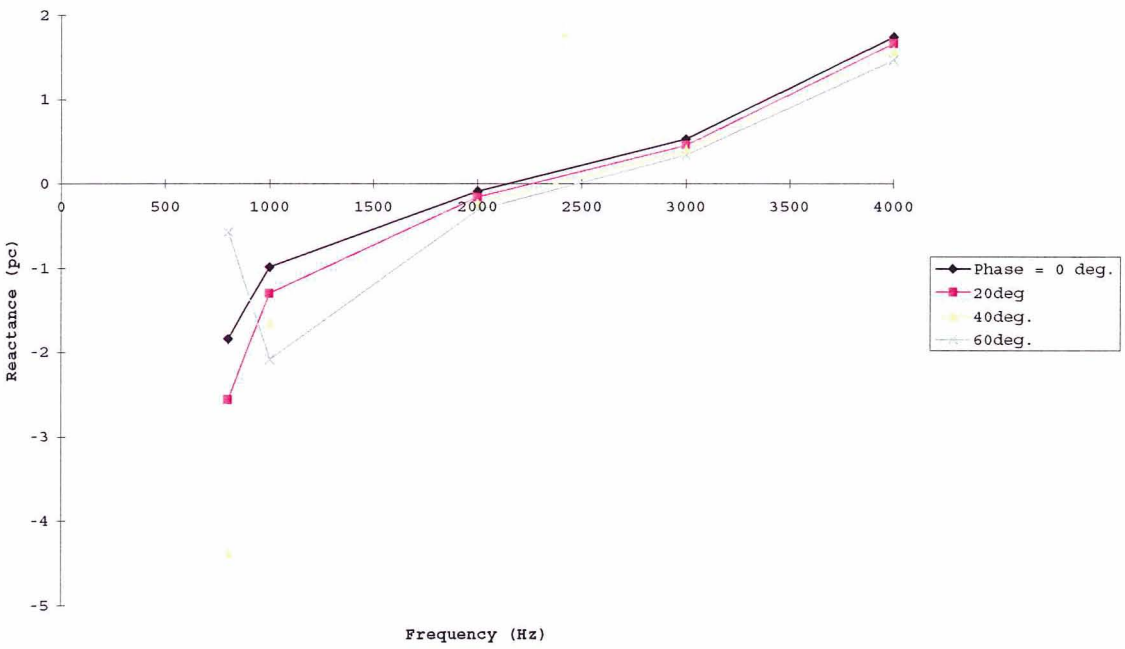
Double Impedance Tube Reactance, 40 Rayl Face Sheet and Wall, Cell 2
Reactance (pc)
Frequency (Hz)
Phase = 0 deg.
20deg
40deg.
60deg.

Fig. 6

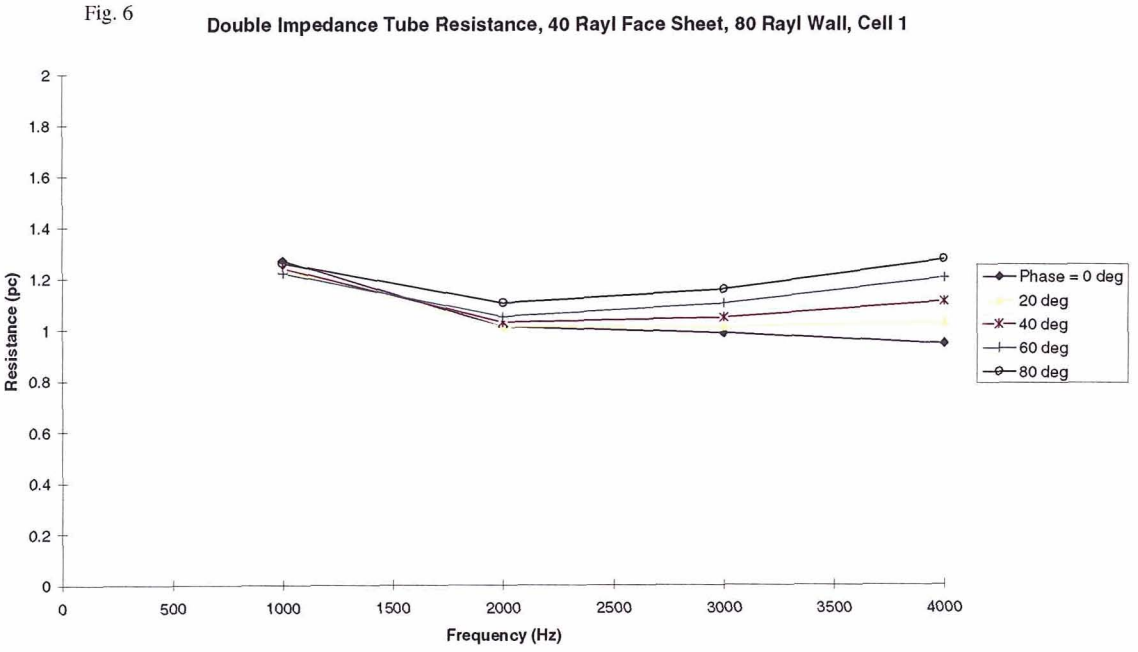
Double Impedance Tube Resistance, 40 Rayl Face Sheet, 80 Rayl Wall, Cell 1
Resistance (pc)
Frequency (Hz)
Phase = 0 deg
20 deg
40 deg
60 deg
80 deg

Fig. 7

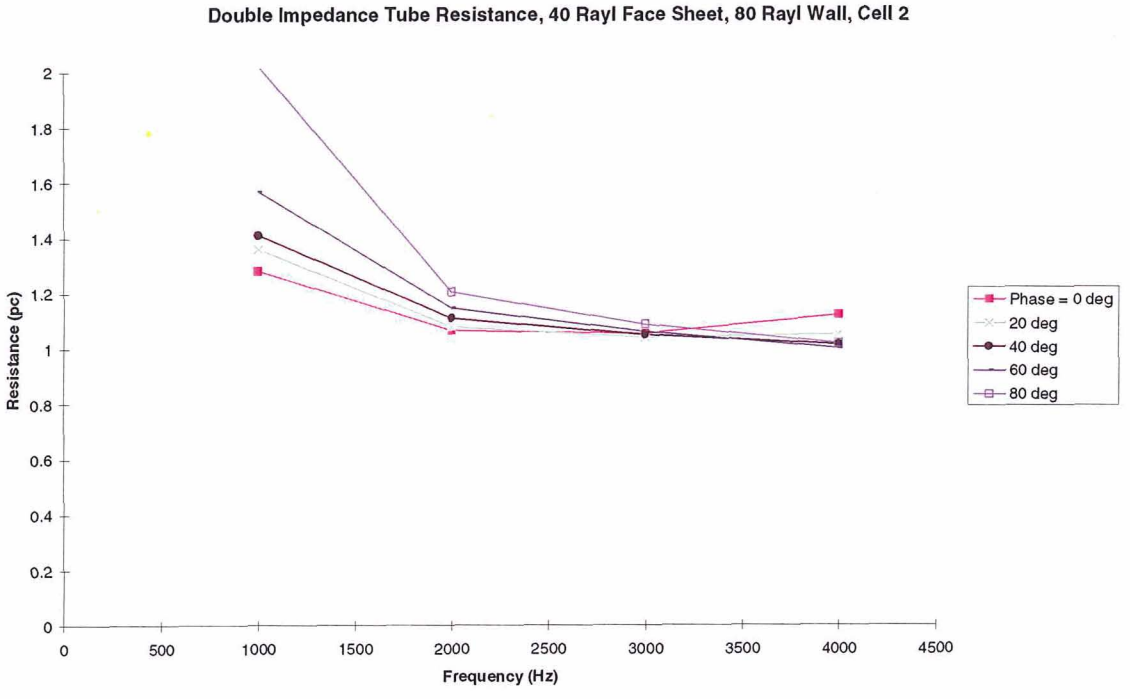
Double Impedance Tube Resistance, 40 Rayl Face Sheet, 80 Rayl Wall, Cell 2
Resistance (pc)
Frequency (Hz)
Phase = 0 deg
20 deg
40 deg
60 deg
80 deg

Fig. 8

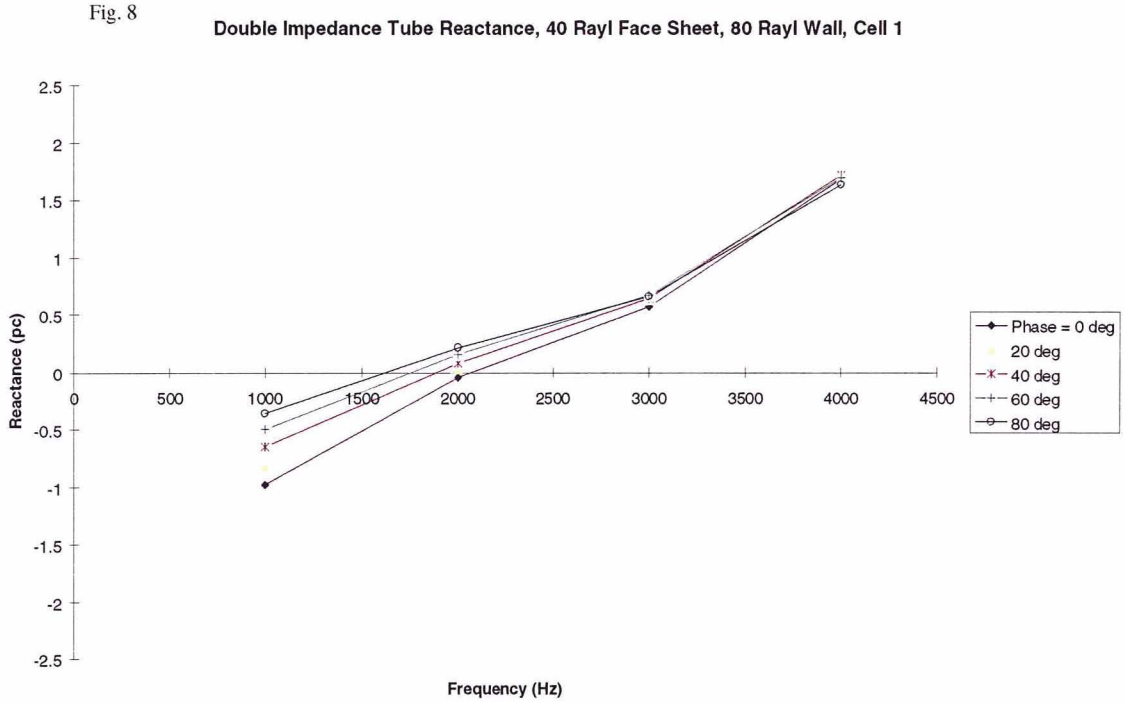
Double Impedance Tube Reactance, 40 Rayl Face Sheet, 80 Rayl Wall, Cell 1
Reactance (pc)
2.5
2
1.5
1
0.5
0
-0.5
-1
-1.5
-2
-2.5
0
500
1000
1500
2000
2500
3000
3500
4000
4500
Frequency (Hz)
Phase = 0 deg
20 deg
40 deg
60 deg
80 deg

Fig. 9

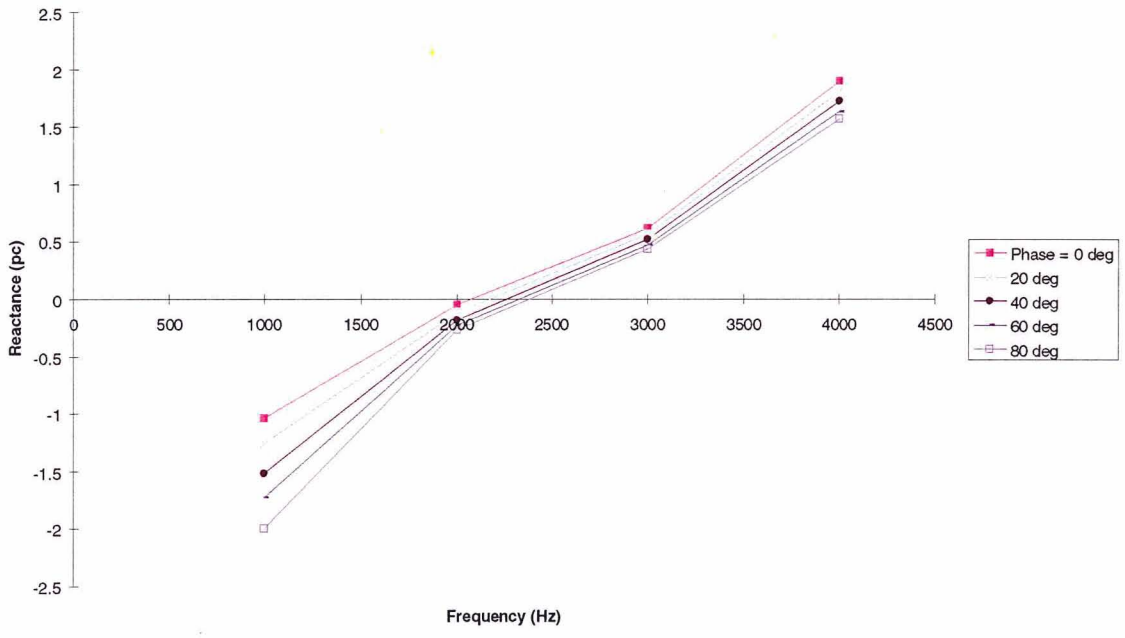
Double Impedance Tube Reactance, 40 Rayl Face Sheet, 80 Rayl Wall, Cell 2
Reactance (pc)
2.5
2
1.5
1
0.5
0
-0.5
-1
-1.5
-2
-2.5
0
500
1000
1500
2000
2500
3000
3500
4000
4500
Frequency (Hz)
Phase = 0 deg
20 deg
40 deg
60 deg
80 deg

Fig. 10

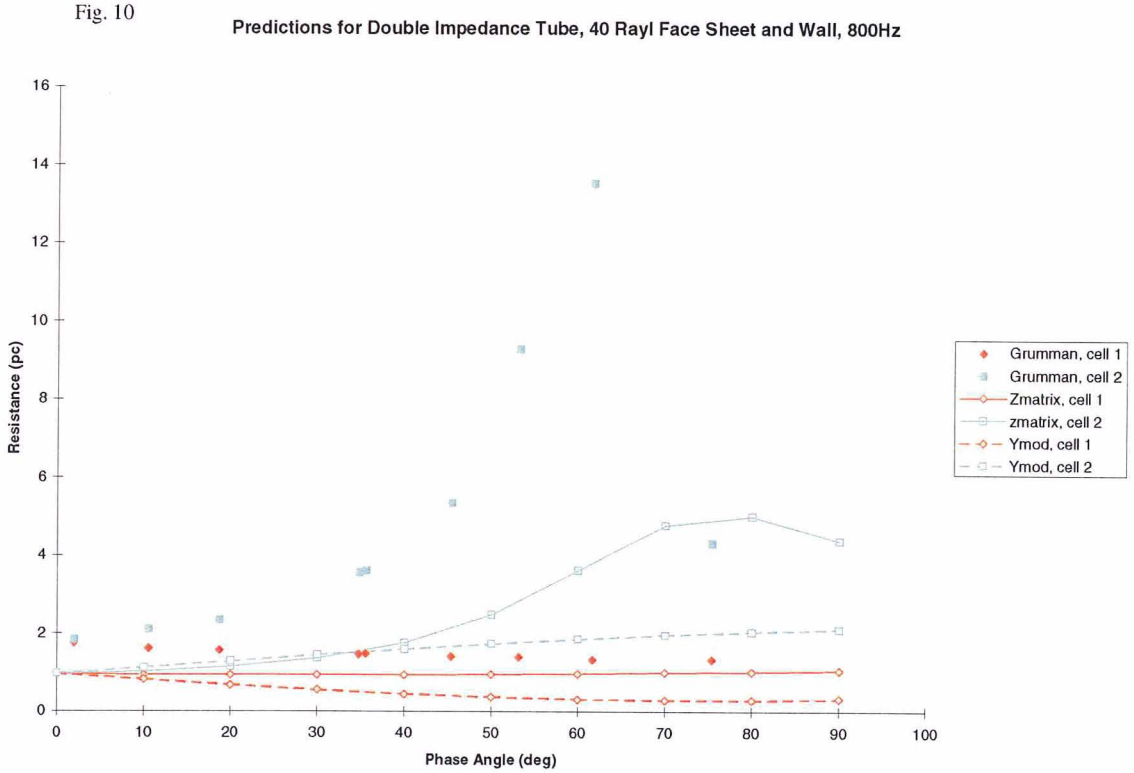
Predictions for Double Impedance Tube, 40 Rayl Face Sheet and Wall, 800Hz
Resistance (pc)
Phase Angle (deg)
Grumman, cell 1
Grumman, cell 2
Zmatrix, cell 1
zmatrix, cell 2
Ymod, cell 1
Ymod, cell 2

Fig. 11

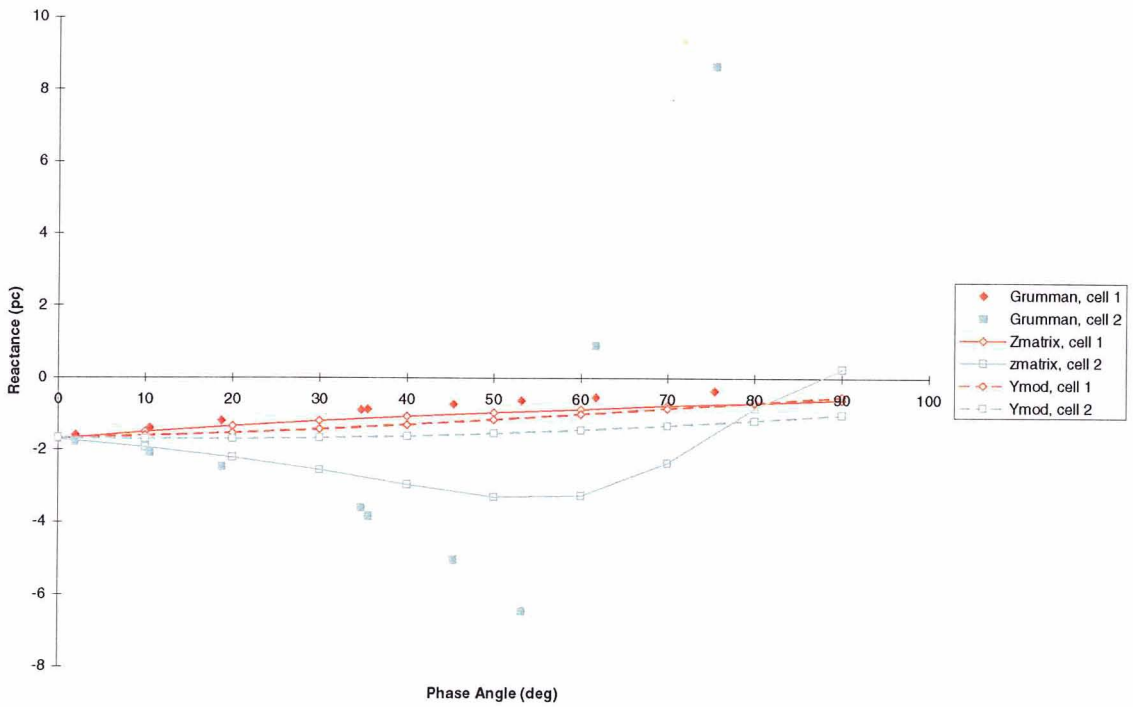
Predictions for Double Impedance Tube, 40 Rayl Face Sheet and Wall, 800Hz
Reactance (pc)
Phase Angle (deg)
Grumman, cell 1
Grumman, cell 2
Zmatrix, cell 1
zmatrix, cell 2
Ymod, cell 1
Ymod, cell 2

Fig. 12

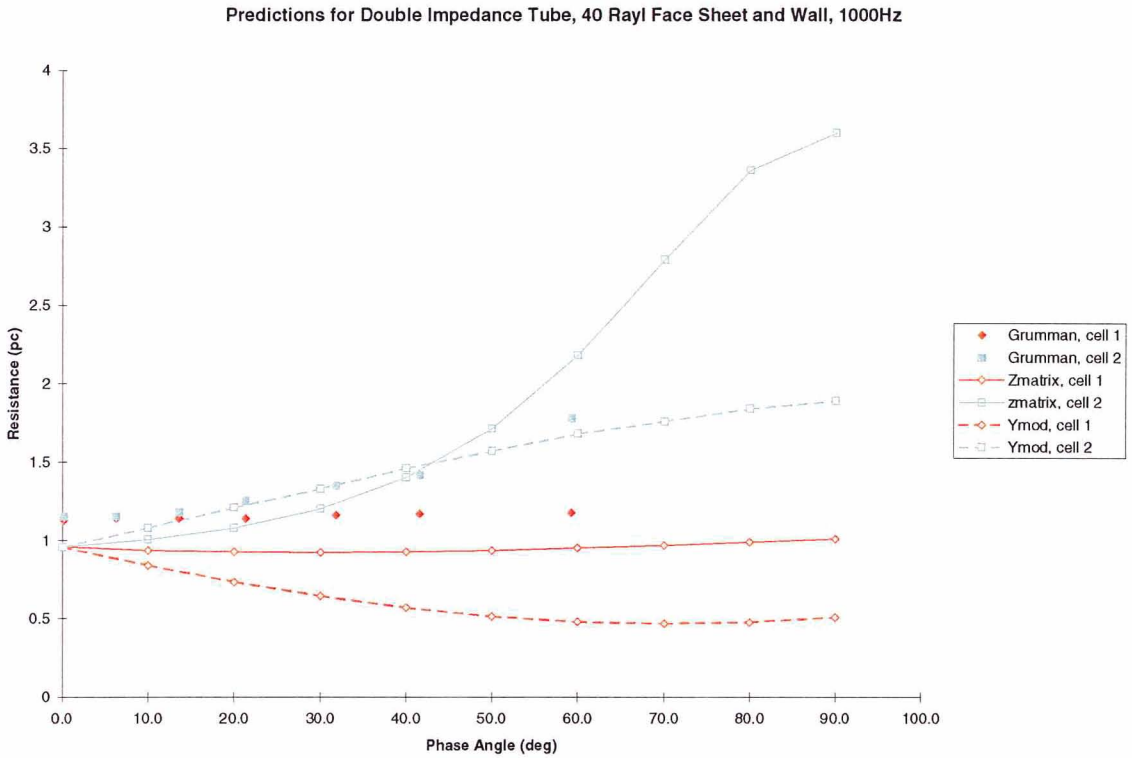
Predictions for Double Impedance Tube, 40 Rayl Face Sheet and Wall, 1000Hz
Resistance (pc)
Phase Angle (deg)
Grumman, cell 1
Grumman, cell 2
Zmatrix, cell 1
zmatrix, cell 2
Ymod, cell 1
Ymod, cell 2

Fig. 13

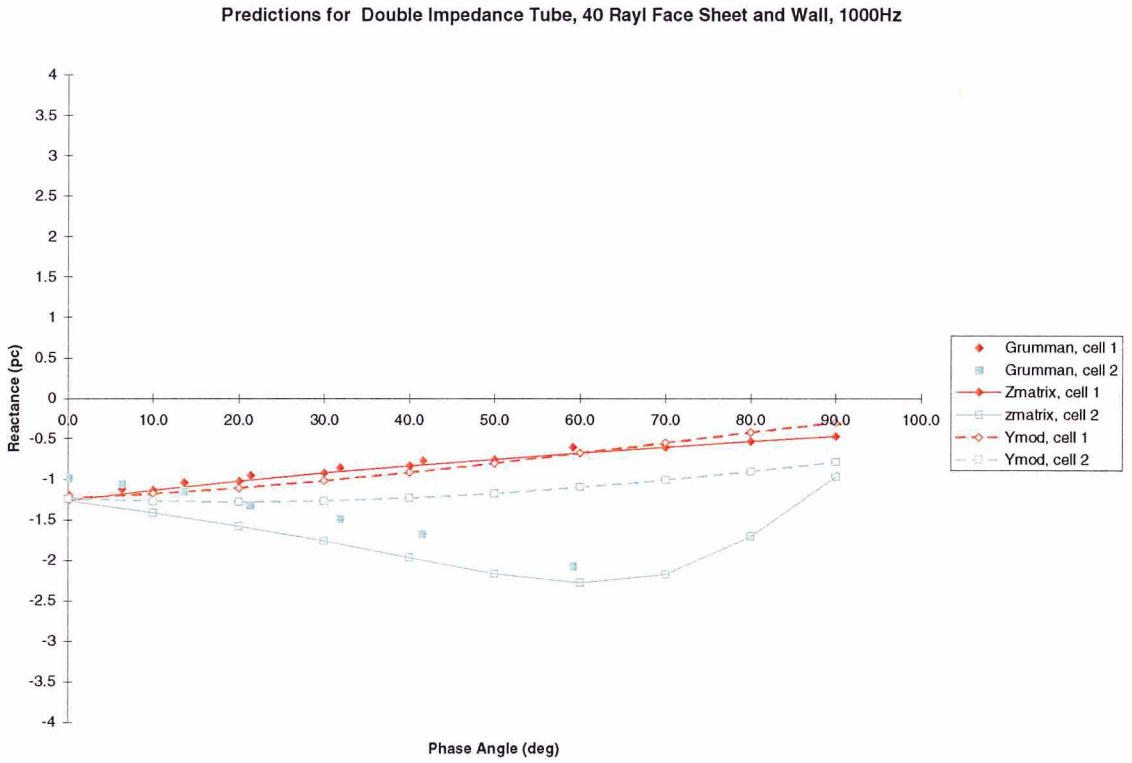
Predictions for Double Impedance Tube, 40 Rayl Face Sheet and Wall, 1000Hz
Reactance (pc)
Phase Angle (deg)
Grumman, cell 1
Grumman, cell 2
Zmatrix, cell 1
zmatrix, cell 2
Ymod, cell 1
Ymod, cell 2

Fig. 14

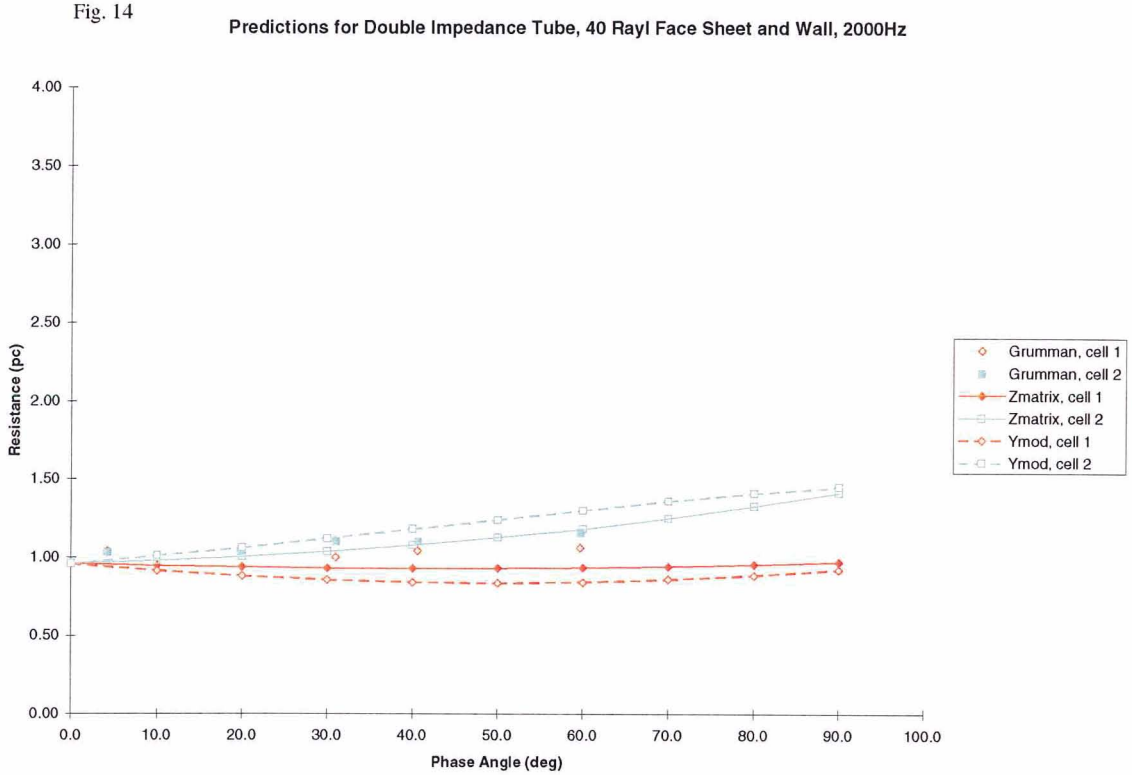
Predictions for Double Impedance Tube, 40 Rayl Face Sheet and Wall, 2000Hz
Resistance (pc)
4.00
3.50
3.00
2.50
2.00
1.50
1.00
0.50
0.00
0.0
10.0
20.0
30.0
40.0
50.0
60.0
70.0
80.0
90.0
100.0
Phase Angle (deg)
Grumman, cell 1
Grumman, cell 2
Zmatrix, cell 1
Zmatrix, cell 2
Ymod, cell 1
Ymod, cell 2

Fig. 15

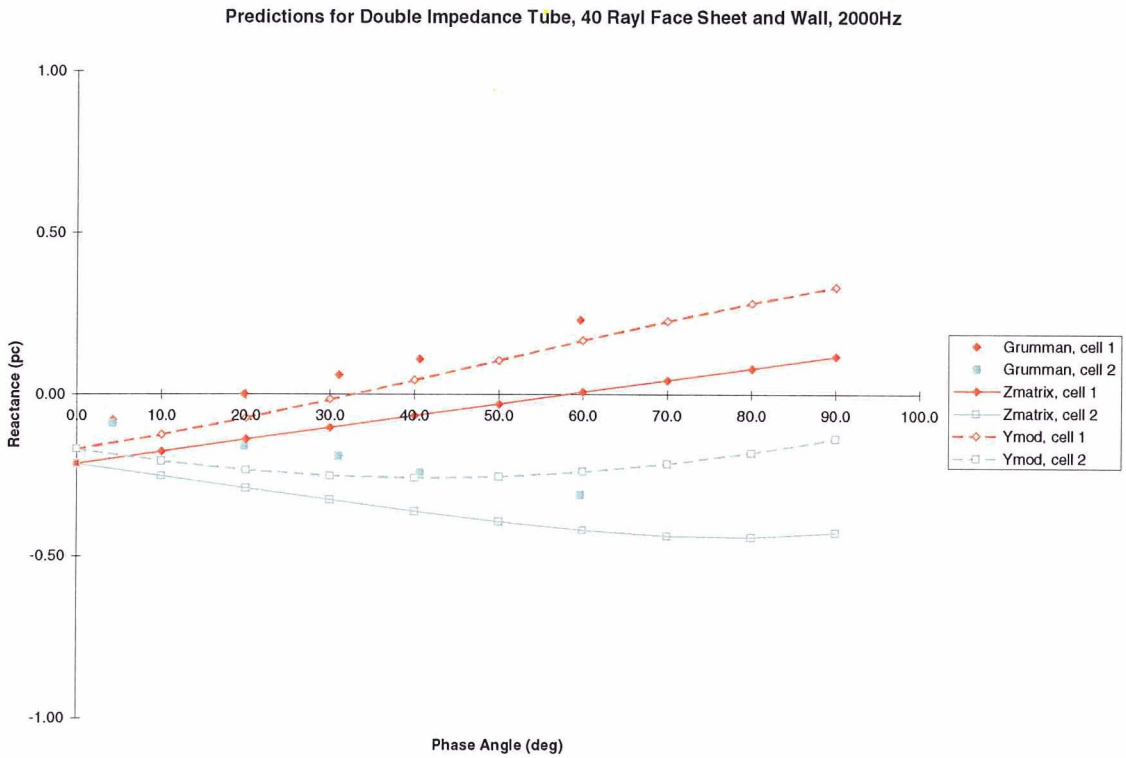
Predictions for Double Impedance Tube, 40 Rayl Face Sheet and Wall, 2000Hz
Reactance (pc)
1.00
0.50
0.00
-0.50
-1.00
0.0
10.0
20.0
30.0
40.0
50.0
60.0
70.0
80.0
90.0
100.0
Phase Angle (deg)
Grumman, cell 1
Grumman, cell 2
Zmatrix, cell 1
Zmatrix, cell 2
Ymod, cell 1
Ymod, cell 2

Fig. 16

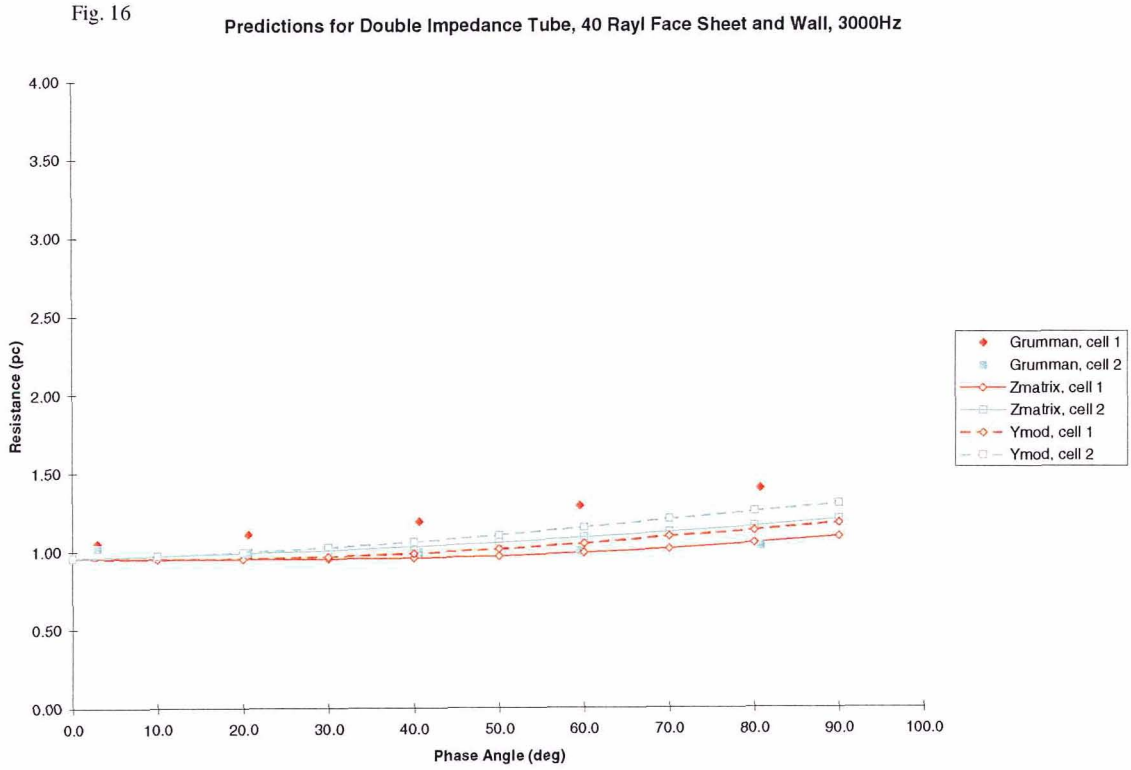
Predictions for Double Impedance Tube, 40 Rayl Face Sheet and Wall, 3000Hz
Resistance (pc)
4.00
3.50
3.00
2.50
2.00
1.50
1.00
0.50
0.00
0.0
10.0
20.0
30.0
40.0
50.0
60.0
70.0
80.0
90.0
100.0
Phase Angle (deg)
Grumman, cell 1
Grumman, cell 2
Zmatrix, cell 1
Zmatrix, cell 2
Ymod, cell 1
Ymod, cell 2

Fig. 17

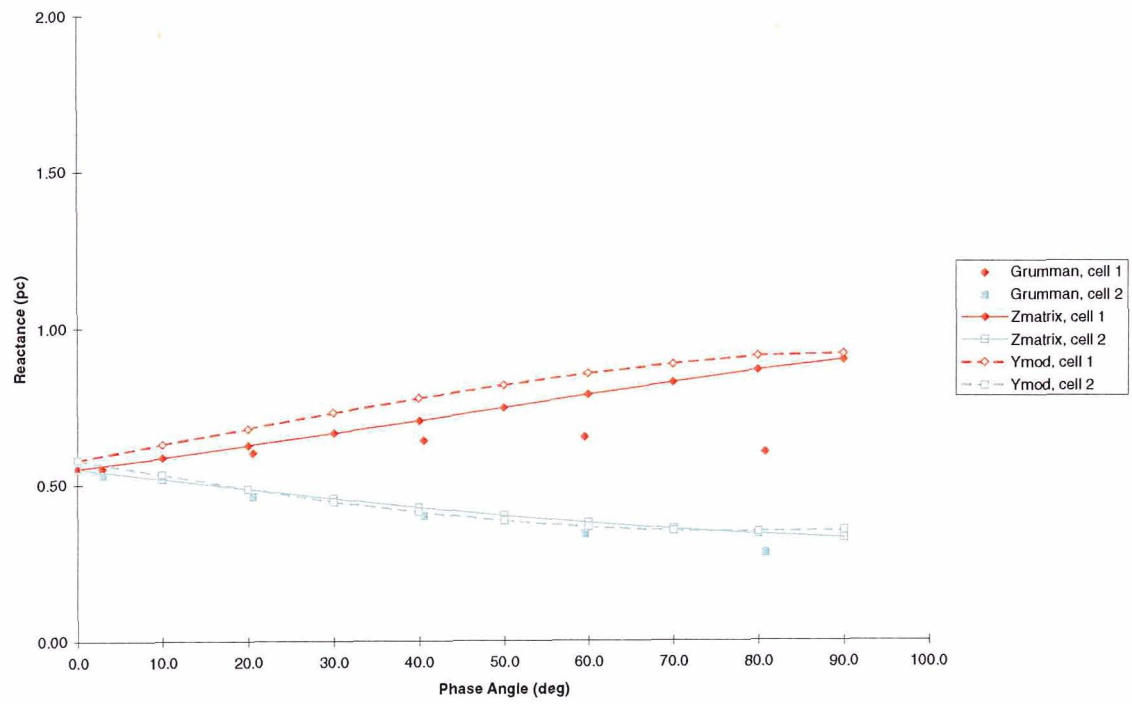
Predictions for Double Impedance Tube, 40 Rayl Face Sheet and Wall, 3000Hz
Reactance (pc)
2.00
1.50
1.00
0.50
0.00
0.0
10.0
20.0
30.0
40.0
50.0
60.0
70.0
80.0
90.0
100.0
Phase Angle (deg)
Grumman, cell 1
Grumman, cell 2
Zmatrix, cell 1
Zmatrix, cell 2
Ymod, cell 1
Ymod, cell 2

Fig. 18

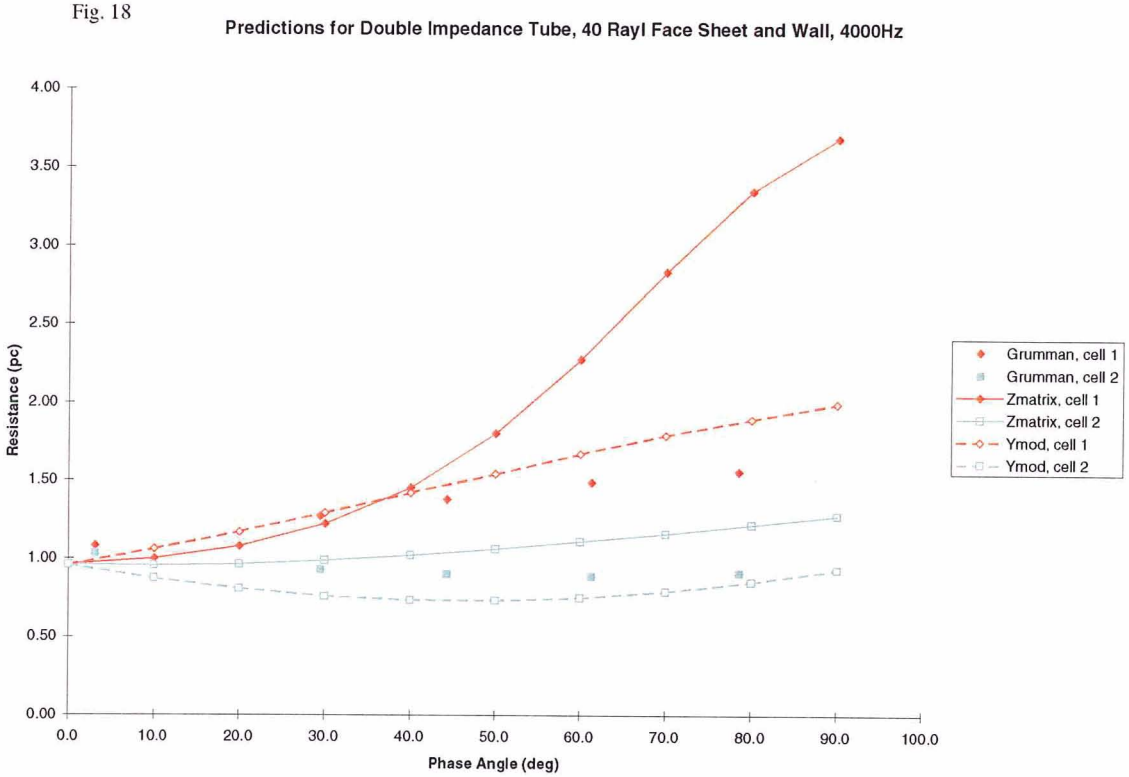
Predictions for Double Impedance Tube, 40 Rayl Face Sheet and Wall, 4000Hz
Resistance (pc)
4.00
3.50
3.00
2.50
2.00
1.50
1.00
0.50
0.00
0.0
10.0
20.0
30.0
40.0
50.0
60.0
70.0
80.0
90.0
100.0
Phase Angle (deg)
Grumman, cell 1
Grumman, cell 2
Zmatrix, cell 1
Zmatrix, cell 2
Ymod, cell 1
Ymod, cell 2

Fig. 19

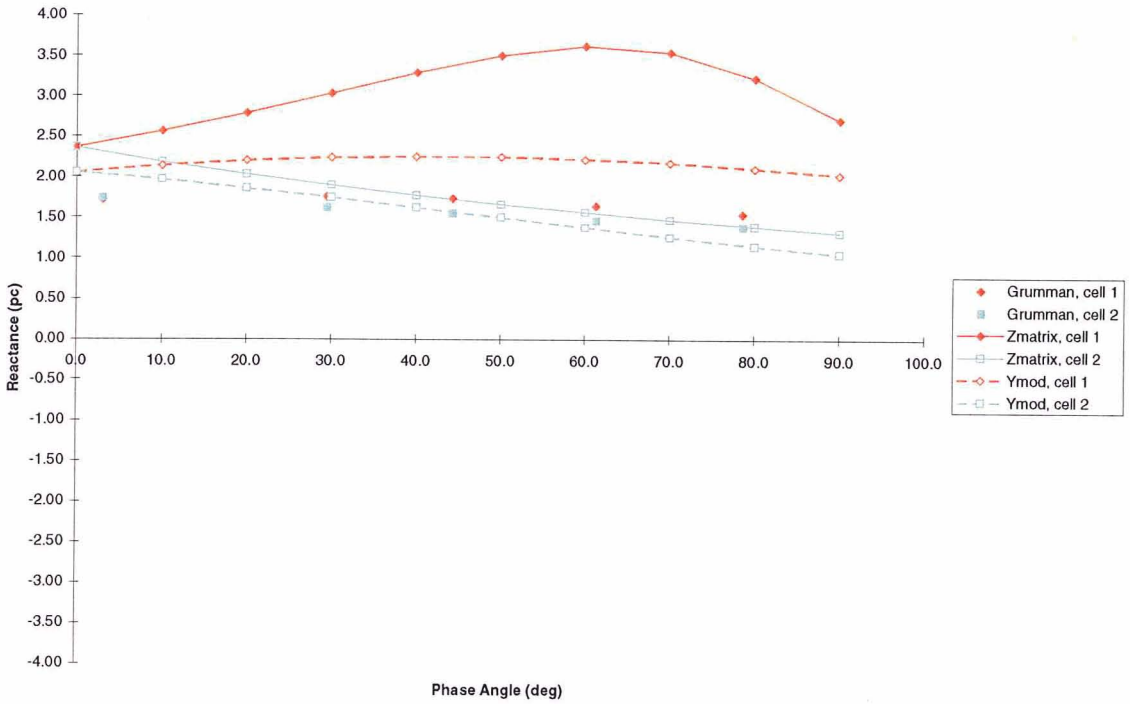
Predictions for Double Impedance Tube, 40 Rayl Face Sheet and Wall, 4000Hz
Reactance (pc)
4.00
3.50
3.00
2.50
2.00
1.50
1.00
0.50
0.00
-0.50
-1.00
-1.50
-2.00
-2.50
-3.00
-3.50
-4.00
0.0
10.0
20.0
30.0
40.0
50.0
60.0
70.0
80.0
90.0
100.0
Phase Angle (deg)
Grumman, cell 1
Grumman, cell 2
Zmatrix, cell 1
Zmatrix, cell 2
Ymod, cell 1
Ymod, cell 2

Fig. 20

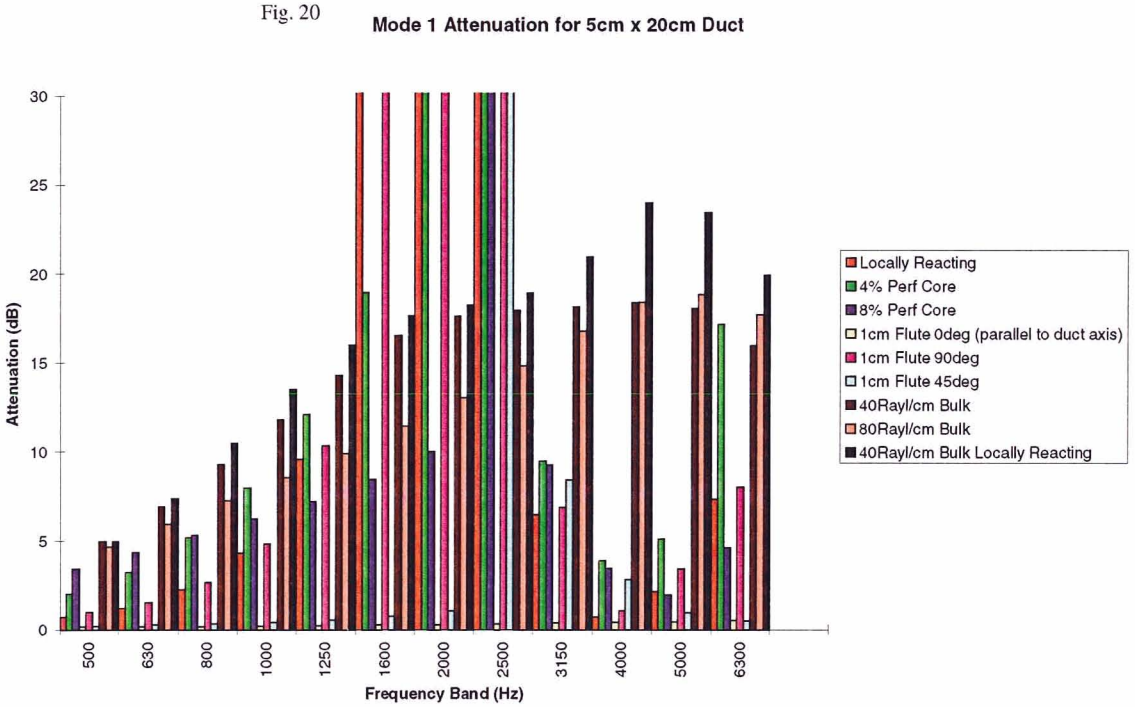
Mode 1 Attenuation for 5cm x 20cm Duct
Attenuation (dB)
30
25
20
15
10
5
0
500
630
800
1000
1250
1600
2000
2500
3150
4000
5000
6300
Frequency Band (Hz)
Locally Reacting
4% Perf Core
8% Perf Core
1cm Flute 0deg (parallel to duct axis)
1cm Flute 90deg
1cm Flute 45deg
40Rayl/cm Bulk
80Rayl/cm Bulk
40Rayl/cm Bulk Locally Reacting

Fig. 21

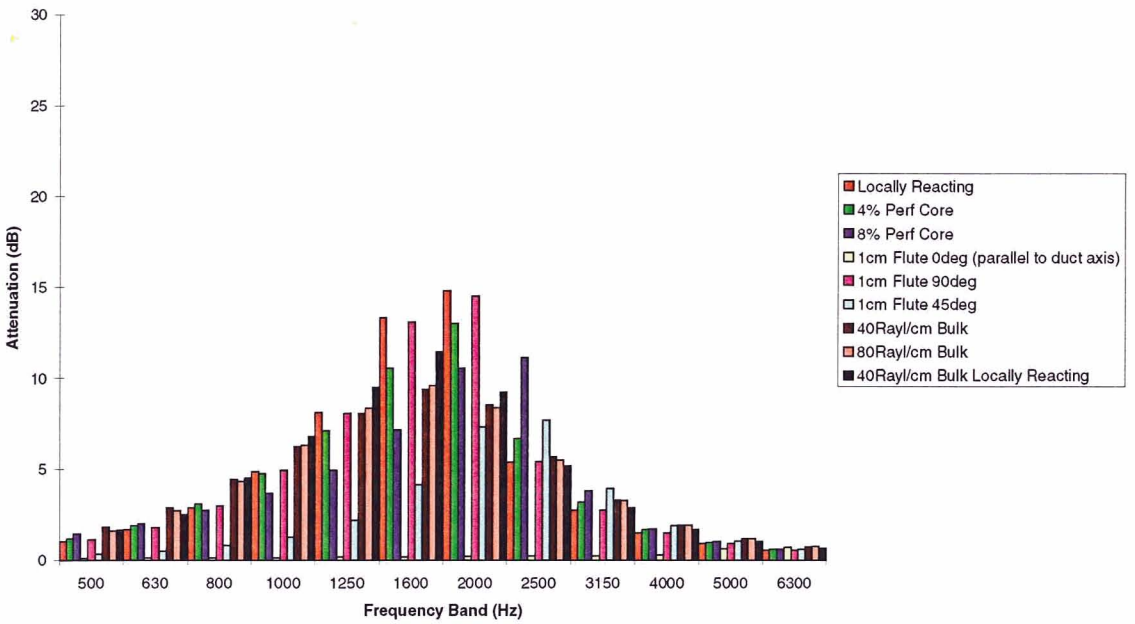
Mode 1 Attenuation for 50cm x 200cm Duct
Attenuation (dB)
30
25
20
15
10
5
0
500
630
800
1000
1250
1600
2000
2500
3150
4000
5000
6300
Frequency Band (Hz)
Locally Reacting
4% Perf Core
8% Perf Core
1cm Flute 0deg (parallel to duct axis)
1cm Flute 90deg
1cm Flute 45deg
40Rayl/cm Bulk
80Rayl/cm Bulk
40Rayl/cm Bulk Locally Reacting

Fig. 22 **Mode 2 Attenuation for 50cm x 200cm Duct**

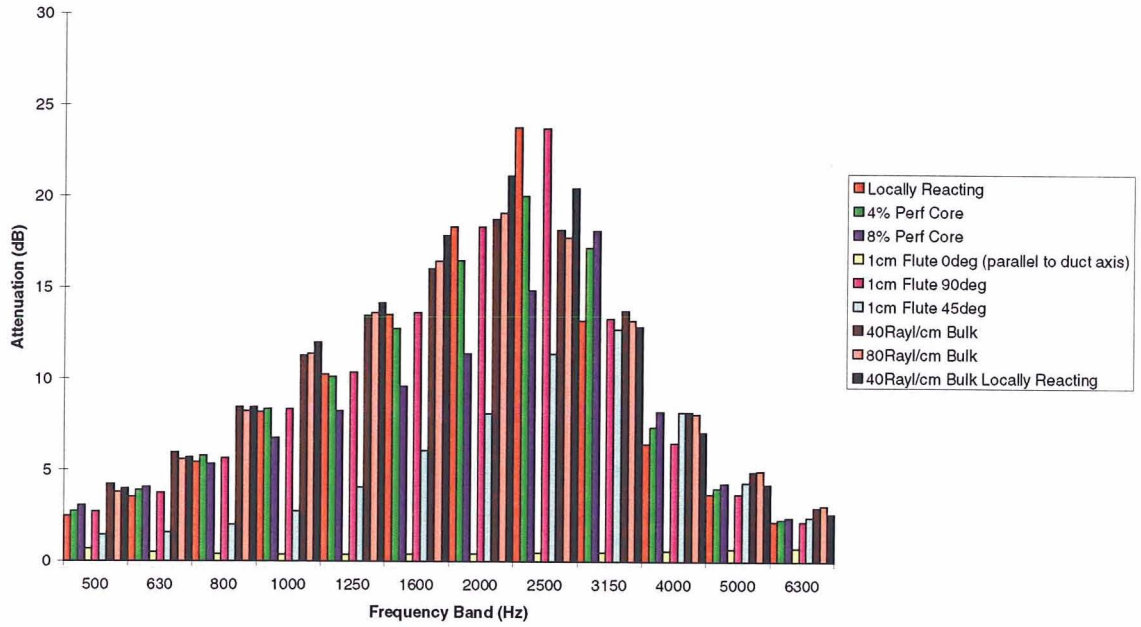

Fig. 23 **Attenuation for Rectangular 50cm x200cm Duct**

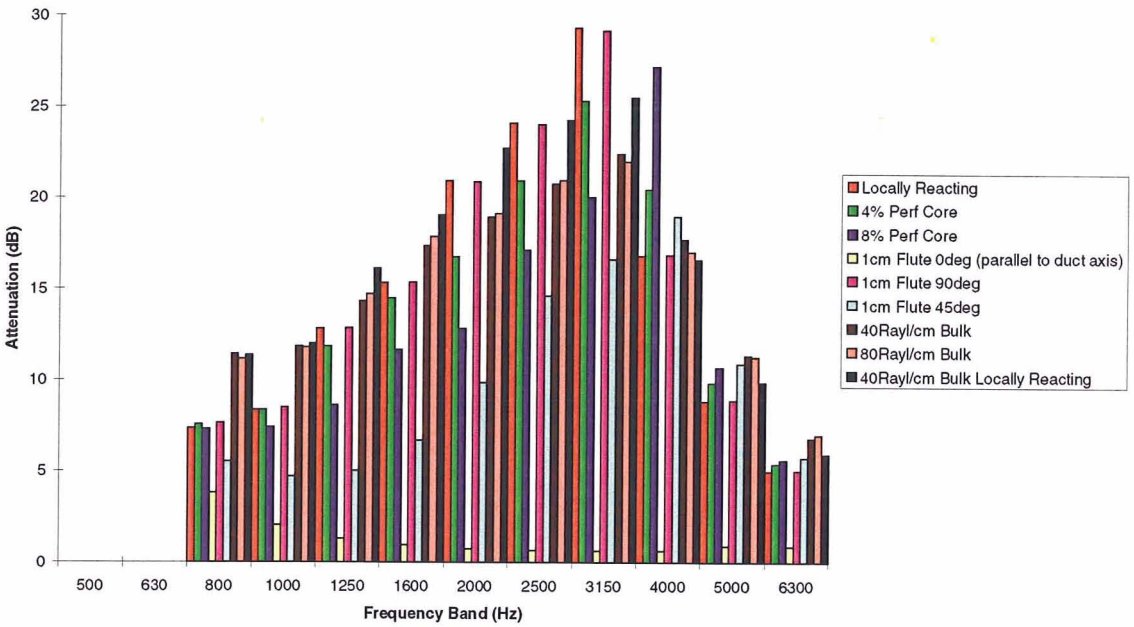

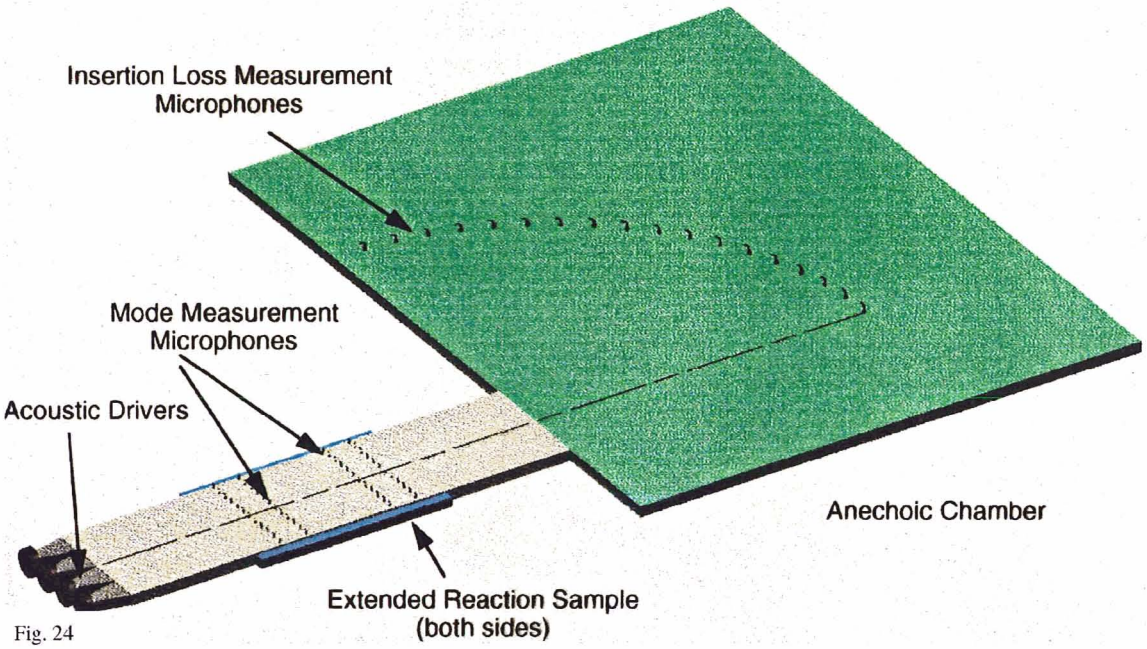

Fig. 24

Test Set-Up

Fig. 25 MELO Predicted Attenuations for the Test Samples

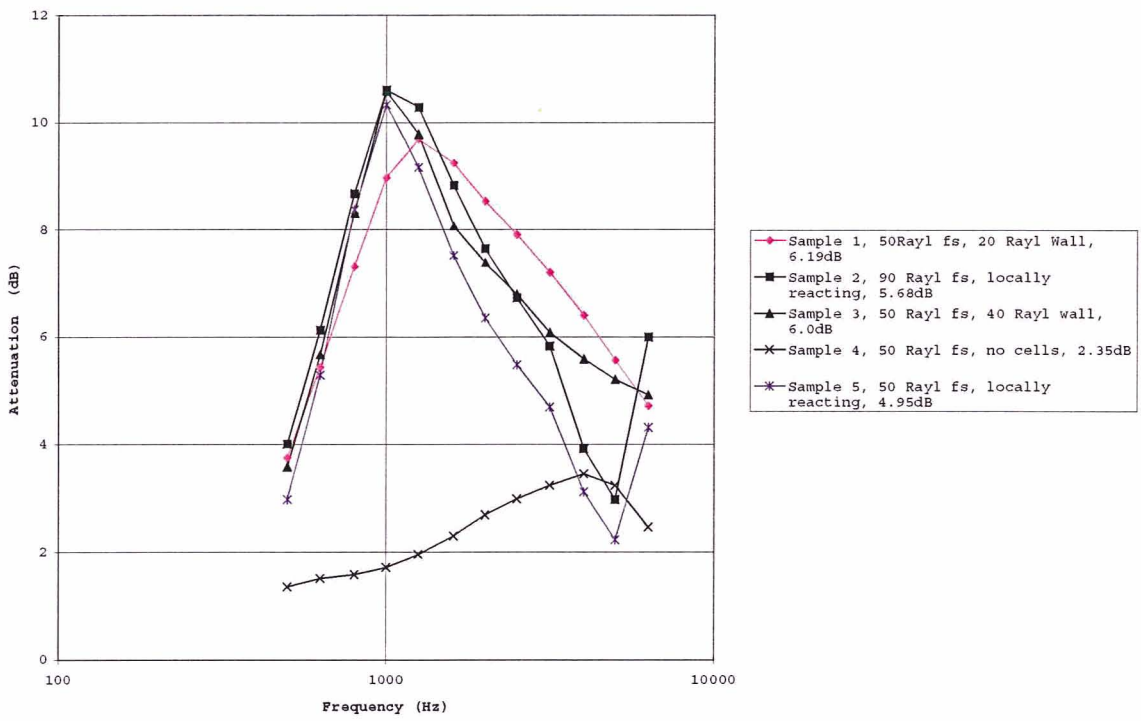

Fig. 26

PNLT Optimized Liners for M0.51 Mid Twin Wide Chord Fan Duct

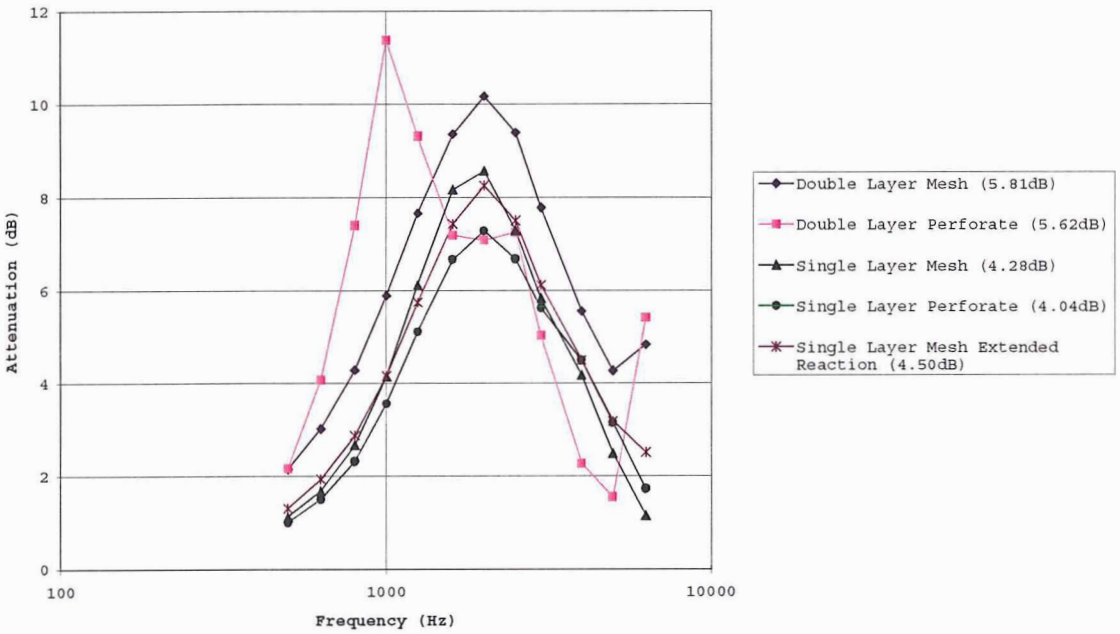

APPENDIX 5 - Tests and Analysis - Hybrid Active/Passive Lining Concept Hersh Acoustical Engineering, Inc.

Introduction

Under Boeing Purchase Order #JR5935 (Task 4 under NASA Contract NAS1-97040) , Hersh Acoustical Engineering, Inc. (HAE) has undertaken a four-part initial investigation of simplifications that might be applied to active control of rotor/stator tones in turbofan engine inlets. The underlying concept upon which this investigation was based assumed that only a subset of the total number of cut-on modes would have a significant impact on sideline tone nose. If this subset could be controlled with a less extensive array of active control actuators than required by the full sound field, reduced active control system complexity and space/weight would be achieved.

The four major parts of the project were as follows:

1. Design and constuct a static test facility for generating and measuring multiple spinning order and multiple radial order propagation modes in a circular duct.
2. Establish microphone arrays and signal processing systems for simultaneous measurement of in-duct and far-field radiated sound.
3. Design and fabricate a linear microphone array to be mounted alongside the duct inlet and used as an error signal sensor for far-field radiation in specific directional sectors.
4. Install an active/passive hybrid liner in the test duct and incorporate it with the linear microphone array to assess feasibility of simplified ANC to suppress multi-radial order tones.

Test Facility Design and Construction:

48-Inch Test Duct:

The test duct, modeled after the ANCF inlet at NASA Glenn Research Center, has a 48-inch inside diameter and a total length of 96 inches, divided into two 48-inch sections. Each duct section is constructed of ½-inch thickness high density resin-impregnated cardboard cylinder, intended for use as concrete forms. Mating flanges were added to allow ease of fitting up and reinforcement of the circular cross section. To minimize shape distortion due to gravity and to allow free-field measurements, the duct is oriented vertically, with the inlet opening though the lab roof as shown in Figure 1.

Although it is a no-flow facility, an inlet bell-mouth was incorporated to provided a realistic inlet radiation termination. To maintain similarity with the ANCF inlet, the mold used to make the ANCF bell-mouth was shipped to HAE and used as a form for an epoxy-covered foam unit of the same shape as the fiberglass unit at ANCF. The shape of the bell-mouth is shown in Figure 2.

Mode Synthesizer:

The useful operating range of the actuators employed in the hybrid liner is 400-1,250 Hz. In order to simplify existing active control systems, it was decided that a sound field of four radial orders should be addressed with an active liner element consisting of two rows of controlled sources. This combination of frequency range and mode requirement dictated that circumferential modes $m = 1$ or $m = 2$ should be used. Characteristics of these modes (plus the first cut-off mode) are shown in Table 1. Here α_{mn} are the hardwall duct eigenvalues, F_{co} is the modal cutoff frequency and ϕ is the effective propagation angle relative to the duct axis at a preselected frequency of 1228 Hz (corresponding to 2300 CRPM at ANCF).

Table 1 - Mode Characteristics Based on 1228 Hz Nominal Test Frequency

Circ. Order	$m = 1$			$m = 2$		
Radial Order	α_{mn}	F_{co} 48"	ϕ at 1228 Hz	α_{mn}	F_{co} 48"	ϕ at 1228 Hz
0	0.5861	164 Hz	7.7 deg	0.9723	272 Hz	12.8 deg
1	1.6972	474 Hz	22.7 deg	2.1346	596 Hz	29.0 deg
2	2.7172	759 Hz	38.2 deg	3.1732	886 Hz	46.2 deg
3	3.7261	1041 Hz	57.9 deg	4.1917	1171 Hz	72.4 deg
4	4.7312	1321Hz	Cut Off	5.2036	1453 Hz	Cut Off

The variation in propagation angle for mode $m = 2$ was selected for initial investigation, but capabilities for synthesis of both modes were incorporated into the system design.

In order to generate four radial order modes, a disk was designed containing five circular arrays of high quality 3-inch electrodynamic transducers (loudspeakers). The highest circumferential order mode that will propagate in the 48-inch duct at 1228 Hz is $m = \pm 11$. Aliasing considerations therefore dictate that for excitation of $m = 2$, a minimum of 14 actuators must be provided around each circular array. In practice, 16 actuators were provided in the three outer circles of the source array, as shown in Figure 3. However, for the two inner circles, the number was reduced to 8 actuators per circle, resulting in aliased radiation into mode $m = -6$, for which two radials are cut on.

The radial sound pressure distributions of target mode (2,0) and potential aliased mode (6,1) are presented in Figure 4. Near the center, the mode strength of (6,1) is weak compared to that of (2,0), although for the second loudspeaker circle ($r/R = .3958$) the difference is only about 1.7 dB. Thus, a mode combination that relies heavily on this row would be expected to have significant contamination by mode $m = -6$ and should be flagged for avoidance.

Signal distribution to the five loudspeaker circles is accomplished with a computer-controlled analog network as shown in Figure 5. A master oscillator signal is split into quadrature components by a 90° offset network. Analog four-quadrant multipliers (Analog Devices AD532) are used to establish the real and imaginary components of the array drive signals under DC control from a digital to analog converter. The drive signals for the individual arrays are again split into quadrature components and then further split into 0°, 90°, 180° and 270° busses by means of inverting amplifiers.

Each loudspeaker is driven by an individual 15-watt amplifier with a summing junction. Input summing resistors of conductance proportional to $|\cos(m\theta)|$ and $|\sin(m\theta)|$ (where θ is the angular position of the speaker and m is the circumferential mode order) are connected to the appropriate signal buss to achieve the $e^{im\theta}$ spinning excitation for the array. An example for achieving a 315° loudspeaker output signal is shown in Figure 6.

In-Duct Mode Measurements:

A microphone rake was designed and fabricated for measuring the radial, azimuthal and axial distribution of sound pressure in the test duct. Ten miniature condenser microphones are located on a radial arm at equally spaced radii 3 to 23 inches. This arm pivots about the duct center and can be positioned axially via a track system. Signals from the microphones are digitized and cross-correlated with quadrature reference signals to obtain absolute amplitude and phase as shown in the block diagram of Figure 7. A single measurement consists of recording radial pressures at 24 angles on 15° increments. Circumferential modes at each radius are computed by a spatial Fourier transform. Radial decomposition of each circumferential mode is computed as a least squares fit to the basis functions

$$J_m(\pi\alpha_{mn}\frac{r}{R})$$

where α_{mn} are the hardwall mode eigenvalues.

In principle, the ten microphones would allow resolution of up to ten radial orders. However, only six radials (one more than the maximum cut on for any circumferential order) are included in the least-squares computation.

Far Field Measurement System:

As shown on Figure 1, the far field measurement is accomplished on the lab roof with a single microphone moved along an arc at a distance 6 radii (12 ft) from a reference point near the inlet bell-mouth to duct transition at the center of the duct. The measurements are taken using a Rion NA-29 precision sound level meter with ½-inch condenser microphone. The signal output of the NA-29 is digitized and cross-correlated with quadrature reference signals to obtain amplitude and phase as for the in-duct microphones. Each measurement is an average of three to five individual readings to allow for minor variations due to atmospheric disturbances. Measurements are taken on an arc from 0° to 105° in 5° increments.

Mode Synthesis System Calibration:

For reference, the four radial modes at m = 2 targeted for radiation by the mode synthesis system are shown in Figure 8. The mode synthesis system was calibrated for generation of specific radial order modes by the following procedure:

1. The rotating microphone rake was positioned at an axial reference 84 inches from the plane of the synthesizer source.
2. Each of the five loudspeaker rings on the source was activated in sequence with control amplitude (5.0 + 0.0*i*) and the amplitude and phase of the radiated modes was measured with the rake.

3. A system of 5 equations in N (<5) unknowns was solved to provide a minimum norm ring excitation vector for each of the N cut-on radial modes.
4. The modal drive vectors were stored in the synthesizer control program.

Observe in Figure 8 that the ring at r/R = .39 is located close to a nodal circle for mode (2,3) and the ring at r/R = .75 is close to a nodal circle for mode (2,1). Poor modal coupling is expected for these combinations.

Measured modal amplitudes (complex) are shown in the following tables. A summary, showing SPL only, is presented in Figure 9.

Table 2 - Radial Mode Amplitudes for m = 2 1228 Hz, Ring at r/R = .9167

Radial Order	Real	Imaginary
0	0.46314689	2.1170874
1	-1.8544016	0.46812057
2	-1.2366257	1.7544158
3	0.63846207	-3.0299787
4	-0.069316579	0.036991828
5	-0.075379865	-0.002928982

Table 3 - Radial Mode Amplitudes for m = 2, 1228 Hz, Ring at r/R = .7500

Radial Order	Real	Imaginary
0	-0.04961697	1.7046361
1	0.11647735	-0.075199437
2	2.3356021	-1.3921607
3	-2.8332281	6.2587749
4	0.082525076	-0.07393977
5	0.08949218	0.13130459

Table 4 - Radial Mode Amplitudes for m = 2, 1228 Hz, Ring at r/R = .5833

Radial Order	Real	Imaginary
0	0.38172216	0.96099738
1	2.0703876	-0.66168278
2	0.6721825	-1.5043112
3	-0.61601518	-4.1768641
4	-0.032007551	0.03986563
5	-0.071255363	-0.044649256

Table 5 - Radial Mode Amplitudes for $m = 2$, 1228 Hz, Ring at $r/R = .3958$

Radial Order	Real	Imaginary
0	0.1748744	0.20718574
1	1.0486539	-0.50273155
2	-0.68697006	1.474515
3	-0.007250865	-0.34829738
4	-7.77628E-05	-0.008053407
5	-0.000728595	0.004134448

Table 6 - Radial Mode Amplitudes for $m = 2$, 1228 Hz, Ring at $r/R = .2708$

Radial Order	Real	Imaginary
0	0.14893129	0.25747607
1	0.79314236	0.35062669
2	-1.8952537	0.62643183
3	-2.9997514	2.9749977
4	0.14678428	0.02820488
5	-0.055210458	0.10412994

In Figure 9 are seen the modal amplitudes (in dB re .00002 Pa) produced by driving individual source rings. One may observe the "dropouts" of (2,1) for $r/R = .75$ and (2,3) for $r/R = .39$ as predicted in Figure 8. Also observe the general weakening of (2,0) as r/R decreases and the generally (except at $r/R = .39$) high value of (2,3), owing to its low cutoff ratio. Cutoff modes (2,4) and (2,5) are typically suppressed 30 dB. The residual is due to minor alignment fluctuations in the rake axis.

The result of the modal excitation vector computation is presented in Table 7. Linear combinations of these individual modal drives may be applied to provide any combination of mode amplitudes and phases desired at any point in the duct.

Table 7 - Speaker Ring Drive Vectors for 1 Pa Mode Amplitude at 0° Phase, Axially 84 inches from Source Plane

r/R	(2,0)	(2,1)	(2,2)	(2,3)
.92	0.3270 - 1.1607i	-0.6058 - 0.0537i	-0.1855 - 0.3117i	0.0391 + 0.1375i
.75	-0.0728 - 0.8662i	-0.0524 + 0.0218i	0.4005 + 0.2323i	-0.1145 - 0.2847i
.58	0.2776 - 0.6972i	0.9426 + 0.4279i	0.1444 + 0.2434i	0.0087 + 0.2808i
.39	0.1339 - 0.2970i	0.7608 + 0.3585i	-0.2199 - 0.5398i	0.0459 - 0.0298i
.27	-0.0613 - 0.2301i	0.6420 - 0.3824i	-0.7455 - 0.2264i	-0.1900 - 0.2438i

Figure 10 shows a general indication of the modal isolation achieved by the above procedure. These are radial mode separations from a single rake angle (i.e., no m-order separation) and therefore include some effects of modal spillover. It is still clear that the modal isolation procedure is effective and will provide a means for evaluating liner and control function using mode mixture as a test parameter. Figure 11 shows the full mode measurement for excitation of Mode (2,0). Note that on a sound power basis, the target mode is isolated by nearly 30 dB from the other $m = 2$ radials. Spurious m-orders are suppressed approximately 20 dB and are partly the result of rake-axis fluctuation.

Modal Propagation Investigation:

Setting the mode mixture at arbitrary axial position requires verification of modal propagation characteristics within the duct. To accomplish this, the outer source ring ($r/R = .92$) was driven and the full mode measurement procedure was undertaken at several axial positions of the rake. The amplitude and phase of each radial order mode was plotted (Figure 12 and Figure 13) and a regression analysis was used to determine the wave number for each mode. In Figure 12, the mode amplitudes are seen to be reasonably independent of axial position and the two cut-off modes are suppressed 25 dB. Figure 13 shows that the phase vs axial distance is virtually a perfect straight line with all collapsing to nearly 0° at the origin (note that the phases of the odd n modes were offset 180° to allow easier comparison). Wave-numbers computed from the measured phase rates and predicted from the duct geometry are shown in Table 8. Agreement is within 1% except for mode (2,3), which is barely cut-on and therefore most sensitive to errors in temperature measurement or small non-zero duct boundary admittance.

These results verify both that propagation in the test duct exhibits circular duct spinning mode characteristics and that the bell-mouth termination as installed at ANCF and on the test ducts essentially eliminates reflections.

Table 8 - Measured and Predicted Axial Wavenumbers at 1228 Hz

Mode	Measured k_z (m^{-1})	Predicted k_z (m^{-1})
(2,0)	22.13	22.10
(2,1)	19.91	19.81
(2,2)	15.79	15.69
(2,3)	7.11	6.85

Radiation Directivity:

Since the program objective is to develop an error sensing array that allows far-field directivity control, a prediction and measurement was made to determine far-field radiation properties of the test facility. In addition, as an aid in the design process, the sound field was computed in the proposed error array location to determine the relationships between the quasi-near-field and far-field.

The predictions were computed by W. Eversman. Complex sound pressure amplitudes were tabulated for radii 4 to 6 ft in 3-inch increments and then at radius 12 ft.to represent the far field. Approximately 800 angular positions were computed for each radius, from 0° (duct inlet axis) to 120°. A sampling of the prediction results ($r = 4$, 6 and 12 ft) is presented in Figure 14

From Figure 14 it is clear that the directivity pattern evolves from the near to far field, so that error measurements taken within the 4 to 6 ft radius zone will require processing to allow use for controlling far-field radiation patterns.

As an initial check on the predictions and the roof-top measurement system, the mode synthesizer was set to generate the modes (2,0) – (2,3) in succession and measurements of SPL at 12 ft radius were taken on 5° increments from 15° to 105°. (Angles 0° – 10° were omitted due to difficulties with the positioning system.)

The predicted and measured SPL were plotted as shown in Figure 15. Although there are some deviations, the general trends agree very well. Some of the variations in detail are attributed to the imperfect radial mode isolation and contamination by spurious m-orders, which are suppressed by only 20 dB.

Boom Microphone Design:

A linear microphone array was designed using an airfoil shaped tube as a mount and six miniature condenser microphones spaced over a 6-foot span. Various spacing patterns are being investigated. Preliminary measurements were taken with uniform spacing, but a better mode separation capability appears to result from a logarithmic spacing as shown in Table 9 and Figure 16.

Table 9 - Example of Microhone Weightings For Radial Mode Separation from Linear Boom Array

Mic Elev\Mode	(2,0)	(2,1)	(2,2)	(2,3)
2	1.0000	-0.6790+0.5544i	0.2637+0.5442i	-1.2664-0.2043i
2.64	-0.0694-0.4109i	0.3322+0.2686i	0.3227-0.2754i	-0.3709+0.9409i
3.48	-0.0940-0.9019i	0.4332+0.5527i	0.2252+0.1089i	0.7404+0.4627i
4.59	0.3950-0.1980i	-0.3506+0.3572i	-0.3397+0.1926i	-0.8708+0.2756i
6.06	1.1929-1.1933i	-0.2064+1.0080i	1.0121+0.1048i	-0.2181+1.0388i
8	-1.3353+0.0405i	0.4996-1.3168i	-0.4780-0.0164i	0.2316-0.3856i

Hybrid Liner Installation:

The hybrid liner used for the tests has been extensively described in (Parente *et al*) "Hybrid Active/Passive Jet Engine Noise Suppression System," NASA CR-1999-208875, February, 1999. It is a 24-inch long, 48-inch diameter duct section divided into two segments. Segment 1 is two rows of 16 each active Helmholtz resonators, with 2-inch diameter orifices spaced axially 5.5 inches and circumferentially 22.5°. Segment 2 is a 14-inch long linear passive liner with a wire mesh face sheet and a 2.2-inch deep honeycomb core. The liner is installed in the test duct with the active segment facing the source.

The original design of the hybrid liner was directed at controlling modes (4,0) and (4,1) at 1000 Hz. The "upstream" active segment redirects energy for more effective absorption by the passive segment. For the two-mode environment, attenuation of both modes by over 30 dB has been achieved.

Active Control System Implementation:

Active control for the study was implemented using a variation of the Adaptive Quadrature algorithm. At the system excitation frequency, transfer functions from the actuators in the active resonators to the error microphone array(s) are measured directly (Figure 17) and then inverted to determine an excitation matrix to minimize the error signal.

In order to simplify control processing, signals to the resonator actuators are pre-processed to modal phase relationships (45° retard per actuator for 16 resonators at mode $m = 2$). This allows the controller to "view" each resonator row as a single source in the axisymmetric environment. If multiple circumferential order modes were to be controlled, a separate distribution network would be applied for each mode and the signals summed at the actuator amplifier.

Far Field Control Demonstration:

As an initial demonstration, a far field microphone was positioned at radius 12 feet, polar angle 45° and azimuth approximately 270° relative to the duct inlet reference. The linear "boom" microphone array was set up parallel to the duct axis 4 feet to the side at an azimuth angle of 190° and with the uppermost microphone on the array 6 feet above the duct highlight. The far field and boom microphones were placed at different azimuths to minimize the probability of a false success indication from interference between spill-over *m*-order modes.

The control system was set up using the upper three microphones in the linear array as independent error signals. The mode $m=2$ drives to each of the two active resonator arrays in the hybrid liner were used as control signals.

The mode synthesizer system was set to excite predominantly mode (2,2), which is well cut on and has a strong radiation lobe in the direction 40 45°. Measurements of the SPL at 1228 Hz were made at the far field microphone and at each of the upper three boom microphones for control on and control off conditions.

Preliminary indication was that with 2x2 control (upper two boom microphones only), the control system reduced the SPL at the error sensors by over 30 dB and reduced the far-field radiated tone SPL by 7-8 dB. Final tests, conducted with gusty winds affecting the microphone positions and propagation, showed 18-22 dB tone reduction at the two upper boom microphones and 2.0-3.3 dB tone reduction at the far field microphone.

For reference, the results of the final roof-top demonstration test are shown in Table 10

Table 10 - Summary of Far-Field Attenuation Test Results

Condition	Far Field SPL	Boom Mic	Boom Mic SPL
Control Off	70.5	B1	77.1
Control 3x2	68.5	B1	57.1
Control Off	70.1	B2	75.3
Control 3x2	68.0	B2	58.8
Control Off	70.2	B3	72.8
Control 3x2	67.5	B3	73.4
Control 2x2	67.2	B1	55.0

Summary and Conclusions:

The roof-top static 48-inch test duct facility was designed, constructed and calibrated for radiation of modes (2,0) - (2,2) either in isolation or in combination.

Radiation characteristics for the individual modes were computed in near and far field.

A linear microphone array and signal processing system were designed to sample the near sound field and provide control system error signals relating to far-field radiation.

Far field sideline radiation suppression was demonstrated using a Hybrid active/passive liner employing two rows of active Helmholtz resonators to control a four-radial in-duct sound field.

Concept Extension and Refinement:

Under NASA Langley NAS1 99059, the mode generation and sound field sensing concepts developed and studied for feasibility under this program are being extended to include full use of the near-radiation field mode separation and to control multiple circumferential modes and BPF harmonic tones simultaneously.

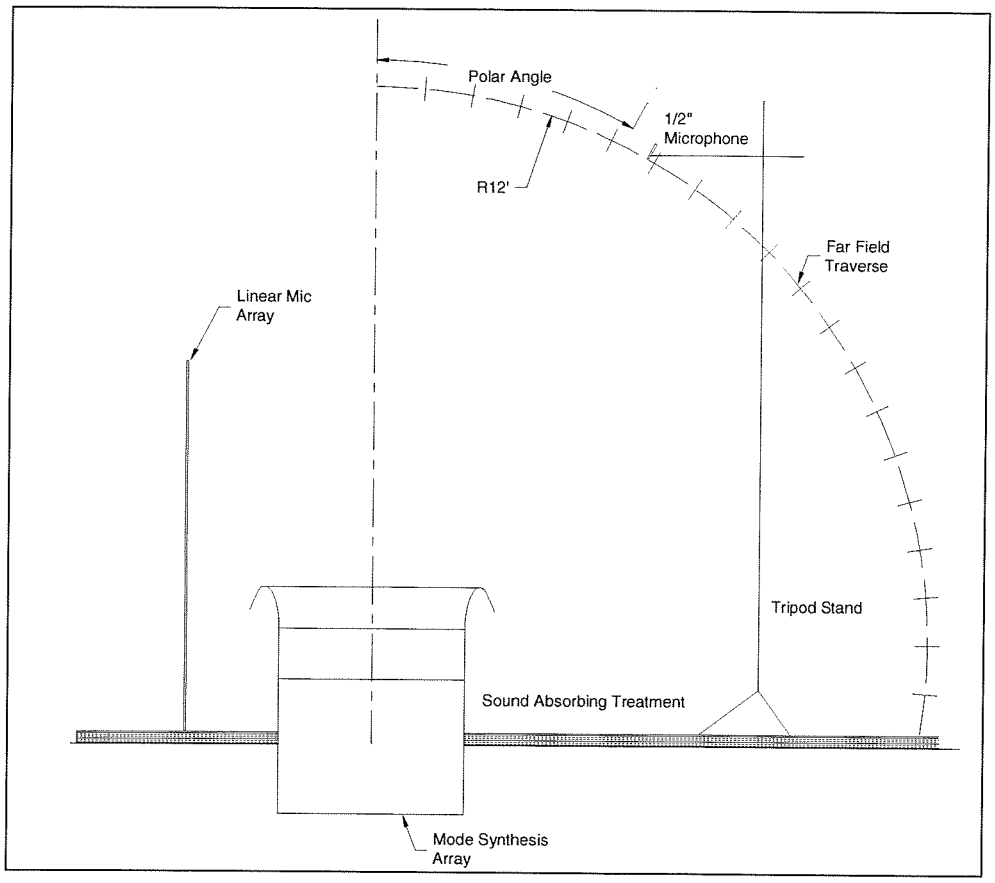

Figure 1 - Schematic of Roof-Top Measurement System with Vertical Axis Duct

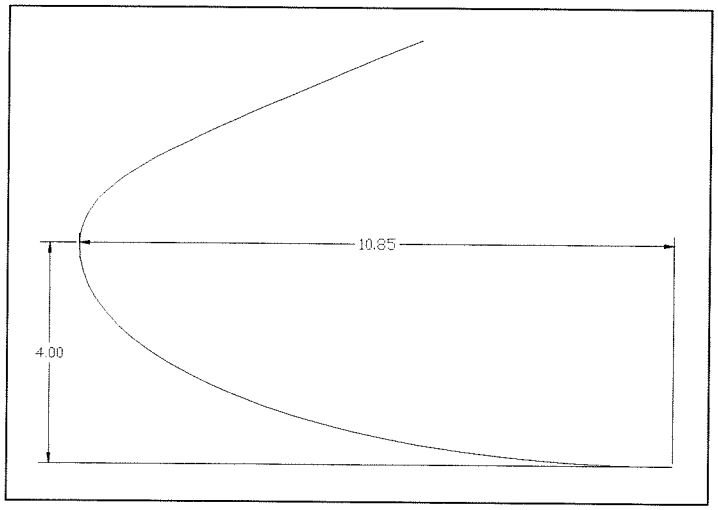

Figure 2 - Section Through ANCF Bell-Mouth

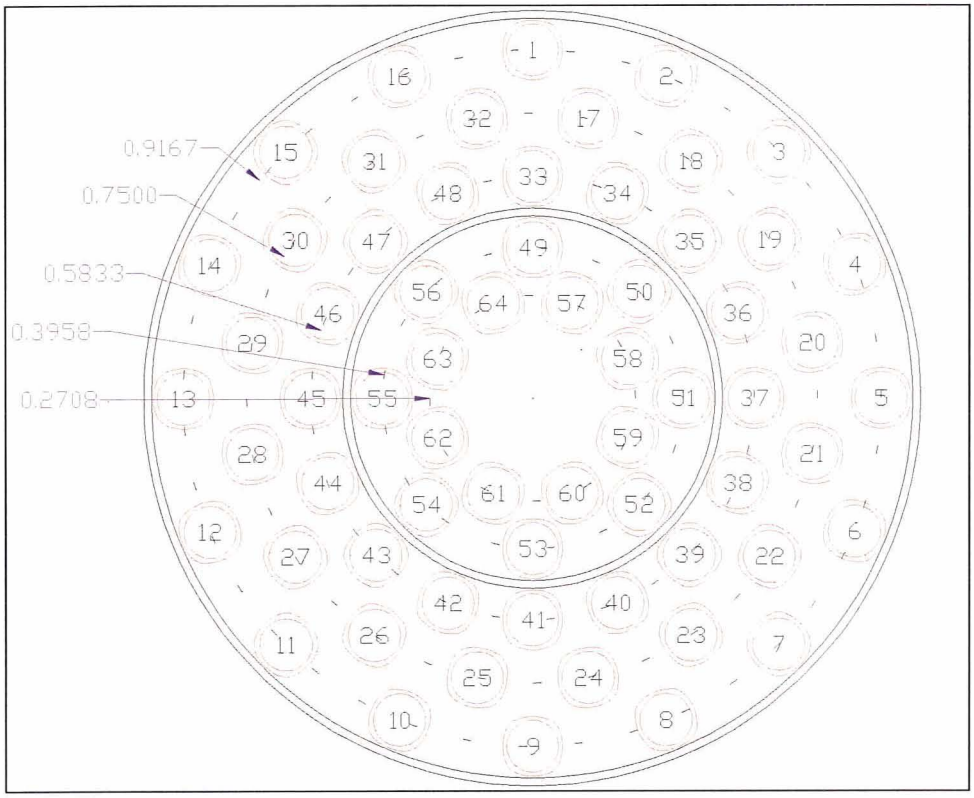

Figure 3 - Mode Synthesizer Transducer Layout Showing Radius Ratios of Mounting Circles

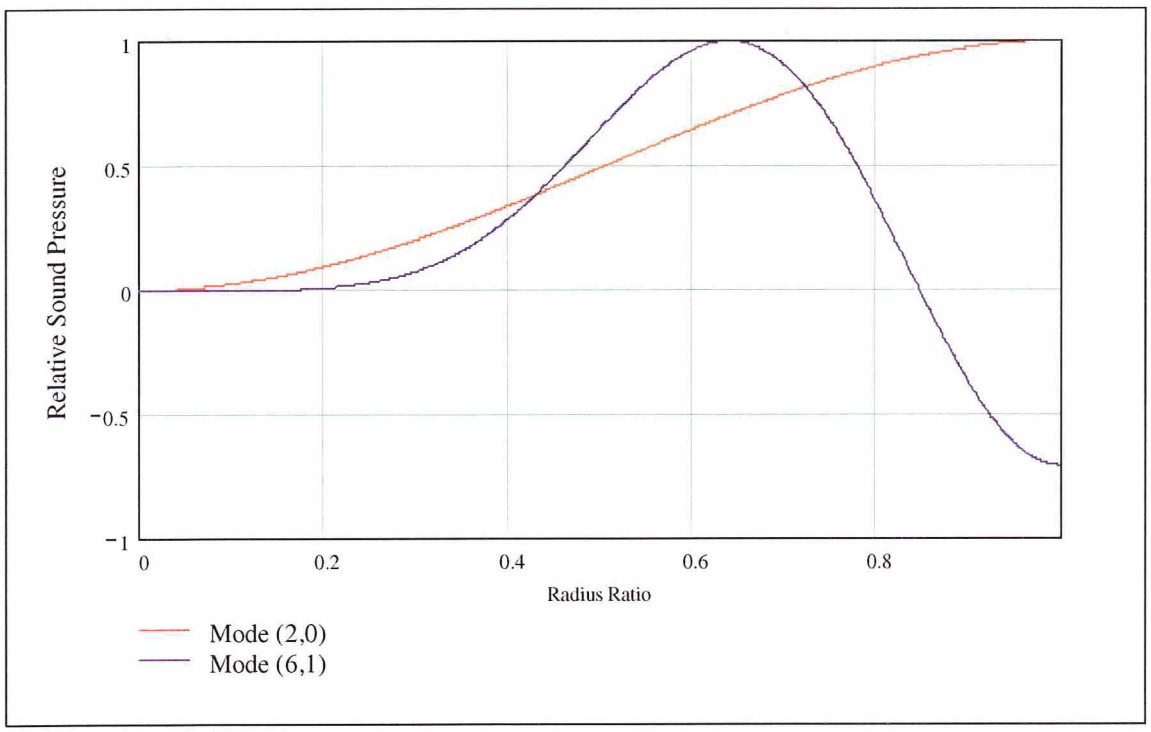

Figure 4 - Comparison of Modes (2,0) and (6,1) re Coupling Near Origin

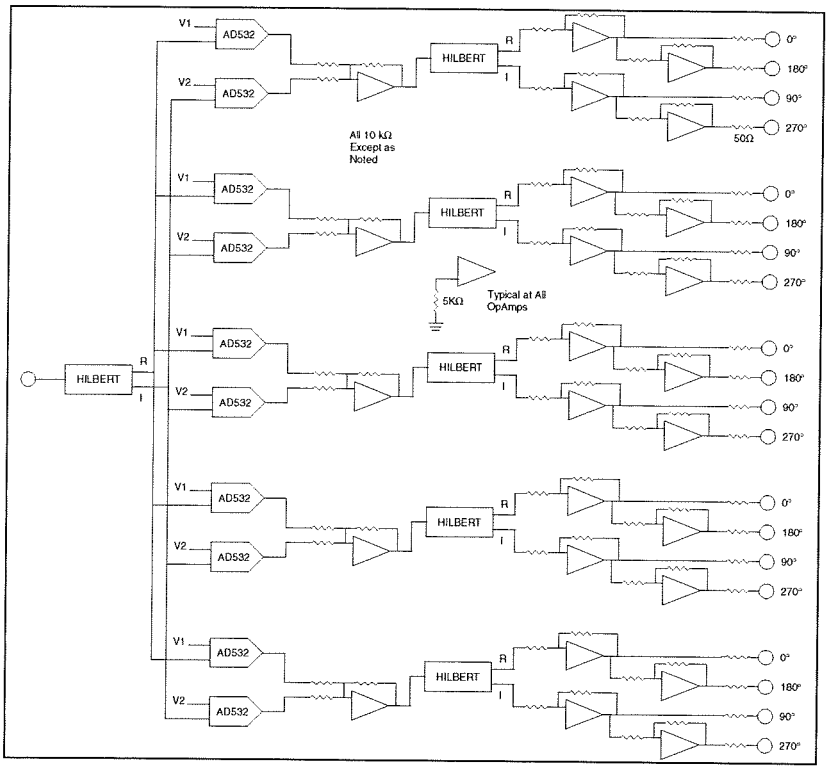

Figure 5 - Modal Synthesis Signal Distribution Network

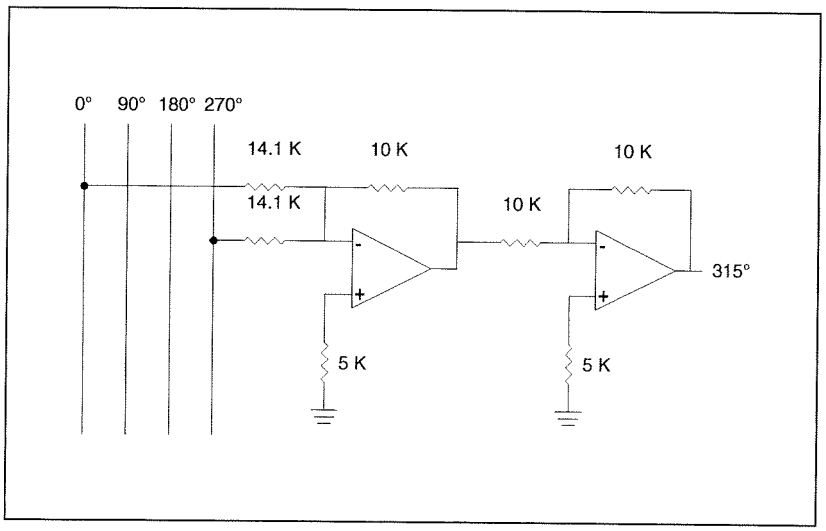

Figure 6 - Summing Input Power Amplifier Example for 315°

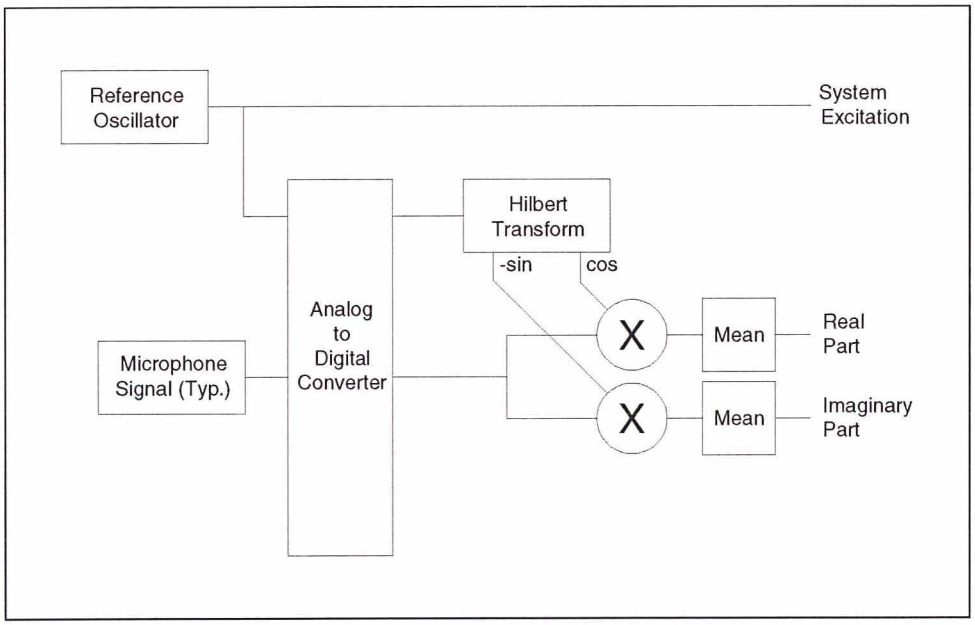

Figure 7 - Block Diagram of Microphone Signal Processing Channel

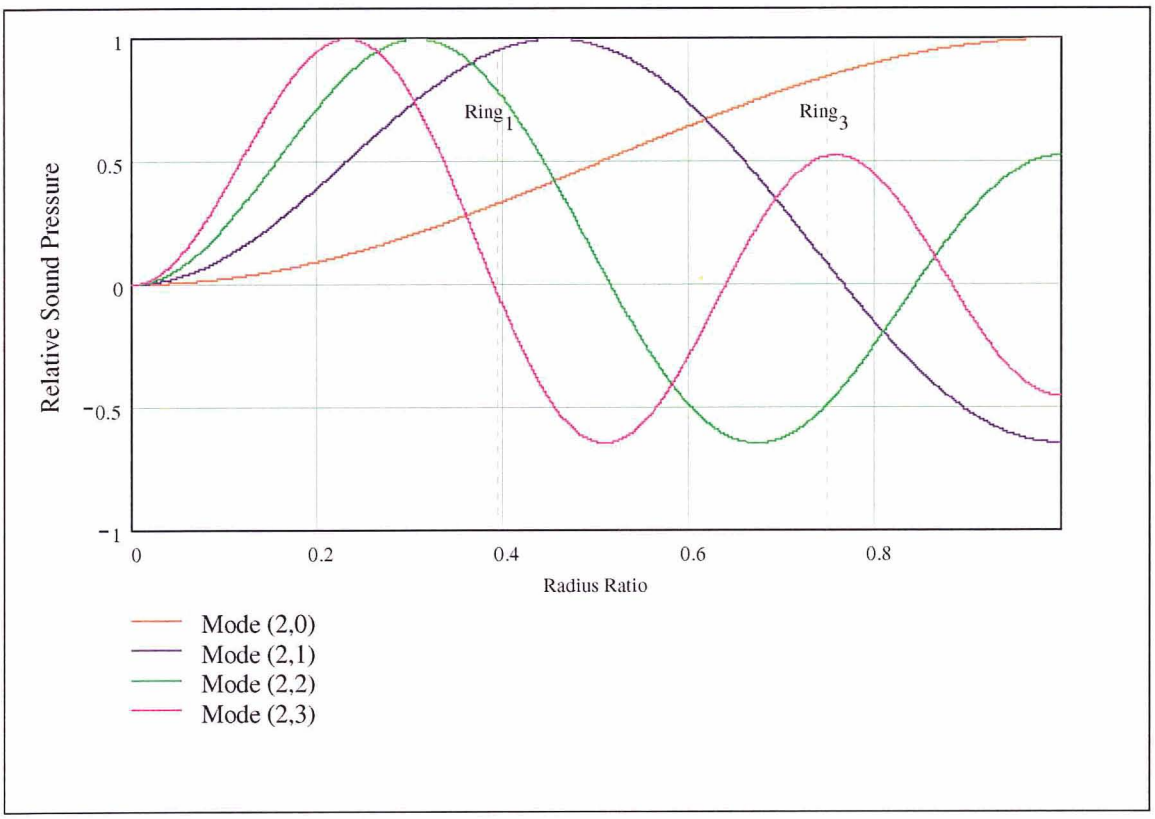

Figure 8 - Mode Shapes for m = 2 Cut On Radials

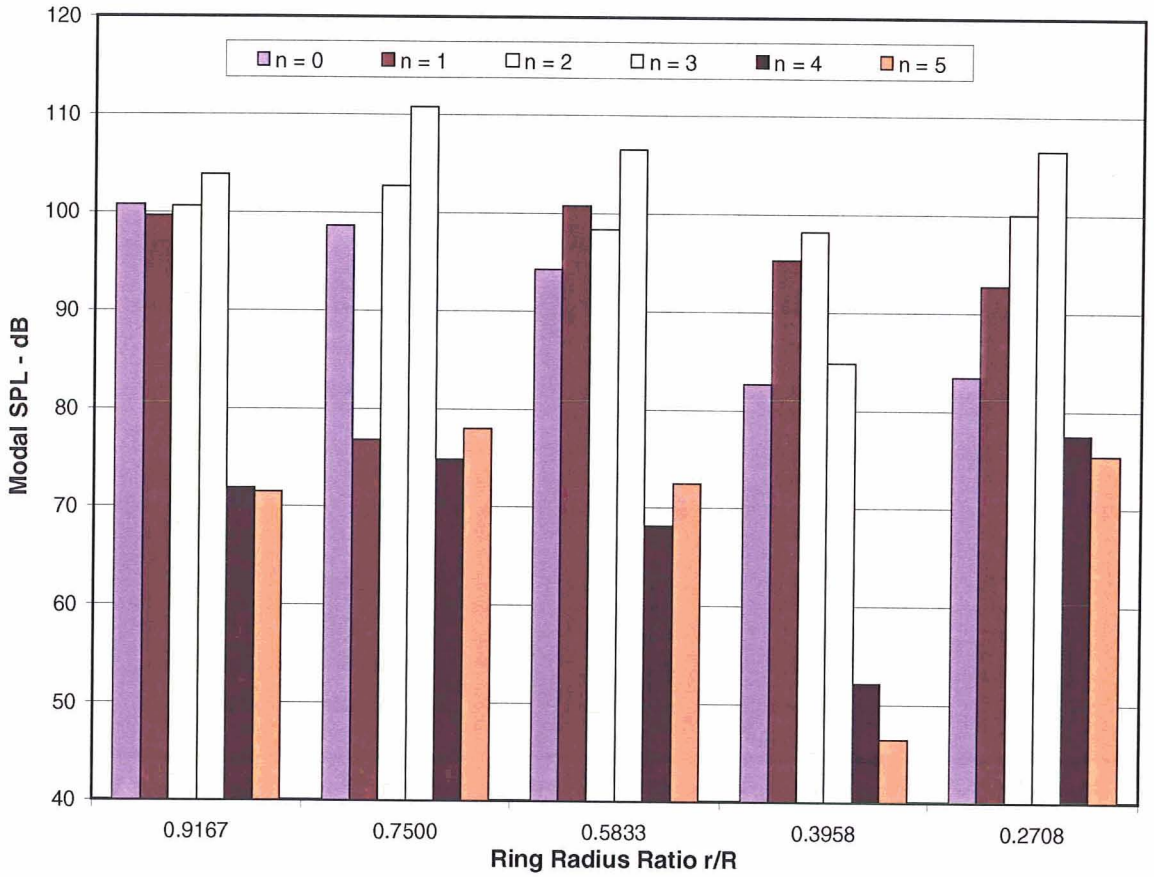

Figure 9 - Relative SPL of Radial Modes for $m = 2$ at 1228 Hz as a Function of Excitation Radius

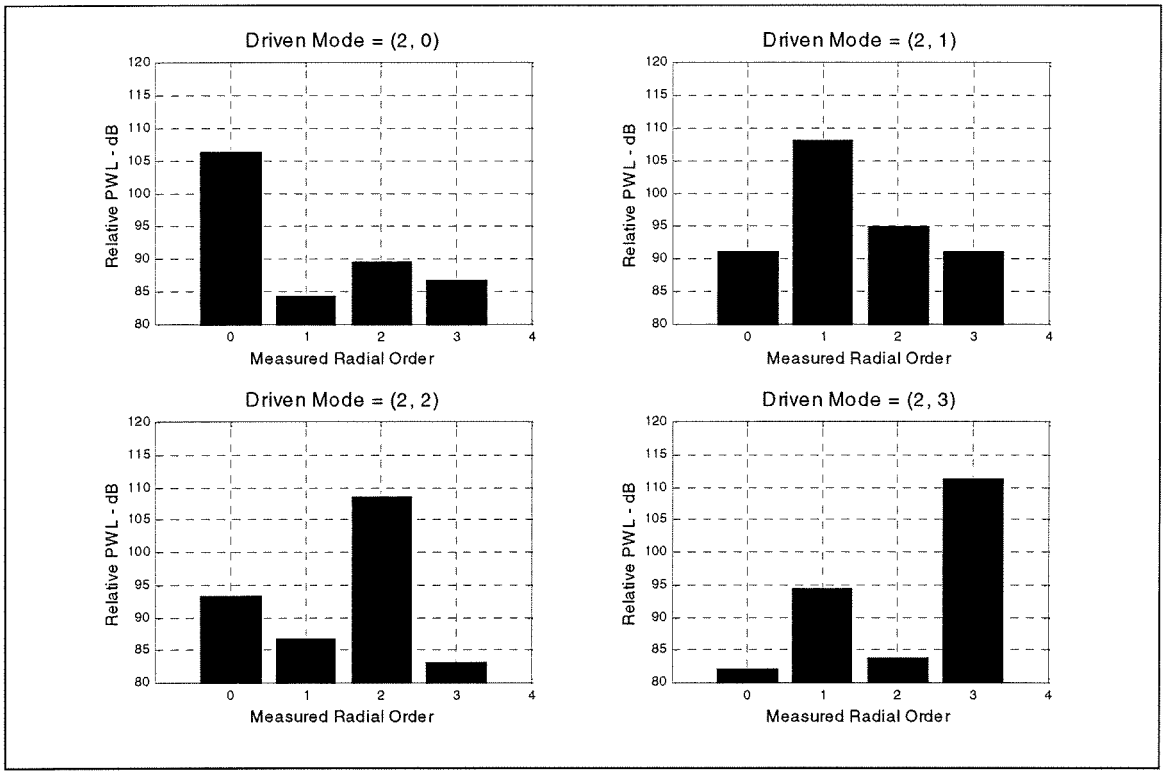

Figure 10 - Modes Measured at Single Rake Angle vs Modal Excitation Vector

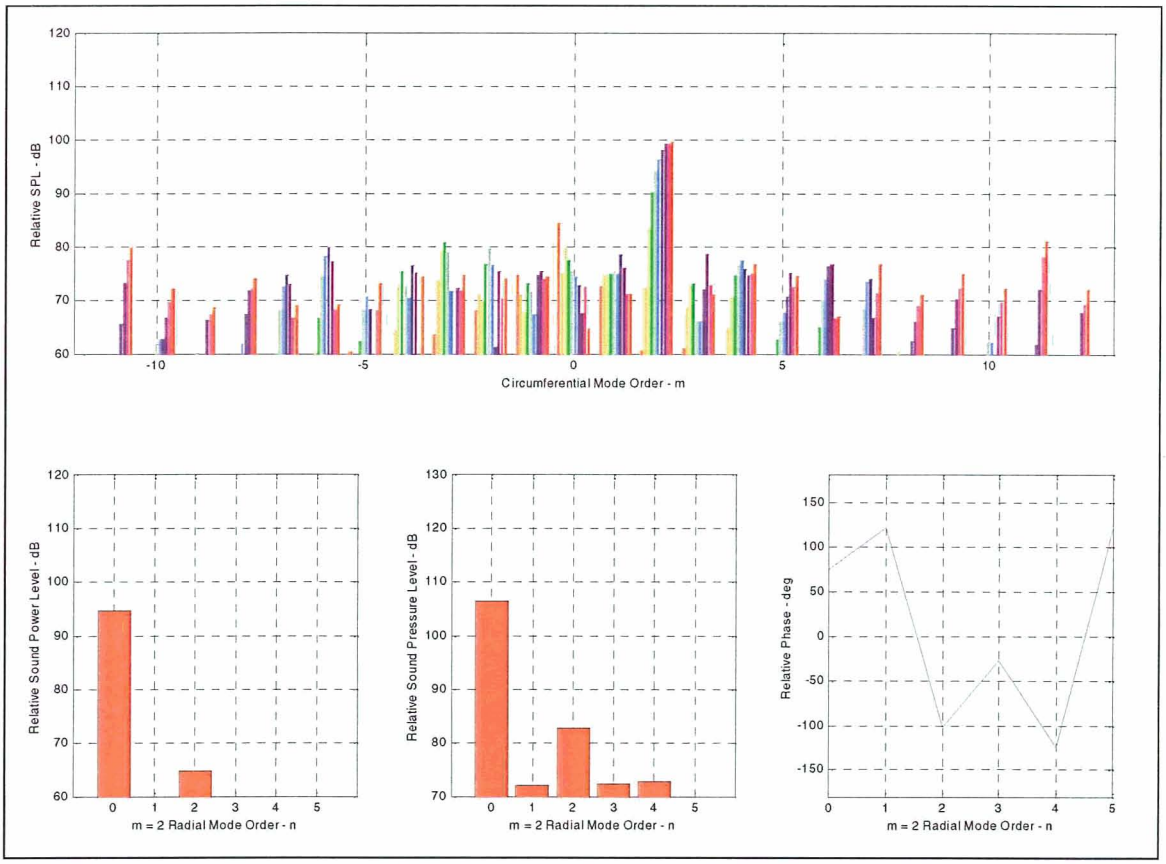

Figure 11 - Isolation of Mode (2,0) and Measured *m*-Order Spillover

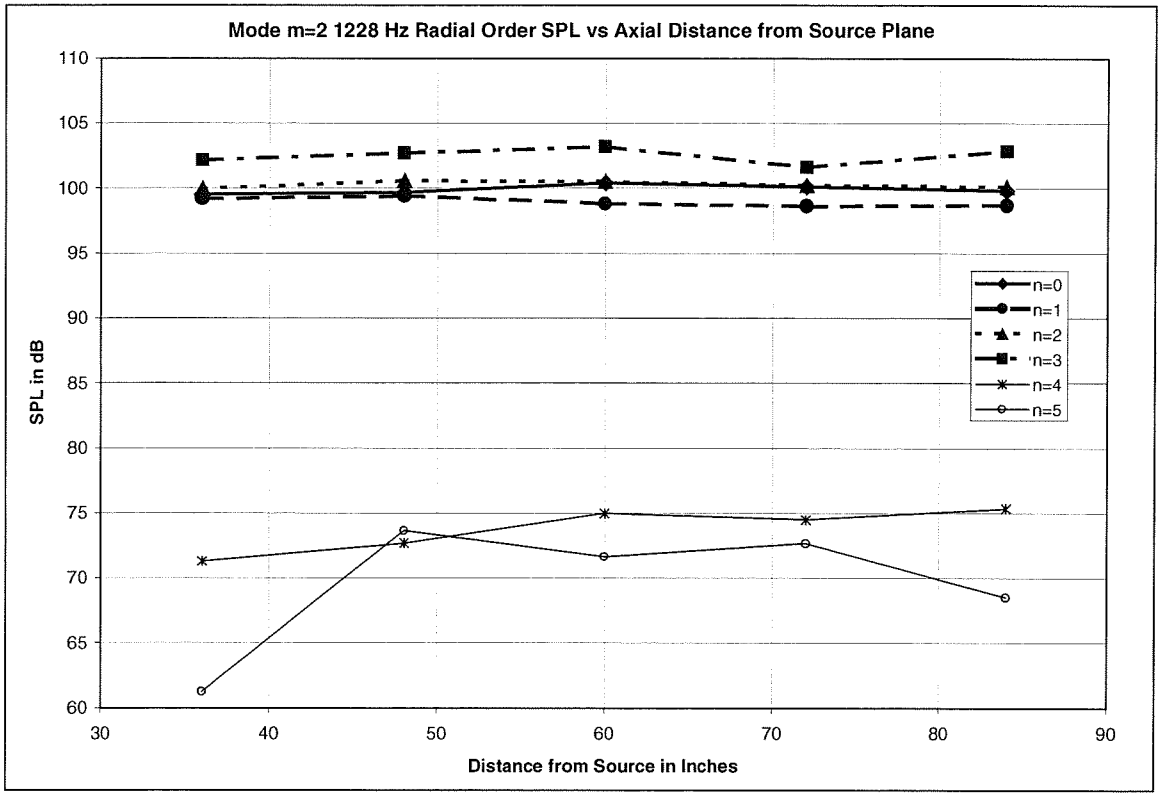

Figure 12 - Amplitudes of m = 2 Radial Modes vs Distance from Source Plane

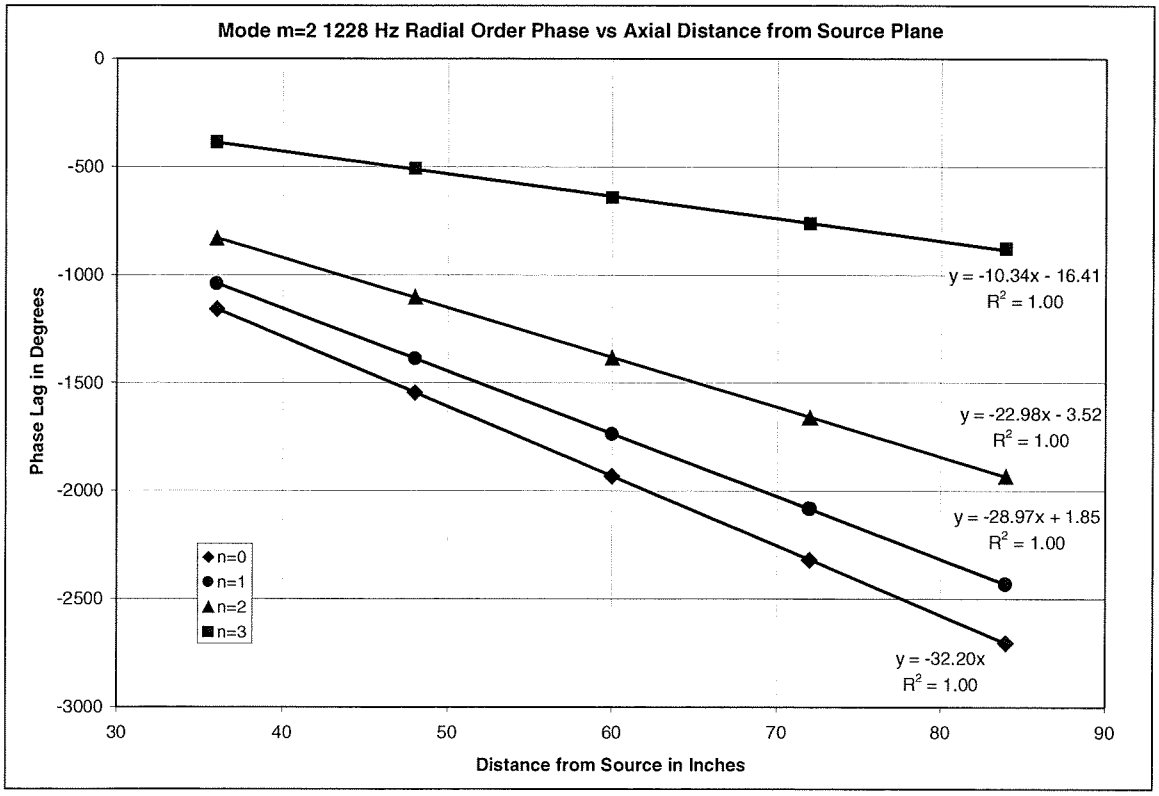

Figure 13 - Measured Propagation Rates for *m* = 2 Radial Order Modes at 1228 Hz

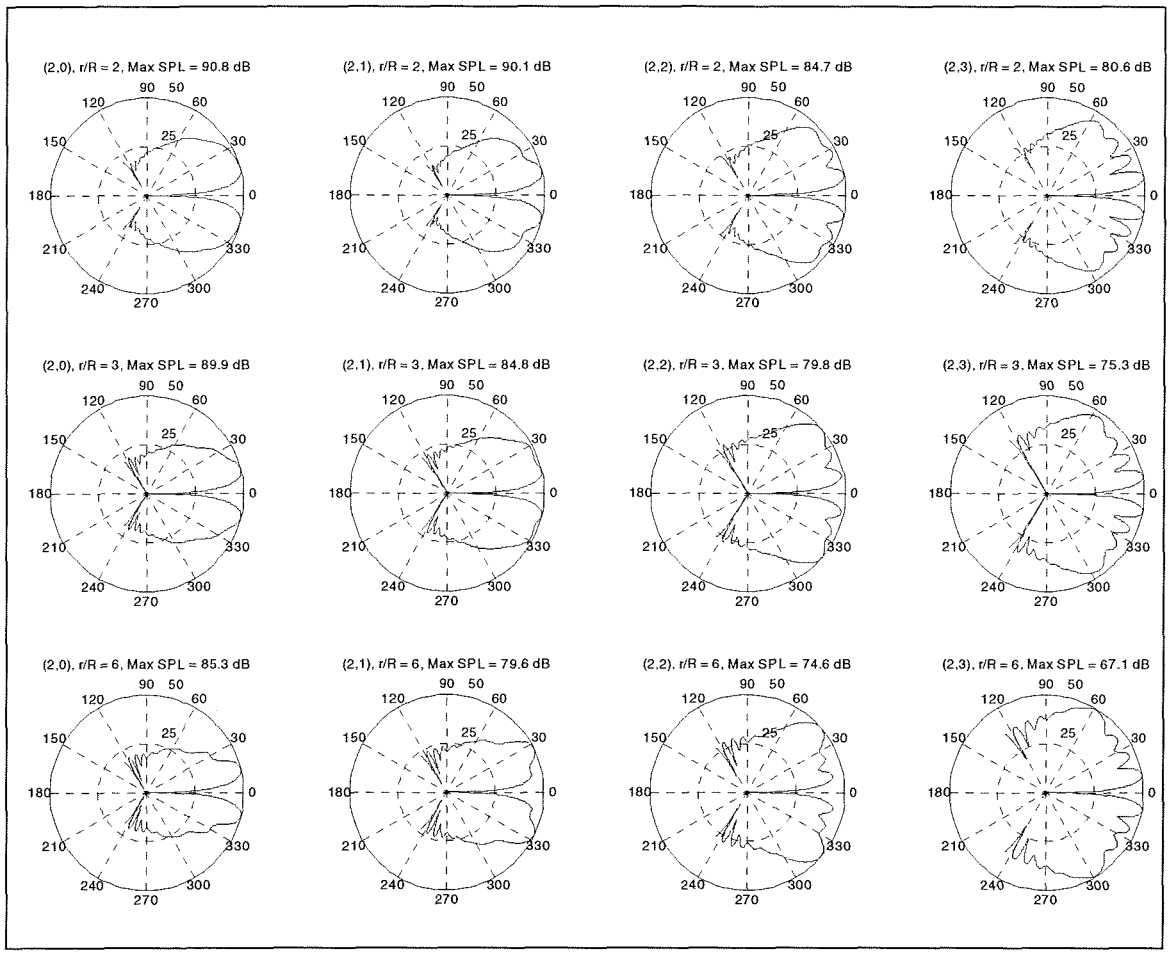

Figure 14 - W. Eversman-Computed Directivity of Modes vs Distance at 1228 Hz

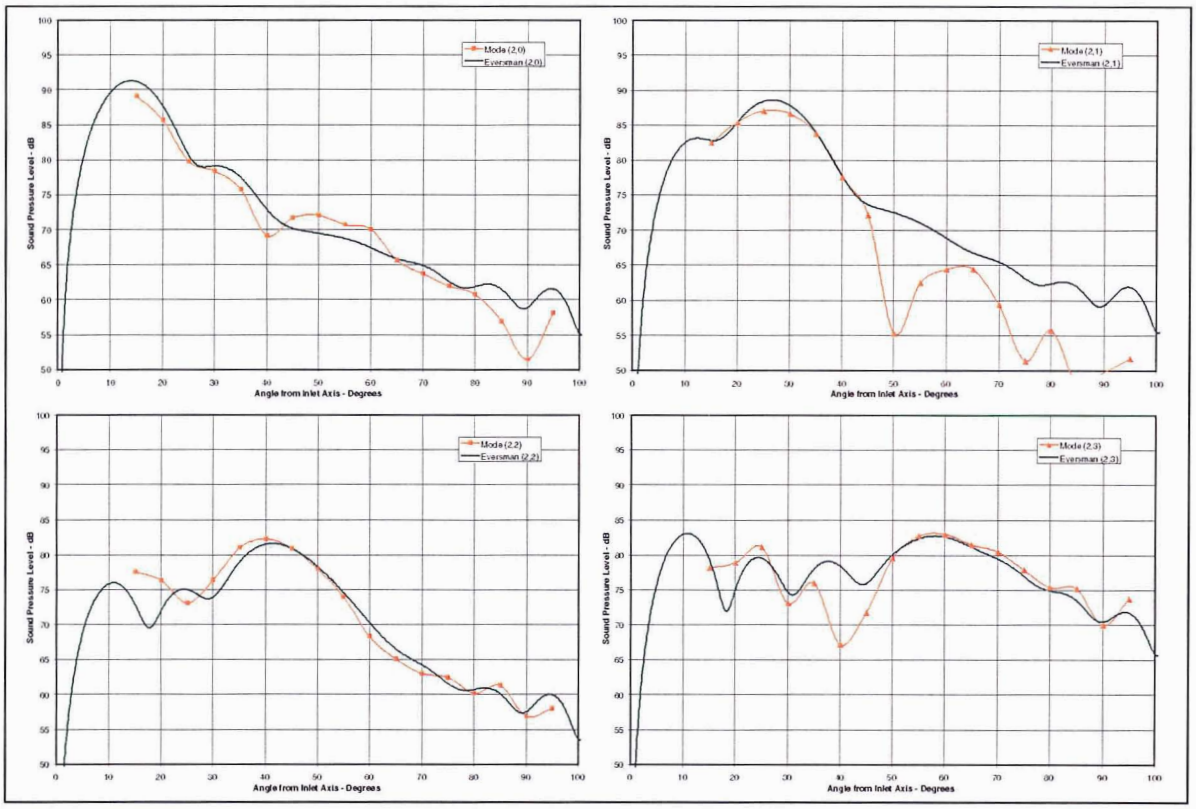

Figure 15 - Measured and Predicted Directivity at r/R = 6 for Modes (2,0) - (2,3)

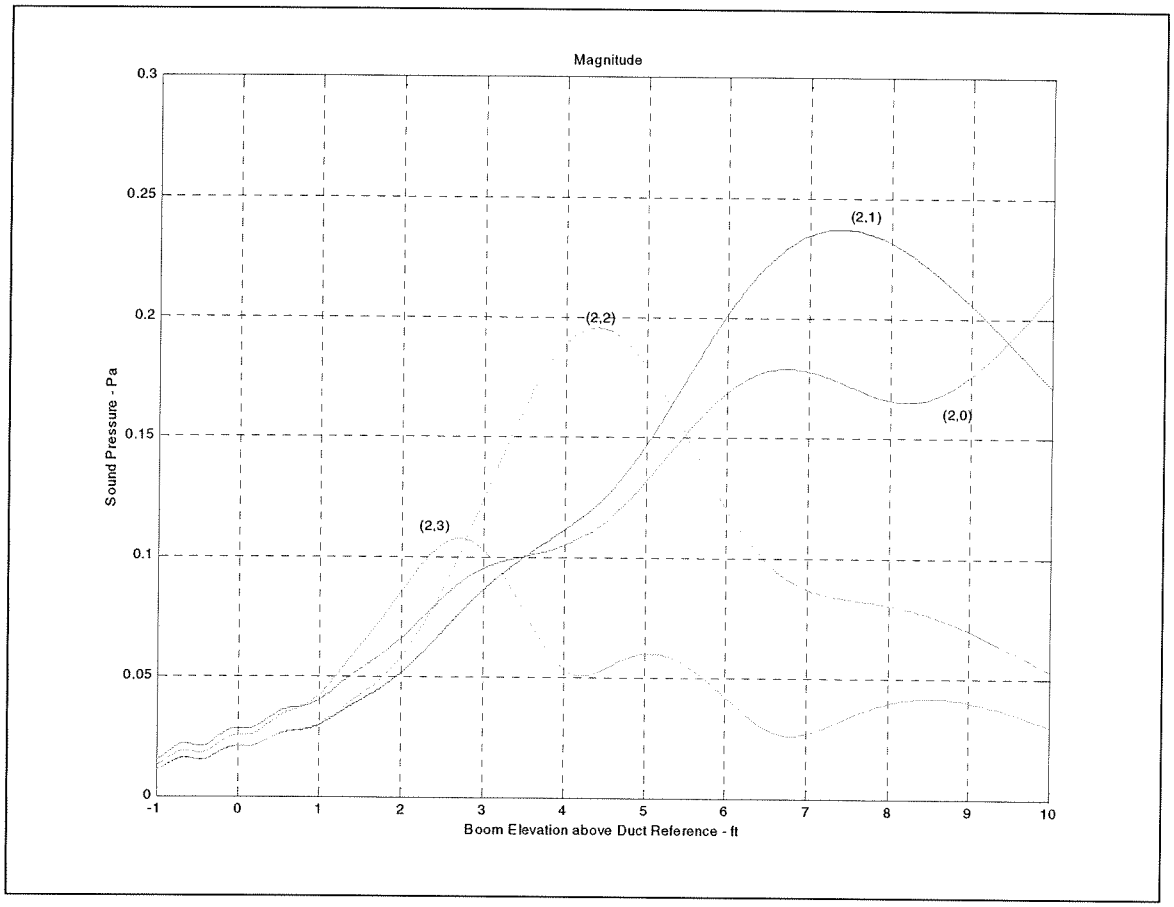

Figure 16 - Modal Pressure Amplitude Distribution along Linear Mic Boom

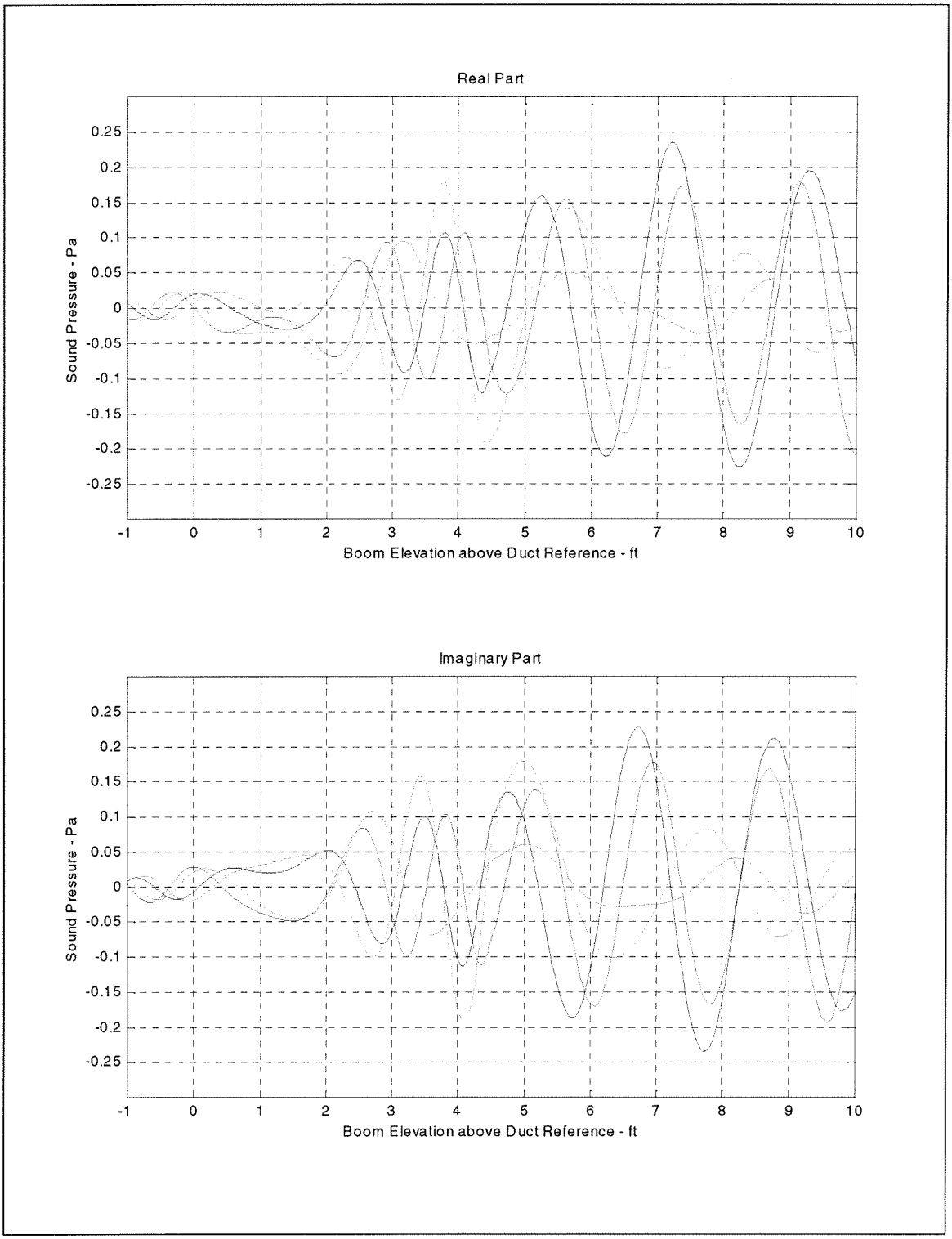

Figure 17 - Predicted Transfer Functions from Radial Modes to Boom Mic at 4 ft to Side of Duct Axis

REPORT DOCUMENTATION PAGE

Form Approved
OMB No. 0704-0188

1. AGENCY USE ONLY *(Leave blank)*	2. REPORT DATE	3. REPORT TYPE AND DATES COVERED
	August 2002	Contractor Report

4. TITLE AND SUBTITLE
Advanced Nacelle Acoustic Lining Concepts Development

5. FUNDING NUMBERS
NAS1-97040
Task 4

781-30-14-01

6. AUTHOR(S)
G. Bielak, J. Gallman, R. Kunze, P. Murray, J. Premo, M. Kosanchick, A. Hersh, J. Celano, B. Walker, J. Yu, H. W. Kwan, S. Chiou, J. Kelly, J. Betts, J. Follet, R. Thomas

7. PERFORMING ORGANIZATION NAME(S) AND ADDRESS(ES)
Boeing Commercial Airplane Company
Seattle, Washington 98124-2207

8. PERFORMING ORGANIZATION REPORT NUMBER

9. SPONSORING/MONITORING AGENCY NAME(S) AND ADDRESS(ES)
National Aeronautics and Space Administration
Langley Research Center
Hampton, VA 23681-2199

10. SPONSORING/MONITORING AGENCY REPORT NUMBER
NASA/CR-2002-211672

11. SUPPLEMENTARY NOTES
NASA Langley technical monitor: Tony L. Parrott

12a. DISTRIBUTION/AVAILABILITY STATEMENT
Unclassified–Unlimited
Subject Category 71 Distribution: Nonstandard
Availability: NASA CASI (301) 621-0390

12b. DISTRIBUTION CODE

13. ABSTRACT *(Maximum 200 words)*
The work reported in this document consisted of six distinct liner technology development subtasks: 1) Analysis of Model Scale ADP Fan Duct Lining Data (Boeing): An evaluation of an AST Milestone experiment to demonstrate 1995 liner technology superiority relative to that of 1992 was performed on 1:5.9 scale model fan rig (Advanced Ducted Propeller) test data acquired in the NASA Glenn 9 x 15 foot wind tunnel. The goal of 50% improvement was deemed satisfied. 2) Bias Flow Liner Investigation (Boeing, VCES): The ability to control liner impedance by low velocity bias flow through liner was demonstrated. An impedance prediction model to include bias flow was developed. 3) Grazing Flow Impedance Testing (Boeing): Grazing flow impedance tests were conducted for comparison with results achieved at four different laboratories. 4) Micro-Perforate Acoustic Liner Technology (BFG, HAE, NG): Proof of concept testing of a "linear liner." 5) Extended Reaction Liners (Boeing, NG): Bandwidth improvements for non-locally reacting liner were investigated with porous honeycomb core test liners. 6) Development of a Hybrid Active/Passive Lining Concept (HAE): Synergism between active and passive attenuation of noise radiated by a model inlet was demonstrated.

14. SUBJECT TERMS
Acoustic liner concepts, Aircraft Nacelles

15. NUMBER OF PAGES
205

16. PRICE CODE

17. SECURITY CLASSIFICATION OF REPORT	18. SECURITY CLASSIFICATION OF THIS PAGE	19. SECURITY CLASSIFICATION OF ABSTRACT	20. LIMITATION OF ABSTRACT
Unclassified	Unclassified	Unclassified	UL